Titre: Title:	Hydrodynamique des jets de gaz orientés vers le haut et vers le bas dans les lits fluidisés gaz-solide
Auteur: Author:	Pierre Sauriol
Date:	2011
Type:	Mémoire ou thèse / Dissertation or Thesis
Référence: Citation:	Sauriol, P. (2011). Hydrodynamique des jets de gaz orientés vers le haut et vers le bas dans les lits fluidisés gaz-solide [Thèse de doctorat, École Polytechnique de Montréal]. PolyPublie. https://publications.polymtl.ca/666/

UNIVERSITÉ DE MONTRÉAL

HYDRODYNAMIQUE DES JETS DE GAZ ORIENTÉS VERS LE HAUT ET VERS LE BAS DANS LES LITS FLUIDISÉS GAZ-SOLIDE

PIERRE SAURIOL

DÉPARTEMENT DE GÉNIE CHIMIQUE

ÉCOLE POLYTECHNIQUE DE MONTRÉAL

THÈSE PRÉSENTÉE EN VUE DE L'OBTENTION

DU DIPLÔME DE PHILOSOPHIAE DOCTOR

(GÉNIE CHIMIQUE)

AOÛT 2011

UNIVERSITÉ DE MONTRÉAL

ÉCOLE POLYTECHNIQUE DE MONTRÉAL

Cette thèse intitulée:

HYDRODYNAMIQUE DES JETS DE GAZ ORIENTÉS VERS LE HAUT ET VERS LE BAS DANS LES LITS FLUIDISÉS GAZ-SOLIDE

Présentée par : SAURIOL Pierre

en vue de l'obtention du diplôme de : Philosophiae Doctor

a été dûment acceptée par le jury d'examen constitué de :

M. PATIENCE Gregory S., Ph. D., président

M. CHAOUKI Jamal, Ph. D., membre et directeur de recherche

M. FRADETTE Louis, Ph. D., membre

M. BRIENS Cédric, Ph. D., membre

DÉDICACE

À Mónica et à mes parents

Merci pour tout, surtout votre patience.

REMERCIEMENTS

Au cours de mes études j'ai eu la chance de croiser le chemin d'un grand nombre de personnes qui m'ont grandement marqué, m'ont montré à avoir du plaisir tout en apprenant, à me motiver et me défier.

Je tiens particulièrement à remercier mon professeur Jamal Chaouki, qui m'a toujours donné une grande liberté, ce qui m'a permis d'apprendre énormément sur toutes les techniques de mesure dont dispose son laboratoire. Ses interventions bien dosées et constructives lors de la rédaction des articles et préparation des présentations ont été grandement appréciées et m'ont permis de m'améliorer continuellement. J'apprécie surtout le support inconditionnel qu'il m'a accordé depuis mon retour à l'école, suite à une escapade de quelques années.

Je ne voudrais pas passer sous silence la patience, compréhension et acceptation dont ont fait preuve mes proches: mon épouse Mónica, mes parents, ma famille et ma belle famille. Merci énormément pour vos encouragements et votre support.

J'ai eu le privilège d'avoir cotoyé un bon nombre de chercheurs qui m'ont partagé leurs visions, connaissances, et de leur temps. Je remercie en particulier Rahmat Sotudeh-Gaarebagh pour m'avoir initié à la recherche; Mel Pell, Scott F. Mitchell et Ibrahim Karidio, qui m'ont montré diverses facettes de la recherche industrielle et grandement aidé à développer mes habiletés pour la communication scientifique; Prof. Xiaotao Bi et Jürgen Stumper qui m'ont montré que le baggage de connaissances acquises dans les lits fluidisés pouvait aussi être appliqué à d'autres disciplines, telles que les piles à hydrogène.

Je tiens aussi à remiercier mes collaborateurs et amis qui m'ont fait passer de bons moments, en particulier Heping et Arturo avec qui ce fut un plaisir de travailler; Mouna et Adil qui ont été en quelque sorte des cobayes à travers leur projet de PFE, et mes confrères et amis Rachid, Ramin, Tomás, Guillermo, Régis, Pierre, Yann et Sylvain.

Derniers mais non les moindres, les techniciens du département de génie chimique dont les idées et le travail bien fait ont permis la réalisation des expériences décrites dans le document qui suit; un gros merci à Éric, Jean, Robert et Gino.

RÉSUMÉ

L'injection de gaz dans un lit fluidisé peut mener à la formation de "jets" qui sont caractérisés par leurs hauts taux de transfert de quantité de mouvement, de matière et d'énergie. Ces jets peuvent s'avérer importants sur la performance des réacteurs à lit fluidisés, cependant, malgré plusieurs études antérieures ayant traité des jets dans les lits fluidisés, la compréhension du phénomène est insuffisante afin de rendre le dimensionnement des systèmes d'alimentation une tâche facile. En particulier, le niveau de connaissance en ce qui a trait aux buses d'injection orientées vers le bas est limité et l'avantage d'un choix d'orientation sur la performance des réacteurs n'est pas bien établi.

Les travaux accomplis dans la réalisation de cette thèse ont principalement visé le développement de nouvelles techniques de mesure pour la caractérisation de jets. Ces approches ont ciblé deux aspects importants reliés aux jets dans les lits fluidisés: le mélange entre le gaz du lit et le gaz du jet, et les frontières du jet.

L'hypothèse a été posée que le mélange gaz–gaz pouvait être quantifié au moyen de radiotraceur, communément utilisé dans l'analyse de distribution des temps de séjour. Une étape préliminaire d'évaluation a permis de mettre en évidence que la technique de mesure était caractérisée par une distribution non uniforme de l'efficacité du détecteur en raison du facteur de vue (angle solide) et de l'atténuation des rayons gamma dans le milieu étudié. En combinaison avec l'incertitude associée à la forme et les forts gradients de vitesse et de concentration au cœur même d'un lit contenant un jet isolé, la technique a été jugée trop risquée pour permettre son implémentation dans le contexte des jets. Les travaux initiés ont été appliqués à l'analyse de la technique de radiotraceurs dans l'étude de distributions des temps de séjour. L'analyse à permis de mettre en évidence une forte dépendance de la distribution de l'efficacité du détecteur et les courbes obtenus lors des essais par radiotraceurs et a mené à des recommandations clées, afin d'éviter des artifices introduits par le détecteur même. 1) Il est important d'identifier et de calibrer le modèle de comptage du détecteur afin de linéariser les comptes obtenus. Ce modèle permet de prédire si le détecteur est sujet à saturation et d'établir l'activité maximale de traceur qui peut être employée. 2) Le détecteur peut introduire une dispersion axiale artificielle en raison de la distribution axiale de son efficacité. Les erreurs de mesure associées à la distribution axiale ont été corrélées, ce qui permet d'en estimer la contribution ou de corriger la configuration du détecteur. 3) La

distribution radiale de l'efficacité du détecteur affecte les résultats obtenus lorsque couplés à des gradients radiaux de radiotraceurs. Un trop fort gradient radial implique que le détecteur ne rapporte que les rayons gamma qui sont émis à proximité, ce qui introduit un biais considérable lorsqu'il y a un profil radial de concentration. De la même façon, l'erreur associée au biais radial a été corrélée afin d'estimer ou de rectifier l'influence de la configuration du détecteur.

La structure gaz–solide à proximité d'une buse d'injection a été étudiée au moyen d'une sonde fibre optique. En utilisant une approche par balayage de vitesse pour une sonde positionnée en un point fixe par rapport à la buse d'injection, des vitesses de transitions, auxquelles correspondent les grandeurs caractéristiques des jets définies par Knowlton et Hirsan (1980), ont été trouvées. L'influence de la vitesse d'injection sur la structure locale gaz–solide (fraction de solide moyenne, fraction de solide dans la phase diluée, fraction de phase diluée, fréquence de cycle des phases) donne lieu à des tendances linéaires avec des vitesses de transition communes. L'injection vers le haut mène à trois vitesses de transition correspondant à L_b, L_{max} et L_{min}, tandis que l'injection vers le bas et à l'horizontal mène à deux vitesses de transition correspondant à L_{max} et L_{min}. Les vitesses de transition obtenues pour les jets vers les bas et horizontaux sont de grandeurs comparables, tandis que pour les jets vers le haut elles sont plus faibles. L'influence de la distance séparant l'injecteur de la sonde à fibre optique a été étudié pour les jets vers le bas et ont montré que lorsque elle accrue, les vitesses de transition augmentent. La fréquence de pulsation du jet vers le bas a été estimée à 1-1.5 Hz.

Au moyen de l'approche de mesure par fibre optique, une batterie de tests a été entreprise sur des jets orientés vers le haut et vers le bas dans un lit fluidisé. Plusieurs paramètres expérimentaux ont été étudiés: orientation du jet, diamètre de l'orifice, nature du gaz injecté, type de particule, vitesse superficielle et la hauteur du lit. Il a été trouvé que l'orientation, la vitesse d'injection et la densité du gaz injecté étaient les paramètres les plus importants sur la longueur de pénétration des jets. Les résultats ont été exploités dans l'élaboration de cinq nouvelles corrélations, permettant d'estimer les diverses longueurs caractéristiques des jets orientés vers le haut et vers le bas. Les corrélations obtenues par construction statistique ont montré une forme différente pour les deux orientations étudiées. L'analyse des corrélations obtenues suggère que pour les jets orientés vers le haut, la dissipation de la quantité de mouvement est due aux forces gravitationnelles, tandis que pour les jets orientés vers le bas, l'entrainement du gaz de fluidisation dans le jet domine.

Dans la majorité des cas, l'augmentation de la vitesse superficielle résulte en des jets plus courts. Les nouvelles corrélations retenues pour les jets vers le haut ont été favorablement comparées à des données obtenues sur des lits fluidisés opérant à haute pression, ce qui suggère une bonne robustesse, même lorsqu'extrapolées à des conditions qui diffèrent significativement des conditions de base.

ABSTRACT

The injection of gas in a fluidized bed may lead to the formation of so-called jets which are characterized by enhanced momentum, mass and energy transfer. Such jets may prove important to the overall performance of fluidized reactors. Although several investigations dedicated to the study of gas jets in fluidized beds have been performed, the general comprehension is often too limited to trivialize the design of injection systems. In particular, the level of knowledge that exists about the injection of downward pointing nozzles is very limited and it is unclear what the impact of nozzle orientation is on the overall reactor performance.

The study described herein focused on the development and implementation of new experimental approaches that can be used to further advance the knowledge of gas jets in fluidized beds. Two important aspects of the jet in fluidized beds were targeted as part of the investigation: the gas–gas mixing resulting from the injection of high momentum jets and the physical boundary of the jet.

It was hypothesized that the gas–gas mixing associated with the jet could be evaluated using a radiotracer technique similar to the one used in residence time experiments. An effort was initiated to evaluate the expected performance of such a technique. It was found that the solid-angle (view factor) and the medium attenuation introduced significant non-uniformity in the detector efficiency distribution. In combination with an uncertain jet shape and strong velocity profile, the technique was deemed too uncertain to pursue. The findings relative to the detector efficiency distribution were however, preserved and implemented in a model based analysis of radiotracers in residence time distribution. The analysis highlighted the strong dependence between the detector efficiency distributions and the response curves obtained. The investigation provides key recommendations: 1) the detector counting model must be determined before hand and calibrated in order to avoid non linear responses. This allows for the maximum tracer activities to be determined to avoid saturating the detectors; 2) the axial spread of the detector efficiency distribution can introduce artificial axial dispersion in the response curves. The error associated with this axial distribution can be estimated from correlated performance data and corrective measures can be implemented with respect to the detector configuration. 3) the radial range of the detector efficiency distribution can result in the effective measurement of the tracer within a narrow range from the detector, any flow model that considers radial velocity and

concentration profiles will be unable to yield satisfactory responses and parameter evaluation. As for the axial spread effect, the radial range was correlated with model data in order to provide an estimate of the error associated with the measurement and corrective measures to be implemented.

The gas–solid structure in the vicinity of a sparger nozzle was investigated using a fiber-optic probe. Using a fixed probe location, and applying a velocity sweep, transition velocities associated with the characteristic jet penetration lengths proposed by Knowlton and Hirsan (1980) could be found. The influence of the injection velocity with respect to the gas–solid structure (average solid holdup, average dilute phase solid holdup, dilute phase fraction, phase changeover frequency) showed nearly linear behavior and common transition velocities. An upward nozzle yields three transition velocities corresponding to L_b, L_{max} and L_{min}. Downward and horizontal nozzles lead to two transition velocities corresponding to L_{max} and L_{min} and of similar magnitude, while the upward nozzle has significantly lower transition velocities. The influence of the distance between the injection point and the fiber-optic probe were investigated for the downward injection and showed that as the distance increased, the transition velocities increased. The frequency of the pulsating jet for the downward nozzle was estimated at 1-1.5 Hz.

Using the fiber-optic probe, an experimental plan was implemented to investigate the jet penetration length of upward and downward jets in fluidized beds. A wide range of operating variables was considered: nozzle orientation, injector diameter, injected gas, particle type, superficial velocity and bed height. Nozzle orientation, injection velocity and injected gas density were found to be the most influent parameters. The results were used to develop five new correlations for the prediction of the various jet penetration lengths with the upward and downward injection. The correlations obtained from statistical construction differed with respect to the injection orientation. Analysis of the resulting correlations suggested that for the upward injection, gravitational forces are responsible for the momentum dissipation, while for the downward nozzle the gas entrainment dominates. In most cases, the jet penetration lengths decrease when the superficial velocity is increased. The new correlations retained for the upward injection were compared favorably with data from high pressure operation which suggests robustness to out of range applications.

TABLE DES MATIÈRES

LISTE DES TABLEAUX

LISTE DES FIGURES

LISTE DES SIGLES ET ABRÉVIATIONS

Notation générale

Les sigles suivants sont employés dans l'ensemble de la thèse à l'exception du Chapitre 3. La notation du Chapitre 3 est présentée après.

Sigles

Ar	Nombre d'Archimedes (Table 5.3), -
C	constante employée avec certaines corrélations (Table 2.1, Eqs. 5.4-5.6 et Table 5.4), -
C_G	constante géométrique utilisée dans la corrélation de Ariyapadi et al. (2004) (Table 2.4), -
d	diamètre, m
f	fréquences de bulle dans la corrélation de Yates et al. (1986) (Table 2.3); fréquence sonore dans la corrélation de Guo et al. (2010) (Table 2.4), s^{-1} aussi désigne une fraction temporelle au Chapitre 4, -
g	constante gravitationnelle, $g = 9.81$ m/s^2
H	hauteur ou position axiale dans le lit, m
L	distance entre la sonde d'échantillonnage et le point d'injection, m
L_b	longueur caractéristique de la pénétration des bulles issues du jet, m
L_j	longueur de jet quelconque (indéterminée), m
L_{max}	longueur caractéristique de la pénétration du jet (longueur maximale de la cavité continue), m
L_{min}	longueur caractéristique de la pénétration du jet (longueur minimale de la cavité continue), m

N_j	nombre d'orifice d'un distributeur à plaque perforée
P	pression, Pa
Q	débit volumique, m^3/s
Fr	nombre de Froude (Table 5.3), -
Re	nombre de Reynolds (Table 5.3), -
S	ratio de la vitesse de gaz par rapport à celle du liquide dans l'injecteur pour la corrélation de Ariyapadi et al. (2004) (Table 2.4), -
SPL	intensité sonore dans la corrélation de Guo et al. (2010) (Table 2.4), dB
T	température, °C
U	vitesse superficielle, m/s
u	vitesse réelle, m/s
u_j	vitesse d'injection, m/s
$u_{j,bubbling}$	vitesse d'injection correspondant à la transition entre les zones "sans impact" et de "bullage intense" pour les jets vers le haut, m/s
$u_{j,onset}$	vitesse d'injection correspondant à la transition entre les zones "sans impact" (vers le bas ou horizontal) ou de "bullage intense" (vers le haut) et de "jet oscillant", m/s
$u_{j,perm}$	vitesse d'injection correspondant à la transition entre les zones de "jet oscillant" et de "jet permanent", m/s
$w_{g,j}$	ratio de masse du gaz par rapport à celle du liquide dans l'injecteur pour la corrélation de Ariyapadi et al. (2004) (Table 2.4)
X_j	distance entre deux injecteurs voisins dans pour le critère de Luo et al. (1999) (Table 2.3), m
x	variable désignant le facteur de mise à l'échelle de la longueur pour désigner certains nombres adimensionnels, m

z variable correspondant à $\ln\left(\rho_j u_j^2\right)$ pour les corrélations de Zenz (1968) (Table 2.1), $\rho_j u_j^2$ est en Pa

Lettres grecques

α exposants employés dans les corrélations génériques de longueur des jets (Eqs. 5.4-5.6 et Table 5.4), -

ε fraction volumique locale instantanée, -

$\overline{\varepsilon}$ fraction volumique locale instantanée (estimée au moyen des Eq. 5.2 et Eq. 5.3), -

φ demi-angle d'ouverture du jet, °

μ viscosité, Pa·s

θ angle d'inclinaison des injecteurs par rapport à l'horizontal pour la corrélation de Hong et al. (1997) (Table 2.5), °

ρ masse volumique, kg/m^3

ξ rayon adimensionnel du jet pour une position axiale donnée (r/R), -

Indices

0 fait référence au lit au repos (U_g = 0 m/s)

1 fait référence au nombre de Froude à une phase (Table 5.3)

2 fait référence au nombre de Froude à deux phases (Table 5.3)

a fait référence à la partie annulaire du jet pour la relation de Luo et al. (1997) (Table 2.4)

bed fait référence au lit à U_g

c fait référence aux conditions de transition au régime de fluidisation turbulente

cf fait référence aux conditions de fluidisation complète

dilute fait référence à la fraction diluée (par opposition à la fraction dense, ou l'émulsion)

div	fait référence à la porosité du lit ayant la probabilité minimale entre la phase dense et diluée
FB	fait référence aux conditions de fluidisation en absence d'injection de gas
g	fait référence au gaz du lit fluidisé à la même position axiale que l'injecteur
g,∞	fait référence au gaz du lit fluidisé à la surface du lit
j	fait référence au gaz injecté (condition à l'intérieur de l'injecteur)
$j, perm$	fait référence au jet permanent
m	fait référence à la condition le long de l'axe du jet pour la relation de Luo et al. (1997) (Table 2.4)
mb	fait référence aux conditions de fluidisation au minimum de bullage
mf	fait référence aux conditions de fluidisation naissante
p	fait référence aux particules
ref	fait référence à une condition connue du lit fluidisé (0 , mb or mf)
s	fait référence à la fraction solide
se	fait référence aux conditions de fluidisation au minimum au début du régime de transport (entrainement significatif)
t	fait référence à la colonne

Notation employée pour le Chapitre 3

Sigles

ACE	évolution de la concentration moyenne surfacique au niveau du détecteur, mol/m^3
AS	distribution axiale de l'efficacité du détecteur, m
A_γ	activité du radiotraceur, s^{-1}
C	concentration du traceur, mol/m^3

CDR réponse du détecteur corrigée, -

D réponse brute du détecteur, -

D_a coefficient de dispersion axiale, m^2/s

d_d diamètre du cristal du détecteur, m

d_t diamètre de la colonne, m

D_r coefficient de dispersion radiale, m^2/s

E_c efficacité de comptage du détecteur, -

E_d distribution d'efficacité du détecteur, -

$\bar{\bar{E}}_d$ moyenne tangentielle de la distribution d'efficacité du détecteur, -

$\bar{\bar{\bar{E}}}_d$ moyenne surfacique de la distribution d'efficacité du détecteur, -

ERR_{NACE} erreur de la distribution des temps de séjour (erreur entre $NACE$ et $NCDR$), -

f_p fréquence des photopeaks $f_p = N_p / \Delta t$, s^{-1}

g constante gravitationnelle, $g = 9.81$ m/s^2

h constante de Plank, $h = 6.626 \times 10^{-34}$ J·s

H_d position axiale du centre du détecteur, m

H_t hauteur de la colonne, m

k constant utilisée pour évaluer la viscosité cinématique turbulente, $k = 0.188$

l distance parcourue par le rayon gamma, m

l_d longueur du cristal du détecteur, m

l_s épaisseur du blindage de plomb, m

l_{s-d} distance entre le blindage et plomb et le cristal du détecteur, m

l_{t-s} distance entre la colonne et le blindage de plomb, m

m paramètre d'ajustement des profils de vitesse, -

N nombre de rayons gamma simulés, -

n nombre de moles de radiotraceur injecté, mol

$NACE$ ACE normalisée, s^{-1}

$NCDR$ CDR normalisée, s^{-1}

N_p nombre de photopeaks détectables reçus au cours de l'intervalle de comptage, -

NRR indicateur de distribution radiale de la distribution d'efficacité du détecteur, -

NRR_C indicateur de distribution radiale de la concentration du traceur au niveau du détecteur, -

$P(l)$ distribution cumulative de la probabilité d'interaction d'un rayon gamma après avoir parcouru une distance l, -

P_d probabilité d'un rayon gamma de résulter en un photopeak, -

Pe nombre de Péclet $Pe = \dfrac{UH}{\varepsilon D_a}$, -

P_Ω probabilité associée la l'angle solide, -

r coordonnée radiale, m

RMI indice de maldistribution radiale, -

S amplitude de la fonction d'alimentation échelon, mol/m^3

SDR rapport des écart-types, -

t variable temporelle, s

t_s ouverture du blindage de plomb, m

u vitesse superficielle locale, m/s

U vitesse superficielle (moyenne), m/s

V	variable volumique, m^3
x	coordonnée cartésienne, m
y	coordonnée cartésienne, m
z	coordonnée axiale, m

Lettres grecques

Δt	intervalle de comptage, s
ε	fraction volumique, -
$\overline{\varepsilon}_g$	fraction volumique moyenne du gaz, -
μ	coefficient d'atténuation linéaire, m^{-1}
ν	fréquence des rayons gamma, s^{-1}
ρ	masse volumique, kg/m^3
ρ_l	masse volumique du liquide, kg/m^3
σ_{NACE}	écart-type de la distribution du traceur, s
τ	temps mort associé au détecteur, s
τ_w	contrainte de cisaillement, Pa
υ	rayons gamma émis par désintégration, -
υ_m	viscosité cinématique moléculaire, m^2/s
υ_t	viscosité cinématique turbulente, m^2/s
ξ	rayon adimensionnel $\xi = \frac{2r}{d_t}$, -

INTRODUCTION

L'alimentation aux procédés opérant en continu peut se faire de multiples façons. Le mode d'alimentation choisi peut avoir des conséquences sur la performance du procédé, par exemple en engendrant des profils de concentration importants, en favorisant certains chemins préférentiels (court-circuitage) ou en donnant lieu à des zones mortes. Un système d'alimentation performant au détriment de pertes de charge élevées peut s'avérer trop coûteux en frais d'opération. Au-delà de la performance du procédé, des aspects structurels peuvent aussi être affectés par le mode d'alimentation choisi, par exemple des forces excessives pourraient s'exercer sur des composantes internes du procédé, résultant en une détérioration prématurée des équipements et menant à l'arrêt des opérations. En particulier, l'alimentation de gaz dans les réacteurs à lit fluidisé illustre cette problématique.

Dans le cas des lits fluidisés utilisés comme contacteur pour des réactions gazeuses homogènes ou catalysées, il est souvent requis d'alimenter les réactifs de façon séparée (Dry et Judd (1986)), afin d'éviter des situations potentiellement explosives (e.g. oxydation partielle, combustion). Il peut aussi être avantageux d'étager l'alimentation de certains réactifs, afin de limiter leur niveau de concentration dans le réacteur et ainsi accroître la sélectivité. Dans ces cas, l'alimentation des réactifs se fait, en partie ou en totalité, par le biais d'un réseau de buses d'injection.

L'alimentation de gaz à vitesse élevée dans le lit fluidisé aura des conséquences hydrodynamiques locales indéniables. Plusieurs chercheurs parlent de l'apparition de jets se dégénérant en bulle de façon périodique. Au phénomène des jets on associe des taux importants de transfert de quantité de mouvement, de matière et de chaleur (Vaccaro et al. 1997a). Ces transferts y sont plus élevés qu'ailleurs dans le lit fluidisé. On rapporte aussi des taux importants d'attrition de particules et d'érosion des structures internes dus à l'action du jet. Dans le cas de systèmes réactionnels, la zone d'injection peut être déterminante sur la performance du réacteur et son effet peut être néfaste ou bénéfique selon le type de réaction qui est désirée.

Les jets résultant de l'injection d'un fluide dans un autre est un phénomène assez courant dans l'industrie, la technologie et la nature. Sous l'action des fluides impliqués, le phénomène a priori local, aura une ampleur très variable, principalement en raison de la différence de densité et de vitesse des fluides impliqués (quantité de mouvement). Lorsque deux fluides de densités similaires sont impliqués (e.g. alimentation d'air secondaire dans une bouilloire, éjection de gaz

par une cheminée; arrivée d'une chute d'eau dans un bassin) l'effet pénétrant du fluide injecté peut être de l'ordre de plusieurs dizaines de mètres. En comparaison, lorsqu'un gaz est alimenté dans un fluide dense tels un liquide ou encore un lit fluidisé (e.g. bains de condensation dans le domaine nucléaire; buses d'injection dans les lits fluidisés), l'effet pénétrant sera généralement inférieur à quelques dizaines de centimètres. En raison de l'effet pénétrant, les approches utilisées industriellement diffèrent significativement selon la situation. Ainsi, une bouilloire industrielle aura peu de points d'injection d'air secondaire et généralement répartis le long de deux parois opposées pour une densité de l'ordre de 0.5 point d'injection par mètre de périmètre, tandis que pour un réacteur à lit fluidisé dense, on pourra compter jusqu'à 100 points d'injection par mètre carré de surface d'écoulement.

La problématique des jets dans les lits fluidisés n'est pas récente. Même si les premières expériences en la matière datent d'avant 1950, les connaissances actuelles sont rarement suffisantes et adéquates pour permettre leurs dimensionnement et simulation. Parmi les éléments qui ont limité l'avancement des connaissances sur les jets, on retrouve: 1) la définition même de ce que constitue un jet en raison de sa variabilité spatiotemporelle; 2) la grande variété de configurations expérimentales qui sont souvent comparées entre elles sans distinctions particulières (e.g. orientation et position relative par rapport au distributeur); 3) les conditions expérimentales limitées et souvent lointaines des conditions d'intérêt industriel; 4) les limitations et capacités des techniques de mesures utilisées.

Problématique

À la lumière des travaux de la littérature (qui font l'objet d'une revue approfondie au chapitre 2), on remarque que les ressources nécessaires pour rendre possible le dimensionnement et la simulation des zones de jets dans les réacteurs à lits fluidisés sont déficientes. La majorité des corrélations disponibles afin de prédire la longueur de pénétration des jets ont été développées sur des jets isolés émanant d'un distributeur à plaque poreuse souvent opérée au minimum de fluidisation. Ces corrélations reposent sur des techniques de mesures variées, lesquelles n'adoptent pas toujours la même définition de la longueur de pénétration de jet et dont la plupart ont été obtenues sur des systèmes 2D ou encore 2.5D qui exercent des effets stabilisants sur le jet. Bien que les lits fluidisés aient pour la plupart des distributeurs pour lesquels ces corrélations pourraient êtres appliquées, il est important de souligner que dans un contexte de réaction en lit

fluidisé (e.g. oxydation partielle, combustion), l'alimentation des réactifs se fait principalement de façon séparée afin d'éviter les risques d'explosion et pour minimiser les réactions compétitives. Étant donné le faible rétro-mélange du gaz dans le lit fluidisé, la région à la base du réacteur n'est pas aussi importante que la région où les réactifs secondaires sont introduits dans un contexte de réaction. Les corrélations pour les jets émanant du distributeur sont par contre très importantes dans un contexte de dimensionnement, étant donné qu'elles permettent de déterminer la distance minimale requise entre le distributeur et les composantes internes du réacteur (e.g. réseau d'échangeur de chaleur) afin d'éviter l'érosion prématurée. Il faut souligner que cette longueur de jet pour fin de dimensionnement correspond à la longueur L_b selon Knowlton et Hirsan (1980) et que la majorité des corrélations formulées dans la littérature sont basées sur la longueur L_{max} qui lui est inférieure. De plus, aucun travail portant sur l'influence de la proximité des composantes internes et des restrictions résultant de la présence d'un réseau d'échangeur de chaleur (e.g. 20-30% d'occupation de la section transversale) sur les jets n'a été recensé.

Industriellement, les réactions catalytiques en lit fluidisé se font généralement avec des particules de type Geldart A ou B et opèrent à des vitesses élevées, loin du minimum de fluidisation. La pratique a longtemps favorisé l'alimentation des réactifs secondaires par le biais d'un réseau de buses d'injection orientées vers le bas. Ce type de configuration permet de prévenir l'engorgement des buses lors de l'arrêt du réacteur. Cette stratégie est également stimulée par la croyance que cette orientation permet un meilleur contact gaz–gaz–solide. Dans les faits, peu de travaux ont cherché à mettre en évidence cet aspect, même que certains résultats de Shen et al. (1990a, b) et Xuereb et al. (1991a) relèvent certaines caractéristiques qui permettent de mettre en doute cet avantage attribué aux jets orientés vers le bas. De façon générale, peu de corrélations (voire d'études) ont été réalisées dans des circonstances qui s'apparentent aux conditions industrielles, si bien que l'estimation des propriétés des jets dans ces conditions d'opération, et plus particulièrement pour des particules de type Geldart A, est presque impossible avec les connaissances actuelles. Soulignons que seulement deux corrélations (Zenz, 1968 et Yates et al., 1991), permettent d'estimer la longueur des jets orientés vers le bas. Celles-ci sont très modestes, n'étant basées sur peu de données expérimentales.

Finalement, la simulation des jets dans les réacteurs à lit fluidisé nécessite plus d'effort en ce qui a trait aux transferts de matière et de chaleur entre les jets et le lit fluidisé. Actuellement, les travaux pour caractériser le transfert de particules sont limités à des particules de type Geldart D

dans des systèmes 2D et 2.5D. De plus, peu d'études expérimentales ont portées sur l'étude du transfert gazeux entre le jet et le lit fluidisé dans des conditions qui s'apparentent aux conditions industrielles et notamment pour l'injection orientée vers le bas.

Objectifs de recherche

Devant les besoins éminents décrits auparavant, les objectifs suivants sont définis pour le présent projet de recherche:

L'objectif principal est de déterminer les caractéristiques des jets issus des buses d'injection orientées vers le haut et vers le bas dans un lit fluidisé, sous des conditions de particules et de fluidisation qui s'apparentent aux conditions industrielles.

Les sous objectifs consisteront à:

- Évaluer la possibilité d'utiliser les techniques non intrusives radioactives comme méthode d'évaluation du transfert de matière entre un jet et le lit fluidisé.
- Développer une technique de mesure des jets au moyen d'une sonde à fibres optiques qui permette de trouver les longueurs de jets aisément, sans nécessiter le déplacement fréquent de la sonde optique.
- En utilisant la technique précédemment développée, étudier l'influence des paramètres d'opération du lit fluidisé (particules, vitesse superficielle, hauteur du lit, position de la sonde), et des propriétés de l'injecteur (orientation, taille d’injecteur, vitesse d'injection et densité du gaz injecté) afin de développer une corrélation permettant la détermination de la longueur de pénétration des jets issus d'une buse d'injection dans les lits fluidisés.

CHAPITRE 1 ORGANISATION DE LA THÈSE

Le corps de la thèse se décline en 6 chapitres dont 4 sont des articles réalisés dans les cadre du projet, en réponse à des objectifs spécifiques. Ils y sont présentés dans leur intégrité (en anglais). Le tout est précédé d'une introduction générale à la problématique de jets dans les lits fluidisés et à la définition du projet de recherche et est suivi d'une conclusion, recommandations.

Le Chapitre 1 (présent chapitre) à pour objectif de faire le lien entre les différents articles présentés dans la thèse.

Le Chapitre 2 consiste en une revue de la littérature sur les jets dans les lits fluidisés recensés. La version préliminaire de cet article faisait partie de la proposition de recherche. Devant la quantité d'informations recensées, et l'absence d'articles de revue ayant été publié au cours des 20 dernières années (le dernier étant celui de Massimilla en 1985), il a été convenu de convertir la revue de littérature en article de revue. Le contenu de l'article a été mis à jour au terme du projet afin d'y inclure les travaux plus récents ayant été publiés depuis la préparation de la proposition de recherche (incluant les travaux de la présente thèse).

Le Chapitre 3 consiste en un article décrivant les erreurs de mesures associées à l'utilisation de radiotraceurs employés dans l'analyse de distribution des temps de séjours de réacteurs. L'emploie de tels radiotraceurs avait été envisagé afin de permettre l'étude du mélange gaz–gaz entre le jet et la phase dense du lit. L'idée de base était de suivre la concentration du radiotraceur au niveau du jet jusqu'à l'obtention d'un régime permanent. Le radiotraceur gazeux serait alimenté en continue sur une courte période de temps avec le gaz d'injection, donnant ainsi lieu à des mesures quasi instantanées dans le jet. Ceci serait une alternative aux techniques plus répandues des mesures de compositions effectuées dans les jets, nécessitant l'extraction d'un échantillon et son analyse dans un appareil externe, entrainant des délais importants et un moyennage du phénomène.

En préparation à la réalisation de travaux se basant sur l'utilisation de radiotraceurs pour l'étude mélange gaz–gaz avec un jet, il est devenu apparent que les effets atténuants du lit fluidisé et les profils de vitesse existant au cœur du jet augmentaient significativement les difficultés associées à de telles mesures. Une analyse préliminaire a montré que les effets associés à l'angle solide (facteur de vue) et à l'atténuation, associés respectivement à l'agencement du détecteur et aux

propriétés du lit fluidisé, était beaucoup plus important que ce qui était anticipé. Il est devenu apparent que la détermination des concentrations au cœur du jet nécessiterait un outil prédictif du détecteur ainsi qu'un modèle décrivant la forme et les profils de vitesse dans les jets. Devant l'incertitude associée à ces deux aspects, il a été préféré de ne pas pousser plus loin l'idée d'utiliser les radiotraceurs pour évaluer le mélange gaz–gaz avec un jet.

Malgré l'abandon de l'objectif de faire les mesures au niveau des jets, les travaux ont été réorientés vers l'analyse des méthodes de radiotraceurs pour l'analyse de distributions de temps de séjour. Comme les impacts associés aux détecteurs et au milieu sont communs en ce qui a trait à l'emploi de radiotraceurs en analyse de distribution de temps de séjour et puisque l'outil d'analyse (modèle de détection des rayons gamma) avait été développé pour l'analyse des cas traitant des jets, il était possible de traiter ce cas sans avoir à effectuer de changements importants. Des profils de concentration de traceurs générés par simulations d'écoulement typiques tenant compte de la dispersion axiale, radiale et même de profils de vitesse ont été fournis par Sylvain Lefebvre. Le couplage des profils de concentration type avec le modèle de détection de radiation nous a montré que l'emploi de radiotraceurs, même en analyse de distribution de temps de séjour, n'était pas toujours trivial. Un effort a été réalisé afin d'estimer l'impact des propriétés du détecteur et d'écoulement, ainsi que les erreurs associées à la détermination des modèles de mélange sur la base des analyses de distribution de temps de séjour obtenue par radiotraceurs.

Le Chapitre 4 présente les résultats d'une nouvelle approche de mesure des jets au moyen d'une sonde à fibre optique. L'approche est basée sur un balayage de vitesse d'injection à position de sonde fixe et est capable de déterminer les vitesses d'injection auxquelles correspondent les trois longueurs caractéristiques des jets, soient: L_b, L_{max} et L_{min}. L'emploi de la sonde à fibre optique a été préféré aux mesures de pression et de compositions gazeuses qui ont également été testées dans l'évaluation des techniques de mesure, surtout en raison de la netteté des signaux qu'elle permet. Le balayage de vitesse d'injection a été préféré à l'approche classique du déplacement de la sonde, surtout en raison de l'incertitude associée à la détermination de sa position dans un lit fluidisé tridimensionnel. Les essais initiaux ont suggéré que l'incertitude sur la position de la sonde pouvait être de l'ordre de ±5 mm (axiale et radiale) pour un lit fluidisé de 150 mm de diamètre. Par contre, étant donné la taille des jets, cette incertitude est très importante et l'approche par balayage de vitesse lui a été préférée. L'article au Chapitre 4 présente l'approche

de mesure et décrit comment la structure locale du jet varie en fonction de la vitesse d'injection. Les jets orientés vers le bas, le haut, et à l'horizontal ont été étudiés.

Le Chapitre 5 présente les résultats obtenus au moyen de l'approche de mesure introduite au Chapitre 4. Les essais ont été réalisés sur un grand nombre de paramètres d'opération incluant la nature du gaz injecté et l'orientation des jets (haut et bas), la distance entre la sonde et l'injecteur, le diamètre de l'injecteur et la nature des particules constituant le lit. Cinq nouvelles corrélations permettant de prédire les diverses longueurs caractéristiques de pénétration des jets ont été proposées (trois pour le haut et deux pour le bas), ce qui est rendu possible en raison de l'approche introduite au Chapitre 4. Au meilleur de nos connaissances, il s'agit des premières corrélations permettant la prédiction de L_{min}. Cette longueur caractéristique est probablement la plus importante pour la quantification de l'entrainement de gaz dans le jet en raison de gradients de vitesse. L'analyse suggère que le mécanisme responsable de la dissipation de la quantité de mouvement associée au jet est différent selon l'orientation de l'injecteur. Dans le cas des jets orientés vers le haut, l'effet gravitationnel (déplacement du lit par le volume du jet) en serait la cause, tandis que pour les jets orientés vers le bas, l'entraiment de gaz de fluidisation en serait responsable.

Le Chapitre 6 est une discussion générale traitant de l'ensemble de la thèse.

CHAPITRE 2 ARTICLE 1: JETS IN GAS–SOLID FLUIDIZED BEDS – A REVIEW

Pierre Sauriol and Jamal Chaouki

Department of Chemical Engineering, École Polytechnique de Montréal,

P.O. Box 6079, Station Centre-ville, Montréal, Québec, Canada, H3C 3A7

2.1 Introduction

The reactant feeding method in any continuous process is likely to have an impact on the overall process performance, due to the possible generation of concentration profiles, dead zones and/or by-passing of reactants. Particularly, feeding gaseous reactants into gas–solid fluidized bed reactors is a challenge. An efficient feed system can be achieved by using a high pressure drop feed network, but this adds operating costs which can limit the economical viability of the process. Beyond process performance, structural aspects may be affected by the feed system. For example, excessive forces or erosion could be exerted on the process internals, leading to a premature failure of the equipment and unplanned shutdowns; jet attrition can also result from high velocity gas injection. In most catalytic fluidized beds reactors, jet attrition is to be minimized as it may result in costly catalyst losses; in agglomerating systems, such as fluid cokers and cohesive powders, jets can be used to limit particle growth and breakup the agglomerates (McMillan, 2007; Ruud van Ommen and Pfeffer, 2010).

In practice, the fluidization gas is fed at the bottom of the reactor in a manner which ensures uniform distribution over the cross-sectional area. Three categories of distributors are used: porous plates, perforated plates (orifice, nozzles/shrouds, tuyeres) and spargers. These are illustrated in Fig. 2.1. Porous plates yield an excellent gas distribution. However, their use is limited to small-scale fluidized beds due to their high cost and limited structural resistance. For industrial-scale units, perforated plates are usually preferred given their lower cost and simplicity. Note that with certain configurations, such as a "J" type circulating fluidized bed (refer to Fig. 2.2), the use of a perforated plate distributor is atypical, for lack of a base. In such configurations, spargers are usually preferred, although perforated distributors that allow for the simultaneous feeding of gas and solid have also been used.

When fluidized beds are used as reactors for either homogeneous or catalytic reactions, it is often required to feed the reactants separately to avoid potentially explosive mixtures (Dry and Judd, 1986; Patience and Bockrath, 2010). In addition to a distributor providing the main fluidization gas, the use of spargers is often needed to provide separate feeding of a reactant. For certain reactions, selectivity and yield will be favored by limiting the concentration of a reactant. In such cases, multi-level spargers can be used (Patience and Bockrath, 2010).

Sizing a perforated plate or sparger distributor is the result of a compromise. On the one hand, to ensure good coverage, it is preferable to have a large number of orifices or nozzles over the cross-sectional area. However, economic and structural factors limit the number of orifices or nozzles that can be used. Furthermore, uniform gas distribution is achieved by design by ensuring sufficient pressure drop across the distributor which is function of the velocity through the orifices. A distributor pressure drop of at least 30% that of the bed is recommended for upward feeding distributors, while for horizontal and downward feeding sparger nozzles, at least 20% is recommended (Pell, 1990). As a result of the limited number of orifices and the requirement of a minimal distributor pressure drop, the velocity within the orifices will be much higher than anywhere else in the fluidized bed. Elevated velocities will also prevent the weeping of particle through the distributor which can lead to significant erosion or plugging (Briens and Bergougnou, 1984)

Feeding gas at a high velocity within a fluidized bed has an undeniable impact on the local hydrodynamics. This hydrodynamic structure is described as a jet that degenerates periodically into bubbles. Enhanced momentum, and mass and heat transfer rates are associated to the jet phenomenon (Vaccaro et al., 1997a). These transfer rates are greater in the jet region than anywhere else in the fluidized bed. Jets are known to cause particle attrition and surface erosion by impingement. In reactive systems, the jet region can play a critical role on the overall reactor performance which can be beneficial or detrimental depending on the desired reaction.

2.2 Generalities

A jet resulting from the injection of one fluid into another is a common occurrence in the process industry and in nature. Depending on the fluids involved, the jet phenomenon, which is mostly a local one, may vary significantly in its penetration depth. This is mostly the result of the difference in density and velocity (i.e. momentum) of the fluids involved. When two fluids of

similar densities are involved (e.g. feeding of secondary air in a boiler, ejection of flue gases through a chimney, a waterfall into a pool), the penetrating effect of the resulting jet can reach tens of meters. In comparison, when a gas is injected into a dense fluid such as a liquid or a fluidized bed (e.g. a condensing bath, injection nozzles in fluidized beds), the penetrating effect of the resulting jet reaches at most tens of centimeters. Because of differences in the penetration depth, the approach used for feeding gaseous reactants in industrial applications will depend on the application. An industrial boiler will have its secondary air injection points located around its perimeter, often only on two opposite walls to have a coverage of about 0.5 injection point per meter of perimeter, while a dense fluidized bed may have as many as 100 injection points per square meters of cross-sectional area (Patience and Bockrath, 2010).

2.2.1 Homogeneous Jets

Due to soaring aeronautics developments, especially following World War II, several research activities dedicated to the study of high-velocity/high-temperature homogeneous gas jets were conducted. Abramovich (1963) compiled in a reference document many of the results from this period. Despite not being directly applicable to the context of gas jets in fluidized beds, several similarities between the two types of jets exist and have been applied. Most common similarity is the existence of a unique velocity profile which can be described by a Schlichting or Tollmien type equation (Behie et al., 1971; Donsì et al., 1980; Filla et al., 1983; Gbordzoe and Bergougnou, 1990; Indenbirken et al. 2000, Massimilla et al., 1981; Merry, 1971; Molodtsof and Labidi, 1995; Shen et al., 1991; Xuereb et al., 1991b, 1992). Because of the theories and modeling approaches that are described, Abramovich's monograph has provided some of the fundamentals used by researchers and is a good starting point to anyone interested in the study of jets in fluidized beds.

2.2.2 Gas Jets in Gas–Solid Fluidized Beds

Despite the fact that gas jets in fluidized beds have been investigated as early as the 1950s, the current state of knowledge is often too limited to allow for their design and simulation. Several factors have hindered the advancement of knowledge on gas jets in fluidized beds: 1) the jet definition, due to the stochastic nature of the jet structure; 2) the variability in experimental configurations from which results are often compared together without special attention; 3) the

limited range of experimental conditions tested which are usually not representative of those found in industrial applications; 4) the limitations and capabilities of experimental techniques used.

2.2.2.1 Definitions

Ever since the study of gas jets in fluidized beds began, there has been a lack of consensus as to what constitutes a jet. Even nowadays, the definitions used by different authors may differ. Several authors distinguish between bubbling, jetting and spouting and have proposed experimental criteria (Guo and al, 2001a; Yates et al., 1986) or regime maps to predict the dominant phenomenon (Grace and Lim, 1987; Guo and al, 2001b; Huang and Chyang, 1991; Roach, 1993).

A majority of the studies dedicated to the characterization of the jet structure where conducted on experimental units having a flat transparent surface allowing for the direct observation (i.e. naked eye, photography, cine-camera) of the jet. Under such circumstances, jets usually appear as voids whose length oscillates between two extremes, and which degenerate into a bubble when it reaches the maximum length. Using an X-ray imaging technique on a three-dimensional (3D) fluidized bed, Rowe et al. (1979) found that what appears as a continuous void against a flat surface has the appearance of a string of bubbles in a 3D bed. The authors noticed that under non-fluidized conditions, a continuous void may appear near the injection point; however, this void eventually degenerates into a string of bubbles.

Based on their investigation of jets from upward nozzles, Knowlton and Hirsan (1980) proposed a nomenclature which includes most observations from the literature. Their jet is illustrated in Fig. 2.3. The jet is made up of a void whose length oscillates between L_{min} and L_{max}. Between the injection point and L_{min}, the jet appears as a stable flame-like void; between L_{min} and L_{max}, the void appears as a series of bubbles that can interconnect; beyond L_{max}, only bubbles are present. The work of Knowlton and Hirsan also showed that the bubbles issuing from the jet had a penetrating effect — greater momentum than that of other bubbles in the fluidized bed — that extended well beyond L_{max}. The characteristic length L_b was thus introduced. Between L_{max} and L_b, the bubbles issuing from the jet do not deviate significantly from their linear trajectory. According to Knowlton and Hirsan, L_b is the most important length to consider when designing a

feeding system because it corresponds to the minimum distance required between the injector and the bed internals to avoid jet related erosion. Since its introduction in 1980, the definition of Knowlton and Hirsan has been adopted by most researchers and will be used in the remainder of the document.

The jet half-angle is another characteristic of the jet boundary. For given operating conditions, the initial expansion of the jet is nearly linear and yields a noticeable half-angle which some researchers have measured and used to define the jet structure. Merry (1975) estimated the jet length by considering the jet half-angle and the initial bubble diameter upon its release at the tip of the jet void. This approach is illustrated in Fig. 2.4. Vaccaro (1997) showed that the jet half-angle is indicative of the momentum transferred to the entrained gas and solids. A jet having transferred more momentum is slowed down and widens by continuity. It ensues that for the same entering momentum, a jet having a wider half-angle will be shorter.

2.3 Experimental Approaches

The experimental approaches used for the study of gas jets in fluidized beds are characterized by the fluidized bed configuration, the measurement techniques used and the operating conditions.

2.3.1 Fluidized Bed Configurations

To facilitate the use of some measurement techniques, researchers have relied on fluidized bed systems of different dimensions — two-dimensional (2D), semi-cylindrical (2.5D) and three-dimensional (3D). Since the phenomenon associated with the jet is foremost structural in nature (jet, bubble, emulsion), researchers have often preferred measurement techniques based on visual observation (e.g. naked eye, photography, cine-camera) in order to determine the main jet properties. 2D and 2.5D units are well suited for these types on investigations. However, Rowe et al. (1979) and Wen et al. (1982) have cast some doubt as to the validity of results obtained in 2D and 2.5D systems, claiming that the presence of a wall exerted a stabilizing effect on the jet structure. Wen et al. (1982) showed that the jet penetration lengths reported in 2D and 2.5D systems were systematically greater, by at least 30%, to those obtained in 3D fluidized beds operated under otherwise similar conditions. He et al. (1998) also found significant differences when comparing 2.5D and 3D spouted beds. Their findings showed that the not only the size but also the shape of the spout was affected by the wall (from circular cross-section in 3D to an

elliptic shape in 2.5D). Furthermore, the wall of a 2.5D was also shown to hinder the particle movement yielding lower particle velocities (He at al. 1994).

Apart from the nozzle design itself, various injection system and bed geometries are found in the industry and this has impacted the experimental work described in the literature. The most common bed geometries are illustrated in Fig. 2.5. The majority of the earlier experimental efforts focused on the study of single upward nozzles or orifices located at or near the grid plate. The grid plate is typically a porous plate onto which a single upward nozzle is added (Fig. 2.5a). The plate and nozzle feeds are separate allowing for the nozzle injection to be independently investigated. The porous plate provides the background fluidization gas, which in most cases is kept at or near minimum fluidization. Figure 2.5b shows a perforated plate configuration for the study of multiple orifices or nozzles. This configuration allows investigating the effects of the proximity between neighboring jets and also the influence of the local fluidization state between orifices. Jets issuing from spargers nozzles either with or without background fluidization gas have been investigated. Four geometries are found: upward, horizontal, inclined and downward nozzles, respectively depicted in Fig. 2.5c-f. If any, the background fluidization is usually provided by a porous plate. Such spargers can be mounted on circulating fluidized beds in which case, a solid circulation rate would characterize the bed operation. Finally, jetting fluidized beds, mostly intended for use when treating agglomerating solids, such as in biomass/coal gasification and combustion, have been used in the study of gas jets. These jetting fluidized beds are similar to those depicted in Fig. 2.5a and c, but differ in the use of an inclined distributor that converges towards the injection nozzle, which can lay flat with the bottom or be elevated. The most common jetting fluidized bed geometries are depicted in Fig. 2.5g and h.

2.3.2 Measurement Techniques

A wide array of experimental techniques and approaches has been applied to the study of the jet properties in fluidized beds. Certain techniques aim at the measurement of the gas holdup either in a qualitative (e.g. naked eye, photography, cine-camera) or a quantitative manner (e.g. optical counters, capacitance probe, fiber-optic probe, X-ray or gamma-ray transmission). Other techniques are based on the measurement of dynamic properties (e.g. pressure fluctuations, momentum, gas velocity), as well as mixing properties (e.g. gas composition, temperature).

Every measurement technique is characterized by three main properties: scale; intrusivity and response time.

2.3.2.1 Basic Visual Techniques

Most work conducted on 2D and 2.5D units aimed at the direct visualization of the jet phenomena, mostly for the determination of the jet boundaries (e.g. lengths, half-angle). With the modest objective of gathering some characteristic penetration lengths, naked eye measurements were performed (Donadono and Massimilla, 1978; Hirsan et al., 1980; Knowlton and Hirsan, 1980; Luo et al., 1999; Merry, 1971, 1975). However, the stochastic nature of the jet phenomenon favored the use of tools that permit a posteriori measurements and analyses to be conducted. Thus, researchers relied on photography (Donadono and Massimilla, 1978; Donsì et al., 1980; Kuipers et al., 1991; Xuereb et al., 1991a; Zenz, 1968; Zhong and Zhang, 2005) and more importantly on cinecameras (Chiba et al., 1972; Chyang et al., 1997; Cleaver et al., 1995; Filla et al., 1983; Guo et al., 2000, 2001a, b; Hong et al., 1997; Kimura et al., 1994; Massimilla et al., 1981; Merry, 1971; Pei et al., 2011; Rowe et al., 1979; Shen et al., 1990a; Sit and Grace, 1986; Wang (CH) et al., 2010; Xuereb et al., 1991a; Yates et al., 1986, 1991; Zhong and Zhang, 2005). Cine-cameras, in particular, are well suited for the investigation of frequencies associated with the jet structure. Nowadays, aided by digital imaging and image recognition software, the analysis of films can be automated.

Due to their simplicity, low cost, and the fact that the obtained images are usually unambiguous, the basic visual techniques have been the most widely used. Despite their popularity, these techniques are being contested due to the stabilizing effect of the wall on the jet structure which can affect the shape (Müller et al., 2009; Rowe et al., 1979) as well as the length of the jets (Pore et al., 2010; Wen et al., 1982).

In general, the jet penetration length reported from the use of basic visual techniques correspond to L_{max}. L_b and L_{min} are rarely reported but may be determined with such techniques (Knowlton and Hirsan, 1980). The basic visual techniques are global, intrusive (proximity of a wall) and instantaneous.

2.3.2.2 Advanced Visual Techniques

To facilitate detection, some authors have used optical binary sensors and counters to gather statistical data about the presence of jet or bubbles (Freychet et al., 1989; Gbordzoe et al., 1990; Kuipers et al., 1992; Shen et al., 1990a, b). These methods, relying on the optical transmission principle, require the use of 2D beds; they are local, intrusive and instantaneous.

To circumvent the limitations of the basic visual techniques which require the use of 2D or 2.5D units, non-intrusive advanced visual techniques were adapted to the study of jets in 3D fluidized beds. The simplest advanced visual techniques consist in gamma-ray densitometers, which enable the quantification of the average volumetric fraction of gas and solids between the source, located outside the fluidized bed or inside, attached to a moveable rod, and the detector located outside the bed at the same axial level as the source (Basov et al., 1969; Gidaspow et al., 1983a, b). Measurements along the length of the bed allows for the axial profile to be determined and the boundary of the jet to be located. According to Vaccaro et al. (1997a), densitometers as used by Basov yield a length which corresponds to L_b. This technique is local, non-intrusive and slow because it requires averaging of data over time.

A variation of the gamma-ray densitometer is the gamma-ray tomography (Seville et al., 1986). In this case, repeated measurements over several radial positions are acquired at a given axial position. The signals are combined to reconstruct the cross-sectional image of the fluidized bed and jet. The spatial resolution of the image is improved by increasing the number of radial measurements. Thus, only averaged jet properties can be obtained from gamma-ray tomography. This technique is global, non-intrusive and slow.

X-ray based visualization techniques offer the advantage of yielding nearly instantaneous 2D images of the jet structure within a 3D fluidized bed, similar to what is commonly obtained by the basic visual techniques (Ariyapadi et al., 2003, 2004; Chen and Weinstein, 1993; Cleaver et al., 1995; Rowe et al., 1979; Yates et al., 1986, 1991). The penetration length usually reported from investigations with the X-ray technique is L_{max}, but image analysis should enable the determination of L_{min} and perhaps even L_b when coupled with a high speed image recorder. This technique is global, non-intrusive and instantaneous.

Magnetic resonance imaging (MRI) has recently been applied to the study of granular systems and in particular the study of gas jets in fluidized beds (Müller et al., 2008, 2009; Pore et al., 2010; Rees et al., 2006). Despite being in its infancy, the MRI technique shows promise since it yields a high resolution averaged 3D image of the system. The mode of operation can be adapted to enable near instantaneous 2D images of the system, analogous to those obtained by X-ray imagery, or to determine the solid velocity distribution (Müller, 2008). One of the limitations of the MRI technique is that it requires particles that have relaxation properties similar to those of a liquid. Thus, the majority of test conducted so far have used oily particles (e.g. poppy seeds). Such particles are usually coarse (> 1 mm) and have low densities (< 1000 kg/m^3). The classical MRI technique is global, non-intrusive and slow, however, in the fast mode, it can become instantaneous.

Electrical capacitance volume tomography (ECVT) has recently been implemented for the study of gas jets in fluidized beds (Wang (F) et al., 2010). The technique also in its infancy is capable of high speed resolution and yields a 3D image of the studied volume. According to Wang (F) et al., the 300 mm fluidized bed equipped with 12 electrodes was capable of achieving a 20×20×20 pixels spatial resolution. This technique is global, non-intrusive and fast, however, image reconstruction is challenging due to the three-dimensional dependency between the electrical field and the media (Du et al., 2007).

The advanced visual techniques generally offer non-intrusive measurements of the gas–solid structure in the jet region, which is advantageous over the basic visual techniques and the probe-based techniques (next sub-section). With the exception of the optical binary sensors and densitometer, the advanced visualization techniques are capable of global measurements which permit the simultaneous determination of the jet length and half-angle. However, their operation is based on the attenuation of a physical phenomenon, making their application typically limited to modest size systems. Based on the previously cited works, X-ray imaging was applied to beds with a diameter of less than 200 mm; less than 50 mm for MRI and less than 300 mm for ECVT. Furthermore, these techniques are not commonly available; they are costly to own, startup and operate in comparison to the majority of other measurement techniques.

2.3.2.3 Probe-based Techniques

Many types of probes have been developed and used in fluidized beds to measure local instantaneous or averaged properties. Several of these probes have been implemented to the study of gas jets in fluidized beds. Pitot tubes (Behie et al., 1970, 1971; Donsì et al., 1980; Filla et al., 1983; Gbordzoe et al., 1988, 1990; Guo and al., 2001b; Molodtsof and Labidi, 1995; Raghunathan et al., 1988; Xuereb et al., 1991b; Yang and Keairns, 1980) and variations based on impact pressure measurements (Behie et al., 1970; Guo and al, 2001b; Huang and Chyang, 1991; Wang (CH) et al., 2010; Zhong and Zhang, 2005) have been the most commonly used types of probes. The gas issuing from the jet transfers some of its momentum to an impact probe as an increased pressure. This pressure is compared with the one determined on a similar probe located at the same axial location, removed from the influence of the injector, to determine if the injected gas still possesses momentum in excess of that of the fluidized bed. In addition to allow for this distinction, a Pitot tube yields the local gas velocity. It is generally expected that momentum-based measurements will yield jet penetration length corresponding to L_b (Vaccaro et al., 1997a). However, several comparisons between results obtained with Pitot tubes and basic visual techniques suggest that the length obtained is closer to L_{max} (Guo et al., 2001b; Raghunathan et al., 1988; Zhong and Zhang, 2005). Sotudeh-Gaarebagh and Chaouki (2000) proposed a velocity sweep approach which is based on the use of a single impact probe located at a fixed location downstream of an injection nozzle. By varying the injection velocity, they monitored the impact pressure as a function of the injection velocity. Their work showed that there exists a transition velocity above which the jet phenomenon at the probe location changes from a bubbling mode to a jetting mode. The measurement techniques based on pressure probes (including Pitot tubes) are local, intrusive and instantaneous.

Vaccaro et al. (1989) introduced a measurement method based on static pressure propagation in fluidized beds. Their approach is based on the measurement of static pressure fluctuations originating from jet related events between a probe located along the jet axis and another one located near the wall of the bed. During the measurement, the probes are kept fixed and the bed height is varied. The authors report that their approach agrees with L_b measurements (Musmarra, 2000; Musmarra et al., 1992; Vaccaro et al., 1997a, b). This measurement technique is local, intrusive and instantaneous.

Fiber-optic probes are an extension of the optical transmission techniques. The use of optical fibers makes it possible to effectively position the light source and optical receiver in the core of the jet structure within a 3D fluidized bed, in order to obtain local measurements of the gas–solid structure (Guo et al., 2000, 2001b, 2010; Kimura et al., 1995; Oki et al., 1980; Sauriol et al., 2011a, b; Wen et al., 1982). Fiber-optic probes are generally based on the light reflection against the bed particles. During the first implementations, the fiber-optic probes were binary sensors and their operation yielded count rates of dense and dilute phase occurrences (Oki et al., 1980; Wen et al., 1982). Nowadays, the intensity of the reflected light is digitized and found to be a function of the local solid holdup. In 2D beds, Wen et al. (1982) moved the probe along a jet length to determine its length. However, in 3D beds, the difficulty of assessing the probe position lead them to adopting a velocity sweep approach, with the binary fiber-optic probe located in a fixed location downstream of the injection point. They obtained a transition velocity above which the local behavior changed from bubbling to jetting. According to Vaccaro et al. (1997a), fiber-optic probes yield to a jet penetration length corresponding to L_{max}. However, Sauriol et al. (2011a) have shown that applying a velocity sweep approach with a digital fiber-optic probe, can lead to the determination of three different transition velocities to which correspond L_{min}, L_{max} and L_b. Like fiber-optic probes, capacitance probes are capable of determining the local solid holdup in and around jets (Yutani et al., 1983). Their use is not as common as their fiber-optic counterpart, as they are more delicate to operate. Fiber-optic and capacitance probes are local, intrusive and instantaneous.

Berruti et al. (2009) have used a sensor made up of an array of triboelectric probes to delimit jet boundaries in a fluidized bed. The triboelectric technique is based on the transfer of electrostatic charges between the bed particles and the wires making up the sensor. This charge transfer is intensified due to the presence of the jet, where the particles velocity may be important. Berruti et al. used a triboelectric sensor to determine the jet half-angle and the penetration length. The triboelectric sensor is local, intrusive and instantaneous.

Thermal tracers (Ariyapadi et al., 2004; Berruti et al., 2009; Chen and Weinstein, 1997; Chen et al., 2008; Donadono and Massimilla, 1978) and composition tracers (Bi and Kojima, 1996a; Dry and Judd, 1986; Freychet et al., 1989; Gbordzoe and Bergougnou, 1990; Gbordzoe et al., 1988; Kimura et al., 1995; Sit and Grace, 1986; Sotudeh-Gharebaagh and Chaouki, 2000) have been

used to establish the jet boundaries in fluidized beds and estimate the gas mixing resulting from the jet. Their use is however mostly limited to verifying the measurements obtained from other techniques. Gaseous composition measurements often require the withdrawal of a slip stream to be analyzed in an external apparatus (e.g. gas chromatograph). These techniques are local, intrusive and slow, especially in the case of composition measurement.

Most probe-based techniques are capable of directly deciphering the jet boundary. When the probe is located or moved along the jet axis, jet penetration lengths may be determined. Furthermore, if the probes are moved along the jet radius, then the jet half-angle could be determined. Depending on the length of the jet and the half-angle, moving the probe in the vicinity of a jet in a 3D system requires a rugged, precise and exact means to ensure effective probe location.

2.3.2.4 Measurement Technique Implementation and Signal Interpretation

For some of the measurement techniques described earlier, especially probe-based techniques implemented on 3D systems, signal analysis and interpretation are critical. The ability and reliability with which the signal allows to decipher between the jet, the bubbles and the bed, determine the usefulness of the techniques. The present section will summarize some of the salient points from selected techniques and show how they have been applied and their signals interpreted.

The gamma-ray densitometer was used by Basov et al. (1969) to determine the solid holdup distribution above multi-orifice grids. A schematic of the apparatus is depicted in Fig. 2.6, along with typical response curves. As the source/detector arrangement is raised upwards into the bed, the signal first drop to reach a minimum, which corresponds to height with the lowest solid holdup. Beyond this minimum, the signal progressively increases to reach a plateau corresponding to a nearly constant holdup along the length of the fluidized bed. This plateau occurs once the densitometer reaches zones without (or with minimal) impact from the jets issuing from the distributor orifices. Basov recommends using the inflection point as a criterion to establish the jet length. Considering the shape of the curves, two other noticeable transitions could have been defined yielding different jet lengths: the point of minimum solid holdup (consistent with minimum void time of Wen et al. (1982)) and the point where the solid holdup becomes nearly constant. The correlation of Basov et al. (1966) for isolated jets showed good

agreement with the data obtained by the authors using the gamma-ray densitometer on a multi-orifice grid plate (Basov et al. 1969). Over time, and presumably based on differences observed between generally accepted L_{max} correlations and that of Basov, the jet length determined by Basov and the gamma-ray densitometer became recognized as yielding a jet length corresponding to L_b.

Ever since Knowlton and Hirsan (1980) suggested that there existed a length L_b, delimited by high momentum bubbles originating from the jet, Pitot tubes and their derivatives have been regarded as the most suitable measurement techniques to capture it. Raghunathan et al. (1988) introduced a Pitot tube-based approach to determine the jet penetration length. A schematic of their experimental setup is found in Fig. 2.7. A miniature Pitot tube probe is mounted on a structure which allows its positioning along the jet axis as well as distant from the jet in the emulsion phase. Axial momentum flux profiles for both the jet and emulsion phase are obtained and compared. The jet penetration length is defined as the axial position at which the momentum flux profiles intersect. Comparison of the results obtained with a cine-camera show that the jet penetration length obtained following the Pitot tube approach, yields values that are close to L_{max}, and not L_b. Zhong and Zhang (2005) found that the Pitot tube measured jet penetration lengths were on average less than 10% greater than L_{max} determined from basic visual techniques. Zhong and Zhang opted to apply a correction to their Pitot tube determined jet penetration lengths to have them agree with L_{max}.

The differential static pressure fluctuations approach proposed by Vaccaro et al. (1989, 1997a) is illustrated in Fig. 2.8. By tracking the evolution of the average differential static pressure fluctuations for various bed heights, a critical bed height is determined. For bed heights greater than the critical bed height, all jet related fluctuations are considered contained within the bed volume. Thus, all jet penetration lengths are considered smaller than this critical bed height. The authors recommend to use a threshold value of 0.1 with respect to the average fluctuations amplitude, as a criterion for determining the critical bed height which corresponds to L_b, the longest penetration length.

Fiber-optic probes are interesting 3D alternatives to the visual observation in 2D and 2.5D systems. Wen et al. (1982) used a binary fiber-optic probe to determine the jet penetration from a

bed with a multi-orifice grid plate. Their setup is depicted in Fig. 2.9. In a 2D bed, the probe is moved axially along the jet axis. The recorded data were converted to void time fraction and plotted against the position of the probe relative to the injection point (Fig. 2.9b). The position of the probe when the void time fraction reaches a minimum coincides with L_{max} obtained from cine-camera. For the investigation of 3D beds, the authors adapted their approach by performing an injection velocity sweep to avoid having to blindly move the probe in the vicinity of the jet. For these velocity sweeps, the probe is positioned at a fixed location and the injection velocity increased progressively until the void time fraction approached unity.

Sauriol et al. (2011a) applied a velocity sweep approach for a 3D bed, but using a digital fiber-optic probe which enables the instantaneous measurement of the local solid holdup, near a single sparger nozzle. Their test configuration is shown in Fig. 2.10. By tracking the evolution of the average local solid holdup in a fixed location along the jet axis, they found that upward nozzles yielded three noticeable transition velocities, which in increasing order correspond to the jet penetration lengths L_b, L_{max} and L_{min}.

The triboelectric probe proposed by Berruti et al. (2009) is depicted in Fig. 2.11. The triboelectric probe consists of a number of partially insulated wires which are exposed to the fluidized bed in strategically located positions along the jet axis. The measurements are repeated to cover several half-angles. The determination of the jet boundary is achieved in a two step process (Fig. 2.11b). In the expansion region, the presence of the jet is determined by comparing the power spectrum of the triboelectric signals (Fig. 2.11c), while in the far region, the analysis is based on a normalized cumulative triboelectric current distribution (Fig. 2.11d). The resulting jet penetration lengths were in good agreement with predictions from the correlation proposed by Ariyapadi et al. (2004), which conforms to L_{max}.

2.3.3 Design and Operating Conditions

The design and operating conditions include the injector and fluidized bed properties. The fluidized bed is characterized by the density, size and sphericity of the particles, the initial bed height, the nature and superficial velocity of the fluidization gas, and the bed operating pressure and temperature. In the case of circulating fluidized beds, the solid circulation flux may also have an impact on the jet behavior. The injector is characterized by the injection velocity and the

nature of the injected gas, along with the size and shape (e.g. round, rectangular) of the injector, all of which are defined at the tip of the injector just prior to entering the fluidized media as illustrated in Fig. 2.12. Henceforth, the term injector will be used as a generic term to describe any of the configurations depicted in Fig. 2.12.

In most cases the observations are based on the operation of upward orifices and nozzles, and, to a lesser extent, horizontal nozzles. In the following sub-section, upward orientation is assumed by default, unless otherwise specified.

2.3.3.1 Injector Properties

Injection velocity — All surveyed works confirm the influence of the injection velocity on the jet penetration length. Whether L_{min}, L_{max} or L_b and in any orientation, greater injection velocities result in longer jets. The weight attributed to the injection velocity in existing jet penetration length correlations differs significantly between authors, with exponents varying between 0.3 and 1. As for the jet half-angle, Vaccaro (1997) found that an increase in injection velocity will not always lead to a notable change in the jet half-angle. It is conditional upon the injector-to-particle diameter ratio. With an injector-to-particle diameter ratio greater than 7.5, the injection velocity yields a decrease in jet half-angle, while it remains nearly constant at lower ratios.

Injector diameter — All efforts dedicated to establishing the impact of the injector diameter have shown that for a given injection velocity, bigger injector diameter yield longer jets. Inspection of existing correlations confirms this trend with exponents generally varying between 0.3 and 1.4. Only the work of Sauriol et al. (2011b) for downward nozzles suggests that the injector diameter does not impact the jet penetration length. The jet half-angle increases slightly with an increase in injector diameter (Merry, 1975; Vaccaro, 1997).

Orientation — The effect of nozzle orientation on the jet penetration has seldom been systematically investigated within a given effort. Zenz (1968) did it in 2D beds where the nozzles were the only source of fluidization gas. He found that jets issuing from horizontal and downward nozzles were of similar lengths (L_{max}), while upward nozzles resulted in jets that were approximately three times longer. Yates et al. (1991) found a similar ratio when comparing their experimental data obtained with a downward sparger nozzle, and the correlation of Yang and Keairns (1978a) for upward grid nozzles.

Hong et al. (1997) investigated the influence of a small inclination angle (±10°) relative to the horizontal. They found that nozzles that pointed slightly upward (+10°) yield jet lengths that are 10-15% longer than their downward counterpart (-10°). This effect is not as strongly captured in their correlation which only predicts a 1% difference in length between the two extremes. The work of Xuereb et al. (1997a) also covering horizontal and inclined nozzles (±30°) has shown that nozzles that point upward (+30°) are more stable than horizontal or downward ones (-30°). They noticed that jets and bubbles issuing from horizontal and downward pointing nozzles had a tendency to return towards the wall from which the injection occurred.

Comparing correlated data for both upward and downward sparger nozzles, Sauriol et al. (2011b) suggested that the momentum dissipation mechanism differed according to the nozzle orientation. For the upward nozzle, momentum dissipation is believed to be due to gravitational forces acting upon the jet volume, while for the downward nozzle, the dissipation is believed to be controlled by particle entrainment into the jet.

Nature of the injected gas — The majority of existing correlations used to predict the jet penetration lengths show a dependency with respect to the injected gas density and in some cases its viscosity. However, in most cases the density or viscosity of the injected gas were not systematically included as operating variables, and only appear in the correlations through the use of dimensionless numbers. Benjelloun et al. (1991), Sauriol et al. (2011b) and Wang (CH) et al. (2010) compared the jet penetration lengths obtained when injecting different gases. Their results clearly show that denser gases yield longer jet penetration. In Wang (CH) et al., the penetration length of CO_2 jets, which has a molecular mass 50% greater than that of air, resulted in jets that are 25% longer. These trends are consistent with the results obtained in high pressure studies, which show that the injection of higher pressure (higher density) gases yields longer jets (Hirsan et al., 1980; Knowlton and Hirsan, 1980; Yates et al., 1986).

Particle-laden jets and gas–liquid jets have also been investigated by some authors. Behie et al. (1971) found no significant change in penetration length when a solids loading of up to 50% wt of FCC particles (Geldart A) was used. On the other hand, Yang and Keairns (1980) with solids loading of up to 73% wt of polyethylene beads (Geldart D), found that the gas velocity within the jet is higher as the solids loading is increased, which suggests longer jets. Recent work by Ariyapadi et al. (2003) has shown longer jets when the loading is increased in gas–liquid jets.

They also found that the jet half-angle was smaller for the gas–liquid jets, in comparison with gas only jet, which is an indication that the gas–liquid jet preserves its momentum over a longer distance.

Nozzle position within the bed — The influence of the nozzle position within the bed has mostly been treated on the basis of its proximity to the vessel walls. Jets occurring near vessel walls are longer than those within the bed core, due to the stabilizing effect of the wall (Pore et al., 2010; Rowe et al., 1979; Wen et al., 1982). As for the axial position, it has been found that nozzles located near the distributor, especially in the case of perforated plate distributors, can lead to defluidized stagnant zones around the injection point, as a result of gas entrainment into the jet structure. These defluidized zones yield longer jets (Oki et al., 1980; Rowe et al., 1979; Wen et al., 1982). Hong et al. (1997) have shown that as the nozzle position is moved higher within the bed, the jet penetration length increases.

Proximity between multiple nozzles — Jet coalescence can result from the proximity of two neighboring nozzles. Few studies have aimed at determining the conditions where jet coalescence takes place. Luo et al. (1999) and Guo et al. (2000) respectively investigated the probability of coalescence and the height at which the coalescence takes place. Similar jet coalescence was captured by Pore et al. (2010) for a multi-orifice grid plate. They found that jet coalescence started once the superficial velocity approached the minimum fluidizing velocity and that jet coalescence yielded longer jet penetration.

Nozzle design — The simplest nozzles consist of a straight length of piping or tubing with a specific diameter, but even then the length of tubing can have an influence on the jet penetration lengths. When the nozzle is used as a shroud to reduce the effective velocity of the gas exiting an orifice prior to its injection in the fluidized media (Fig 2.12b), the nozzle length should be sufficient to contain a homogeneous gas jet with an expansion half-angle of 5.5° (Zenz, 1989) otherwise, particle may fall within the nozzle thus intensifying the erosion and attrition by impingement.

Behie et al. (1971) showed that longer length of tubing yielded longer jet penetration lengths. They explained their observations on the role that the tubing had on establishing a velocity profile. The nozzle design can be further refined in order to promote higher contacting efficiencies. Ariyapadi et al. (2003) showed that adding a draft tube downstream from the nozzle

yielded longer jet penetration while benefiting from a degree of mixing near the initial ejection point prior to entering the draft tube. Dawe et al. (2007) investigated different nozzle geometries, including convergent-divergent sonic nozzles and showed that the nozzle geometry play a role on the jet penetration.

2.3.3.2 Fluidized Bed Properties

Particles (density, diameter, sphericity) — A large number of studies were conducted with particles of different diameter and density. Due to the difficulty in finding particles varying in only one property, in most of the studies, the influence of particle properties is not investigated in a systematic manner. Knowlton and Hirsan (1980) showed that for particles with similar diameters, the jet penetration lengths were shorter for denser particles. Existing correlations support this trend with coefficients that vary between -0.8 and -0.1 (limiting the analysis to correlations where particle density was varied in the experimental plan). The jet penetration length is usually found to decrease as a result of an increase in particle size. Correlations that account for this effect have exponents ranging between -0.5 and -0.1. The jet half-angle increases with increasing particle density and diameter (Merry, 1975; Vaccaro, 1997).

The influence of the particle sphericity is seldom investigated. Filla et al. (1983) showed that particles with a higher sphericity lead to jets with wider half-angles. This observation suggests that the more spherical particles are more readily entrained within the jet, which should result in shorter jet penetration lengths. None of the correlations surveyed accounted for this effect.

Background fluidization — In those cases where the grid flow is controlled independently from the nozzle injection, the state of the background fluidization was found to have an influence on the penetration length. When the background flow rate is lower than that of minimum fluidization (U_{mf}), an increase in background flow yields an increase in jet penetration length (Benjelloun et al., 1991; Chyang et al., 1997; Müller et al., 2009; Xuereb et al., 1991a). When the beds are fluidized, an increase in background fluidization velocity is usually found to yield a decrease in the jet penetration lengths, as observed by several authors using Geldart B and D particles (Chyang et al., 1997; Hirsan et al., 1980; Vaccaro et al., 1989; Wang (CH) et al., 2010; Yates et al., 1986; Xuereb et al., 1991a). However, using FCC particles (Geldart A) as bed material, Guo et al., (2010) observed the opposite trend when varying the background fluidization

velocity between 1 and 1.5 times U_{mf}. This limited range of superficial velocities when using FCC particles, is likely to be lower than the minimum bubbling velocity (U_{mb}). These observations are not necessarily in contradiction. It can be speculated that U_{mb} corresponds to the transition between the two opposed trends and, since most other studies had been conducted on Geldart B and D particles for which U_{mb} and U_{mf} coincide, this would still be consistent with the observed trends. Vaccaro et al. (1997a) have suggested that the injector diameter also plays a role on the impact of the background fluidization. Using Geldart D particles, they found that for small injectors (< 10 mm) the penetration length increases with an increase in background fluidization, while for large injectors (> 19 mm) a decrease is observed.

Xuereb et al. (1991a) and Wang (F) et al., (2010) have shown that when the background fluidization is in excess of the minimum bubbling velocity and that bubbles are present, the jet can coalesce with neighboring rising bubbles. As a result, the jet momentarily deforms and extends, thus penetrating deeper into the bed. Xuereb et al. (1991a) found that the frequency of these occurrences increased with the background fluidization.

In all of the above mentioned situations, the superficial velocity is well below the onset of transport fluidization so that the fluidized bed remains relatively dense. In the extreme case, where the superficial velocity is high enough to achieve a very dilute medium, such as in transport systems, the jet penetration will approach that of submerged homogeneous jet. Under such circumstances, the jet penetration length is expected to be greater than that in a dense bed, even if operated at a lower superficial velocity. Some authors have considered the impact of a reduced bed solid holdup in the formulation of their correlations, when accounting for the bed material weight. A decrease in solid holdup (following an increase in background fluidization velocity) would result in longer jet penetration.

Operating conditions (pressure and temperature) — Increasing the operating pressure of the fluidized bed was found to yield longer jet penetration lengths (Hirsan et al., 1980; Knowlton and Hirsan, 1980; Yates et al., 1986). Cleaver et al. (1995) have found that an increase in operating pressure resulted in smaller jet half-angle, which is consistent with longer jet penetration. In the latter case, the tests were also conducted at ambient and elevated temperature (up to 800°C). They found that with an increase in temperature, the jet half-angle increased, suggesting shorter

jet penetrations. This trend is consistent with the impact of the temperature on the resulting gas density; however, limited data prevents from assessing if viscous effects also play a role at the higher temperatures.

Fluidized bed height — Very few experimental work focused on establishing the influence of the fluidized bed height on the jet properties. The few groups that experimented on the impact of the initial bed height found that when the bed height is increased, the jet penetration length decreases (Chyang et al., 1997; Wang (CH) et al., 2010; Zhong and Zhang, 2005). This is also consistent with the results of Hong et al. (1997) regarding the influence of the nozzle position with respect to the bed surface.

Solid mass flux — Finally, it is worth noting the lack of investigations that focused on the influence of the solid mass flux on the jet properties in circulating fluidized beds.

2.4 Jet Related Correlations

With the amount of experimental work conducted about the jets in fluidized beds, a large number of correlations have been proposed. These include correlations to estimate the various jet penetration lengths, flow regime maps that try to establish the dominant character of the injected gas, as well as correlations to estimate the jet half-angle and the solid holdup distribution. A compilation of these correlations are presented in this section.

2.4.1 Jet Length Correlations

A large number of correlations have been suggested for the prediction of the jet penetration length in gas-solid fluidized bed (refer to Table 2.1). The majority of the correlations are based on dimensional analysis and the use of dimensionless numbers to represent a jet penetration ratio (L/x).

Intuitively, and based on the existing knowledge from homogeneous jets, the injector diameter is almost always used as the reference length in the jet penetration ratio (L/d_j). Only the work of Sauriol et al. (2011b) has recommended the use of the particle diameter as the length scaling factor for estimating the jet penetration lengths of jets issuing from downward nozzles (L/d_p).

The early attempts to correlate the jet penetration length, indicated that momentum flux of the injected gas played an important role in the jet phenomenon; this is the case of the correlations proposed by Zenz (1968) which show the dependence of the jet penetration length to the momentum flux ($\rho_j u_j^2$). Consequently, later attempts to derive dimensionless correlations gave place to the appearance of the Froude number. Notwithstanding the occasional inclusion of density ratio terms, one of the major differences found in the Froude numbers used in the various correlations is the choice of length scaling factor; 70% of the correlations use the injector diameter, while the others use the particle diameter. Although this choice may appear arbitrary at first glance, both forms can be derived from physical considerations.

Merry (1975), considering the simple geometry depicted by Fig. 2.4, found that the jet length ratio was a function of the jet half-angle and the initial bubble diameter. Using the correlation of Davidson and Harrison (1963) for the initial bubble size, Merry obtained a Froude number with the injector diameter as the scaling factor. Benjelloun et al. (1991) derived their correlation from considering the ratio of injected gas momentum to the gravitational forces acting on the jet volume. By assuming that the jet volume was proportional to Ld_j^2, their analysis yields a two-phase Froude number with the injector diameter as the length scaling factor. This is analogous to the analysis of liquid–liquid injections with buoyancy effects (Turner, 1966).

Merry (1971) obtained correlations with a Froude number that featured the particle size as the length scaling factor. This form was derived by considering that the jet penetration length was a function of the ratio between the momentum flux of the injected gas and the residual momentum at the jet boundary. Merry postulated that the velocity of the jet boundary depended upon the terminal velocity of the entrained particles. Considering a constant drag (Newton's law), substitution of the terminal velocity into the ratio yields a Froude number with the particle diameter as scaling factor. The resulting Froude number is a two-phase Froude number, which includes the injected gas-to-particle density ratio to the power 2. Sauriol et al. (2011b) suggested that for a downward nozzle, the jet boundary conditions can be described by considering the equilibrium between the entrained gas and the immobile solid particles. Considering Stokes' law, their assumption yielded a two-phase Froude number with the particle diameter as the length scaling factor divided by an Archimedes number, which was supported by experimental results.

A number of correlations generated for the prediction of the jet penetration lengths are summarized in Table 2.1. These are presented along with some complementary information about the range of operating conditions covered and the predicted specific jet length. Note that in some cases, especially pre-1990, the specific jet penetration length is not always known. The authors just reported the jet length as L. In these cases, the type of jet length is based upon the description of the experimental procedure given by the authors, and the state of knowledge about the capabilities of the experimental procedure. The results obtained with Pitot tubes and impact pressure probes are especially difficult to interpret given the conflicting data that have recently been presented (Guo et al., 2001b; Raghunathan et al., 1988; Zhong and Zhang, 2005).

2.4.1.1 Sensitivity Analysis

A sensitivity analysis was performed to highlight the trends and capabilities of the tabulated correlations. The base case conditions used in the sensitivity analysis are summarized in Table 2.2. These conditions are taken as the most widely suitable conditions for the correlations. FCC (Geldart A) and sand (Geldart B) particles are both considered. The analysis targeted the influence of the injection velocity, the operating pressure and the background fluidization velocity.

Influence of the injection velocity — Predicted jet penetration length for increasing injection velocities are presented in Fig. 2.13 for upward nozzles and multi-orifice grid plates. The base case conditions were considered to generate the curves, except for the injection velocity which was varied from 1 to 200 m/s. Figures 2.13a-d present respectively the predicted L_b/d_j (including the correlations where $L_j = (L_b + L_{max})/2$), L_{max}/d_j for isolated nozzles, L_{max}/d_j for multi-orifice grid plates and L_{min}/d_j (including the correlations where $L_j = (L_{max} + L_{min})/2$), as a function of the entering momentum flux.

Every correlation shows that increasing the injection velocity results in longer jet penetration. However, the various correlations are far from agreeing with each other, with relative differences between correlations reaching several orders of magnitude. The major source of discrepancy comes from out of range use of correlations, with improperly chosen dimensionless numbers that limit the extrapolation capabilities. Comparison between L_b/d_j and L_{max}/d_j also shows that

most of the L_b/d_j correlations yield penetration lengths which are of similar magnitude to the ones for L_{max}/d_j. This is the case of correlations 1, 6, 13 and 23. Correlation 6 was developed for high pressure operation and is used out of its suitable range in Fig. 2.13; however, correlations 1 and 13 were both intended for atmospheric pressure and particles Geldart A and B, and Geldart B and D respectively. Both are used, at least in part, within their suitable range in Fig. 2.13. The fact that they are systematically low could be an indication that the measurement techniques employed to derive the correlations are more suitable for L_{max}/d_j.

The particle type appears to have a very significant impact on several of the L_{max}/d_j correlations (Fig. 2.13b). Indeed, correlations 11, 12, 21, 24 and 26 all predict high jet penetration lengths with the FCC particles but much lower penetration length with the sand particles. Most correlation exhibit FCC-to-sand jet penetration ratio between 1 and 2, but the ratio for these correlations ranges from 4 up to several orders of magnitude. In all cases, these correlations were developed for Geldart B and/or D particles. Correlations 3, 8, 10 and 25 always predict length in the lower end of the range for both FCC and sand, and of similar size to the L_{min}/d_j (Fig. 2.13d). Correlations for multi-orifice grid plates (Fig. 2.13c) are fewer and distributed in a narrower range, with the exception of correlation 2, which is systematically one order of magnitude lower than the others. Correlation 4 was derived from the same data that were considered in correlation 2, but uses a Stokes number instead of the Reynolds number. The Stokes number, which is an indication of the stopping power of a media, is claimed to be a more appropriate number to account for the effect of the media. The predicted values for L_{min}/d_j are closely grouped together, with the exception of correlation 15, which is greater by a factor 2. L_{min}/d_j values are typically between 0.25 and 0.5 times the value predicted for L_{max}/d_j.

Horizontal and downward jet lengths estimates are presented in Fig. 2.14. Correlation 30 is always higher and in comparison, its upward counterpart (Fig 2.13b) yields penetration of similar length. Correlation 31 is significantly affected by the particle size. It was originally developed for Geldart D particles. Correlation 35 is significantly lower than the others and when compared to correlation 34, which was developed from the same data, it yields L_{min}/L_{max} ratios that are greater than unity. In both cases however, the correlations were meant to be used with beds

operated at superficial velocity in excess of the minimum bubbling velocity, which is not the case here and furthermore, the injector diameters used in the investigation were smaller than the 10 mm considered here.

Influence of the operating pressure — Very few correlations were developed considering high pressure data, however, most reactors operate at pressures that exceed atmospheric pressure. Figure 2.15 presents a sensitivity analysis of the existing correlations for pressure ranging between 1 and 25 atm. Most correlations show that an increase in operating pressure will result in an increase in penetration length. This is not the case with correlations 1 and 14, which do not account (minimally in 14 through U_{mf}) for the injected gas density, and correlations 13 and 19, which predict a decrease of penetration length following an increase in pressure. In the latter cases, the negative impact of the operating pressure results from the formulation of dimensionless numbers, such as the Reynolds number, and density ratios which involve the operating pressure through the injected gas density, despite the fact that it was not varied during the experimental work. As a result, the exponents affected to these dimensionless numbers reflect the effect of other involved parameters such as the velocity, particle and injector diameters, and particle density. The injected gas density is merely a constant which is counterbalanced by the main equation constant to annul the effect of the exponent. Such false constants can lead to misleading behaviors when extrapolating the correlations, such as with correlations 13 and 19.

The correlations of L_b/d_j (Fig. 2.15a) show that only correlations 6 and 17 predict jet penetration lengths which are greater than L_{max}/d_j (Fig. 2.15b). Correlations 1, 13 and 23 are systematically lower than the L_{max}/d_j values for FCC and for most correlations with sand. As was the case in Fig. 2.13, correlations 6 (L_b/d_j) and 5 (L_{max}/d_j), which were developed from the same data set, predict values of similar size. Conversely, correlations 16 and 17, also developed from the same data set have L_b/L_{max} ratios between 1.5 and 2.

As for L_{max}/d_j (Fig. 2.15b), the predicted jet penetration lengths are generally more spread out than with the injection velocity (Fig. 2.13b). Differences between the FCC and sand are similar to the observed trends in Fig. 2.13b discussed earlier. The influence of the operating pressure on the jet length prediction for multi-orifice grid plates (Fig. 2.15c), results in much more spread in

the predicted values than with the injection velocity (Fig. 2.13c). As for L_{min}/d_j values, only correlations 15 and 19 predict values that are lower than the L_{max}/d_j. Correlation 18, which depends on the estimation of a jet half-angle, shows signs of discontinuity due to the difficulty in predicting the jet half-angle at elevated pressure.

For the horizontal and downward jet penetration lengths, the estimates from correlations 34 and 35 are nearly unaffected by the operating pressure, as the influence of the density change in the Froude number is compensated by the Archimedes term. This can be an example of a false constant, as under their operating conditions, the authors of correlations 34 and 35 did not vary the fluidization gas density, included in the Archimedes term. As was the case with Fig. 2.15, the ratio between L_{min}/L_{max} obtained from correlations 34 and 35 are always greater than unity. Correlation 31 and 32 are the ones mostly affected by the operating pressure. In both cases however, pressure was not a system variable during the experiments. The penetration lengths predicted using 30 and 31 for FCC and sand, and 32 for FCC are higher than several of the predictions for upward jet penetration (Fig. 2.15b).

General remarks — As highlighted in the preceding sensitivity analysis, there are several correlations which estimate the jet length penetrations. Although most of them report excellent agreement within their respective experimental data sets (typically better than 30%), there can be several orders of magnitude differences between them, especially when extrapolating to other conditions. In some cases, the correlations may lead to trends which are contrary to most observations. This is often the case when the correlations include dimensionless numbers (e.g. Reynolds, Archimedes, Stokes numbers, or density ratios) that involve system variables that remained nearly constant during the experiments. Such system variables include the gas density and viscosity, as most investigations are performed with a single gas at ambient pressure and temperature. User of correlations should be concerned with the validity domain of the proposed correlations and recognize if they involve such false constants.

2.4.2 Regime Maps and Other Correlations

Several authors have attempted to categorize and predict the dominant gas–solid structure that exists upon injection of gas in a dense fluidized bed and have expressed their findings in the form of criteria or flow regime maps. Some of the criteria are summarized in Table 2.3. Grace and

Lim (1987) considered data from the literature which included 2D fluidized beds as well as 2.5D and 3D fluidized beds and jetting fluidized beds with upward gas injection, either from an isolated grid nozzle or multi-orifice grid plate. They established that the injector-to-particle diameter ratio needed to be less than 25.4 in order for the jetting phenomenon to occur. Similar criteria and flow regime maps have been proposed by Guo et al. (2001b) (jetting fluidized bed with upward jet), Huang and Chyang (1991) (fluidized bed with upward nozzle), Roach (1993) (fluidized bed with multi-orifice grid plate) and Yates et al. (1986) (fluidized bed with isolated upward grid nozzle). Using a jetting fluidized bed equipped with two neighboring nozzles, Luo et al. (1999) proposed a criterion to determine if jet coalescence could be expected.

Other correlations which did not belong to the previous categories are summarized in Table 2.4. They include correlations for predicting the jet penetration of gas–liquid injections into gas–solid fluidized bed (Ariyapadi et al., 2004), the jet half-angle (Rees et al., 2006; Merry, 1975; Vaccaro, 1997; Wu and Whiting, 1988), and the radial solid holdup distribution (Luo et al.,1997).

2.5 Modelling Efforts

In comparison to the experimental efforts, there have been fewer modeling attempts, although, in recent years, with the advances in computational power, the number of papers dealing with jet modeling has increased steadily. The present section will just present a brief overview of the modeling approaches. The interested reader is invited to consult some of the referenced work for more details.

Modeling efforts can be divided into two categories: mechanistic approaches and CFD. The mechanistic approaches have been more commonly used (Beeckmans and Large, 1988; Bi and Kojima, 1996a, b; Donsì et al., 1980; Freychet et al., 1989; Indenbirken et al., 2000; Kimura and Kojima, 1992; Massimilla et al., 1981; Sit and Grace, 1986; Wang (F) et al., 2010; Xuereb et al., 1992) and some of the key features of proposed models were summarized by Massimilla (1985). They consist in models where every aspect pertaining to the jet is evaluated on the basis of a correlation, or is supposed to follow a certain trend (e.g. geometry, transport model, velocity profile) or obey macroscopic balances. These models are relatively simple to solve and usually allow for the estimation of the jet properties, the composition and temperature profiles. They have seldom been used or validated for use in reactive systems and for the most part have been

limited to comparing the predicted steady-state jet structure with that from experimental data (e.g. penetration length, jet half-angle, solid holdup distributions).

The CFD approach has the advantage of not requiring prior knowledge about the jet properties. This more evolved resolution approach allows for the simultaneous resolution of the bed and jet without having to rely on specific correlations on the jet. Resolution of the resulting systems of equations is usually more demanding and is achieved through some important simplifications, such as approximating the system as a 2D geometry. However, current computer capabilities allow for more flexibility and 3D geometries are being considered. Correlations are used to estimate the interphase momentum transfer. The phase viscosities and the restitution coefficient are often used as model adjustment parameters. This type of approach was used and is further described by Dan et al. (2010), Gidaspow and Ettahdieh (1983b), Kuipers et al. (1991, 1992), Hong et al. (1996, 1997), and Patil et al. (2005). In all these cases, only the hydrodynamic aspects of the fluidized bed and jet were evaluated for coarse particles (Geldart B and D).

Recently, Salcudean's group at the University of British Columbia has initiated the modeling of gas and gas–liquid jets in 3D fluidized beds of FCC (Geldart A) using the CFD approach (Li, 2009; Li et al., 2008; Pougatch, 2011; Pougatch and Salcudean, 2010). Because of the length scale associated with their system, the number of calculations required and the resolution time are important (i.e. over a week of computer time to simulate 0.5 s of physical time, Li et al.). The results obtained were found to be in fair agreement with the jet penetration lengths predicted by the correlation of Benjelloun et al. (1991), and the outlook is promising for such approaches to be used in the simulations of reactive systems in the near future.

2.6 Concluding Remarks

The injection of gas in fluidized beds is a potentially critical design aspect which can have a profound influence on the performance of reactive systems, due to the gas and solid entrainment resulting from the presence of jets near the injection points. This document has focused on summarizing the experimental approaches that have been used in the study of jets in fluidized beds with an attempt to highlight their key features and recognized characteristics. The influence of operating and experimental conditions on the jet characteristics was also described. Existing correlations used for the estimation of jet penetration lengths flow regime maps and jet half-angles were also compiled with an attempt to summarize their underlying conditions. The

various jet length correlations were compared under representative fluidized bed conditions in order to highlight the influence that particle type, injection velocity and operating pressure can have on the predictions. An effort was made to emphasize the factors which can lead to correlations failing to provide reliable values when extrapolating to other conditions. False constants introduced in the formulation of dimensionless numbers used in the correlations have been identified as causes for erroneous trends. Finally, a brief summary of past and ongoing modeling efforts was presented.

2.7 List of Symbols

C constant in correlation by Benjelloun et al. (1991) (refer to Table 2.1), -

C_G geometry related constant in correlation by Ariyapadi et al. (2004) (refer to Table 2.4), -

d diameter, m

f bubble frequency in correlation by Yates et al. (1986) (refer to Table 2.3); sound frequency in correlation by Guo et al. (2010) (refer to Table 2.4), Hz

g gravitational constant, $g = 9.81$ m/s^2

H height or axial position in the bed, m

L_b jet bubble penetration length (maximum penetration of high momentum jet bubbles), m

L_j undefined jet length, m

L_{max} maximum jet penetration length (maximum length of pulsating void), m

L_{min} minimum jet penetration length (length of permanent void), m

N_j number of orifices in grid plate, -

P pressure, Pa

Q volumetric flow rate, m^3/s

S	gas-to-liquid velocity ratio in correlation by Ariyapadi et al. (2004) (refer to Table 2.4), -
SPL	sound pressure level in correlation by Guo et al. (2010) (refer to Table 2.4), dB
T	temperature, °C
U	superficial velocity, m/s
u	actual velocity, m/s
$w_{g,j}$	gas-to-liquid mass ratio in injector in correlation by Ariyapadi et al. (2004) (refer to Table 2.4), -
X_j	distance between neighboring nozzles in conditions by Luo et al. (1999) (refer to Table 2.3), m
x	variable used to designate the length scaling factor in dimensionless numbers, m
z	variable equivalent to $\ln\left(\rho_j u_j^2\right)$ used in correlations by Zenz (1968) (refer to Table 2.1), $\rho_j u_j^2$ is in Pa

Greek letters

ε	local volumetric fraction
$\overline{\varepsilon}$	average volumetric fraction
φ	jet half-angle, °
μ	viscosity, Pa·s
θ	nozzle inclination angle relative to horizontal used in correlation by Hong et al. (1997) (refer to Table 2.5), °
ρ	density, kg/m^3
ξ	dimensionless jet radius for a given axial position (r/R), -

Subscripts

0	refers to the fluidized bed at rest (U_g = 0 m/s)

a	refers to the annular part of the jet in relationship by Luo et al. (1997) (refer to Table 2.4)
cf	refers to the fluidized bed at complete fluidization
g	refers to the gas in the fluidized bed at the same axial position as the nozzle tip
j	corresponds to the injected gas (based on conditions within the injector at the tip)
m	refers to the extremum condition along the jet axis in relationship by Luo et al. (1997) (refer to Table 2.4)
mb	refers to the fluidized bed at minimum bubbling
mf	refers to the fluidized bed at minimum fluidization
p	refers to the particles
s	refers to solid fraction
t	refers to the column

2.8 References

Abramovich, G.N., 1963. The Theory of Turbulent Jets, The M.I.T. Press, Cambridge.

Ariyapadi, S., Holdsworth, D.W., Norley, C.J.D., Berruti, F., Briens, C., 2003. Digital X-ray Imaging Technique to Study the Horizontal Injection of Gas–Liquid Jets into Fluidized Beds. International Journal of Chemical Reactor Engineering 1, A56.

Ariyapadi, S., Berruti, F., Briens, C., McMillan, J., Zhou, D., 2004. Horizontal Penetration of Gas–Liquid Spray Jets in Gas–Solid Fluidized Beds. International Journal of Chemical Reactor Engineering 2, A22.

Basov, V.A., Markhevka, V.I., Melik-Akhnazarov, T.K., Orochko, D.I., 1969. Investigation of the Structure of a Nonuniform Fluidized Bed. International Chemical Engineering 9, 263–266.

Beeckmans, J.M., Large, J.F., 1988. Estimated Effects of Process Variables on Jet Temperature in a U-Gas Reactor. Industrial & Engineering Chemistry Research 27, 963–969.

Behie, L.A., Bergougnou, M.A., Baker, C.G.J., Bulani, W., 1970. Jet Momentum Dissipation at a Grid of a Larger Gas Fluidized Bed. The Canadian Journal of Chemical Engineering 48, 158–161.

Behie, L.A., Bergougnou, M.A., Baker, C.G.J., Base, T.E., 1971. Further Studies on Momentum Dissipation of Grid Jets in a Gas Fluidizied Bed. The Canadian Journal of Chemical Engineering 49, 557–561.

Benjelloun, F., Liégeois, R., Vanderschuren, J., 1991. Détermination des longueurs de jets de gaz horizontaux dans les lits fluidisés, in: Laguérie, C., Guigon, P. (Eds.), Récents progrès en génie des procédés: La Fluidisation, pp. 108–115.

Berruti, F., Dawe, M., Briens, C., 2009. Study of Gas–Liquid Jet Boundaries in a Gas–Solid Fluidized Bed. Powder Technology 192, 250–259.

Bi, J., Kojima, T., 1996a. Experimental and Numerical Study on Gas Flow in the Grid Zone of Jetting-fluidized Beds. Chemical Engineering Communications 147, 55–73.

Bi, J., Kojima, T., 1996b. Prediction of Temperature and Composition in a Jetting Fluidized Bed Coal Gasifier. Chemical Engineering Science 51, 2745–2750.

Blake, T.R., Webb, H., Sunderland, P.B., 1990. The Nondimensionalization of Equations Describing Fluidization with Application to the Correlation of Jet Penetration Height. Chemical Engineering Science 45, 365–371.

Blake, T.R., Wen, C.Y., Ku, C.A., 1984. The Correlation of Jet Penetration Measurements in Fluidized Beds Using Nondimensional Hydrodynamic Parameters. AIChE Symposium Series 234, 42–51.

Briens, C.L., Bergougnou, M.A., 1984. Grid Leakage (Weeping and Dumping) in a Pilot Plant Size Gas Fluidized Bed. The Canadian Journal of Chemical Engineering 62, 455–463.

Chen, J., Lu, X., Liu, H., Liu, J., 2008. The Effect of Solid Concentration on the Secondary Air-jetting Penetration in a Bubbling Fluidized Bed. Powder Technology 185, 164–169.

Chen, L., Weinstein, H., 1993. Shape and Extent of Voids Formed by a Horizontal Jet in a Fluidized Bed. AIChE Journal 39, 1901–1909.

Chen, L., Weinstein, H., 1997. Temperatire Distribution around Heated Horizontal Jet in Fluidized Bed. AIChE Journal 43, 2373–2375.

Chiba, T., Terashima, K., Kobayashi, H., 1972. Behaviour of Bubbles in Gas–Solid Fluidized Beds: Initial Formation of Bubbles. Chemical Engineering Science 27, 965–972.

Chyang, C.S., Chang, C.H., Chang, J.H., 1997. Gas Discharge Modes at a Single Horizontal Nozzle in a Two-dimensional Fluidized Bed. Powder Technology 90, 71–77.

Cleaver, J.A.S., Ghardiri, M., Tuponogov, V.G., Yates, J.G., Cheesman, D.J., 1995. Measurement of Jet Angles in Fluidized Beds. Powder Technology 85, 221–226.

Dan, S.; Jianzhi, W.; Huilin, L.; Yunhua, Z.; Juhui, C.; Gidaspow, D.; Ming, C., 2010. Numerical Simulation of Gas-particle Flow with a Second-order Moment Method in Bubbling Fluidized Beds. Powder Technology 199, 213-225.

Dawe, M., Briens, C., Berruti, F., 2007. Study of Horizontal Sonic Gas Jets in Gas–Solid Fluidized Beds, in: Berruti, F., Bi, X.(T.), Pugsley, T. (Eds.), Proceedings of the Twelfth Engineering Foundation Conference on Fluidization, (Vancouver, British Columbia, Canada), Engineering Foundation, New York, pp. 783–790.

Deole, N.R., 1980. Study of Jets in Three Dimensional Gas Fluidized Beds. M.S. Thesis, West Virginia University, Morgantown, WV, USA.

Donadono, S., Massimilla, L., 1978. Mechanisms of Momentum and Heat Transfer between Gas Jets and Fluidized Beds, in: Davidson, J.F., Keairns, D.L. (Eds.), Proceedings of the Second Engineering Foundation Conference on Fluidization, (Cambridge, England), Engineering Foundation, New York, pp. 375–380.

Donsì, G., Massimilla, L., Colantuoni, L., 1980. The Dispersion of Axi-symmetric Gas Jets in Fluidized Beds, in: Grace, J.R., Matsen, J.M. (Eds.), Engineering Foundation Conference on Fluidization of the Third Engineering Foundation Conference on Fluidization, (Henniker, New Hampshire), Engineering Foundation, New York, pp. 297–304.

Dry, R.J., Judd, M.R., 1986. Split Feed Fluidised Bed Reactors: Mass Transfer in the Sparger Region, in: Østergaard, K., Sørensen, A. (Eds.), Proceedings of the Fifth Engineering Foundation Conference on Fluidization, (Elsinore, Denmark), Engineering Foundation, New York, pp. 47–54.

Du, B., Marashdeh, Q., Warsito, W. Park, A.-H.A., Fan, L.-S., 2007. Development of Electrical Capacitance Volume Tomography (ECVT) and Electrostatic Tomography (EST) for 3D Density Imaging of Fluidized Bed System, in: Berruti, F., Bi, X.(T.), Pugsley, T. (Eds.), Proceedings of the Twelfth Engineering Foundation Conference on Fluidization, (Vancouver, British Columbia, Canada), Engineering Foundation, New York, pp. 473–480.

Filla, M., Massimilla, L., Vaccaro, S., 1983. Gas Jets in Fluidized Beds: The Influence of Particle Size, Shape and Density on Gas and Solids Entrainment. International Journal of Multiphase Flow 9, 259–267.

Filla, M., Massimilla, L., Musmarra, D., Vaccaro, S., 1986. Pressure Fluctuations Associated with Gas Injection in Fluidized Beds, in: Østergaard, K., Sørensen, A. (Eds.), Proceedings of the Fifth Engineering Foundation Conference on Fluidization, (Elsinore, Denmark), Engineering Foundation, New York, pp. 71–78.

Freychet, N., Briens, C.L., Bergougnou, M.A., Large, J.F., 1989. A New Approach to Jet Phenomena Gas Entrainment and Recirculation in a Bidimensional Spouted Fluidized Bed. The Canadian Journal of Chemical Engineering 67, 191–199.

Gbordzoe, E.A.M., Freychet, N., Bergougnou, M.A., Large, J.F., 1988. Gas Transfer Between a Central Jet and a Large Two-dimensional Gas-fluidized Bed. Powder Technology 55, 207–222.

Gbordzoe, E.A.M., Bergougnou, M.A., 1990. Mass Transfer from a Central Jet Introduced into a Large Two-dimensional Fluidized Bed. Powder Technology 62, 67–75.

Gidaspow, D., Lin, C., Seo, Y.C., 1983a. Fluidization in Two-dimensional Beds with a Jet. 1. Experimental Porosity Distributions. Industrial & Engineering Chemistry Fundamentals 22; 187–193.

Gidaspow, D., Ettehadieh, B., 1983b. Fluidization in Two-dimensional Beds with a Jet. 2. Hydrodynamic Modeling. Industrial & Engineering Chemistry Fundamentals 22, 193–201.

Grace, J.R., Lim, C.J., 1987. Permanent Jet Formation in Beds of Particulate Solids. The Canadian Journal of Chemical Engineering 65, 160–162.

Guo, Q., Liu, Z., Zhang, J., 2000. Flow Characteristics in a Large Jetting Fluidized Bed with Two Nozzles. Industrial & Engineering Chemistry Research 39, 746–751.

Guo, Q., Yue, G., 2001a. Gas Discharge Pattern in a Large Jetting Fluidized Bed with Vertical Nozzle. Industrial & Engineering Chemistry Research 40, 3689–3696.

Guo, Q., Yue, G., Zhang, J., Liu, Z., 2001b. Hydrodynamic Characteristics of a Two-dimensional Jetting Fluidised Bed with Binary Mixtures. Chemical Engineering Science 56, 4685–4694.

Guo, Q., Si, C., Zhang, J., 2010. Flow Characteristics in a Jetting Fluidized Bed with Acoustic Assistance. Industrial & Engineering Chemistry Research 49, 7638–7645.

He, Y.L., Qin, S.Z., Lim, C.J., Grace, J.R., 1994. Particle Velocity Profiles and Solid Flow Patterns in Spouted Beds. The Canadian Journal of Chemical Engineering 72, 561–568.

He, Y.L., Lim, C.J., Qin, S.Z., Grace, J.R., 1998. Spout Diameters in Full and Half Spouted Beds.

The Canadian Journal of Chemical Engineering 76, 702–706.

Hirsan, I., Sishtla, C., Knowlton, T.M., 1980. The Effect of Bed and Jet Parameters on Vertical Jet Penetration Length in Gas Fluidized Beds. Paper presented at 73rd Annual AIChE Meeting (Chicago, Illinois, USA), AIChE.

Hong, R., Li, H., Cheng, M., Zhang, J., 1996. Numerical Simulation and Verification of a Gas–Solid Jet Fluidized Bed. Powder Technology 87, 73–81.

Hong, R., Li, H., Li, H., Wang, Y., 1997. Studies on the Inclined Jet Penetration Length in a Gas–Solid Fluidized Bed. Powder Technology 92, 205–212.

Huang, C.-C., Chyang, C.-S., 1991. Gas Discharge Modes at a Single Nozzle in Two-dimensional Fluidized Beds. Journal of Chemical Engineering of Japan 24, 633–639.

Indenbirken, M., Schneider, T., Siepmann, V., Strauss, K., 2000. A New Model for the Propagation of Jets in Dilute Gas–Solid Crossflows. The Canadian Journal of Chemical Engineering 78, 468–477.

Kimura, T., Kojima, T., 1992. Numerical Model for Reactions in a Jetting Fluidized Bed Coal Gasifier. Chemical Engineering Science 47, 2529–2534.

Kimura, T., Matsuo, H., Uemiya, S., Kojima, T., 1994. Measurement of Jet Shape and Its Dynamic Change in Three-dimensional Jetting Fluidized Beds. Journal of Chemical Engineering of Japan 27, 602–609.

Kimura, T., Horiuchi, K., Watanabe, T., Matsukata, M., Kojima, T., 1995. Experimental Study of Gas and Particle Behavior in the Grid Zone of a Jetting Fluidized Bed Cold Model. Powder Technology 82, 135–143.

Knowlton, T.M., Hirsan, I., 1980. The Effect of Pressure on Jet Penetration in Semi-cylindrical Gas-fluidized Beds, in: Grace, J.R., Matsen, J.M. (Eds.), Proceedings of the Third Engineering Foundation Conference on Fluidization, (Henniker, New Hampshire), Engineering Foundation, New York, pp. 315–324.

Ku, C.A., 1982. Jetting Phenomena in a High Temperature Fluidized Bed. M.S. Thesis, West Virginia University Morgantown, WV, USA.

Kuipers, J.A.M., Prins, W., van Swaaij, W.P.M., 1991. Theoretical and Experimental Bubble Formation at a Single Orifice in a Two-dimensional Gas-fluidized Bed. Chemical Engineering Science 46, 2881–2894.

Kuipers, J.A.M., Tammes, H., Prins, W., van Swaaij, W.P.M., 1992. Experimental and Theoretical Porosity Profiles in a Two-dimensional Gas-fluidized Bed with a Central Jet. Powder Technology 71, 87–99.

Li, T., 2009. Numerical Investigation of the Gas/Spray Jet Interaction with Fluidized Beds. PhD Thesis, The University of British Columbia, Vancouver, BC, Canada.

Li, T., Pougatch, K., Salcudean, M., Grecov, D., 2008. Numerical Simulation of Horizontal Jet Penetration in a Three-dimensional Fluidized Bed. Powder Technology 184, 89–99.

Luo, C.-H., Uemiya, S., Kojima, T., 1997. Dynamic Behavior and Solid Volume Fraction Distribution in a Jetting Fluidized Bed. Journal of Chemical Engineering of Japan 30, 491–499.

Luo, G., Zhang, J.-Y., Guo, Q., Zhang, B., 1999. Study on Jet Flow from Two Vertical Nozzles in a 500 mm I.D. Semi-circular Fluidized Bed. Chemical Engineering & Technology 22, 247–251.

Madonna, L.A., Lama, R.F., Brisson, W.L., 1961. Solids–Air Jets. British Chemical Engineering 6, 524–528.

Massimilla, L., Donsì, G., Migliaccio, N., 1981. The Dispersion of Gas Jets in Two-dimensional, Fluidized Beds of Coarse Solids. AIChE Symposium Series 77, 17–27.

Massimilla, L., 1985. Gas Jets in Fluidized Beds, in: Davidson, J.F., Clift, R., Harrison, D. (Eds.), Fluidization, second ed. Academic Press, London, pp. 133–172.

McMillan, J., 2007. Characterization of the Interactions between High Velocity Jets and Fluidized Particles. PhD Thesis, The University of Western Ontario, London, ON, Canada.

Merry, J.M.D., 1971. Penetration of a Horizontal Gas Jet into a Fluidized Bed. Transactions of the Institution of Chemical Engineers 49, 189–195.

Merry, J.M.D., 1975. Penetration of Vertical Jets into Fluidized Beds. AIChE Journal 21, 507–510.

Miller, D.R., 1962. Injection Mixing of Gaseous Reactants. Chemical Engineering Progress 58, 77–84.

Molodtsof, Y., Labidi, F., 1995. Jets in Fluidized Beds: Flow Structure and Gas Mixing, in: Large, J.F., Laguérie, C. (Eds.), Proceedings of the Eighth Engineering Foundation Conference on Fluidization, (Tours, France), Engineering Foundation, New York, pp. 279–285.

Mudde, R.F.; Harteveld, W.K.; van den Akker, H.E.A.; van der Hagen, T.H.J.J.; van Dam, H., 1999. Gamma Radiation Densitometry for Studying the Dynamics of Fluidized Beds. Chemical Engineering Science 54, 2047–2054.

Müller, C.R., Holland, D.J., Sederman, A.J., Mantle, M.D., Gladden, L.F., Davidson, J.F., 2008. Magnetic Resonance Imaging of Fluidized Beds. Powder Technology 183, 53–62.

Müller, C.R., Holland, D.J., Davidson, J.F., Dennis, J.S., Gladden, L.F., Hayhurst, A.N., Mantle, M.D., Sederman, A.J., 2009. Geometrical and Hydrodynamical Study of Gas Jets in Packed and Fluidized Beds Using Magnetic Resonance. The Canadian Journal of Chemical Engineering 87, 517–525.

Musmarra, D., Vaccaro, S., Filla, M., Massimilla, L., 1992. Propagation Characteristics of Pressure Disturbances Originated by Gas Jets in Fluidized Beds. International Journal of Multiphase Flow 18, 965–976.

Musmarra, D., 2000. Influence of Particle Size and Density on the Jet Penetration Length in Gas Fluidized Beds. Industrial & Engineering Chemistry Research 39, 2612–2617.

Oki, K., Ishida, M., Shirai, T., 1980. The Behaviour of Jets and Particles near the Gas Distributor in a Three-dimensional Fluidized Bed, in: Grace, J.R., Matsen, J.M. (Eds.), Proceedings of the Third Engineering Foundation Conference on Fluidization, (Henniker, New Hampshire), Engineering Foundation, New York, pp. 421–428.

Patience, G.S., Bockrath, R.E., 2010. Butane Oxidation Process Development in a Circulating Fluidized Bed. Applied Catalysis A: General 376, 4–12.

Patil, D.J.; van Sint Annaland, M.; Kuipers, J.A.M., 2005. Critical Comparison of Hydrodynamic Models for Gas–Solid Fluidized Beds - Part I: Bubbling Gas–Solid Fluidized Beds Operated with a Jet. Chemical Engineering Science 60, 57-72.

Pei, P., Zhang, K., Yu, B., Gao, J., Wu, G., Wen, D., 2011. Dynamic Characteristics of Binary Mixtures in a Two-jet Fluidized Bed. Chemical Engineering Science 66, 1702–1714.

Pell, M., 1990. Gas Fluidization, Elsevier, Amsterdam.

Pore, M., Holland, D.J., Chandrasekera, T.C., Müller, C.R., Sederman, A.J., Dennis, J.S., Gladden, L.F., Davidson, J.F., 2010. Magnetic Resonance Studies of a Gas–Solids Fluidised Bed: Jet–Jet and Jet–Wall Interactions. Particuology 8, 617–622.

Pougatch, K., 2011. Mathematical Modelling of Gas and Gas–Liquid Jets Injected into a Fluidized Bed. PhD Thesis, The University of British Columbia, Vancouver, BC, Canada.

Pougatch, K., Salcudean, M., 2010. Numerical Simulation of Liquid Spray Dispersion in a Fluidized Bed. The Canadian Journal of Chemical Engineering 88, 648–654.

Raghunathan, K., Mori, H., Whiting, W.B., 1988. A Technique for Measurement of Jet Penetration in Hot Fluidized Beds. Industrial & Engineering Chemistry Research 27, 1011–1016.

Rees, A.C., Davidson, J.F., Dennis, J.S., Fennell, P.S., Gladden, L.F., Hayhurst, A.N., Mantle, M.D., Müller, C.R., Sederman, A.J., 2006. The Nature of the Flow just Above the Perforated Plate Distributor of a Gas-fluidised Bed, as Imaged Using Magnetic Resonance. Chemical Engineering Science 61, 6002–6015.

Roach, P.E., 1993. Differentiation between Jetting and Bubbling in Fluidized Beds. International Journal of Multiphase Flow, 19, 1159–1161.

Rowe, P.N., MacGillivray, H.J., Cheesman, D.J., 1979. Gas Discharge from an Orifice into a Gas Fluidised Bed. Transactions of the Institution of Chemical Engineers 57, 194–199.

Ruud van Ommen, J., Pfeffer, R., 2010. Fluidization of Nanopowders: Experiments, Modeling, and Applications, in: Kim, S.D., Kang, Y., Lee. J.K., Seo, Y.C. (Eds.), Proceedings of the Thirteenth Engineering Foundation Conference on Fluidization, (Gyeong-ju, Korea), Engineering Foundation, New York, pp. 479–486.

Sauriol, P., Cui, H., Chaouki, J., (submitted 2011a). Gas–Solid Structure in the Vicinity of a Sparger Nozzle in a Fluidized Bed. Powder Technology.

Sauriol, P., Cui, H., Chaouki, J., (submitted 2011b). Gas Jet Penetration Lengths from Upward and Downward Nozzles in Dense Gas–Solid Fluidized Beds. Chemical Engineering Science.

Seville, J.P.K., Morgan, J.E.P., Clift, R., 1986. Tomographic Determination of the Voidage Structure of Gas Fluidised Beds in the Jet Region, in: Østergaard, K., Sørensen, A. (Eds.), Proceedings of the Fifth Engineering Foundation Conference on Fluidization, (Elsinore, Denmark), Engineering Foundation, New York, pp. 87–94.

Shen, Z., Briens, C.L., Kwauk, M., Bergougnou, M.A., 1990a. Study of a Downward Grid Jet in a Large Two-dimensional Gas-fluidized Bed. Powder Technology 62, 227–234.

Shen, Z., Briens, C.L., Kwauk, M., Bergougnou, M.A., 1990b. Study of a Downward Gas Jet in a Two-dimensional Fluidized Bed. The Canadian Journal of Chemical Engineering 68, 534–540.

Shen, Z., Briens, C.L., Bergougnou, M.A., Kwauk, M., 1991. Jet Presence Probability in a Two-dimensional Fluidized Bed. Powder Technology 67, 93–101.

Sit, S.-P., Grace, J.R., 1981. Hydrodynamics and Mass Transfer in the Distributor Zone of Fluidized Beds, in: 2nd World Congress of Chemical Engineering, pp. 81–84.

Sit, S.-P., Grace, J.R., 1986. Interphase Mass Transfer during Bubble Formation in Fluidized Beds, in: Østergaard, K., Sørensen, A. (Eds.), Proceedings of the Fifth Engineering Foundation Conference on Fluidization, (Elsinore, Denmark), Engineering Foundation, New York, pp. 39–46.

Sotudeh-Gharebaagh, R., Chaouki, J., 2000. Gas Mixing in a Turbulent Fluidized Bed Reactor. The Canadian Journal of Chemical Engineering 78, 65–74.

Vaccaro, S., Musmarra, D., Costanza, F., Filla, M., Massimilla, L., 1989. Diagnostics of Gas Injection in Fluidized Beds by Pressure Signal Analysis, in: Grace, J.R., Shemilt, L.W., Bergounou, M.A. (Eds.), Proceedings of the Sixth Engineering Foundation Conference on Fluidization, (Banff, Alberta, Canada), Engineering Foundation, New York, pp. 245–252.

Vaccaro, S., 1997. Analysis of the Variables Controlling Gas Jet Expansion Angles in Fluidized Beds. Powder Technology 92, 213–222.

Vaccaro, S., Musmarra, D., Petrecca, M., 1997a. Evaluation of the Jet Penetration Depth in Gas-fluidized Beds by Pressure Signal Analysis. International Journal of Multiphase Flow 23, 683–698.

Vaccaro, S., Musmarra, D., Petrecca, M., 1997b. A Technique for Measurement of the Jet Penetration Height in Fluidized Beds by Pressure Signal Analysis. Powder Technology 92, 223–231.

Wang, C.H., Zhong, Z.P., Li, R., E, J.Q., 2010. Prediction of Jet Penetration Depth Based on Least Square Support Vector Machine. Powder Technology 203, 404–411.

Wang, F., Yu, Z., Marashdeh, Q., Fan, L.-S., 2010. Horizontal Gas and Gas/Solid Jet Penetration in a Gas–Solid Fluidized Bed. Chemical Engineering Science 65, 3394–3408.

Wen, C.Y., Horio, H., Krishnan, R., Khosravi, R., Rengarajan, P., 1977. Jetting Phenomena and Dead Zone Formation on Fluidized Bed Distributors, in: The Second Pacific Chemical Engineeering Congress (Denver, Colorado), AIChE, New York, pp. 1182–1189.

Wen, C.Y., Deole, N.R., Chen, L.H., 1982. A Study of Jets in a Three-dimensional Gas Fluidized Bed. Powder Technology 31, 175–184.

Wu, C.-S.; Whiting, W.B., 1988. Interacting Jets in a Fluidized Bed. Chemical Engineering Communications 73, 1-17.

Xuereb, C., Laguérie, C., Baron, T., 1991a. Étude du comportement des jets continus horizontaux ou inclinés introduits dans un lit fluidisé par un gaz, I: Morphologie des jets. Powder Technology 67, 43–56.

Xuereb, C., Laguérie, C., Baron, T., 1991b. Étude du comportement des jets continus horizontaux ou inclinés introduits dans un lit fluidisé par un gaz, Deuxième partie: Profils de vitesse du gaz dans les jets horizontaux. Powder Technology 64, 271–283.

Xuereb, C., Laguérie, C., Baron, T., 1992. Étude du comportement des jets continus horizontaux ou inclinés introduits dans un lit fluidisé par un gaz, III: Modélisation de la zone d'écoulement développé du jet. Powder Technology 72, 7–16.

Yang, W.-C., 1981. Jet Penetration in a Pressurized Fluidized Bed. Industrial & Engineering Chemistry Fundamentals 20, 297–300.

Yang, W.-C., Keairns, D.L., 1978a. Design and Operating Parameters for a Fluidized Bed Agglomerating Combustor/Gasifier, in: Davidson, J.F., Keairns, D.L. (Eds.), Proceedings of the Second Engineering Foundation Conference on Fluidization, (Cambridge, England), Engineering Foundation, New York, pp. 208–214.

Yang, W.-C., Keairns, D.L., 1978b. Design of Recirculating Fludidized Beds for Commercial Applications. AIChE Symposium Series 74, 218–228.

Yang, W.-C., Keairns, D.L., 1979. Estimating the Jet Penetration Depth of Multiple Vertical Grid Jets. Industrial & Engineering Chemistry Fundamentals 18, 317–320.

Yang, W.-C., Keairns, D.L., 1980. Momentum Dissipation of and Gas Entrainment into a Gas-fluidized Two-phase Jet in a Fluidized Bed, in: Grace, J.R., Matsen, J.M. (Eds.), Proceedings of the Third Engineering Foundation Conference on Fluidization, (Henniker, New Hampshire), Engineering Foundation, New York, pp. 305–314.

Yang, W.C., Revay, D., Anderson, R.G., Chelen, E.J., Keairns, D.L., Cicero, D.C., 1983. Fluidization Phenomena in a Large Scale Cold Flow Model, in: Kunii, D., Toei, R. (Eds.), Proceedings of the Fourth Engineering Foundation Conference on Fluidization, (Kashikojima, Japan), Engineering Foundation, New York, pp. 77–84.

Yates, J.G., Bejcek, V., Cheesman, D.J., 1986. Jet Penetration into Fluidized Beds at Elevated Pressures, in: Østergaard, K., Sørensen, A. (Eds.), Proceedings of the Fifth Engineering Foundation Conference on Fluidization, (Elsinore, Denmark), Engineering Foundation, New York, pp. 79–86.

Yates, J.G., Cobbinah, S.S., Cheesman, D.J., Jordan, S.P., 1991. Particle Attrition in Fluidized Beds Containing Opposing Jets. AIChE Symposium Series 87, 13–19.

Yates, J.G., 1996. Effect of Temperature and Pressure on Gas–Solid Fluidization. Chemical Engineering Science 51, 167–205.

Yutani, N., Ho, T.C., Fan, L.T., Walawender, W.P., Song, J.C., 1983. Statistical Study of the Grid Zone Behavior in a Shallow Gas–Solid Fluidized Bed Using a Mini-capacitance Probe. Chemical Engineering Science 38, 575–582.

Zenz, F.A., 1968. Bubble Formation and Grid Design. Institution of Chemical Engineers Symposium Series 30, 136–139.

Zenz, F.A., 1989. Fluidization and Fluid–Particle Systems, PEMM-Corp, Nelsonville, NY.

Zhong, W., Zhang, M., 2005. Jet Penetration Depth in a Two-dimensional Spout–fluid Bed. Chemical Engineering Science 60, 315–327.

Table 2.1: Correlations for the estimation of the jet penetration lengths in gas–solid fluidized beds.

Author	Correlations	Conditions
Upward		
Basov et al. (1966), from Basov et al. (1969)	$\frac{L_j}{d_j} = \frac{u_j^{0.35}}{d_j^{0.3}} \cdot \frac{1.65\times10^5 d_p}{\left(1+8.09\times10^4 d_p\right)}$ $L_j = L_{max}$ according to Massimilla (1985); $L_j = L_b$ according to Vaccaro, (1997a) Note: converted to SI units (kg–m–s)	Configuration: 3D-a Measurement: Gamma-ray densitometer Geldart: A and B u_j = 10–150 m/s d_p = 65, 140, and 540μm $U_g = U_{mf}$
Blake et al. (1984) and Blake et al. (1990)	General (single nozzles and multi-orifice grid plates) (1984) $\frac{L_j}{d_j} = 110\left(\frac{u_j^2}{gd_j}\right)^{0.304}\left(\frac{\rho_j}{\rho_p}\right)^{0.513}\left(\frac{\rho_p u_j d_p}{\mu_j}\right)^{-0.189}$ Single nozzles (1990) $\frac{L_j}{d_j} = 26.9\left(\frac{u_j^2}{gd_j}\right)^{0.322}\left(\frac{\rho_j}{\rho_p}\right)^{0.325}\left(\frac{\rho_p u_j d_p^2}{\mu_j d_j}\right)^{-0.124}$ Multi-orifice grid plates (1990) $\frac{L_j}{d_j} = 55.6\left(\frac{u_j^2}{gd_j}\right)^{0.251}\left(\frac{\rho_j}{\rho_p}\right)^{0.322}\left(\frac{\rho_p u_j d_p^2}{\mu_j d_j}\right)^{-0.134}$ The authors report that when both L_{max} and L_{min} are given (Knowlton and Hirsan; Yang and Keairns) in referenced work, the average value is used. $L_j = L_{max}$ according to Zhong and Zhang (2005)	Data from the literature Configuration: 2.5D-a-c and 3D-a-b Geldart: A, B, and D P_g = 1, 3.4–51 atm T = ambient, 20–700°C Includes data from: Basov et al. (1969); Behie et al. (1971); Deole (1980); Knowlton and Hirsan (1980); Ku (1982); Markheva et al. (1971); Sit (1981); Tanaka et al. (1980); Yang and Keairns (1978); Yang et al. (1983)

Table 2.1: Correlations for the estimation of the jet penetration lengths in gas–solid fluidized beds (continued).

Author	Correlations	Conditions
Upward (continued)		
Hirsan et al. (1980)	$\frac{L_{max}}{d_j} = 19.3\left[\left(\frac{\rho_j}{\rho_p}\right)^2 \cdot \frac{u_j^2}{g d_p}\right]^{0.415} \left(\frac{U_g}{U_{cf}}\right)^{-0.54}$ $\frac{L_b}{d_j} = 26.6\left[\left(\frac{\rho_j}{\rho_p}\right)^2 \cdot \frac{u_j^2}{g d_p}\right]^{0.335} \left(\frac{U_g}{U_{cf}}\right)^{-0.24}$	Configuration: 2.5D-c Measurement: visual observation Geldart: B d_j = 13–38 mm u_j = 0.8–48 m/s d_p = 120, 210, 480, 500, 595 μm ρ_p = 1150, 2600, 4000 kg/m^3 U_g = 1–3 U_{cf} P_g = 3.4–51 atm
Guo et al. (2001b)	$\frac{L_{max}}{d_j} = \begin{cases} 19.18\left[\frac{\rho_j}{(\rho_p - \rho_j)} \cdot \frac{u_j^2}{g d_j}\right]^{0.2383} \left(\frac{U_g}{U_{mf}}\right)^{-0.3616} & \text{for } 0 < \frac{U_g}{U_{mf}} \le 2.5 \\ 11.52\left[\frac{\rho_j}{(\rho_p - \rho_j)} \cdot \frac{u_j^2}{g d_j}\right]^{0.1966} & \text{for } \frac{U_g}{U_{mf}} > 2.5 \end{cases}$	Configuration: 2D-h Measurement: Pitot tubes, pressure probes, fiber-optic probe, cine-camera Geldart: B and D d_j = 8–16 mm u_j = 5–70U_{mf} d_p = 217, 347, 745, 1135, 1640 μm ρ_p = 1475, 1335, 2550, 2675 kg/m^3 U_g = 1–3U_{mf} H_0 = 80–435 mm

Table 2.1: Correlations for the estimation of the jet penetration lengths in gas–solid fluidized beds (continued).

Author	Correlations	Conditions
Upward (continued)		
Ku (1982), from Wu and Whiting (1988)	$\frac{L_j}{d_j} = 821\left[\frac{\left(u_j - u_{j,mf}\right)^2}{g d_p}\right]^{0.34}\left[\frac{\rho_j\left(u_j - u_{j,mf}\right)d_p}{\mu_j}\right]^{-0.34}\left(\frac{\rho_j}{\rho_p}\right)^{0.67}\left(\frac{d_j}{d_p}\right)^{-0.43}$ $L_j = L_{max}$ Wu and Whiting (1988)	Configuration: 2.5D-a Geldart: B d_j = 1.4, 3.3, 6 mm u_j = 6–609 m/s d_p = 250, 550, 770 μm ρ_p = 2600 kg/m^3 T = 20, 400–700°C
Luo et al. (1999)	$\frac{L_{max}}{d_j} = 119\left(\frac{u_j^2}{g d_j}\right)^{0.18}\left(\frac{\rho_p u_j d_p^2}{\mu_j d_j}\right)^{-0.024}\left(\frac{\rho_j}{\rho_p}\right)^{0.49}$	Configuration: 2.5D-h Measurement: Visual observation Geldart: D d_j = 42 mm (2.5D) u_j = 12–32 m/s d_p = 1640 μm ρ_p = 1335 kg/m^3 $U_g = U_{mf}$ Also includes data from: Behie et al. (1970, 1971) (Geldart A); Basov et al. (1969) (Geldart A); Luo et al. (1996, 1997) (Geldart D)

Table 2.1: Correlations for the estimation of the jet penetration lengths in gas–solid fluidized beds (continued).

Author	Correlations	Conditions
Upward (continued)		
Merry (1975)	$\frac{L_j}{d_j} = 5.2\left(\frac{\rho_j d_j}{\rho_p d_p}\right)^{0.3}\left[1.3\left(\frac{u_j^2}{g d_j}\right)^{0.2} - 1\right]$ $L_j = L_{max}$ according to Massimilla (1985)	Configuration: 2D-a Measurement: Visual observation System: Liquid–Solid Geldart: D d_j = 19×12 mm^2 d_p = 1000, 2000 μm ρ_p = 11750 kg/m^3 $U_g = U_{mf}$
Müller et al. (2009)	Penetration of a single jet issuing from an upward orifice into a fixed bed Form 1 (corrected) $\frac{L_j}{d_j} = 0.59\left(\frac{u_j^2}{g d_j}\right)^{0.24}\left(\frac{U_{mf}^2}{g d_j}\right)^{-0.28}$ Form 2 $\frac{L_j}{d_j} = 8.7\left(\frac{u_j^2}{g d_j}\right)^{0.31}\left(\frac{\rho_j d_j}{\rho_p d_p}\right)^{0.64}$ L_j considered as L_{max}	Configuration: 3D-a Measurement: MRI Geldart: D d_j = 1–4 mm u_j = 10–200 m/s d_p = 500, 900, 1200 μm ρ_p = 900 kg/m^3 (from Rees et al., 2006) U_g = 0 m/s $Q < 0.7\,Q_{mf}$ d_t = 50 mm

Table 2.1: Correlations for the estimation of the jet penetration lengths in gas–solid fluidized beds (continued).

Author	Correlations	Conditions
Upward (continued)		
Musmarra (2000)	$\frac{L_b}{d_j} = 3.0\left(\frac{u_j^2}{g d_j}\right)^{0.32}\left(\frac{\rho_j u_j d_p}{\mu_j}\right)^{-0.37}\left(\frac{\rho_j}{\rho_p}\right)^{-0.33}\left(\frac{d_p}{d_j}\right)^{0.24}$	Configuration: 3D-a Measurement: Impact pressure probe Geldart: B and D d_j = 10 mm u_j = 5–120 m/s d_p = 190, 240, 300, 1220 μm ρ_p = 1250, 2500, 2600, 5050 kg/m^3 $U_g = U_{mf}$ + 0.2 m/s Also includes data from: Basov et al. (1969) 3D-b (gamma-ray densiometer, Geldart A); Behie et al. (1971) (Pitot tube, Geldart A); Vaccaro et al. (1997a) 3D-a (Impact pressure probe Geldart D)

Table 2.1: Correlations for the estimation of the jet penetration lengths in gas–solid fluidized beds (continued).

Author	Correlations	Conditions
Upward (continued)		
Rees et al. (2006)	$\frac{L_j}{d_j} = 3.53\left(\frac{u_j^2}{gd_j}\right)^{0.24}\left(\frac{U_{mf}^2}{gd_j}\right)^{-0.034}\left[N_j \cdot \left(\frac{d_j}{d_t}\right)^2\right]^{0.29}$ L_j considered as L_{max}	Configuration: 3D-b Measurement: MRI Geldart: B and D d_j = 1, 1.5 mm N_j =15, 19, 26, 39 u_j = 5–100 m/s d_p = 500, 1200 μm ρ_p = 900 kg/m^3 d_t = 50 mm
Sauriol et al. (2011b)	$\frac{L_{min}}{d_j} = 2.99\left[\frac{\rho_j u_j^2 + \left(P_j - P_g\right)}{\bar{\varepsilon}_s \rho_p g d_j}\right]^{0.35}\left(\frac{U_g}{U_{mb}}\right)^{-0.35}$ $\frac{L_{max}}{d_j} = 8.37\left[\frac{\rho_j u_j^2 + \left(P_j - P_g\right)}{\bar{\varepsilon}_s \rho_p g d_j}\right]^{0.30}\left(\frac{U_g}{U_{mb}}\right)^{-0.30}$ $\frac{L_b}{d_j} = 23.1\left[\frac{\rho_j u_j^2 + \left(P_j - P_g\right)}{\bar{\varepsilon}_s \rho_p g d_j}\right]^{0.25}\left(\frac{U_g}{U_{mb}}\right)^{-0.30}$ Note: $\bar{\varepsilon}_s$ is estimated from expression provided by the author, and $\left(P_j - P_g\right)$ only applies to choked flow (speed of sound is reached within the nozzle)	Configuration: 3D-c Measurement: Fiber-optic probe Geldart: A and B d_j = 2.4, 4.9, 7.2 mm u_j = 0.08–1013 m/s Injected gases: Helium, Air, Argon, CO_2 d_p = 70–405 μm ρ_p = 880, 1200, 1675, 2650, 3930 kg/m^3 U_g = 0.011–0.65 m/s (> 1.3U_{mb}) H_0 = 230–770 mm H_j = 124–274 mm

Table 2.1: Correlations for the estimation of the jet penetration lengths in gas–solid fluidized beds (continued).

Author	Correlations	Conditions
Upward (continued)		
Shakhova (1968) from Massimilla (1985)	$\frac{L_j}{d_j} = 13\left[\left(\frac{\rho_j}{\rho_p}\right)^2 \cdot \frac{u_j^2}{g d_p}\right]^{0.5} - 0.5\cot\varphi$ $L_j = \left(L_{max} + L_{min}\right)/2$ according to Massimilla (1985)	Geldart: D d_j = 4, 6 mm u_j = 83–192 m/s d_p = 3250 μm ρ_p = 1000 kg/m^3 $U_g = 1.1 U_{mf}$
Wen et al. (1977) from Yang and Keairns (1979)	$\frac{L_j}{d_j} = 814.2\left(\frac{u_j^2}{g d_j}\right)^{0.47}\left(\frac{\rho_j u_j d_j}{\mu_j}\right)^{-0.654}\left(\frac{\rho_p d_p}{\rho_j d_j}\right)^{-0.585}$ $L_j = \left(L_{max} + L_{min}\right)/2$ according to Zhong and Zhang (2005)	Configuration: 2D-b Geldart: B d_j = 3.2, 8 mm u_j = 14–75 m/s d_p = 280, 450, 830 μm ρ_p = 1060, 2410, 2640 kg/m^3

Table 2.1: Correlations for the estimation of the jet penetration lengths in gas–solid fluidized beds (continued).

Author	Correlations	Conditions
Upward (continued)		
Wen et al. (1982)	Atmospheric pressure fluidized bed (3D) $\frac{L_j}{d_j} = 1.15\times10^4 \left[\frac{\left(u_j - u_{j,mf}\right)^2}{g d_p}\right]^{0.42} \left(\frac{\rho_j \left(u_j - u_{j,mf}\right) d_p}{\mu_j}\right)^{-0.42} \left(\frac{\rho_j}{\rho_p}\right) \left(\frac{d_j}{d_p}\right)^{-0.66}$ $L_j = L_{max}$ according to Massimilla (1985), and $L_j = \left(L_{max} + L_{min}\right)/2$ according to Zhong and Zhang (2005)	Configuration: 3D-b Measurement: Fiber-optic probe Geldart: B d_j = 3.2, 6.4 mm u_j = 10–150 m/s d_p = 133, 250, 500 μm ρ_p = 2520, 2570 kg/m^3 Also includes data from: Basov et al. (1969) 3D-b (gamma-ray densiometer, Geldart A); Behie et al. (1971) (Pitot tube, Geldart A); Gharidi and Clift (1980) 3D-b (Geldart B); Markheva et al. (1971) 3D-a (Geldart A); Tanaka et al. (1980) 2.5D-b (Geldart B); Vakhrushev (1972) 3D-a (Geldart A)

Table 2.1: Correlations for the estimation of the jet penetration lengths in gas–solid fluidized beds (continued).

Author	Correlations	Conditions
Upward (continued)		
Wen et al. (1982)	High pressure fluidized beds (2.5D) $\frac{L_j}{d_j} = 1.3\left(\frac{u_j^2}{g d_p}\right)^{0.38}\left(\frac{\rho_j u_j d_p}{\mu_j}\right)^{0.13}\left(\frac{\rho_j}{\rho_p}\right)^{0.56}\left(\frac{d_j}{d_p}\right)^{0.25}$ $L_j = L_{max}$ according Massimilla (1985) and Zhong and Zhang (2005)	Data from the literature Configuration: 2.5D-c Geldart: B and D d_j = 25.4, 38, 54 mm d_p = 430, 2800 μm ρ_p = 210, 1160, 2630, 4000 kg/m^3 P_g = 1, 3.4–51 atm Includes data from: Knowlton and Hirsan (1980) 2.5D-c (visual observation, Geldart B); Yang and Keairns (1978b) 2.5D-c (Geldart B and D)
Yang and Keairns (1978), from Yang (1981)	$\frac{L_{max}}{d_j} = 6.5\left[\frac{\rho_j}{\left(\rho_p - \rho_j\right)} \cdot \frac{u_j^2}{g d_j}\right]^{0.5}$	

Table 2.1: Correlations for the estimation of the jet penetration lengths in gas–solid fluidized beds (continued).

Author	Correlations	Conditions
Upward (continued)		
Yang and Kearns (1979)	$\frac{L_j}{d_j} = 15.0\left[\frac{\rho_j}{\left(\rho_p - \rho_j\right)} \cdot \frac{u_j^2}{g d_j}\right]^{0.187}$ $L_j = L_b$ according to Musmarra (2000) and $L_j = L_{max}$ according to Zhong and Zhang (2005)	Data from the literature Configuration: 2D-b, 3D-b Geldart: A and B d_j = 3–20 mm d_p = 50, 125, 280, 450, 830 μm ρ_p = 1000, 2410, 2635 kg/m^3 Includes data from: Basov et al. (1969) 3D-b (gamma-ray densiometer, Geldart A); Behie et al. (1971) (Pitot tube, Geldart A); Wen et al. (1977) (Geldart B)
Yang (1981)	$\frac{L_{max}}{d_j} = 7.65\left[\frac{U_{cf,atm}}{U_{cf,p}} \cdot \frac{\rho_j}{\left(\rho_p - \rho_j\right)} \cdot \frac{u_j^2}{g d_j}\right]^{0.472}$	Data from Knowlton and Hirsan (1980) Configuration: 2.5D-c Geldart: B d_j = 25.4 mm d_p = 430 μm ρ_p = 1160, 2630, 4000 kg/m^3 P_g = 3.4–51 atm

Table 2.1: Correlations for the estimation of the jet penetration lengths in gas–solid fluidized beds (continued).

Author	Correlations	Conditions
Upward (continued)		
Yates et al. (1986)	$\frac{L_{max}}{d_j} = 21.2\left(\frac{u_j^2}{gd_p}\right)^{0.37}\left(\frac{\rho_j u_j d_p}{\mu_j}\right)^{0.05}\left(\frac{\rho_j}{\rho_p}\right)^{0.68}\left(\frac{d_p}{d_j}\right)^{0.24}$	Configuration: 3D-a Measurement: X-ray, cine-camera Geldart: B d_j = 2–3.4 mm u_j = 30–180 m/s d_p = 260, 320 μm ρ_p = 1420, 1550 kg/m^3 $U_g = 0–3U_{mf}$ P_g = 1, 5, 10, 20 atm
Yates and Cheesman (1987), from Yates (1996)	$\frac{L_{max}}{d_j} = 9.77\left[\frac{U_{cf,atm}}{U_{cf,p}}\cdot\frac{\rho_j}{\left(\rho_p-\rho_j\right)}\cdot\frac{u_j^2}{gd_j}\right]^{0.38}$	Configuration: 3D Particles: coarse powders (not specified) P_g = up to 20 atm (ambiant temperature) T = up to 800°C (atmospheric pressure)

Table 2.1: Correlations for the estimation of the jet penetration lengths in gas–solid fluidized beds (continued).

Author	Correlations	Conditions
Upward (continued)		
Zenz (1968) adapted from Fig. 3–1 in Pell (1990)	$\frac{L_{max}}{d_j} = \begin{cases} 0.1810z + 2.427 & \text{for } \rho_j u_j^2 \le 25 \text{ Pa} \\ 0.2882z^3 - 3.183z^2 + 11.71z - 11.34 & \text{for } 25 \text{ Pa} < \rho_j u_j^2 \le 1825\times10^4 \text{ Pa} \\ 12.66z - 75.90 & \text{for } \rho_j u_j^2 > 1825 \text{ Pa} \end{cases}$ where $z = \ln\left(\rho_j u_j^2\right)$. First segment corresponds to data from Harrison and Leung (1961) for gas bubbling into a liquid. Third segment corresponds to Zenz's correlated data for gas jetting in a bed of solid particles. Second segment is a cubic spline fit connecting the first and third segments.	Configuration: 2D-a Measurement: visual observation, photography and cine-camera Geldart: A and D d_j = 19, 25, 51 mm u_j = 25, 33, 66 m/s d_p = 50, 3810 μm U_g = 0 m/s Also includes data from: Madonna et al. (1961) (Geldart D)
Zhong and Zhang (2005)	$\frac{L_{max}}{d_j} = 10.86\left[\frac{\rho_j}{\left(\rho_p - \rho_j\right)} \cdot \frac{u_j^2}{g d_j}\right]^{0.39} \left(\frac{\rho_j u_j d_p}{\mu_j}\right)^{-0.03} \left(\frac{U_g}{U_{mf}}\right)^{-0.11} \left(\frac{H_0}{d_t}\right)^{-0.17}$	Configuration: 2D-g Measurement: Impact pressure probe, cine-camera, photography Geldart: D d_j = 10×, 20×, 30×30 mm^2 u_j = 7–37 m/s d_p = 1300, 1600, 2800, 3200 μm ρ_p = 810, 1330, 1640, 2600 kg/m^3 $U_g = 0\text{–}3U_{mf}$ H_0 = 250–550 mm

Table 2.1: Correlations for the estimation of the jet penetration lengths in gas–solid fluidized beds (continued).

Author	Correlations	Conditions
Horizontal and inclined		
Benjelloun et al. (1991)	$\frac{L_{max}}{d_j} = C\left[\frac{\rho_j}{\left(\rho_p - \rho_j\right)} \cdot \frac{u_j^2}{g d_j}\right]^{0.27}$ $C = 5.52$ when total gas (background and injected) is that at minimum fluidization ($U_g + U_j = U_{mf}$); $C = 6.86$ when background fluidization is such that $U_g = U_{mf}$; $C = 3.28$ for a fixed bed (U_g = 0 m/s).	Configuration: 3D-d Measurement: visual observation Geldart: d_j = 4, 8 mm u_j = 20–120 m/s Injected gases: Helium, Air d_p = 50, 240, 310 μm ρ_p = 1760, 2373, 2442 kg/m^3 $U_g + U_j = U_{mf}$
Guo et al. (2010)	$\frac{L_{max}}{d_j} = 4.84\times10^{-2}\left[\frac{\rho_j}{\left(\rho_p - \rho_j\right)} \cdot \frac{u_j^2}{g d_j}\right]^{0.125}\left(\frac{\rho_j u_j d_j}{\mu_j}\right)^{0.559}\left(\frac{U_g}{U_{mf}}\right)^{1.794}$ Note: Constant adjusted to agree with reported data	Configuration: 3D-d Measurement: Fiber-optic probe Geldart: A and B d_j = 1.5–8 mm u_j = 15–142 m/s d_p = 85, 115 μm ρ_p = 1810, 2650 kg/m^3 U_g = 1–1.5U_{mf}

Table 2.1: Correlations for the estimation of the jet penetration lengths in gas–solid fluidized beds (continued).

Author	Correlations	Conditions
Horizontal and inclined (continued)		
Hong et al. (1997)	$\frac{L_{max}}{d_j} = 1.64\times10^{6}\left(\frac{\rho_j}{\bar{\varepsilon}_s\rho_p}\cdot\frac{u_j^2}{gd_p}\right)^{0.327}\left(\frac{\rho_j}{\rho_p}\right)^{1.974}\left(\frac{d_p}{d_j}\right)^{-0.040}\left(\frac{\theta}{180°}+\frac{\pi}{2}\right)^{0.148}\left(\frac{H_j}{H_0}\right)^{0.028}-3.8$	Configuration: 2D-e–d Measurement: cine-camera Geldart: D d_j = 5–10 mm u_j = 26–218 m/s θ = -10, 0, 10° d_p = 1430, 2250 μm ρ_p = 1350, 1400, 1580 kg/m^3 (note: reported density of sand particles is unusally low) U_g = 0.74–1.3 m/s H_j = 43, 103, 163, 223 mm H_0 = 1.25–5 H_j

Table 2.1: Correlations for the estimation of the jet penetration lengths in gas–solid fluidized beds (continued).

Author	Correlations	Conditions
Horizontal and inclined (continued)		
Merry (1971)	$\frac{L_{max}}{d_j} = 5.25\left(\frac{\rho_j}{\bar{\varepsilon}_s \rho_p} \cdot \frac{u_j^2}{g d_p}\right)^{0.4} \left(\frac{\rho_j d_p}{\rho_p d_j}\right)^{0.2} - 4.5$	Configuration: 3D-d Measurement: visual observation, cine-camera Particles: Geldar B and D d_j = 2.5–14.3 mm u_j = 40–300 m/s d_p = 180–4000 μm ρ_p = 1000, 2500, 2640, 7430 kg/m^3 U_g = 1.2, 1.5, 1.85, $2U_{mf}$ Also includes data from: Shavhova (1968) (Geldart D); Lumni and Baskakov (1967) (concentration tracer, Geldart B)

Table 2.1: Correlations for the estimation of the jet penetration lengths in gas–solid fluidized beds (continued).

Author	Correlations	Conditions
Horizontal and inclined (continued)		
Zenz (1968) adapted from Fig. 3–1 in Pell (1990)	$\frac{L_{max}}{d_j} = \begin{cases} 0.1810z + 2.427 & \text{for } \rho_j u_j^2 \le 150 \text{ Pa} \\ 4.266\times10^{-2}z^3 - 0.4055z^2 + 1.032z + 2.979 & \text{for } 150\ Pa < \rho_j u_j^2 \le 1.5\times10^4 \text{ Pa} \\ 5.067z - 35.39 & \text{for } \rho_j u_j^2 > 1.5\times10^4 \text{ Pa} \end{cases}$ $z = \ln\left(\rho_j u_j^2\right)$. First segment corresponds to data from Harrison and Leung (1961) for gas bubbling into a liquid. Third segment corresponds to Zenz's correlated horizontal and downward jet penetration data. Second segment is a cubic spline fit connecting the first and third segments.	Data from literature Measurement: visual observation, photography and cine-camera Geldart: B, and D d_j = 1.9–280 mm d_p = 200–3810 μm U_g = 0 m/s Includes data from: Miller (1962) gas–gas jets; Martin and Lavanas (1962) gas–liquid jets; Elliott et al. (1952) (Geldart B and D); Kozin and Baskakov (1967) (Geldart B)
Downward		
Sauriol et al. (2011b)	$\frac{L_{max}}{d_p} = 93.8\left[\frac{\rho_j u_j^2 + \left(P_j - P_g\right)}{\rho_p g d_p}\right]^{0.30}\left[\frac{g d_p^3 \rho_g \left(\rho_p - \rho_g\right)}{\mu_g^2}\right]^{-0.25}\left(\frac{U_g}{U_{mb}}\right)^{0.05}$ $\frac{L_{min}}{d_p} = 40.6\left[\frac{\rho_j u_j^2 + \left(P_j - P_g\right)}{\rho_p g d_p}\right]^{0.40}\left[\frac{g d_p^3 \rho_g \left(\rho_p - \rho_g\right)}{\mu_g^2}\right]^{-0.25}\left(\frac{U_g}{U_{mb}}\right)^{-0.25}$ Note: $\left(P_j - P_g\right)$ only applies to choked flow (speed of sound is reached within the nozzle)	Configuration: 3D-f Measurement: Fiber-optic probe Geldart: A and B d_j = 2.4, 4.9, 7.2 mm u_j = 0.08–1013 m/s Injected gases: Helium, Air, Argon d_p = 70–405 μm ρ_p = 880, 1675, 2650, 3930 kg/m^3 U_g = 0.015–0.64 m/s (> $1.3U_{mb}$) H_0 = 190–740 mm H_j = 161–307 mm

Table 2.1: Correlations for the estimation of the jet penetration lengths in gas–solid fluidized beds (continued).

Author	Correlations	Conditions
Downward (continued)		
Yates et al. (1991)	$\frac{L_{max}}{d_j} = 2.8\left[\frac{\rho_j}{\left(\rho_p - \rho_j\right)} \cdot \frac{u_j^2}{g d_j}\right]^{0.4}$	Configuration: 3D-f Measurement: X-ray Geldart: A d_j = 5.1, 7.6, 10.2, 15.2 mm u_j = 10–110 m/s d_p = 55 μm ρ_p = 1500 kg/m^3 $U_g = U_{mf}$
Zenz (1968) adapted from Fig. 3–1 in Pell (1990)	$\frac{L_{max}}{d_j} = \begin{cases} 0.1810z + 2.427 & \text{for } \rho_j u_j^2 \le 150 \text{ Pa} \\ 4.266\times10^{-2} z^3 - 0.4055 z^2 + 1.032 z + 2.979 & \text{for } 150\ Pa < \rho_j u_j^2 \le 1.5\times10^4 \text{ Pa} \\ 5.067 z - 35.39 & \text{for } \rho_j u_j^2 > 1.5\times10^4 \text{ Pa} \end{cases}$ where $z = \ln\left(\rho_j u_j^2\right)$. First segment corresponds to data from Harrison and Leung (1961) for gas bubbling into a liquid. Third segment corresponds to Zenz's correlated data for horizontal and downward jet penetration data. Second segment is a cubic spline fit connecting the first and third segments.	Configuration: 2D–f Measurement: visual observation, photography and cine-camera System: Gas–, Liquid–Solid Geldart: A and D d_j = 8.2, 11 mm u_j = 2.5–120 m/s d_p = 170, 1000 μm U_g = 0 m/s

Table 2.2: Reference conditions for sensitivity analysis of the various jet penetration length correlations.

Particle properties			
Particle name (Geldart type)		FCC (A)	Sand (B)
Particle diameter (d_p) (μm)		75	300
Particle density (ρ_p) (kg/m^3)		1500	2650
Minimum fluidizing velocity (U_{mf})		Calculated (Wen and Yu)	Calculated (Grace)
Minimum bubbling velocity (U_{mb})		$2U_{mf}$	U_{mf}
Solid holdup at minimum fluidization ($\varepsilon_{s,mf}$)		0.45	0.55
Injection and bed conditions			
Injected gas	Air	Fluidizing gas	Air
Injection velocity (u_j) (m/s)	40	Bed diameter (d_t) (mm)	300
Injector diameter (d_j) (mm)	10	Background fluidization (U_g) Does not apply to multi-orifice grids	U_{mf}
Injector location (H_j) (mm) Only applies to sparger type	200	Initial bed height (H_0) (mm)	500+ H_j
Grid plate open area (β) Only applies to multi-orifice grid plates	0.03	Temperature (°C)	25
		Pressure (atm)	1

Table 2.3: Flow regime criteria relative to the injection of gas in gas–solid fluidized beds.

Author	Criteria	Conditions
Grace and Lim (1987)	Condition for jetting: $\frac{d_j}{d_p} \leq 25.4$ required but not sufficient for jetting (otherwise bubbling)	Data from literature (18 sources) Configuration: 2D-a-b, 2.5D-a-g, 3D-a-b-g Geldart: A, B and D d_j = 0.5–210 mm u_j = 1–226 m/s d_p = 70–6700 μm P_g = ambiant, 3.4–51 atm
Guo et al. (2001b)	Conditions for jetting: $0.0449\left[\frac{\rho_j}{(\rho_p-\rho_j)}\cdot\frac{u_j^2}{gd_p}\cdot\frac{d_j}{H_0}\right]^{0.915}+0.929<\frac{U_g}{U_{mf}}<2.18$ $0.172\exp\left\{2.067\left[\frac{\rho_j}{(\rho_p-\rho_j)}\cdot\frac{u_j^2}{gd_p}\cdot\frac{d_j}{H_0}\right]^{0.095}\right\}\leq\frac{U_g}{U_{mf}}<2.8$ Conditions for transition: $0.0449\left[\frac{\rho_j}{(\rho_p-\rho_j)}\cdot\frac{u_j^2}{gd_p}\cdot\frac{d_j}{H_0}\right]^{0.915}+0.929<\frac{U_g}{U_{mf}}$ $\frac{U_g}{U_{mf}}<0.172\exp\left\{2.067\left[\frac{\rho_j}{(\rho_p-\rho_j)}\cdot\frac{u_j^2}{gd_p}\cdot\frac{d_j}{H_0}\right]^{0.095}\right\}$ Condition for fountain: $1<\frac{U_g}{U_{mf}}\leq 0.0449\left[\frac{\rho_j}{(\rho_p-\rho_j)}\cdot\frac{u_j^2}{gd_p}\cdot\frac{d_j}{H_0}\right]^{0.915}+0.929$	Configuration: 2D-h Measurement: Pitot tubes, pressure probes, fiber-optic probe, cine-camera Geldart: B and D d_j = 8–16 mm u_j = 5–70U_{mf} d_p = 217, 347, 745, 1135, 1640 μm ρ_p = 1475, 1335, 2550, 2675 kg/m^3 U_g = 1–3U_{mf} H_0 = 80–435 mm

Table 2.3: Flow regime criteria relative to the injection of gas in gas–solid fluidized beds (continued).

Author	Criteria	Conditions
Huang and Chyang (1991)	Conditions for quiescent fludization: $\frac{H_0}{d_j} > 21.9 \exp\left\{0.076\left[\frac{\rho_j}{(\rho_p-\rho_j)}\cdot\frac{u_j^2}{g d_p}\right]^{0.5}\right\}$ Condition for fountain: $\frac{H_0}{d_j} < 3.56\left[\frac{\rho_j}{(\rho_p-\rho_j)}\cdot\frac{u_j^2}{g d_p}\right]^{0.34}$ Conditions for jetting: Not quiescent and not fountain $\frac{H_0}{d_j} > 23.1$ Conditions for bubbling: Not quiescent and not fountain $\frac{H_0}{d_j} < 23.1$	Configuration: 2D-a Measurement: impact pressure Geldart: B d_j = 3.2, 6, 8 mm u_j = 1–120 m/s d_p = 215, 360, 545 μm ρ_p = 2500 kg/m^3 $U_g = U_{mf}$ H_0 = 50–300 mm Also includes data from: Hsuing and Grace (1978) 3D-a (Geldart B); Rowe et al. (1979) 3D-a (Geldart B and A); Sit and Grace (1986) 2.5D-a (Geldart B); Filla et al. (1986) 2D-a (Geldart B); Oki et al. (1980) 3D-b (Geldart B).
Luo et al. (1999)	Condition for jet coalescence: $\left(\frac{X_j}{d_j}\right)^{0.91}\left(\frac{u_j}{U_{mf}}\right)^{-0.16} \le 3.745$	Configuration: 2.5D-h Measurement: visual observation Geldart: D d_j = 25.7 mm (2.5D) u_j = 12–32 m/s d_p = 1640 μm ρ_p = 1335 kg/m^3 $U_g = U_{mf}$ X_j = 175–324 mm

Table 2.3: Flow regime criteria relative to the injection of gas in gas–solid fluidized beds (continued).

Author	Criteria	Conditions
Roach (1993)	Condition for jetting (otherwise bubbling) In terms of superficial velocity $\sqrt{N_j} \cdot \frac{\rho_p d_j^2}{\rho_j d_p d_t} \cdot \frac{U_g^2}{g d_p} \le 2.7 \times 10^5$ In terms of injection velocity $N_j^{2.5} \cdot \frac{\rho_p d_j^6}{\rho_j d_p d_t^5} \cdot \frac{u_j^2}{g d_p} \le 2.7 \times 10^5$	Data from Wen et al. (1982) Configuration: 3D-b Measurement: Fiber-optic probe Geldart: B d_j = 3.2, 6.4 mm u_j = 10–150 m/s d_p = 133, 250, 500 µm ρ_p = 2520, 2570 kg/m^3
Yates et al. (1986)	Conditions for jetting (otherwise bubbling) $\left(\frac{u_j^2}{g d_p}\right)^{0.37} \left(\frac{\rho_j u_j d_p}{\mu_j}\right)^{0.05} \left(\frac{f d_j}{u_j}\right)^{0.33} \left(\frac{\rho_f}{\rho_p}\right)^{0.68} \left(\frac{d_p}{d_j}\right)^{0.24} > 0.0270$ where f = 8 Hz, is the bubble frequency.	Configuration: 3D-a Measurement: X-ray, cine-camera Geldart: B d_j = 2–3.4 mm u_j = 30–180 m/s d_p = 260, 320 µm ρ_p = 1420, 1550 kg/m^3 U_g = 0–3 U_{mf} P_g = 1, 5, 10, 20 atm

Table 2.4: Correlations for estimating other jet properties in gas–solid fluidized beds.

Author	Correlation	Conditions
Ariyapadi et al. (2004)	Jet penetration length for injection of gas–liquid mixtures into gas–solid fluidized beds: $\frac{L_{max}}{d_j} = 5.52 C_G \left[\frac{\rho_l \left(1-\varepsilon_{g,j}\right)}{\left(\rho_p - \rho_{g,j}\right)} \cdot \frac{u_{l,j}^2 \left(1 + w_{g,j} S_{g,j}\right)}{g d_j} \right]^{0.27}$ where C_G is a nozzle geometry-dependent constant. The values of $\varepsilon_{g,j}$, $S_{g,j}$ and $\rho_{g,j}$ are determined from gas–liquid slip velocity considerations, following a procedure described by the authors.	Configuration: 3D-d Measurement: X-ray, temperature System: Gas/Liquid–Gas/Solid Geldart: A and B d_j = 0.8, 1.5, 1.6, 2.2 mm W_l = 0, 0.7–8.3, 14–71 g/s $x_{g,j}$ = 0, 0.85–3.3, 7.7–11.8%, infinite Injected liquid: Ethanol Injected gas: Helium, air d_p = 70, 150 μm ρ_p = 1400, 1500 kg/m^3 U_g = 0.04, 0.05, 0.1 m/s
Guo et al. (2010)	Jet penetration length with supersonic assistance: $\frac{L_{max}}{d_j} = 0.5444 \left[\frac{\rho_j}{\left(\rho_p - \rho_j\right)} \cdot \frac{u_j^2}{g d_j} \right]^{0.261} \left(\frac{\rho_j u_j d_j}{\mu_j} \right)^{0.454} \left(\frac{U_g}{U_{mf}} \right)^{1.636} \times \left(\frac{f}{f_c} \right)^{-0.061} \exp\left[0.169 \left(\frac{SPL}{SPL_c} - 1 \right) \right]$	Configuration: 3D-d Measurement: Fiber-optic probe Geldart: A and B d_j = 1.5–8 mm u_j = 15–142 m/s d_p = 85, 115 μm ρ_p = 1810, 2650 kg/m^3 $U_g = 1\text{–}1.5 U_{mf}$ f = 50–400 Hz (f_c = 150 Hz) SPL = 90–120 dB (SPL_c = 100 dB)

Table 2.4: Correlations for estimating other jet properties in gas–solid fluidized beds (continued).

Author	Correlation	Conditions
Luo et al. (1997)	Radial solid holdup in jet: $\varepsilon_s = \varepsilon_{s,m} - \left(\varepsilon_{s,m} - \varepsilon_{s,a}\right)\xi^2$ Note: $\varepsilon_{s,a} \approx 0.9\varepsilon_{s,mf}$	Configuration: 3D-g, 2.5D-g Measurement: fiber-optic probe, cine-camera Geldart: B d_j = 19 mm u_j = 10–38 m/s d_p = 275, 465, 650 μm ρ_p = 1500 kg/m^3 $U_g = U_{mf}$
Merry (1975)	Jet half–angle: $\cot\varphi = 10.4\left(\frac{\rho_j d_j}{\rho_p d_p}\right)^{0.3}$	Configuration: 2D-a Measurement: Visual observation System: Liquid–Solid Geldart: D d_j = 19×12 mm^2 d_p = 1000, 2000 μm ρ_p = 11750 kg/m^3 $U_g = U_{mf}$

Table 2.4: Correlations for estimating other jet properties in gas–solid fluidized beds (continued).

Author	Correlation	Conditions
Rees et al. (2006)	Jet half–angle $\varphi = 2.86\left(\frac{u_j^2}{gd_j}\right)^{-0.059}\left(\frac{U_{mf}^2}{gd_j}\right)^{0.33}\left[N_j \cdot \left(\frac{d_j}{d_t}\right)^2\right]^{-0.41}\ (\text{deg})$	Configuration: 3D-b Measurement: MRI Geldart: B and D d_j = 1, 1.5 mm N_j =15, 19, 26, 39 u_j = 5–100 m/s d_p = 500, 1200 μm ρ_p = 900 kg/m^3 d_t = 50 mm
Vaccaro (1997)	Jet half–angle (derived from author's Fig. 2.5): $\varphi = 36\left[\frac{\rho_j}{(\rho_g - \rho_j)} \cdot \frac{u_j^2}{gd_p}\right]^{-0.24}\ (\text{deg})$ when $d_j/d_p > 7.5$.	Data from literature Geldart: A, B and D d_j = 0.5–17.5 mm d_p = 107–1900 μm P_g = 1, 10, 15, 20 atm T = 20, 650, 800°C Includes data from Cleaver et al. (1995); Donadono et al. (1980); Filla et al. (1981, 1983); Massimila (1985)

Table 2.4: Correlations for estimating other jet properties in gas–solid fluidized beds (continued).

Author	Correlation	Conditions
Wu and Whiting (1988)	Jet half–angle: $\cot\varphi = 8.79\left(\frac{\rho_j d_j}{\rho_p d_p}\right)^{0.236}$	Configuration: 2.5D-a-b Measurement: Pitot tube Geldart: B d_j = 31.7, 33, 50 mm u_j = 31–121 m/s d_p = 550 μm ρ_p = 2600 kg/m^3 U_g = 1–2.25U_{mf} T = 20–540°C Also includes data from unspecified sources.

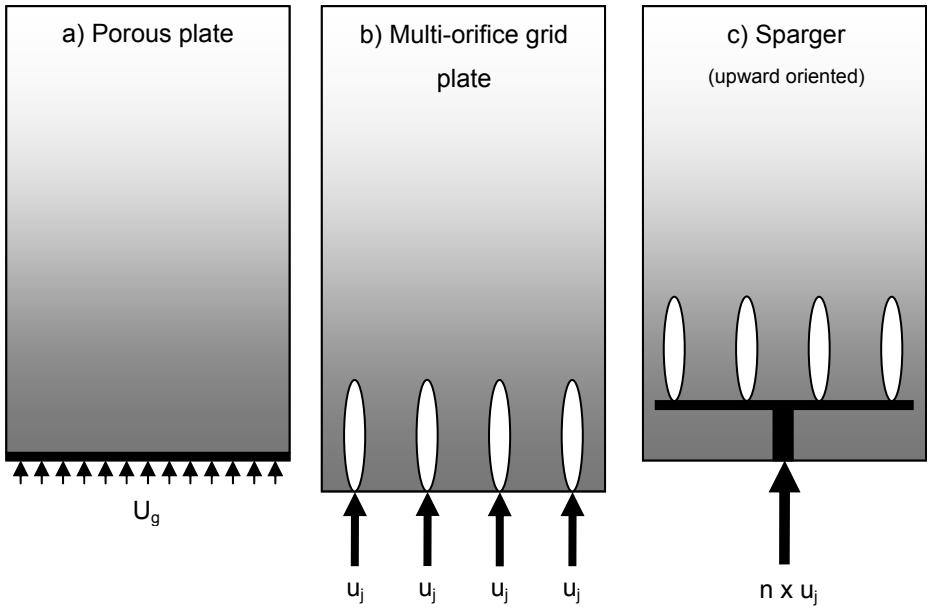

Figure 2-1: Types of fluidized bed distributors.

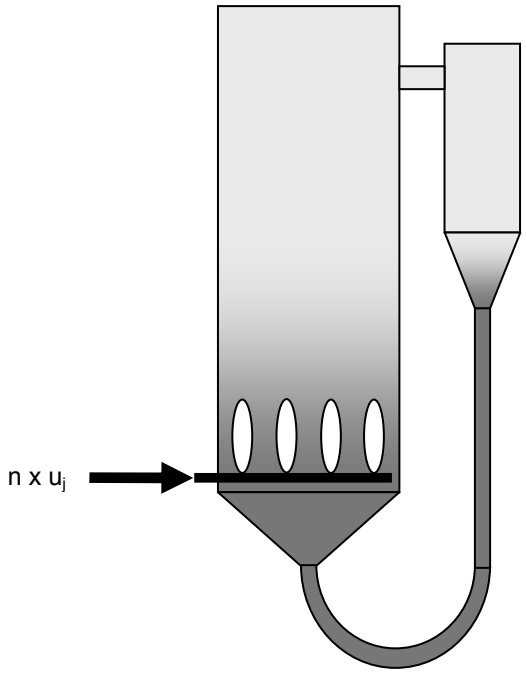

Figure 2-2: Schematic of a "J"-type circulating fluidized bed.

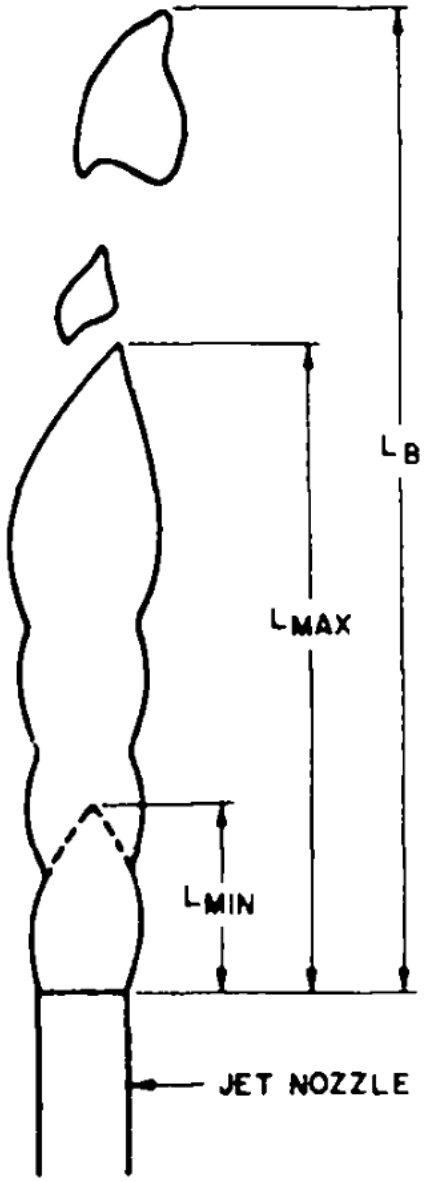

Figure 2-3: Jet structure according to Knowlton and Hirsan (1980) (image from Knowlton and Hirsan, 1980).

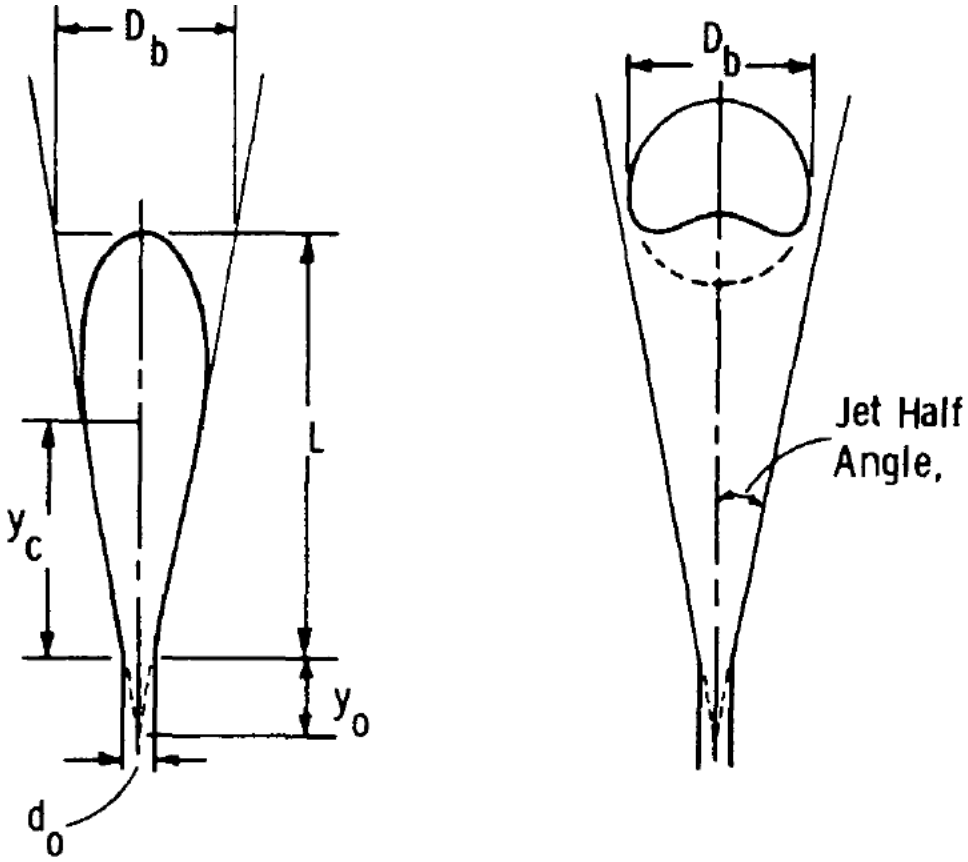

Figure 2-4: Jet structure and half-angle according to Merry (1975) (image from Merry, 1975).

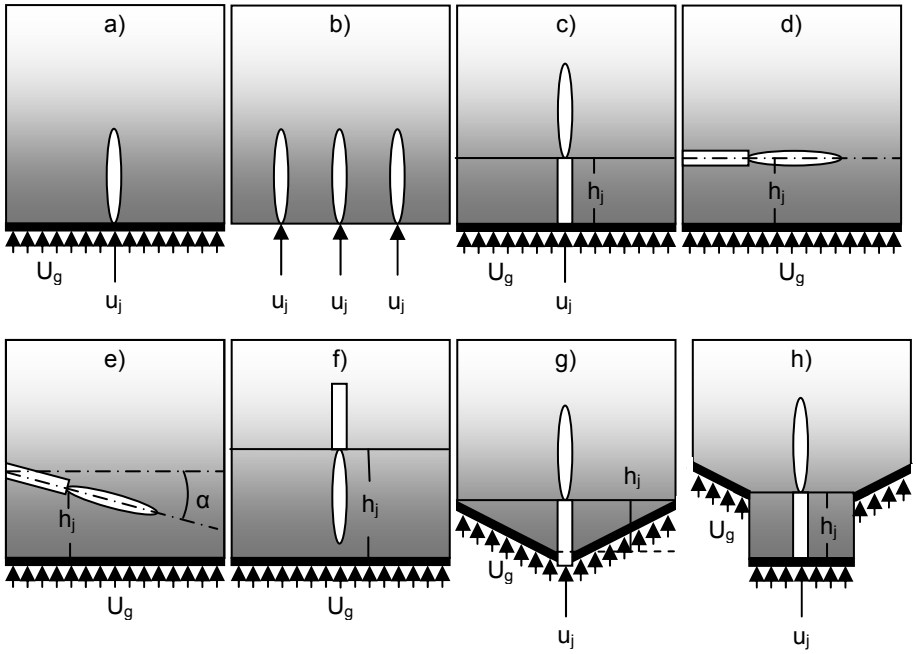

Figure 2-5: Most common geometries used in the study of jets in fluidized beds: a) studied nozzle mounted on porous plate distributor; b) multi-orifice grid plate; c-f) respectively upward, horizontal, inclined and downward sparger nozzles; g-h) jetting fluidized beds.

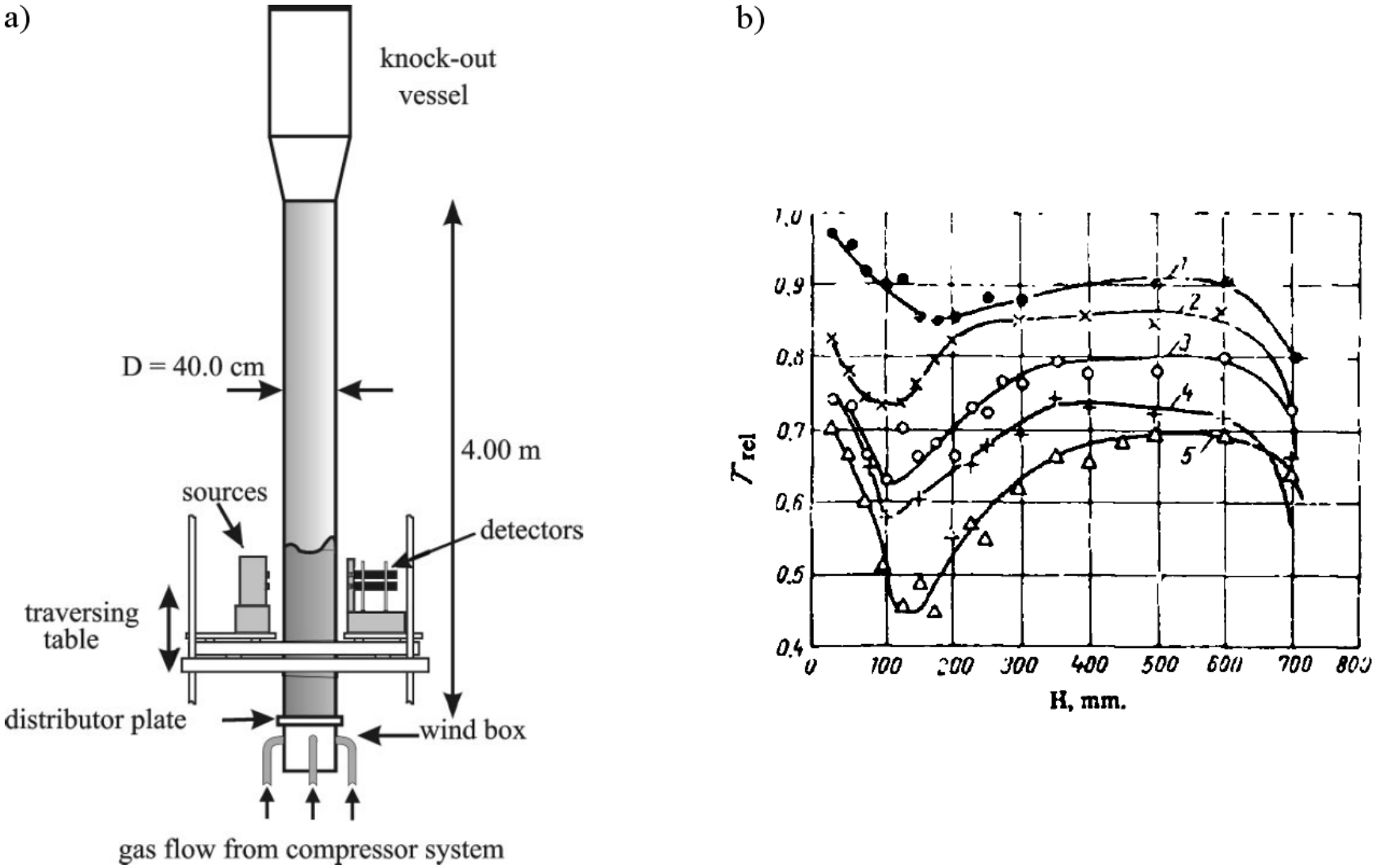

Figure 2-6: Gamma-ray densitometer approach used by Basov et al. (1969): a) Schematic diagram of fluidized bed; b) Typical response curves (images from a) Mudde et al. (1999); b) Basov et al. (1969)).

a)

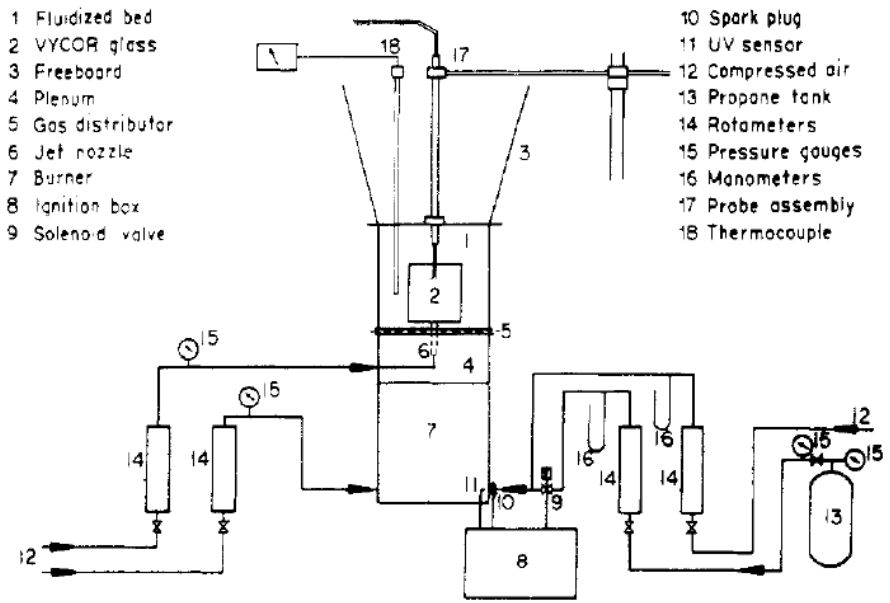

b)

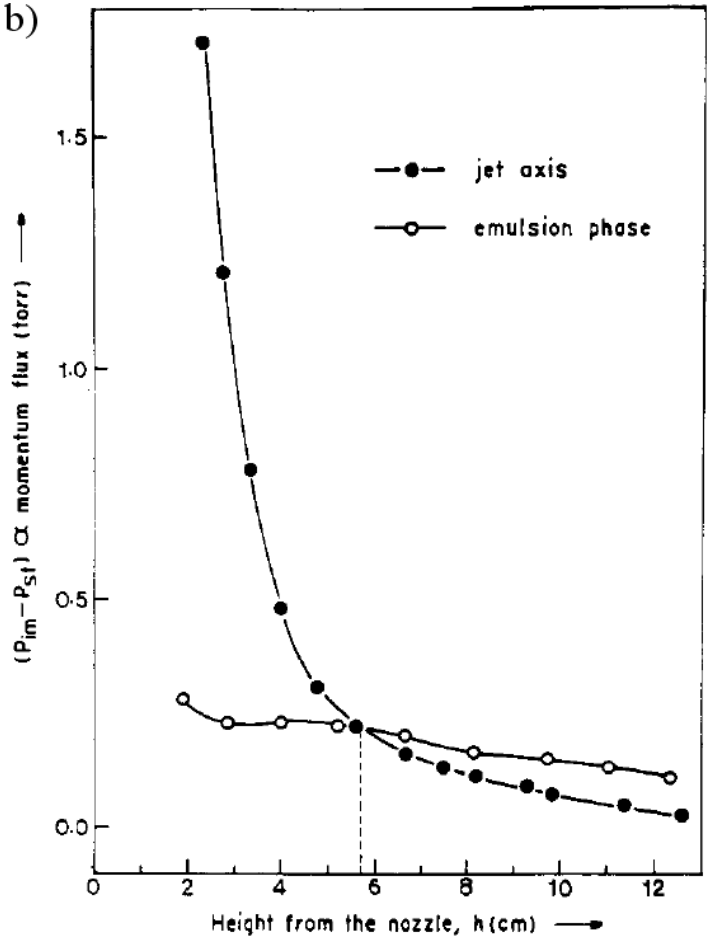

Figure 2-7: Pitot tube approach used by Raghunathan et al. (1988): a) Schematic diagram of fluidized bed; b) Typical response curve (images from Raghunathan et al. (1988)).

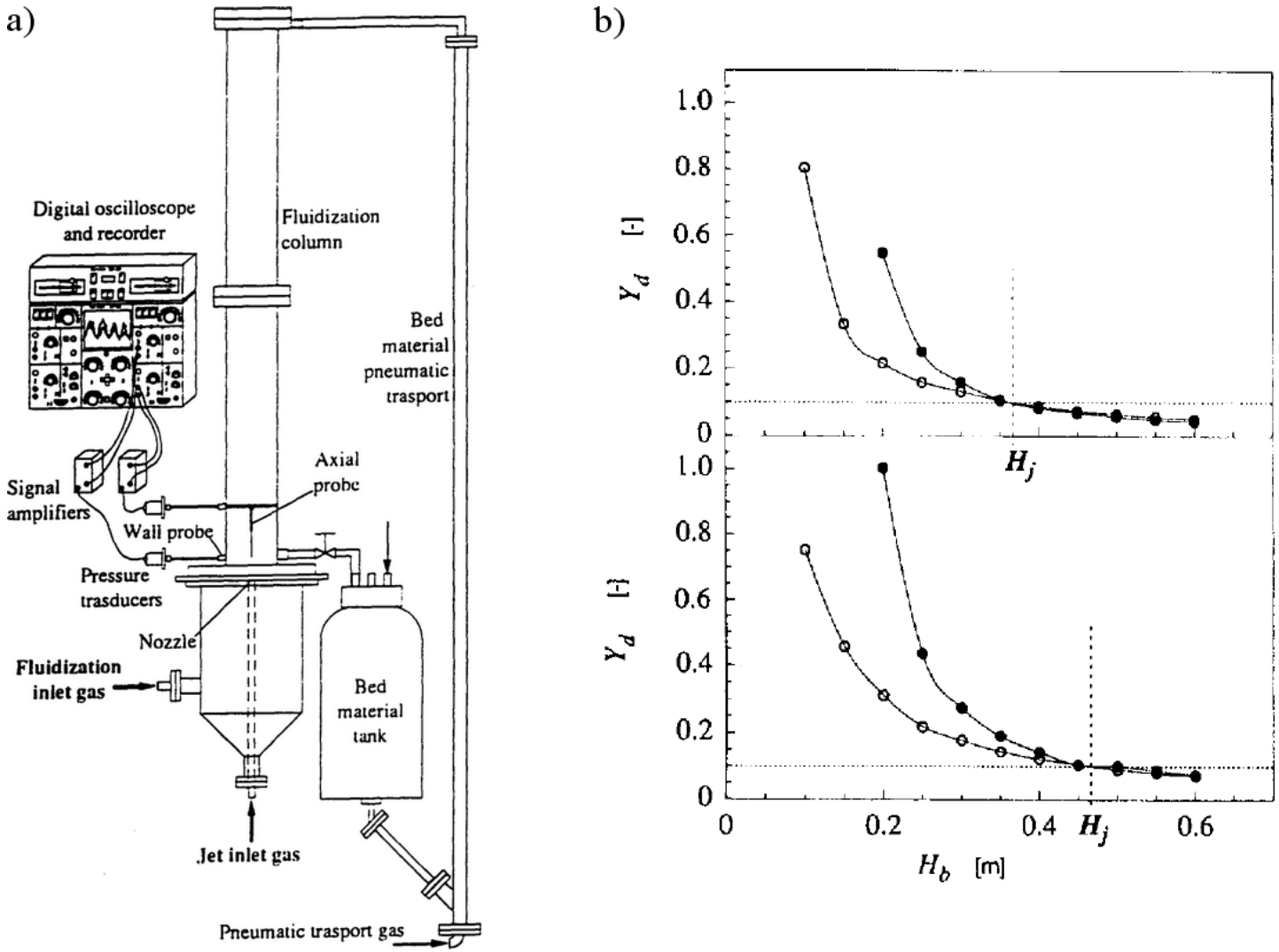

Figure 2-8: Differential pressure approach introduced by Vaccaro et al. (1997a): a) Schematic diagram of fluidized bed; b) Typical response curves (images from Vaccaro et al. (1997a)).

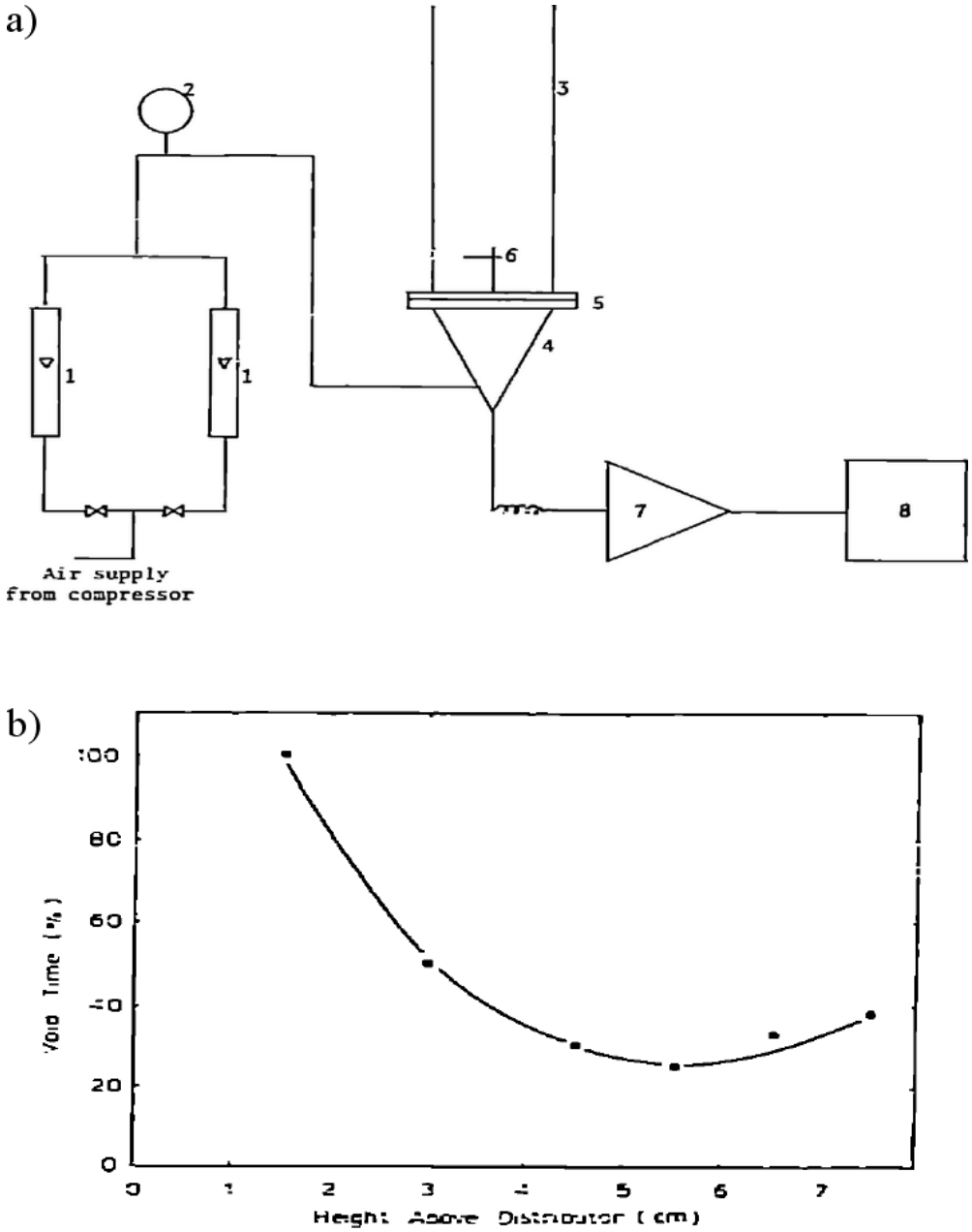

Figure 2-9: Binary fiber-optic approach introduced by Wen et al. (1982): a) Schematic diagram of fluidized bed; b) Typical response curve, L_{max} taken at minimum void time (5.5 cm) (images from Wen et al. (1982)).

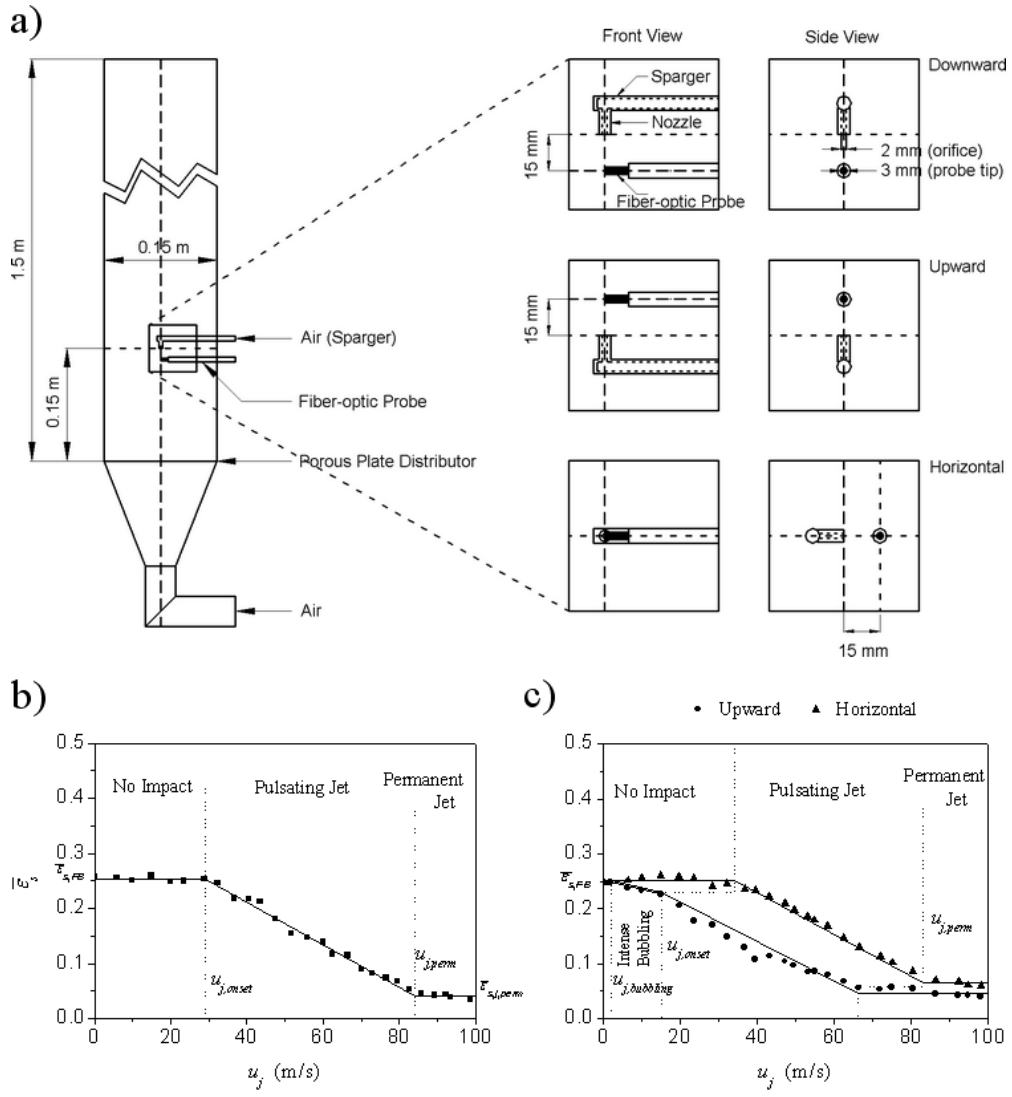

Figure 2-10: Digital fiber-optic approach proposed by Sauriol et al. (2011a): a) Schematic diagram of fluidized bed; Typical response curves: b) downward nozzle injection; c) upward and horizontal nozzles (images from Sauriol et al. (2011a)).

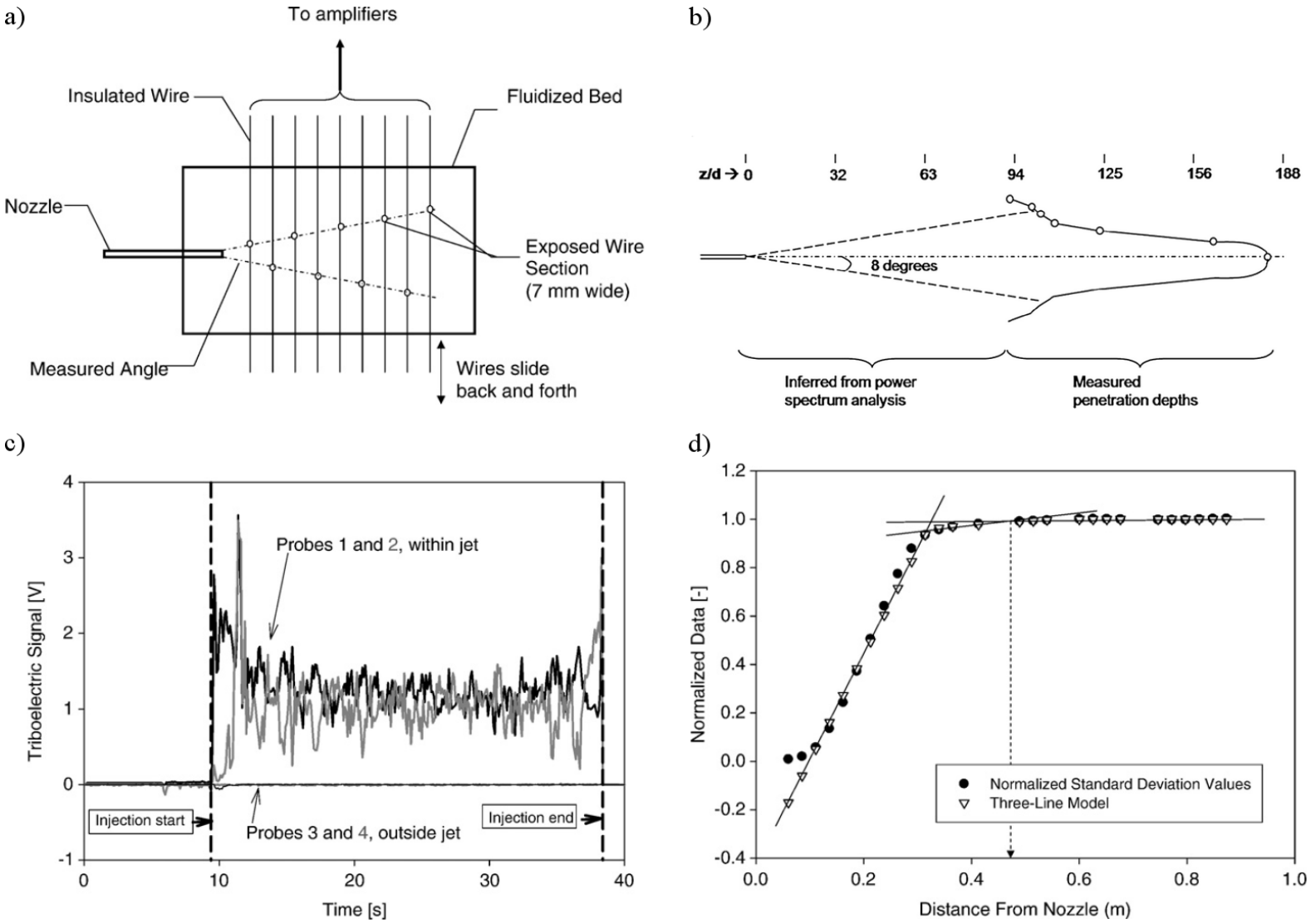

Figure 2-11: Triboelectric probe approach proposed by Berruti et al. (2009): a) Schematic diagram of probe in fluidized bed; b) typical jet boundary; c) Boundary in the expansion region; d) boundary in the far region (images from Berruti et al. (2009)).

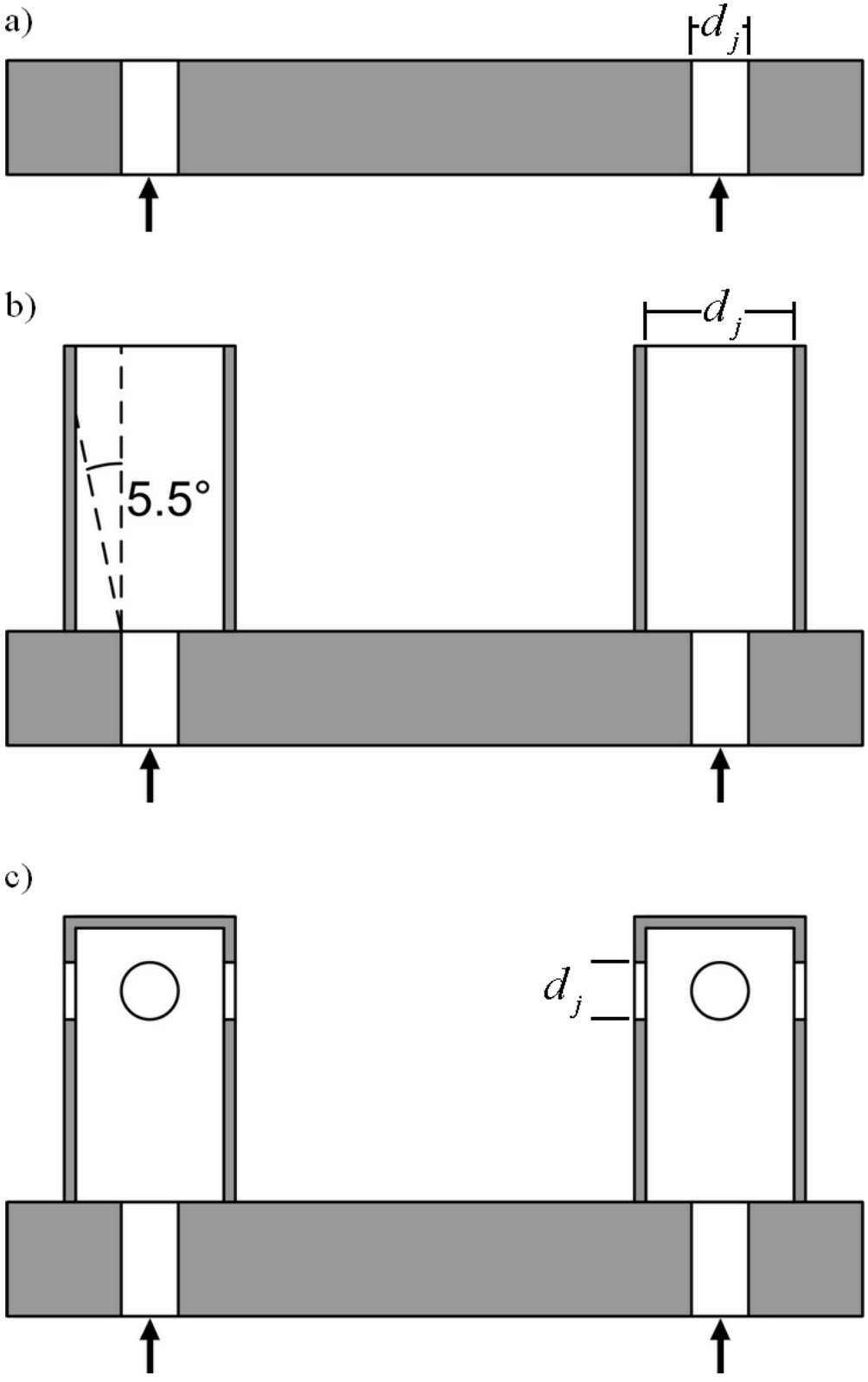

Figure 2-12: Common injector configurations and effective injector diameter (d_j): a) Orifice; b) Nozzle/Shroud; c) Tuyere.

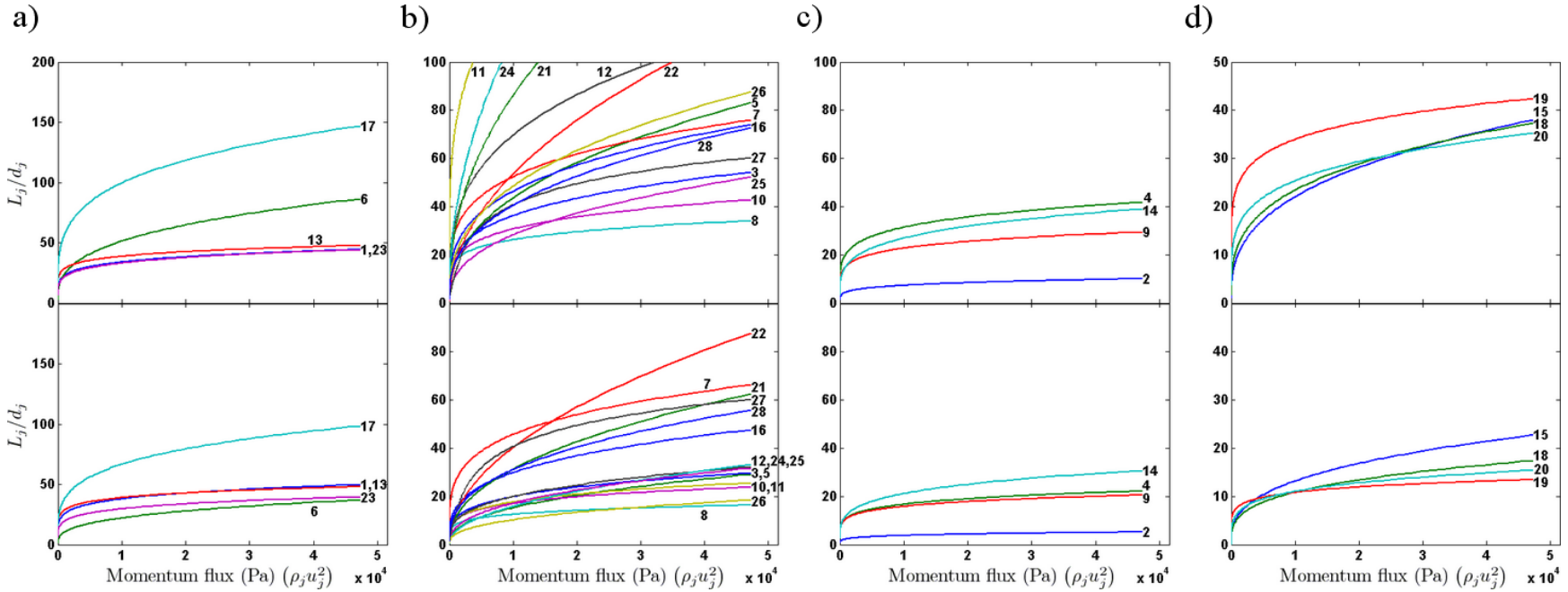

Figure 2-13: Influence of injection velocity (ranging from 1 to 200 m/s) on predictions of upward jet length correlations (top: FCC; bottom: sand): a) L_b (1: Basov et al. (1966); 6: Hirsan et al. (1980); 13: Musmarra (2000); 17: Sauriol et al. (2011b); 23: Yang and Keairns (1979)); b) L_{max} (isolated nozzles) (3: Blake et al. (1990); 5: Hirsan et al. (1980); 7: Guo et al. (2001); 8: Ku (1982); 10: Merry (1975); 11: Müller et al. (2009) form 1; 12: Müller et al. (2009) form 2; 16: Sauriol et al. (2011b); 21: Wen et al. (1982); 22: Yang and Keairns (1978); 24: Yang (1981); 25: Yates et al. (1986); 26: Yates and Cheesman (1987); 27: Zenz (1968); 28: Zhong and Zhang (2005)); c) L_{max} (grid nozzles) (2: Blake et al. (1984); 4: Blake et al. (1990); 9: Luo et al. (1999); 14: Rees et al. (2006)); d) L_{min} (15: Sauriol et al. (2011b); 18: Shakhova et al. (1968) (with jet half-angle estimated using correlation by Wu and Whiting, 1988); 19: Wen et al. (1977); 20: Wen et al. (1982)).

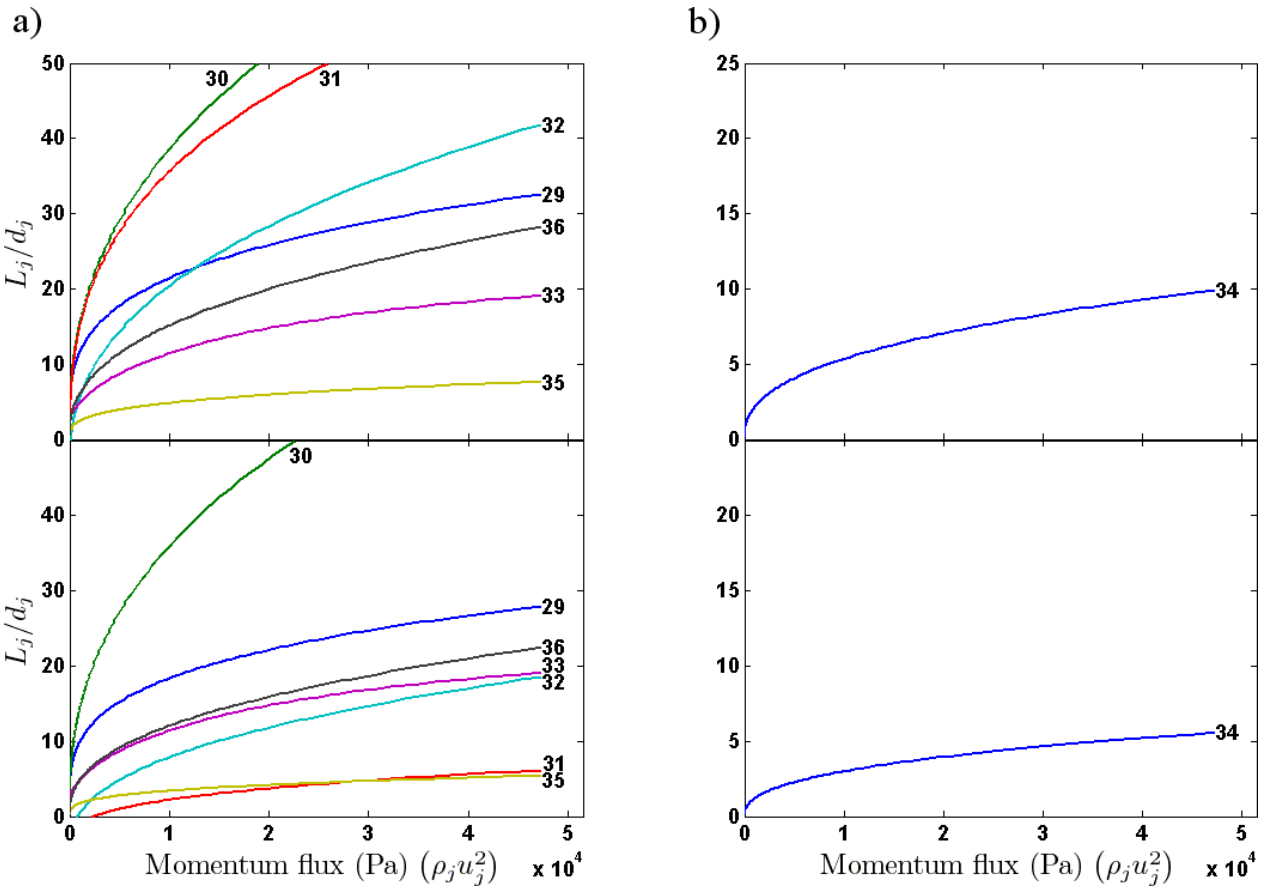

Figure 2-14: Influence of injection velocity (ranging from 1 to 200 m/s) on predictions of horizontal and downward jet length correlations (top: FCC; bottom: sand): a) L_{max} (29: Benjelloun et al. (1991); 30: Guo et al. (2010); 31: Hong et al. (1997) ; 32: Merry (1971) ; 33: Zenz (1968) ; 35: Sauriol et al. (2011b); 36: Yates et al. (1990)); b) L_{min} (34: Sauriol et al. (2011b)).

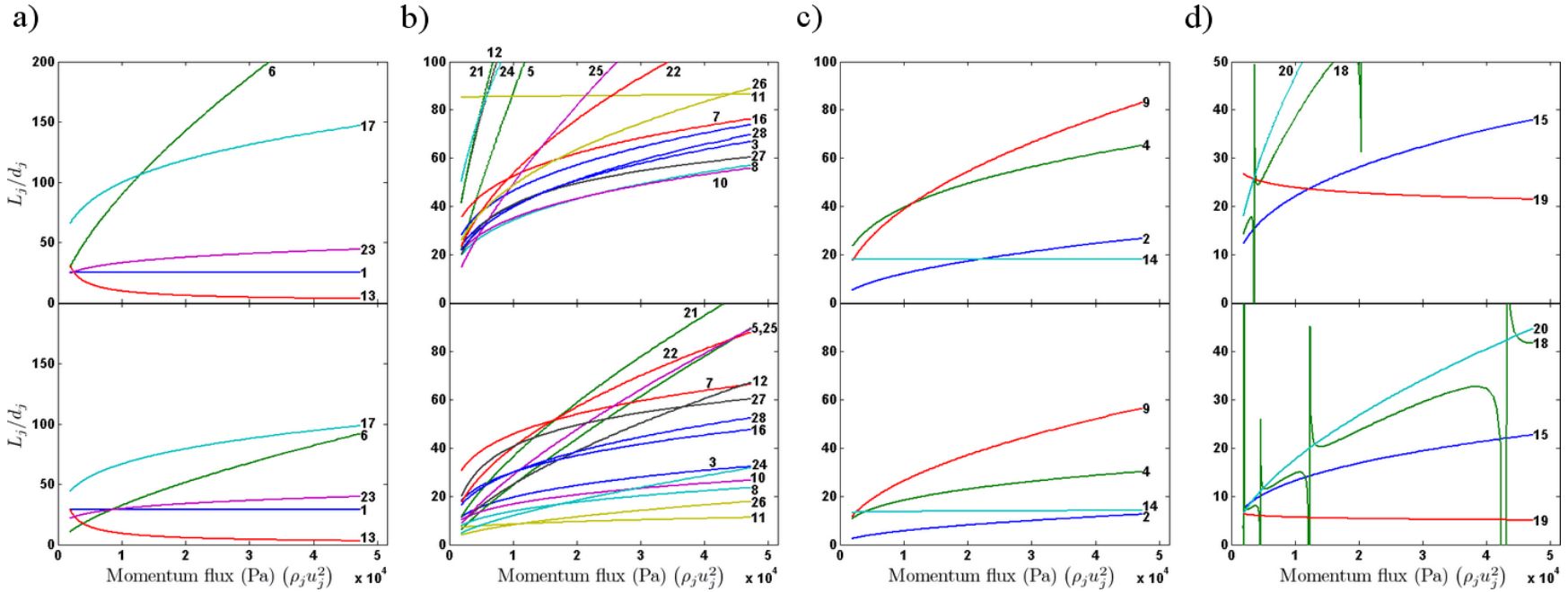

Figure 2-15: Influence of operating pressure (ranging from 1 to 25 atm) on predictions of upward jet length correlations (top: FCC; bottom: sand): a) L_b ; b) L_{max} (isolated nozzles); c) L_{max} (grid nozzles); d) L_{min} (refer to Fig. 2.13 for list of corresponding corrleations).

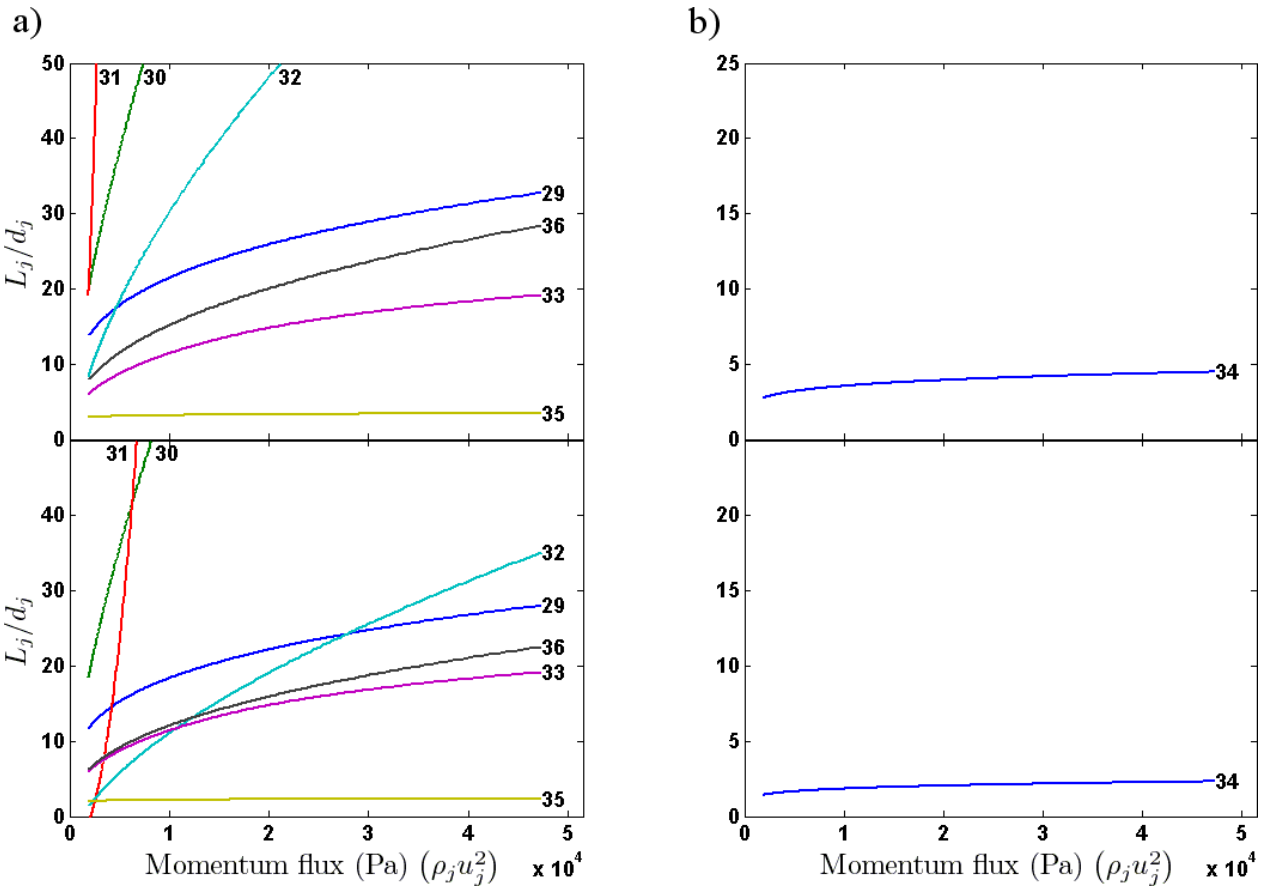

Figure 2-16: Influence of operating pressure (ranging from 1 to 25 atm) on predictions of horizontal and downward jet length correlations (top: FCC; bottom: sand): a) L_{max} ; b) L_{min} (refer to Fig. 2.14 for list of corresponding correlations).

CHAPITRE 3 ARTICLE 2: MODEL-BASED ANALYSIS OF RADIOTRACERS IN RESIDENCE TIME DISTRIBUTION EXPERIMENTS

Pierre Sauriol, Sylvain Lefebvre, Jamal Chaouki

Department of Chemical Engineering, École Polytechnique de Montréal,

P.O. Box 6079, Station Centre-ville, Montréal, Québec, Canada, H3C 3A7

Arturo Macchi

Department of Chemical Engineering, Ottawa University,

161 Louis Pasteur, Ottawa, Ontario, Canada, K1N 6N5

3.1 Abstract

A simple mathematical model is formulated to predict the efficiency distributions of detectors employed in residence time distribution experiments using radiotracers. The conditions most suitable for the use of radiotracers are then determined. The effects of column scale and media density are assessed and show that radiotracers can be used even in large industrial-scale units over a limited range of media densities and radial tracer concentration profiles. For existing units where density and scale are given parameters, options regarding the detector setup are suggested to improve their reliability. Typical experiments, generated by way of simulation, were used to evaluate the influence of several detector parameters. The simulations yielded three major recommendations: 1) a preliminary calibration of the detector counting efficiency should be performed in order to avoid overestimated dispersion coefficients when working with raw detector responses; 2) a standard deviation ratio is introduced to limit errors resulting from the axial detector efficiency distribution; 3) a radial maldistribution index is introduced to minimize the impact of the radial detector efficiency distribution and radial tracer concentration profile.

Keywords: Fluid mechanics and transport phenomena; Multiphase reactors; Hydrodynamics; Residence time distribution; Non-intrusive measurement; Radiotracer.

3.2 Introduction

Residence time distribution (RTD) measurements are an efficient way to evaluate the mixing quality of a reactor or a process. In recent years, an increasing number of such RDT measurements have been reported on laboratory- to industrial-scale systems through the use of non-intrusive radiotracers (Degaleesan et al., 1997; Din et al., 2008, 2010; Hyndman and Guy, 1995; Kasban et al., 2010; Lin et al., 1999; Mumuni et al. 2011; Nigam et al., 2001; Pablo Ramírez and Eugenia Cortés, 2004; Pant and Yelgoankar, 2002; Pant et al., 2009a,b; Patience et al., 1993; Santos and Dantas, 2004; Stegowski and Fruman, 2004; Yelgaonkar et al., 2009; Yianatos et al., 2010). Since such techniques do not require significant modifications to the tested vessels, besides a tracer injection point, their use in the troubleshooting of industrial-scaled units is expected to continue to increase as more laboratories are getting equipped to perform such measurements. Furthermore, according to Pant and Yelgoankar (2002), radiotracer techniques are often the only viable way to provide troubleshooting at the industrial-scale level regarding issues such as leakage, blockage, bypassing, backmixing, and maldistribution. As a result, it becomes ever more important to verify the conditions most suitable for their application to reduce the risk of misleading conclusions.

Thus far, most researchers have treated the detectors used in radiotracer studies as perfect integrators of the target stream. They neglected accounting for the detector view factor (detection efficiency distribution) which a preliminary analysis has shown to be strongly dependent upon system properties, system dimensions and detector configuration (Patience, 1990; Radmanesh and Sauriol, 2001). In most of the published efforts, the detectors were located on inlet and outlet lines (Kasban et al., 2010; Mumuni et al. 2011; Pablo Ramírez and Eugenia Cortés, 2004; Pant and Yelgoankar, 2002; Pant et al., 2009b; Stegowski and Fruman, 2004; Yelgaonkar et al., 2009; Yianatos et al., 2010) where boundary conditions are easier to define and where such factors may be negligible. However, in some cases the detectors were located near the studied vessels themselves (Din et al., 2008, 2010; Lin et al., 1999; Nigam et al., 2001; Pant et al., 2009a; Patience et al., 1993; Santos and Dantas, 2004), which may be required especially when considering the investigation of existing industrial applications.

Until the detector measurement capability and its impact on the perceived tracer measurement can be assessed, the results from such radiotracer RTD should be interpreted with caution as the

efficiency distributions from such detector setups may result in distorted tracer residence time distributions. The present work consists in the mathematical exploration of the gamma-ray emitting radiotracer technique as a means to study the hydrodynamics of laboratory to industrial-scale units. At first, an investigation of the parameters affecting the efficiency distribution of the gamma-ray detection device is performed. Afterwards, simulated signals generated from common hydrodynamic models under various operating conditions are analyzed to highlight the capabilities and limits of the radiotracer technique.

3.3 Detector Response Model

The detector response in radiotracer studies is a combination of three aspects: the space–time tracer concentration distribution, the detector efficiency and the counting efficiency. All three aspects are independent and it's only when generating the response curve that they are combined according to Eq. (3.1).

$$D(t) = E_c \, N_p\Big|_{t-\Delta t}^{t} = E_c \frac{\upsilon A_\gamma}{n} \int_{t-\Delta t}^{t} \int_{V} C E_d \, dV dt \tag{3.1}$$

3.3.1 Detector Efficiency

The detector efficiency is defined as the fraction of all gamma-rays emitted from a given position resulting in a detectable photopeak within the detector crystal. The efficiency will vary with respect to the point source location, media, gamma-ray initial energy, distance from the detector and the detector configuration, thus for every media, gamma-ray and detector configuration considered, a detector efficiency distribution needs to be evaluated.

Gamma-rays are emitted from a source in a random direction and can interact with matter in one of four ways: photoelectric absorption; Compton scattering; Rayleigh or coherent scattering; pair production. The probability of each type of interaction occurring strongly depends on the gamma-ray's energy and atomic number of the atoms making up the encountered media. Since most radiotracers commonly used emit gamma-rays with energies between 0.5 and 2 MeV, photoelectric absorption and Compton scattering are usually sufficient to describe the gamma-ray attenuation. Some examples of typical radiotracers employed in RTD experiments are given in

Table 3.1. Furthermore, this study will only address cases where the tracer releases mono-energetic gamma-rays, which is the case of most commonly used tracers.

3.3.1.1 Monte-Carlo Calculations

A Monte-Carlo calculation scheme loosely based on the one proposed by Beam et al. (1978) is used to determine the detector efficiency. Only photoelectric absorption and Compton scattering are considered. For both types of interactions the ensuing electron is assumed to die off near the interaction point rendering it undetectable when the interaction occurs within the media and potentially detectable when it occurs within the detector, providing it carries enough energy. The generation of secondary radiation (bremsstrahlung) is neglected. The probability, type and location of the interactions are determined at random from linear attenuation coefficients according to Eq. (3.2). The direction of the scattered photon following a Compton scattering event are determined using Klein–Nishina's differential scattering cross-section (Dunn and Gardner, 1972) and its residual energy calculated from Compton's scattering law.

$$P(l) = 1 - \exp\left(-\int_0^l \sum_j \sum_i \varepsilon_i \mu_{i,j} dl \right) \tag{3.2}$$

where i and j represent respectively the phases present in the media and the types of attenuations considered.

In a first step, the importance of Compton scattering within the media was evaluated for a typical tracer and media. The results from 100000 histories are presented in Fig. 3.1. For a point source located at the origin and emitting along the x axis, the gamma-ray location and energy were tracked until its residual energy dropped below the Compton edge, at which point the gamma-ray is considered to have too little energy to be detected. The interaction locations are reported on Fig. 3.1 and are identified according to the detectability of the gamma-ray. The results show that the gamma-ray interaction locations are distributed symmetrically with respect to the y and z axis. Furthermore, the detectable gamma-rays are distributed within a narrow cone having a half-angle of less than 9°. If the gamma-rays deviate from their initial trajectory by more than 9° due to Compton scattering events, they will have become undetectable. Furthermore, a cumulative distribution shows that nearly 80% of all detectable gamma-rays will not have deviated at all, their first and only interaction being photoelectric absorption. 95% of all detectable gamma-rays

will have deviated by less than 4°. Similar results were obtained for gamma-rays initial energy ranging from 0.5 MeV to 2 MeV and media densities ranging from 200 to 1500 kg/m^3. This suggests that to reduce the number of calculations when calculating the response of a detector with respect to a point source, the initial orientation of the emitted gamma-rays can be limited to a solid-angle that comprises the detector incremented by an angle corresponding to the maximum deviation angle and applying a correction factor based on the probability associated with the considered solid-angle.

In most applications, the gamma-ray detectors are shielded and collimated so that the measured signal reflects the concentration of tracer passing directly in front of it. For the present case, generic detector configurations and shielding as depicted in Fig. 3.2 will be considered. Typically, a 50 mm thick lead brick will absorb 99.9996% of all gamma-rays with energies of 0.5 MeV, 99.88% for 1 MeV and 98.6% for 2 MeV. Hence, throughout the calculations, it is assumed that the lead bricks block all gamma-rays penetrating them. The angles depicted in Fig. 3.2 will serve to define the solid-angle for a given point source.

Interactions within the vessel structure and internals will be neglected, however, when these are made of thick, high weight materials, their interactions with the gamma-rays may not be negligible and a similar treatment to that given to the media should be implemented. The interactions of the gamma-rays within the detector are assumed to be limited to the detector crystal, since the detector components other than the crystal (e.g. casing) are made up of thin lightweight materials. For each simulated gamma-ray, the absorption and Compton scattering are considered. The gamma-ray history is tracked until the gamma-ray exits the detector or decays within it. The amount of energy transferred by each gamma-ray to the detector is cumulated. If this amount exceeds the Compton edge, the gamma-ray is considered to have resulted in a detectable photopeak ($P_d = 1$), otherwise the gamma-ray is considered undetectable ($P_d = 0$). Per the results from Fig. 3.1, backscattering of the exiting gamma-rays is neglected since the residual energy is typically too low for detection to be achieved. Simultaneity of interactions of multiple concurrent gamma-ray events within the detector is neglected.

3.3.1.2 Detector Efficiency Distribution

The detector efficiency distribution is generated by dividing the column into cell volumes (V_i) for which the detector efficiency is computed. The cell volume is chosen so that there is between 1000 and 2000 cells over the cross-section. Since gamma-rays emitted from the point source may penetrate various parts of the detector crystal, the detector efficiency consists in an average based on several gamma-ray histories (ranging from 100 to 10000 gamma-rays that interact with the detector per cell). Within each volume element, the gamma-rays have their starting point and initial trajectory randomly selected, limiting the emission angle to within the solid-angle described earlier. The detector efficiency for the cell volume is then determined from Eq. (3.3).

$$E_d\left(V_i\right) = \frac{\sum P_\Omega P_d}{N} \tag{3.3}$$

3.3.2 Detector Counting Efficiency

The detectors are affected by a dead-time which influences the measured count rates. This dead-time may be a characteristic of the detector itself or of the electronics associated with it and causes a non-linearity between the actual number of detectable photopeaks and the reported count. Two types of detector counting models are often considered: a non-paralyzable detector (Eq. 3.4) and a paralyzable detector (Eq. 3.5). The non-paralyzable detector model is characterized by a plateau upon increasing the photopeak rate, while the paralyable detector reaches a maximum value and decreases if the photopeak rate increases beyond this maximum.

$$E_c = \frac{1}{1 + f_p \tau} \tag{3.4}$$

$$E_c = \exp\left(-f_p \tau\right) \tag{3.5}$$

3.3.3 Space–Time Tracer Concentration Distribution

Typical space–time tracer concentration distributions are predicted using hydrodynamic models developed for multiphase systems. Since local measurements obtained in most multiphase systems have shown non-uniform velocity profiles, a generalized dispersion model (GDM) which is capable of accounting for non-uniform velocity profiles will be considered. By combining it

with velocity distribution models, the GDM is deemed to possess sufficient flexibility to generate space–time tracer concentration distributions that are representative of multiphase systems that could be tested with radiotracers and that will provide an adequate means for the evaluation of the radiotracer RTD performances through the detector model presented earlier.

The GDM is expressed by considering two general Fickian terms to represent the axial and radial dispersion. The axial (D_a) and radial (D_r) dispersion coefficients are assumed to depend only on the system geometry and operating conditions.

$$\frac{\partial C}{\partial t} = D_a \frac{\partial^2 C}{\partial z^2} + D_r \frac{1}{r} \cdot \frac{\partial C}{\partial r}\left(r \cdot \frac{\partial C}{\partial r} \right) - \frac{u}{\varepsilon} \cdot \frac{\partial C}{\partial z} \tag{3.6}$$

The GDM equation is solved using the fractional step method (Yanenko, 1971) for a step input, which is easier to define numerically. The space–time concentration distribution for the pulse input is obtained by differentiation of the calculated step input space–time concentration distributions. The resolution is achieved with the following initial and boundary conditions:

$$\begin{aligned}
&\frac{u}{\varepsilon} C\Big|_{z=0^-} = \frac{u}{\varepsilon} C\Big|_{z=0^+} - D_a \frac{\partial C}{\partial z}\Big|_{z=0^+} && \text{for } z = 0 \\
&\frac{u}{\varepsilon} C\Big|_{z=H_t^-} - D_a \frac{\partial C}{\partial z}\Big|_{z=H_t^-} = \frac{u}{\varepsilon} C\Big|_{z=H_t^+} && \text{for } z = H_t \\
&\frac{\partial C}{\partial r} = 0 && \text{for } \xi = 0 \text{ and } \xi = 1 \\
&C = 0 && \text{for } t < 0 \\
&C\Big|_{z=0^-} = S && \text{for } t > 0
\end{aligned} \tag{3.7}$$

where S is the amplitude of the step input. These boundary conditions are valid for systems closed to dispersion or having a uniform concentration (CSTR) at the inlet and outlet.

Axial dispersion model — For the ADM, the GDM is simplified by eliminating the radial dispersion term and assuming uniform velocity (and tracer concentration) over the system cross-section.

System without recirculation — For most multiphase systems exhibiting non-recirculating flow patterns, the velocity is smaller near the column wall and reaches a maximum value along the centerline. This kind of velocity profile is reported for the gas phase in bubble columns (Yao et

al., 1991). For a system without recirculation, the following relationship is used to compute a parabolic velocity profile (Eq. 3.8). Typically, a m value of 2 describes a laminar flow.

$$u = U\left(\frac{m+2}{m}\right)\left(1-\xi^m\right) \tag{3.8}$$

System with recirculation — Multiphase systems which exhibit recirculation have been reported for the liquid phase in bubble columns (Dudukovic et al., 1991; Franz et al., 1984) and three-phase fluidized beds (Morooka et al., 1982); the solid phase (batch) in three-phase fluidized beds (Larachi et al., 1996) and circulating fluidized bed risers (Godfroy et al., 1999; Samuelsberg and Hjertager, 1996). To account for flow reversal near the column wall, two continuously stirred tank reactors (CSTR), one at each end, are included in the model. Each CSTR is given a height equal to the column diameter. For bubble columns, considering only the axial component of the liquid velocity and a parabolic gas holdup profile, the radial distribution of the liquid velocity profile was modeled by applying a momentum balance (Gharat and Joshi, 1992a,b) (Eq. 3.9) and using the turbulent viscosity relation of Reichardt (Luo and Svendsen, 1991) (Eq. 3.10). A k value of 0.188 was reported for low viscosity liquids in a bubble column (Menzel et al., 1990). The velocity profile is iteratively determined via τ_w in order to respect the mass balance. It should be noted that the parameter m in Eq. (3.9) is used to adjust the radial velocity profile.

$$\frac{du}{dr} = \frac{\tau_w \xi}{\left(\upsilon_t + \upsilon_m\right)\rho_l}\left[1 - \frac{\rho_l g \bar{\varepsilon}_g d_t}{2m\tau_w}\left(1-\xi^m\right)\right] \tag{3.9}$$

$$\upsilon_t = k\frac{d_t}{2}\sqrt{\frac{\tau_w}{\rho_l}}\left(1+2\xi^2\right)\left(1-\xi^2\right) \tag{3.10}$$

3.4 Simulation Results and Discussion

The presentation of the simulation results is divided in two parts. The first part focuses on determining and quantifying the parameters that influence the detector efficiency distribution. The second part consists in giving a quantitative appreciation of the radiotracer technique by comparing the detector responses to model generated tracer evolutions and an ideal response, which is considered as the instantaneous space averaged tracer concentration over the vessel cross-section facing the detector.

3.4.1 Parameters Affecting the Detector Efficiency Distribution

The calculation procedure and experimental setup have an influence on the detector efficiency distribution. This section is divided in two series of calculations. The first series aims at determining the optimal number of gamma-rays simulated in each cell required to generate reliable detector efficiency distributions. Because the calculation procedure uses a Monte-Carlo approach, the number of gamma-rays simulated for each position needs to be determined to minimize the scatter in the computed results. The second series of calculations illustrates the effects of various detector parameters (detector crystal size and detector/shield configuration), column parameters (diameter, media density) and radiotracer parameter (initial energy of the gamma-ray) on the detector efficiency distribution.

3.4.1.1 Determination of the Optimal Number of Gamma-rays Simulated in Each Cell

For three sets of detector, column and tracer parameters, the detector efficiency distributions were generated with 100 to 10000 simulated gamma-rays per cell. A conservative value of 2500 simulated gamma-rays per cell is used throughout the rest of the calculations. Combined with the number of cell ranging between 3400 up to 90000 depending on the configuration, this ensures that the calculation of the detector responses through Eq. (3.1) will have typically less than 1% variability from the random scattering included in the detector efficiency distributions.

3.4.1.2 Investigation of the Parameters Affecting the Detector Efficiency Distribution

A detector efficiency distribution is generated based on the equipment previously used in our facility, see Table 3.2 for details. Figure 3.3 shows the efficiency distributions for three axial levels located 5, 25 and 55 mm from the detector centerline. Figure 3.3a) illustrates that the detector preferentially perceives the gamma-rays emitted closer to it. These gamma-rays are less subject to attenuation inside the column and benefit from more favorable solid-angles. As for axial levels farther from the detector centerline, Fig. 3.3b) and c), the presence of shielding lead bricks results in a transition in the trend. For a specific axial level, gamma-rays emitted farther from the detector are subject to greater attenuation, but lose less in terms of the probability associated to the solid-angle, resulting in flatter detector efficiency distributions. The significance of this reversal in trend is generally rendered trivial due to the low detector

efficiency attained at those axial levels, sometimes a few orders of magnitude lower than the peak values along the detector centerline.

In order to better describe the detector efficiency distribution, one has to recall that the purpose of the detector is to generate integrated curves analogue to averaged tracer concentration curves over the cross-section facing the detector, which can be used to extract mixing parameters. In that perspective, it becomes important to look at the spatial non-uniformity of the detector efficiency distribution as it will artificially increase the axial distribution. Ideally, the detector should only perceive the concentrations distributed over the column cross-section along the detector centerline. Furthermore, the concentrations should be uniformly weighted when integrated by the detector in order to eliminate any radial bias in case the tracer concentration is not uniformly distributed over the column cross-section. Thus, two properties are defined to express the degree of axial and radial non-uniformity in the detector efficiency distribution. The axial spread (AS) of the detector efficiency is defined in Eq. (3.11) as the standard deviation of the cross-sectional average of the efficiency distribution and should be minimized in order to achieve a better agreement with the actual concentration data. The normalized radial range (NRR), as defined in Eq. (3.12), accounts for all axial levels and provides an estimate of the radial non-uniformity over the entire measurement volume. Ideally, the NRR value should be close to zero in order to minimize the radial bias introduced by the measurement technique.

$$AS = \sqrt{\frac{\int_0^{H_t} \left(z - H_d\right)^2 \bar{\bar{E}}_d dz}{\int_0^{H_t} \bar{\bar{E}}_d dz}} \tag{3.11}$$

$$NRR = \frac{\int_0^{H_t} \left(\bar{E}_d\big|_{\xi=1} - \bar{E}_d\big|_{\xi=0} \right) dz}{\int_0^{H_t} \bar{\bar{E}}_d dz} \tag{3.12}$$

In the following sub-sections, the column diameter, the media density, the radiotracer energy, the shielding bricks opening, the detector crystal diameter, the detector crystal length, the distance between the column and the shield, and the distance between the shield and the detector crystal are investigated to illustrate their effect on the detector efficiency distribution.

Combined influence of the column diameter and media density — Generally, the column diameter and media density will not be assigned by the experimenter. Thus, both aspects are analyzed together in order to identify tendencies and limitations of the experimental technique. Figure 3.4 presents results for units varying from laboratory- to large industrial-scale with media densities varying between 1 kg/m³ (e.g. pneumatic transport) and 1500 kg/m³ (e.g. fixed bed). All other parameters are taken as specified in Table 3.2. All calculations are based on a generic media for which the total mass attenuation coefficients against gamma-ray energy are reported in Table 3.3. The table also gives density correction factors for alternate media.

The influence of the media density on the AS and NRR increases as the system scale increases. When the media density is low, greater column diameters give larger AS and negative NRR values. At media densities greater than 800 kg/m³, all column sizes give similar AS values due to high attenuation in the column media. However, at these media densities, the NRR values are positive and greater for the larger column diameters.

Influence of selected independent parameters — In order to adjust the AS and/or NRR resulting from the column size and media density, one may vary the independent experimental parameters described henceforth. The influence of these parameters on the AS and NRR are summarized in Table 3.4 for four system scales (laboratory: $d_t = 0.1$ m, pilot: $d_t = 0.3$ m, small industrial: $d_t = 1.0$ m and large industrial: $d_t = 4.0$ m) and three media densities (1, 800 and 1500 kg/m^3) with all other parameters taken as specified in Table 3.2. The influence of all system parameters is reported by estimates of their partial derivatives which will also be useful to estimate the AS and NRR for alternate system parameters and detector setups. Furthermore, Table 3.4 illustrates the influence of the media and gamma-ray energy on the attenuation coefficients used in the calculations. When working with a media that differs from the generic media used in the calculations, it is necessary to correct for the density in order to match the linear attenuation coefficients.

As shown in Table 3.1, many potential gamma-ray emitting tracers may be considered for experimental work. The tracer is primarily characterized by the energy of the gamma-rays it emits, which mostly impacts the attenuation coefficients of the media, column structure and detector crystal. The attenuation coefficients usually decrease when the energy level is increased. For systems with average (800 kg/m^3) to high (1500 kg/m^3) density media, this results in a

significant increase in the detector efficiency particularly in the locations more subject to attenuation, leading to a slight increase in the AS but a considerable decrease in the NRR. The opposite trend is observed for systems with low density media.

The interactions within the detector crystal play an important role in the gamma-ray detection. In general, as long as the detector crystal diameter is greater than the shield opening, detector crystals of smaller diameter yield smaller AS and NRR. As for the detector crystal length, longer crystals will generally reduce AS and NRR except in large scale systems with a low density media where the AS increases.

Shielding the detector with lead bricks is a good way to limit the AS by reducing the solid-angle. For laboratory- and pilot-scale systems, when the shield opening is increased, the AS increases while the NRR decreases. For industrial-scale systems, the AS increases with the shield opening while the NRR is unaffected. Furthermore, the influence of the shield opening on the AS is more important on systems with low density media and on larger scale systems.

As the distance between the column and the shield increases, the AS increases since the measurement is conducted over a greater column height (greater solid-angle). The AS of small scale systems are more affected by changes in the distance between the column and the shield regardless of the media density. The media density only becomes a factor in large scale systems. Generally, the NRR increases when the distance between the column and the shield is increased. On the other hand, a greater distance between the shield and the detector crystal reduces the AS but increases the NRR. The impact of the distance between the shield and the detector crystal is greater for large scale systems with low density media.

From Table 3.4, it is possible to estimate the AS and NRR for alternate system parameters using the conditions that most resemble the new setup as a starting point. The partial derivatives are then used to obtain the AS and NRR for the desired conditions. Two examples are summarized in Table 3.5. Both examples consider the system described in Table 3.2 with the exception of the media and column diameter.

3.4.2 Comparison between the Detector Response and the Average Concentration Evolution

Now that it has been demonstrated that several parameters affect the detector efficiency distribution, the relevance of the AS and NRR may be assessed by considering various time-space tracer concentration distributions. Residence time distributions are defined for systems where the concentration profile is averaged based on the flow rate. This is readily achieved when the velocity is constant over the cross-section at the location where the concentration measurement is performed (e.g. ADM) and as long as there are no other bias from the measurement device. Systems without a uniform velocity yield an average concentration evolution (ACE) in the best condition (i.e. unbiased measurements). The ACE is not weighted by the flow rate and is defined as a time distribution of the tracer concentration cross-sectional average at the detector location. The model parameters may still be obtained from the ACE , and the RTD determined from the model afterwards. Table 3.6 details the parameters used for each hydrodynamic model.

Space–time tracer concentration distributions and detector efficiency distributions are generated to obtain the detector response, which is then compared with the ACE . Three main aspects of the gamma-ray detection system are investigated: the detector counting efficiency, the AS and the NRR associated to a specific detector setup.

3.4.2.1 Influence of the Detector Counting Efficiency

Most studies reported in the literature using gamma-ray tracers do not specify whether the detectors' counting efficiency is accounted for. In this work, several detector responses are generated by varying the tracer activity by up to a factor of 100. The span of activities was chosen to cover a wide range of applications from low velocity liquid phase tracers in bubble columns (0.1 m/s, sampling period of 1s) to high velocity solids in circulating fluidized bed risers (10 m/s, sampling period of 0.01s). For each detector counting model, a dead-time of 6 μs (typical to our detectors) was used throughout the calculations. Once normalized, detector responses obtained with a greater dead-time would have effects similar to working at a greater tracer activity (Eqs. 3.4-3.5).

Raw detector responses for several tracer activities were generated for a space–time tracer concentration distribution based on the ADM, a given detector efficiency distribution and a non-paralyzable detector counting model. The raw detector responses are normalized and fitted in order to extract the ADM parameters. The fitted parameters are then compared to the input parameters used to generate the space–time tracer concentration distributions. Figure 3.5 presents the ratio of the fitted axial dispersion coefficient to the model input for several tracer activities and two Peclet numbers (Pe). As the tracer activity increases, the error on the predicted axial dispersion coefficient increases. This increase is more important for lower axial mixing. For the same tracer activity, lower axial mixing results in the detector crystal being exposed to greater tracer concentrations (i.e. more gamma-rays) which are subject to lower counting efficiencies. The reduced counting efficiency gives broader and flatter normalized raw detector responses explaining why lower axial mixing leads to a greater error. Considerable improvements in the parameter determination are achieved when calibrating the detector and correcting the detector responses. The detector is calibrated by determining the detector counting model and dead-time. For paralyzable detectors it is important that the detector configuration and tracer activity are selected not to exceed the maximum count-rate ($f_p = 1/\tau$) otherwise it becomes nearly impossible to correct the detector response. The corrected detector response (CDR) is obtained by dividing the raw detector response with the detector counting efficiency.

In Fig. 3.6, the normalized ACE ($NACE$), the normalized CDR ($NCDR$) and the normalized raw paralyzable and non-paralyzable detector responses are depicted for hydrodynamic models with and without recirculation. The raw detector responses were generated for high tracer activities. The $NCDR$ and $NACE$ are in very good agreement compared to the normalized raw detector responses which are broader and flatter. There is an important influence of the detector counting model on the normalized raw detector responses. At such high tracer activities, responses from paralyzable detectors may greatly differ from the $NACE$. For example, the normalized raw detector response for a hydrodynamic model without recirculation may present two peaks suggesting recirculation.

3.4.2.2 Influence of the Degree of Non-uniformity in the Detector Efficiency Distribution

This section evaluates the effects of detector efficiency distributions on the corrected detector response curves. An attempt is made to elucidate the discrepancies between the *NACE* and the *NCDR*.

Detector axial spread — To eliminate the influence of the *NRR* on the response curve, this section is limited to the ADM for which the tracer concentrations are uniform over the column cross-section. Levenspiel and Fitzgerald (1983) demonstrated that the ADM yields a linear relationship between the change in *NACE* variance and the axial distance separating two detectors and ($\Delta\sigma^2_{NACE} \propto \Delta H_d$) for low axial dispersion systems (Pe>100). Simulations were performed to test this relationships for many sets of hydrodynamic models and detector setups covering a wide range of *AS*. These relationship holds true for the radiotracer technique, as long as the detector setup is identical at every axial level (i.e. same detector efficiency distributions), allowing for the determination of the appropriate hydrodynamic model. Two approaches are considered when attempting to determine the hydrodynamic model parameters. One approach consists in fitting a single *NCDR* considering a tracer input. The second consists in determining the hydrodynamics from the convolution of two *NCDR*s obtained at different axial levels. The results from both approaches are compared with the actual model parameters. Errors are observed when fitting the model parameters using a single *NCDR*, as well as by convolution of two *NCDR*s obtained from detectors having different efficiency distributions (i.e. different *AS* and *NRR*). This is especially true when the *AS* associated to the detector setup is important and when the standard deviation of the tracer concentration at the measurement location is low. However, when performing convolution from two identical detector setups, the hydrodynamic parameters are determined with very little error. Even though convolution minimizes the impact of the *AS*, this approach is subject to certain limitations. It requires at least two detectors with identical efficiency distributions and is limited to systems for which the model predicted RTD over any axial span may be evaluated directly. Given these limitations, convolution is not likely to be possible at all time. In some instances, the experimenter will have no alternative than to work with a single *NCDR*.

In that perspective, a relationship is required to quantify the impact of the *AS* on the agreement between the *NACE* and the *NCDR*. Collating results from over 50 space–time tracer

concentration distributions with flat velocity profiles and over 200 detector efficiency distributions, the $NACE$ error (ERR_{NACE}) was calculated according to Eq. (3.13) and plotted in Fig. 3.7 against the standard deviation ratio (SDR) defined in Eq. (3.14). Overall, there is a good agreement between the ERR_{NACE} and the SDR. Essentially, to maintain ERR_{NACE} below 1%, the AS should be chosen such that the SDR is less than 0.20; to achieve an error below 0.1% error, the SDR should be less than 0.06.

$$ERR_{NACE} = \frac{\int_0^{\infty} |NACE - NCDR| \, dt}{2} \tag{3.13}$$

$$SDR = \frac{AS}{\left(\frac{u}{\varepsilon}\right) \cdot \sigma_{NACE}} \tag{3.14}$$

Detector normalized radial range — In the presence of radial concentration profiles, limiting the AS such as proposed in the previous section is not sufficient to limit the differences between the $NACE$ and $NCDR$ to an acceptable level. These discrepancies are greater when the radial dispersion coefficient is small and the detector NRR is large.

As for the AS, an effort is made towards determining a relationship that could serve as a guideline for selecting a detector setup that minimizes the effects of the radial detector efficiency maldistribution. Similarly, several sets of detector efficiency and tracer concentration distributions are collated to determine the relation between the NRR and the ERR_{NACE}. To minimize the contribution of the AS in the ERR_{NACE}, only space–time tracer distributions and detector pairing yielding SDR values below 0.025 are considered. From Fig. 3.6, this should ensure that the AS accounts for less than 0.01% in the reported ERR_{NACE}. An additional condition is imposed where the NRR absolute value should be less than 2. This condition ensures fair detector coverage over the whole column cross-section. Greater NRR values may lead to irremediable biases. As seen in Fig. 3.4, this suggests that for a limited range of density media, columns of large diameter may be investigated by means of radiotracers without showing strong biases due to the radial detector efficiency distribution. A radial maldistribution index (RMI), as defined by Eqs (3.15-3.16), is used to relate the detector and tracer radial

maldistribution to the ERR_{NACE}. The results are presented in Fig. 3.8. Two zones are clearly displayed depending on the dominant factor affecting the ERR_{NACE}. For RMI values above 5×10^{-3}, radial maldistribution accounts for most of the ERR_{NACE}, while below this value the contribution of the AS is no longer negligible. This RMI transition value corresponds to the selected SDR limitation imposed. To limit the ERR_{NACE} below 1%, the RMI should be kept below 0.21; and for a 0.1% error, the RMI should be less than 0.022.

$$NRR_C = \frac{\int_0^{\infty}\left[\max\left(C\big|_{z=H_d}\right)-\min\left(C\big|_{z=H_d}\right)\right]dt}{\int_0^{\infty} ACEdt} \tag{3.15}$$

$$RMI = \left|NRR\right| NRR_C \tag{3.16}$$

3.4.2.3 Impact of the ERR_{NACE} on the model predictions

In the previous sub-section, errors introduced by the detector were compared on the basis of the distributions ($NACE$ and $NCDR$) and termed ERR_{NACE}. The impact of the ERR_{NACE} on model parameters was not established. To provide an order of magnitude as to the potential impact of the ERR_{NACE} on the determined model parameters, several RTD profiles for the ADM were generated for Pe ranging between 2^{-3} and 2^{-8} (powers of 2). For every pairing of RTD profiles the ERR_{NACE} was calculated, the profile having the higher Pe was considered to be exact (i.e. $NACE$) and the profile with the lower Pe value to be the $NCDR$. The results show that the ERR_{NACE} is only function of the Pe ratio (i.e. Pe_{NACE}/Pe_{NCDR}). Making use of the independence of the absolute Pe, the procedure was repeated for a refined range of Pe ratios. The results are presented in Fig. 3.9. For the ADM model, an ERR_{NACE} of 0.01 yields a 4% error in Pe, while an ERR_{NACE} of 0.1 yields a 34% error in Pe.

3.4.2.4 Application of the Axial and Radial Non-uniformity Relationships

There are two ways to utilize the axial and radial non-uniformity relationships: a priori detector setup adjustment and a posteriori ERR_{NACE} assessment. Both are developed in the following examples.

In addition to providing an estimate of the detector efficiency distribution parameters, Table 3.4 also gives directions for potential improvements to the detector efficiency distribution based on the axial and radial non-uniformity relationships presented in Fig. 3.7 and 3.8.

Adjusting the detector setup to minimize the error — Pursuing with the first example (d_t = 0.12 m and ρ = 600 kg/m^3) introduced in Table 3.5, it is assumed that the system hydrodynamics are described by the ADM such that at the measurement location, $\overline{\left(\frac{u}{\varepsilon}\right)}\cdot\sigma_{NACE}$ is 0.1 m and that an ERR_{NACE} of 1% is tolerated for the purpose of the analysis. From Fig. 3.7, this ERR_{NACE} corresponds to an SDR of 0.2, hence, the AS should be lower than 2×10^{-2} in order to meet the desired ERR_{NACE} requirement. Any independent detector parameter or combination of parameters may be adjusted to achieve the required AS. For example, the distance between the shield and the detector crystal, for which $\Delta AS/\Delta l_{s-d}$ is -2.15×10^{-1}, could be increased to 8.76×10^{-2} m. However, as a consequence, the NRR will increase from -6.969×10^{-1} to -5.989×10^{-1}.

Estimating the error introduced by the detector setup — Figure 3.10 illustrates detector responses in the presence of strong radial tracer concentration profiles, which impact the reliability of the RTD experiments. All cases are based on the same time–space tracer concentration distributions generated for the generalized dispersion model with a low radial dispersion coefficient and without recirculation. The detector responses are presented for two column diameters and two tracer energy levels. The results are fully detailed in Table 3.7 and show how the axial and radial non-uniformity relationships can be used to estimate the ERR_{NACE}. The ERR_{NACE} estimated from the AS and NRR of the detector efficiency distributions are in good agreement with the calculated values.

3.5 Conclusion and Recommendations

A model was developed to predict the detector efficiency distribution in residence time distribution from radiotracer studies. The spatial uniformity of the detector efficiency distribution was quantified by the axial spread and normalized radial range. The effects of scale, media density and detector setup were investigated and showed that radiotracers may be used even on industrial scale units over a limited range of media density and radial tracer concentration profile. The axial spread and normalized radial range were tabulated for a series of scales, media and detector configurations to allow for their quick estimate.

Simulations were performed to generate typical space–time tracer concentration distributions, which then were collated with the detector efficiency distributions to predict detector responses. The results were analyzed considering the detector counting model and detector efficiency distribution. It was shown that calibration of the detector and correction of the raw detector responses should be performed in order to reduce the peak broadening resulting from the detector counting capabilities and avoid the artificial double peaks which can result from the use of paralyzable detectors. It was also determined that contributions of the axial spread and normalized radial range to the error in the normalized corrected detector response were additive. Both contributions were correlated against a standard deviation ratio (axial spread) and a radial maldistribution index (normalized radial range). These contributions can be used a priori to determine the most suitable detector configuration to minimize the resulting error, or a posteriori once the model parameters are estimated to estimate the error associated with the detector setup.

The recommendations derived herein are necessary to ensure proper interpretation of experimental data from radiotracer experiments, but do not suffice to make the analysis of such experimental data trivial due to the scattering often associated with the measurements. Nevertheless, the recommendations concerning the detector efficiency distribution still apply and may even be extended to other experimental techniques such as conductivity tracers.

3.6 Notation

ACE	average concentration evolution (time distribution of the tracer concentration cross-sectional average at the detector location), mol/m^3
AS	axial spread associated to the detector efficiency distribution, m

A_γ activity of the radiotracer, s^{-1}

C tracer concentration, mol/m^3

CDR corrected detector response, -

D raw detector response, -

D_a axial dispersion coefficient, m^2/s

d_d detector crystal diameter, m

d_t column diameter, m

D_r radial dispersion coefficient, m^2/s

E_c detector counting efficiency, -

E_d detector efficiency distribution, -

$\overline{E}_d$ tangential average of the detector efficiency distribution, -

$\overline{\overline{E}}_d$ cross-sectional average of the detector efficiency distribution, -

ERR_{NACE} $NACE$ error (error between the $NACE$ and $NCDR$), -

f_p photopeak rate $f_p = N_p / \Delta t$, s^{-1}

g gravitational acceleration constant, $g = 9.81$ m/s^2

h Plank constant, $h = 6.626 \times 10^{-34}$ J·s

H_d axial position of the detector centerline, m

H_t column height, m

k constant used for determining the turbulent kinematic viscosity, $k = 0.188$

l distance traveled by the gamma-ray, m

l_d detector crystal length, m

l_s shield opening, m

l_{s-d} distance between the shield and detector crystal, m

l_{t-s} distance between the column and shield, m

m parameter used for velocity profiles, -

N number of gamma-ray histories considered in the Monte-Carlo procedure, -

n number of moles of activated tracer, (mol)

$NACE$ normalized ACE, s^{-1}

$NCDR$ normalized CDR, s^{-1}

N_p number of detectable photopeaks received over the detector counting period, -

NRR normalized radial range associated to the detector efficiency distribution, -

NRR_C normalized radial range of the tracer concentration at H_d, -

$P(l)$ cumulative probability of interaction of a gamma-ray after traveling a linear distance l, -

P_d probability of the gamma-ray to result in a detectable photopeak, -

Pe Péclet number $Pe = \frac{UH}{\varepsilon D_a}$, -

P_Ω probability associated to the solid-angle, -

r radial coordinate, m

RMI radial maldistribution index, -

S amplitude of the step function input, mol/m^3

SDR standard deviation ratio, -

t time variable, s

t_s shield opening, m

u local superficial velocity, m/s

U	superficial velocity, m/s
V	volume variable, m^3
x	Cartesian coordinate, m
y	Cartesian coordinate, m
z	axial coordinate, m

Greek letters

Δt	detector counting period, s
ε	local phase holdup, -
$\overline{\varepsilon}_g$	average gas holdup, -
μ	linear attenuation coefficient, m^{-1}
ν	frequency of gamma-ray, s^{-1}
ρ	density, kg/m^3
ρ_l	liquid density, kg/m^3
σ_{NACE}	standard deviation of the tracer distribution, s
τ	dead time associated with the detector, s
τ_w	shear stress, Pa
υ	gamma-ray released per disintegration, -
υ_m	molecular kinematic viscosity, m^2/s
υ_t	turbulent kinematic viscosity, m^2/s
ξ	dimensionless radius $\xi = \frac{2r}{d_t}$, -

3.7 Acknowledgements

The authors would like to acknowledge Prof. N. Mostoufi and Prof. G. Kennedy for their valuable insights.

3.8 References

Beam, G.M., Wielopolski, L., Gardner, R.P., Verghese, K., 1978. Monte Carlo Calculations of Efficiencies of Right-circular Cylindrical NaI Detectors for Arbitrarily Located Point Sources. Nuclear Instruments and Methods 154, 501–508.

Degaleesan, S., Dudukovic, M.P., Toseland, B.A., Bhatt, B.L., 1997. A Two-compartment Convective–Diffusion Model for Slurry Bubble Column Reactors. Industrial & Engineering Chemistry Research 36, 4670–4680.

Din, G.U., Chughtai, I.R., Inayat, M.H., Khan, I.H., 2008. Axial Dispersion, Holdup and Slip Velocity of Dispersed Phase in a Pulsed Sieve Plate Extraction Column by Radiotracer Residence Time Distribution Analysis. Applied Radiation and Isotopes 66, 1818–1824.

Din, G.U., Chughtai, I.R., Inayat, M.H., Khan, I.H., Qazi, N.K., 2010. Modeling of a Two-phase Countercurrent Pulsed Sieve Plate Extraction Column – A Hybrid CFD and Radiotracer RTD Analysis Approach. Separation and Purification Technology 73, 302–309.

Dudukovic, M.P., Devanathan, N., Holub, R., 1991. Multiphase Reactors. Models and Experimental Verification. Revue de l'Institut Français du Pétrole. 46, 439–465.

Dunn, W.L., Gardner, R.P., 1972. Determination of Intrinsic Gamma-ray Detection Efficiencies for Cylindrical Geiger–Müller Tubes by Monte Carlo Methods. Nuclear Instruments and Methods 103, 373–384.

Franz, K., Boerner, T., Kantorek, H.J., Buchholz, R., 1984. Flow Structure in Bubble Columns. German Chemical Engineering 7, 365–374.

Gharat, S.D., Joshi, J.B., 1992a. Transport Phenomena in Bubble Column Reactors. I. Flow Pattern. Chemical Engineering Journal and the Biochemical Engineering Journal 48, 141–151.

Gharat, S.D., Joshi, J.B., 1992b. Transport Phenomena in Bubble Column Reactors. II. Pressure Drop. Chemical Engineering Journal and the Biochemical Engineering Journal 48, 153–166.

Godfroy, L., Larachi, F., Chaouki, J., 1999. Position and Velocity of a Large Particle in a Gas/Solid Riser Using the Radioactive Particle Tracking Technique. The Canadian Journal of Chemical Engineering 77, 253–261.

Hyndman, C.L., Guy, C., 1995. Gas Phase Flow in Bubble Columns: A Convective Phenomenon. The Canadian Journal of Chemical Engineering 73, 426–434.

Kasban, H., Zahran, O., Arafa, H., El-Kordy, M., Elaraby, S.M.S., Abd El-Samie, F.E., 2010. Laboratory Experiments and Modeling for Industrial Radiotracer Applications. Applied Radiation and Isotopes 68, 1049–1056.

Larachi, F., Cassanello, M., Chaouki, J., Guy, C., 1996. Flow Structure of the Solids in a 3-D Gas–Liquid–Solid Fluidized Bed. AIChE Journal 42, 2439–2452.

Levenspiel, O., Fitzgerald, T.J., 1983. A Warning on the Misuse of the Dispersion Model. Chemical Engineering Science 38, 489–491.

Lin, W., Weinell, C.E., Hansen, P.F.B., Dam-Johansen, K., 1999. Hydrodynamics of a Commercial Scale CFB Boiler-study with Radioactive Tracer Particles. Chemical Engineering Science 54, 5495–5506.

Luo, H., Svendsen, H.F., 1991. Turbulent Circulation in Bubble Columns from Eddy Viscosity Distributions of Single-phase Pipe Flow. The Canadian Journal of Chemical Engineering 69, 1389–1394.

Menzel, T., In der Weide, T., Staudacher, O., Wein, O., Onken, U., 1990. Reynolds Shear Stress for Modeling of Bubble Column Reactors. Industrial & Engineering Chemistry Research 29, 988–994.

Morooka, S., Ushida, K., Kato, Y., 1982. Recirculating Turbulent Flow of Liquid in Gas–Liquid–Solid Fluidized Bed. Journal of Chemical Engineering of Japan 15, 29–34.

Mumuni, I.I., Dagadu, C.P.K., Danso, K.A., Adu, P.S., Affum, H.A., Lawson, I., Appiah, G.K., Coleman, A., Addo, M.A., 2011. Radiotracer Investigation of Clinker Grinding Mills for Cement Production at GHACEM. Research Journal of Applied Sciences, Engineering and Technology 3, 26–31.

Nigam, K.D.P., Saroha, A.K., Kundu, A., Pant, H.J., 2001. Radioisotope Tracer Study in Trickle Bed Reactors. The Canadian Journal of Chemical Engineering 79, 860–865.

Pablo Ramírez, F., Eugenia Cortés, M., 2004. The Determination of Residence Times in a Pilot Plant. Nuclear Instruments and Methods in Physics Research B 213, 144–148.

Pant, H.J., Sharma, V.K., Nair, A.G.C., Tomar, B.S., Nathaniel, T.N., Reddy, A.V.R., Singh, G.,2009a. Application of ^{140}La and ^{24}Na as Intrinsic Radiotracers for Investigating Catalyst Dynamics in FCCUs. Applied Radiation and Isotopes 67, 1591–1599.

Pant, H.J., Sharma, V.K., Vidya Kamudu, M., Prakash, S.G., Krishanamoorthy, S., Anandam, G., Seshubabu Rao, P., Ramani, N.V.S., Singh, G., Sonde, R.R., 2009b. Investigation of Flow Behaviour of Coal Particles in a Pilot-scale Fluidized Bed Gasifier (FBG) Using Radiotracer Technique. Applied Radiation and Isotopes 67, 1609–1615.

Pant, H.J., Yelgoankar, V.N., 2002. Radiotracer Investigations in Aniline Production Reactors. Applied Radiation and Isotopes 57, 319–325.

Patience, G.S., 1990. Circulating Fluidized Beds: Hydrodynamics and Reactor Modelling. PhD Thesis, École Polytechnique de Montréal, Montréal, QC, Canada.

Patience, G., Chaouki, J., 1993. Gas Phase Hydrodynamics in the Riser of a Circulating Fluidized Bed. Chemical Engineering Science 48, 3195–3205.

Radmanesh, R., Sauriol, P., 2001. Évaluation du mélange de la phase liquide d'un lit fluidisé triphasique par traçage radioactif. (unpublished results).

Samuelsberg, A., Hjertager, B.H., 1996. Computational Modeling of Gas/Particle Flow in a Riser. AIChE Journal 42, 1536–1546.

Santos, V.A., Dantas, C.C., 2004. Transit Time and RTD Measurements by Radioactive Tracer to Assess the Riser Flow Pattern. Powder Technology 140, 116–121.

Stegowski, Z., Furman, L., 2004. Radioisotope Tracer Investigation and Modeling of Copper Concentrate Dewatering Process. International Journal of Mineral Processing 73, 37–43.

Yanenko, N.N., 1971. The Method of Fractional Steps: The Solution of Problems of Mathematical Physics in Several Variables, Springer–Verlag, Berlin.

Yao, B.P., Zheng, C., Gasche, H.E., Hofmann, H., 1991. Bubble Behaviour and Flow Structure of Bubble Columns. Chemical Engineering and Processing 29, 65–75.

Yelgaonkar, V.N., Jayakumar, T.K., Singh, S., Sharma, M.K., 2009. Combination of Sealed Source and Radiotracer Technique to Understand Malfunctioning in a Chemical Plant. Applied Radiation and Isotopes 67, 1244–1247.

Yianatos, J., Contreras, F., Díaz, F., 2010. Gas Holdup and RTD Measurement in an Industrial Flotation Cell. Minerals Engineering 23, 125–130.

Table 3.1: Examples of radioactive tracers used in residence time distribution experiments.

Radiotracer	Studied phase	Half-life (h)	Energy of gamma-ray, $h\nu_0$ (MeV)	Gamma-rays per disintegration, υ
^{38}Cl	Liquid (disolved in water)	0.64	1.60 2.17	0.38 0.422
^{68}Ga	Solid	1.13	1.08	0.030
^{41}Ar	Gas	1.83	1.293	0.99
^{56}Mn	Solid	2.57	0.837	0.99
^{99m}Tc	Liquid (disolved in water)	6.02	0.140	0.91
^{64}Cu	Solid	12.7	0.510	0.38
^{24}Na	Solid (in FCC)	14.7	1.369 2.754	1 1
^{82}Br	Gas (as CH_3Br)	35.3	0.554	0.66
	Liquid (as dibromobiphenyl dissolved)		0.619 0.777	0.41 0.83
^{140}La	Solid (in FCC)	40.3	0.329 0.487	0.21 0.40
	Solid (as La_2Cl_3 adsorbed)		0.815 1.596	0.24 0.96
^{198}Au	Solid (as $AuCl_4$ adsorbed)	64.8	0.412	0.95
	Solid (as $HAuCl_4$ solution agglomerated with cement powder)			
^{99}Mo	Liquid/Solid	66.0	0.740	0.12
^{131}I	Liquid (as NaI disolved)	193	0.284 0.364 0.637	0.05 0.82 0.07

Table 3.2: Base conditions of detector and column setup.

Energy of gamma-ray, $h\nu_0$	1.0 MeV
Media density, ρ	800 kg/m^3 (pseudo-homogeneous mixture of air and water)
Column diameter, d_t	0.1 m
Distance column–shield, l_{t-s}	5×10^{-2} m
Shield opening (infinitely wide slot), l_s	2.5×10^{-2} m
Shield thickness, t_s	5×10^{-2} m
Distance shield–detector, l_{s-d}	0 m
Detector crystal diameter, d_d	5×10^{-2} m
Detector crystal length, l_d	0.1 m
Detector crystal density, ρ_d	3667 kg/m^3
Detector crystal composition	NaI

Table 3.3: Influence of the media and gamma-ray energy on the attenuation coefficients.

Media	Energy of gamma-ray, $h\nu_0$ (MeV)	Total mass attenuation coefficients, μ/ρ (m^2/kg)	Density correction factor
Generic media used in calculations	0.5	9.665×10^{-3}	N/A
	1.0	7.066×10^{-3}	
	2.0	4.901×10^{-3}	
Water	0.5	9.687×10^{-3}	1.002×10^{0}
	1.0	7.072×10^{-3}	1.001×10^{0}
	2.0	4.942×10^{-3}	1.008×10^{0}
Air	0.5	8.721×10^{-3}	9.024×10^{-1}
	1.0	6.366×10^{-3}	9.009×10^{-1}
	2.0	4.452×10^{-3}	9.083×10^{-1}
Silica (SiO_2)	0.5	8.738×10^{-3}	9.042×10^{-1}
	1.0	6.367×10^{-3}	9.001×10^{-1}
	2.0	4.469×10^{-3}	9.119×10^{-1}
Alumina (Al_2O_3)	0.5	8.579×10^{-3}	8.877×10^{-1}
	1.0	6.252×10^{-3}	8.848×10^{-1}
	2.0	4.388×10^{-3}	8.952×10^{-1}
Kerosene (C: 0.858; H: 0.141; S: 0.001 %mass)	0.5	9.924×10^{-3}	1.027×10^{0}
	1.0	7.246×10^{-3}	1.025×10^{0}
	2.0	5.053×10^{-3}	1.031×10^{0}
Detector crystal (NaI)	0.5	Absorption/Compton: $1.684\times10^{-3}/7.351\times10^{-3}$	N/A
	1.0	$3.491\times10^{-4}/5.413\times10^{-3}$	
	2.0	$9.761\times10^{-5}/3.764\times10^{-3}$	

Table 3.4: Effects of various column, detector and radioactive tracer parameters on the detector efficiency distributions.

Scale (d_t, m)	ρ (kg/m^3)	Y (units)	Value of Y	$\frac{\Delta Y}{\Delta d_t}$ (units of $Y \div$m)	$\frac{\Delta Y}{\Delta \rho}$ (units of $Y \times$m^3/kg)
Lab. (0.1)	1	*AS* (m)	2.438×10^{-2}	8.73×10^{-2}	-9.88×10^{-7}
		NRR (-)	-1.768×10^{-1}	-3.36×10^{0}	1.16×10^{-4}
	800	*AS* (m)	2.361×10^{-2}	7.06×10^{-2}	-1.03×10^{-6}
		NRR (-)	-7.292×10^{-2}	-2.25×10^{0}	1.67×10^{-4}
	1500	*AS* (m)	2.296×10^{-2}	5.79×10^{-2}	8.93×10^{-7}
		NRR (-)	5.504×10^{-2}	-5.43×10^{-1}	1.91×10^{-4}
Pilot (0.3)	1	*AS* (m)	4.330×10^{-2}	1.00×10^{-1}	-8.99×10^{-6}
		NRR (-)	-8.914×10^{-1}	-2.33×10^{0}	3.16×10^{-4}
	800	*AS* (m)	3.635×10^{-2}	5.11×10^{-2}	-7.18×10^{-6}
		NRR (-)	-5.476×10^{-1}	5.07×10^{-1}	7.86×10^{-4}
	1500	*AS* (m)	3.134×10^{-2}	2.18×10^{-2}	-5.90×10^{-6}
		NRR (-)	2.432×10^{-2}	2.64×10^{0}	8.58×10^{-4}
Small industrial (1)	1	*AS* (m)	1.145×10^{-1}	1.01×10^{-1}	-1.56×10^{-4}
		NRR (-)	-1.638×10^{0}	-4.14×10^{-1}	1.92×10^{-3}
	800	*AS* (m)	5.295×10^{-2}	4.19×10^{-3}	-4.22×10^{-5}
		NRR (-)	7.174×10^{-1}	2.42×10^{0}	3.52×10^{-3}
	1500	*AS* (m)	3.502×10^{-2}	1.59×10^{-3}	-1.41×10^{-5}
		NRR (-)	2.425×10^{0}	2.96×10^{0}	1.90×10^{-3}
Large industrial (4)	1	*AS* (m)	4.105×10^{-1}	8.26×10^{-2}	-1.47×10^{-3}
		NRR (-)	-2.091×10^{0}	4.08×10^{-2}	1.41×10^{-2}
	800	*AS* (m)	5.458×10^{-2}	[b]1.54×10^{-4}	-4.57×10^{-5}
		NRR (-)	5.261×10^{0}	1.24×10^{0}	5.96×10^{-3}
	1500	*AS* (m)	3.530×10^{-2}	[a]2.00×10^{-4}	-1.33×10^{-5}
		NRR (-)	8.871×10^{0}	1.64×10^{0}	4.75×10^{-3}

All first derivative estimates are reported with less than 10% error, except "a" with less than 25% and "b" with less than 50%.

Table 3.4: Effects of various column, detector and radioactive tracer parameters on the detector efficiency distributions (continued).

Scale (d_t, m)	ρ (kg/m^3)	Y (units)	$\frac{\Delta Y}{\Delta h\nu_0}$ (units of $Y \div$MeV)	$\frac{\Delta Y}{\Delta d_d}$ (units of $Y \div$m)	$\frac{\Delta Y}{\Delta l_d}$ (units of $Y \div$m)
Lab. (0.1)	1	AS (m)	-2.21×10^{-4}	6.04×10^{-2}	-9.39×10^{-3}
		NRR (-)	2.28×10^{-3}	5.48×10^{0}	-2.60×10^{0}
	800	AS (m)	≈0	5.84×10^{-2}	-7.73×10^{-3}
		NRR (-)	[a] -1.07×10^{-1}	5.99×10^{0}	-2.76×10^{0}
	1500	AS (m)	2.46×10^{-4}	5.71×10^{-2}	-7.71×10^{-3}
		NRR (-)	-1.32×10^{-1}	6.13×10^{0}	-2.82×10^{0}
Pilot (0.3)	1	AS (m)	-7.04×10^{-4}	7.53×10^{-2}	9.98×10^{-3}
		NRR (-)	[a] 3.41×10^{-2}	2.49×10^{1}	-1.30×10^{1}
	800	AS (m)	1.90×10^{-3}	6.92×10^{-2}	7.54×10^{-3}
		NRR (-)	-1.28×10^{-1}	2.73×10^{1}	-1.42×10^{1}
	1500	AS (m)	3.52×10^{-3}	6.95×10^{-2}	-8.89×10^{-3}
		NRR (-)	-5.64×10^{-1}	2.57×10^{1}	-1.34×10^{1}
Small industrial (1)	1	AS (m)	-1.87×10^{-3}	1.73×10^{-1}	5.00×10^{-2}
		NRR (-)	[a] 7.82×10^{-2}	2.96×10^{1}	-1.78×10^{1}
	800	AS (m)	1.43×10^{-2}	1.13×10^{-1}	≈0
		NRR (-)	-1.21×10^{0}	1.26×10^{1}	-6.73×10^{0}
	1500	AS (m)	9.66×10^{-3}	8.07×10^{-2}	-1.07×10^{-2}
		NRR (-)	-1.37×10^{0}	8.70×10^{0}	-4.54×10^{0}
Large industrial (4)	1	AS (m)	-5.25×10^{-3}	7.89×10^{-1}	1.79×10^{-1}
		NRR (-)	[a] 4.38×10^{-2}	3.69×10^{1}	-2.12×10^{1}
	800	AS (m)	2.10×10^{-2}	1.34×10^{-1}	-5.02×10^{-3}
		NRR (-)	-1.89×10^{0}	[a] 4.18×10^{0}	-9.50×10^{0}
	1500	AS (m)	1.03×10^{-2}	8.13×10^{-2}	-4.93×10^{-3}
		NRR (-)	-3.29×10^{0}	[a] 6.32×10^{0}	[a] -6.40×10^{0}

All first derivative estimates are reported with less than 10% error, except "a" with less than 25% and "b" with less than 50%.

Table 3.4: Effects of various column, detector and radioactive tracer parameters on the detector efficiency distributions (continued).

Scale (d_t, m)	ρ (kg/m^3)	Y (units)	$\frac{\Delta Y}{\Delta l_s}$ (units of $Y \div$m)	$\frac{\Delta Y}{\Delta l_{t-s}}$ (units of $Y \div$m)	$\frac{\Delta Y}{\Delta l_{s-d}}$ (units of $Y \div$m)
Lab. (0.1)	1	*AS* (m)	7.034×10^{-1}	1.83×10^{-1}	-1.30×10^{-1}
		NRR (-)	[a] -4.42×10^{0}	1.19×10^{0}	1.39×10^{0}
	800	*AS* (m)	6.78×10^{-1}	1.83×10^{-1}	-1.23×10^{-1}
		NRR (-)	[a] -2.56×10^{0}	1.38×10^{0}	1.38×10^{0}
	1500	*AS* (m)	6.57×10^{-1}	1.82×10^{-1}	-1.18×10^{-1}
		NRR (-)	-2.78×10^{0}	1.28×10^{0}	1.45×10^{0}
Pilot (0.3)	1	*AS* (m)	1.17×10^{0}	1.74×10^{-1}	-2.69×10^{-1}
		NRR (-)	-5.01×10^{0}	4.46×10^{0}	4.95×10^{0}
	800	*AS* (m)	9.81×10^{-1}	1.73×10^{-1}	-2.15×10^{-1}
		NRR (-)	[a] -3.74×10^{0}	4.64×10^{0}	5.24×10^{0}
	1500	*AS* (m)	8.32×10^{-1}	1.72×10^{-1}	-1.77×10^{-1}
		NRR (-)	-4.03×10^{0}	5.16×10^{0}	4.69×10^{0}
Small industrial (1)	1	*AS* (m)	2.99×10^{0}	1.45×10^{-1}	-7.63×10^{-1}
		NRR (-)	-6.44×10^{0}	3.27×10^{0}	3.42×10^{0}
	800	*AS* (m)	1.32×10^{0}	1.54×10^{-1}	-3.25×10^{-1}
		NRR (-)	≈0	1.06×10^{0}	1.12×10^{0}
	1500	*AS* (m)	8.87×10^{-1}	1.65×10^{-1}	-2.02×10^{-1}
		NRR (-)	≈0	[a] 7.34×10^{-1}	[a] 6.07×10^{-1}
Large industrial (4)	1	*AS* (m)	7.70×10^{0}	1.43×10^{-1}	-2.68×10^{0}
		NRR (-)	3.57×10^{0}	1.11×10^{0}	1.46×10^{0}
	800	*AS* (m)	1.32×10^{0}	1.60×10^{-1}	-3.29×10^{-1}
		NRR (-)	≈0	[a] -4.11×10^{0}	[a] -4.40×10^{0}
	1500	*AS* (m)	8.57×10^{-2}	1.52×10^{-1}	-1.97×10^{-1}
		NRR (-)	≈0	-3.71×10^{0}	[a] -6.20×10^{0}

All first derivative estimates are reported with less than 10% error, except "a" with less than 25% and "b" with less than 50%.

Table 3.5: Estimation of the detector efficiency distribution properties using Table 3.4.

New setup				Reference setup from Table 3.4						New setup
d_t (m)	ρ (kg/m^3)			d_t (m)	ρ (kg/m^3)	Y	Value of Y	$\frac{\Delta Y}{\Delta d_t}$	$\frac{\Delta Y}{\Delta \rho}$	Estimated value of Y
	Original	Media (correction factor)	Equivalent generic media							
0.12	675	Alumina (8.848×10^{-1})	597.2	0.10	800	AS (m) NRR (-)	2.361×10^{-2} -7.292×10^{-2}	7.06×10^{-2} -2.25×10^{0}	-1.03×10^{-6} 1.67×10^{-4}	2.523×10^{-2} -1.518×10^{-1}
1.25	960	Kerosene (1.025×10^{0})	984.0	1.0	800	AS (m) NRR (-)	5.295×10^{-2} 7.174×10^{-1}	4.19×10^{-3} 2.42×10^{0}	-4.22×10^{-5} 3.52×10^{-3}	4.623×10^{-2} 1.970×10^{0}

Table 3.6: Parameters used to generate the space–time tracer concentration distributions for several hydrodynamic models.

Model	Related Eqs.	D_a (m^2/s)	D_r (m^2/s)	m
ADM	(3.6-3.7)	2×10^{-4}–4.5×10^{-2}	0	N/A
GDM without recirculation	(3.6-3.8)	1×10^{-3}–5×10^{-2}	1×10^{-6}–5×10^{-3}	2–100
GDM with recirculation	(3.6-3.7, 3.9-3.10)	1×10^{-3}–5×10^{-2}	5×10^{-4}–5×10^{-3}	2–100

Table 3.7: Example on estimating the *NACE* error for detector setups and space-time tracer distribution corresponding to Fig. 3.10.

Figure 3.10	a)	b)	c)	d)
d_t (m)	0.1	0.1	0.3	0.3
$h\nu_0$ (MeV)	1.0	0.5	1.0	0.5
AS (m)	0.023	0.012	0.029	0.013
NRR	0.153	0.470	0.539	1.687
$\overline{\left(\frac{u}{\varepsilon}\right)}\cdot\sigma_{NACE}$	0.978			
NRR_{NACE}	1.970			
SDR	0.024	0.011	0.030	0.013
$\left(ERR_{NACE}\right)_{SRD}$	1.67×10^{-4}	4.07×10^{-5}	2.60×10^{-4}	5.60×10^{-5}
RMI	0.301	0.926	1.062	3.323
$\left(ERR_{NACE}\right)_{MRI}$	1.44×10^{-2}	4.55×10^{-2}	5.23×10^{-2}	1.68×10^{-1}
$\left(ERR_{NACE}\right)_{SDR+MRI}$	1.46×10^{-2}	4.56×10^{-2}	5.26×10^{-2}	1.68×10^{-1}
ERR_{NACE} (from curves)	1.53×10^{-2}	5.69×10^{-2}	6.17×10^{-2}	1.86×10^{-1}

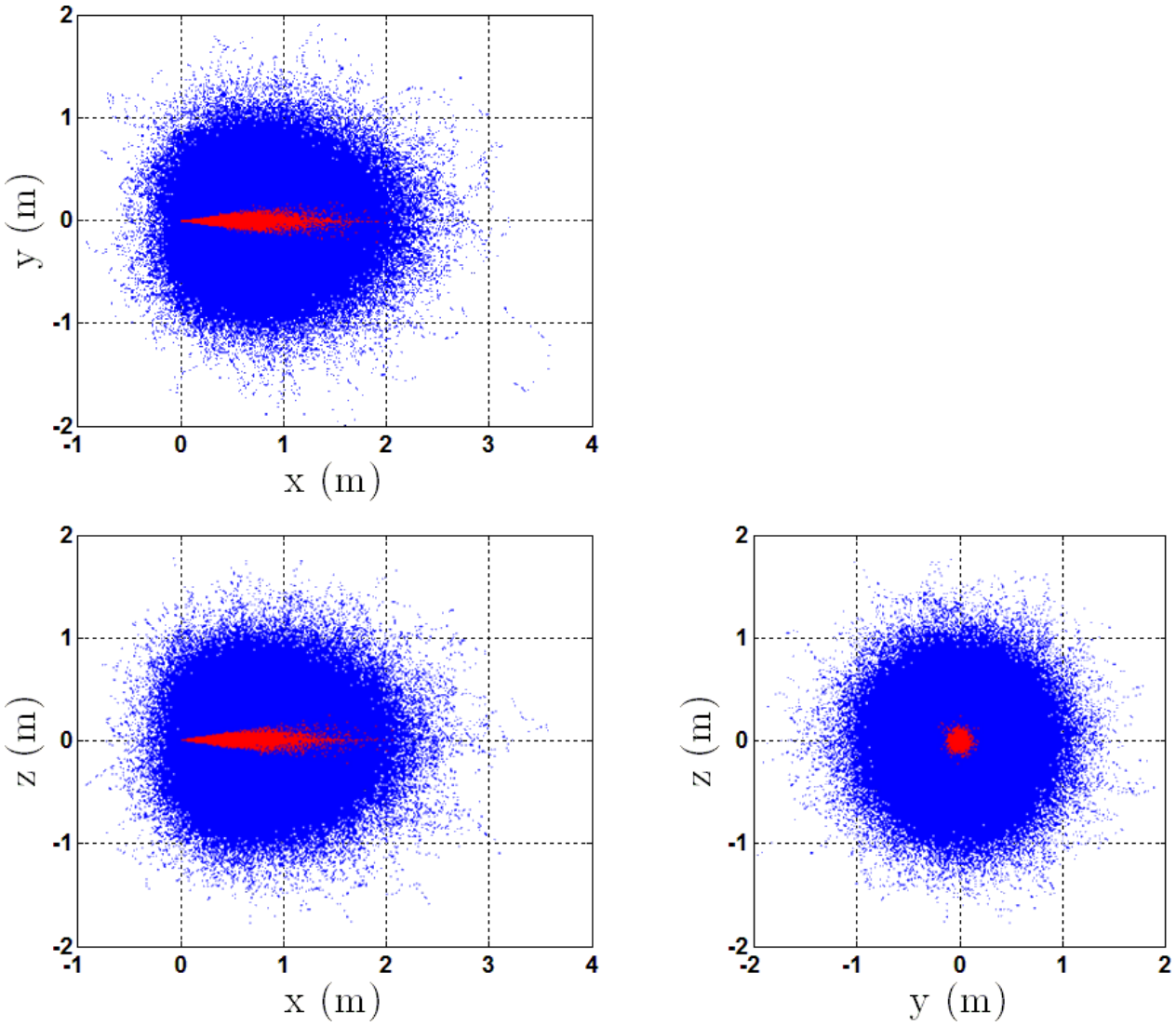

Figure 3-1: Impact of the Compton scattering on the outcome of a full energy 1 MeV gamma-ray issuing from the origin towards x > 0 in a media with a density of 800 kg/m^3: Red dots have energy greater than Compton edge and will be detectable; Blue dots have a residual energy lower than the Compton edge.

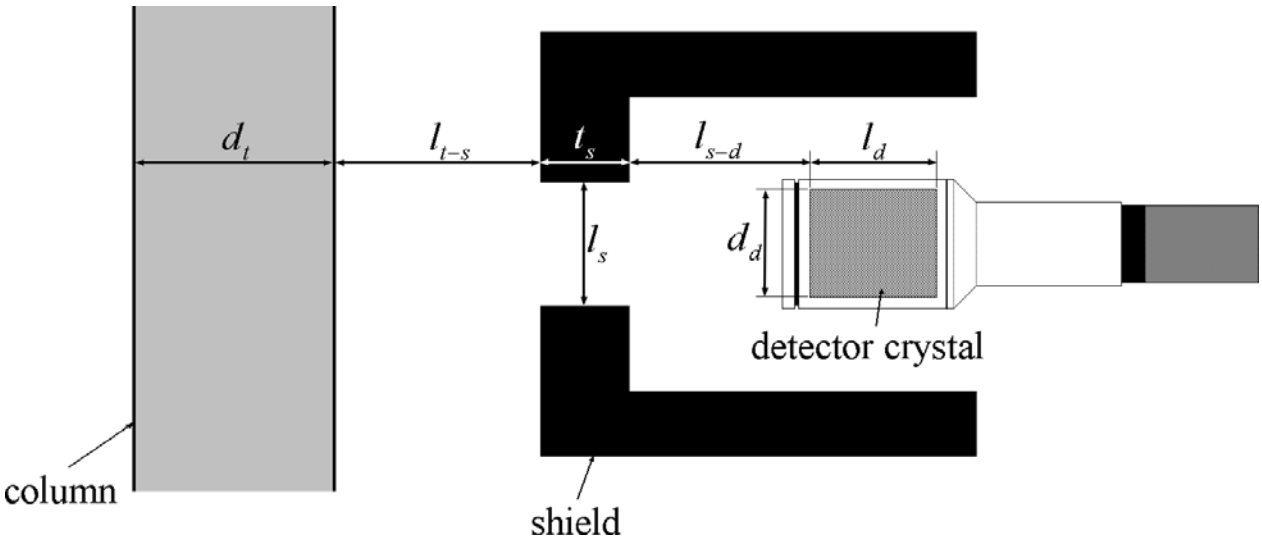

Figure 3-2: Generic column and detector setup considered for the calculations.

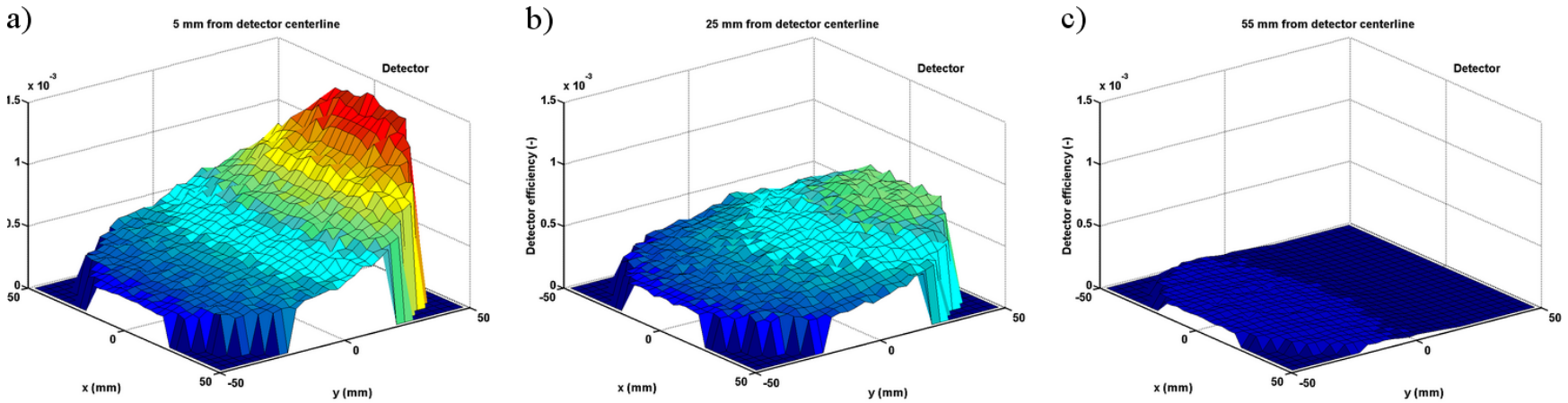

Figure 3-3: Typical efficiency distributions at different axial positions relative to the detector centerline (detector centerline is located along $x = 0$ and its face is close to $y = 50$); a) $z = 5$ mm from detector centerline; b) $z = 25$ mm from detector centerline; c) $z = 55$ mm from detector centerline.

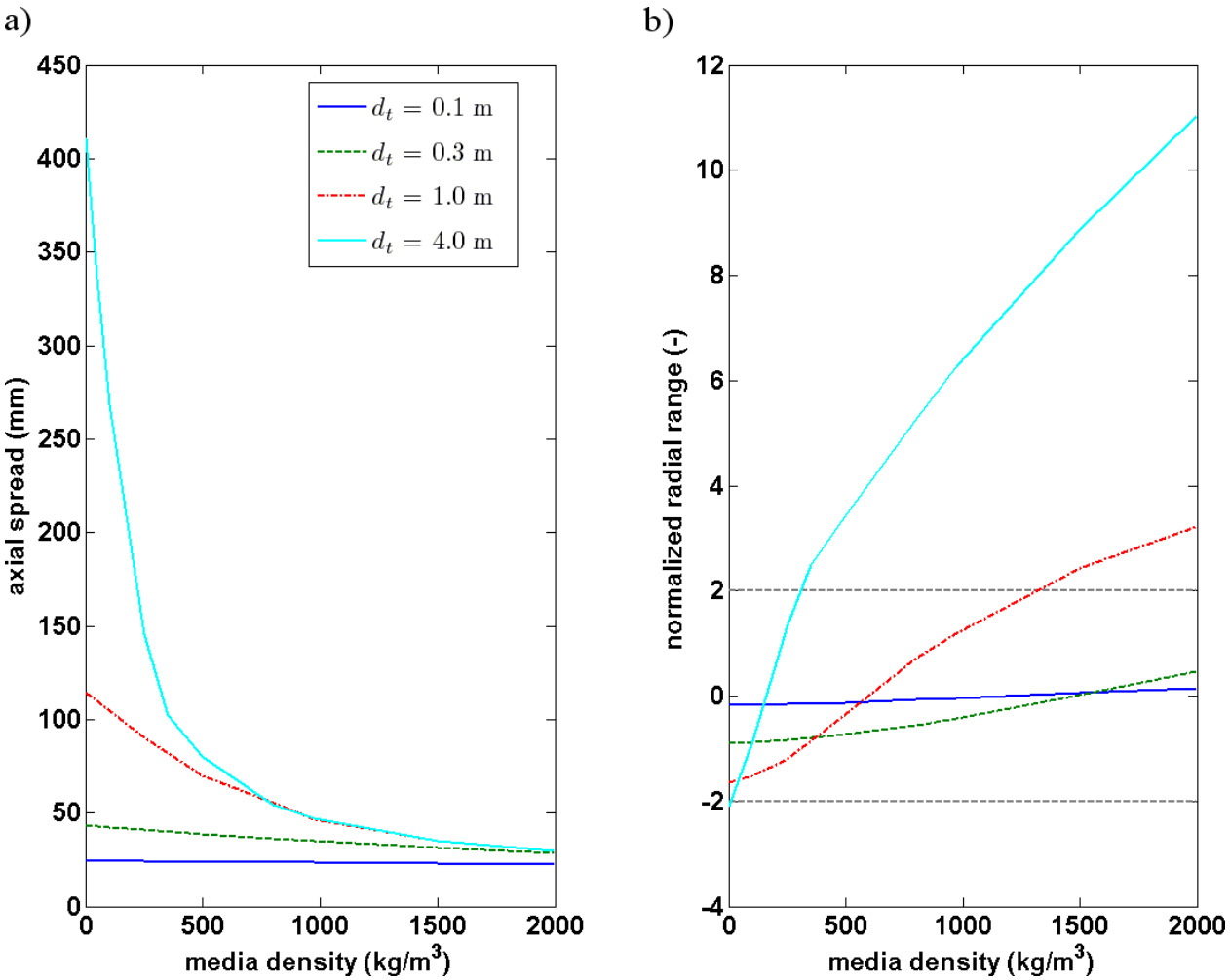

Figure 3-4: Influence of the media density and column diameter on the degree of non-uniformity in the detector efficiency distribution; a) axial spread (*AS*); b) normalized radial range (*NRR*).

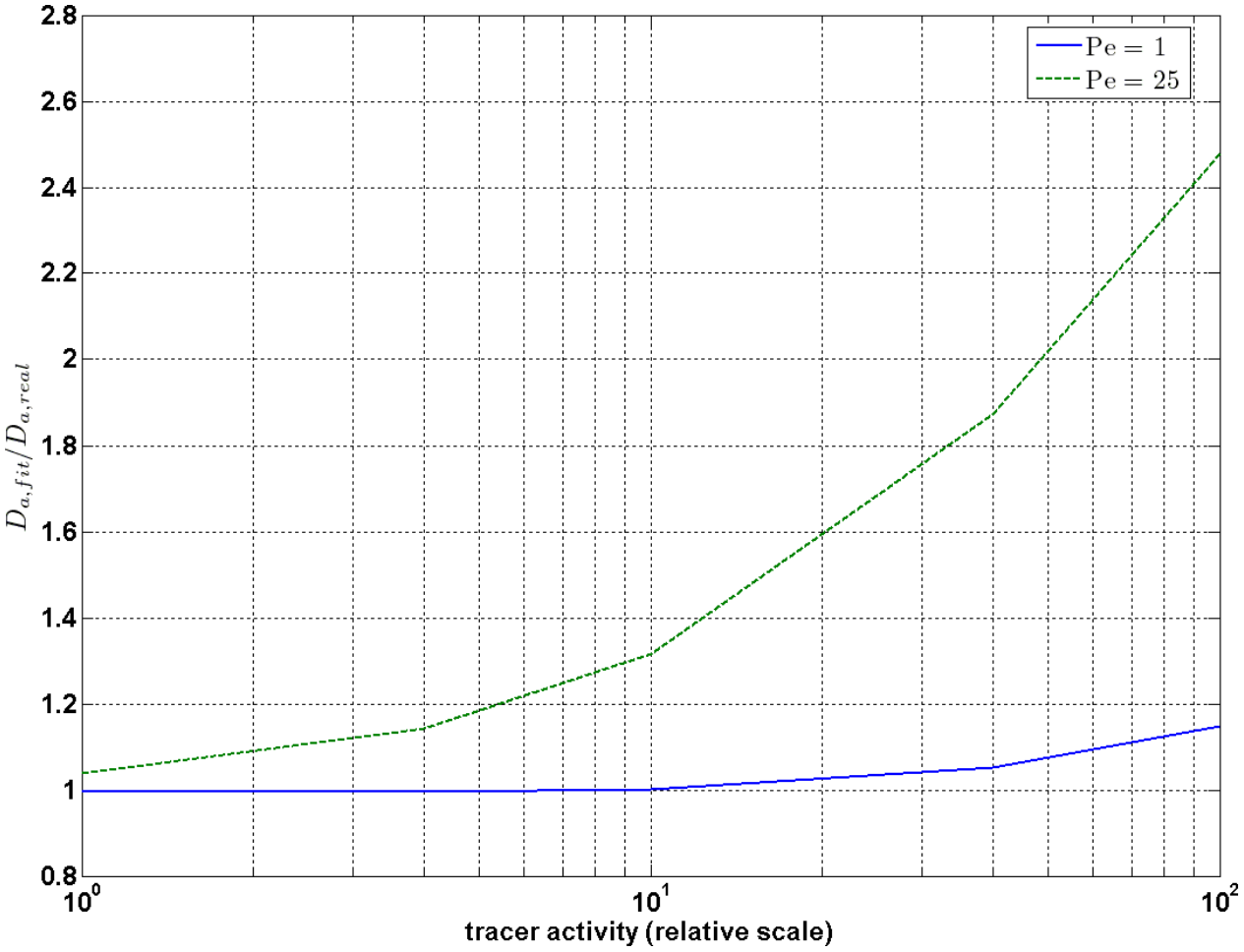

Figure 3-5: Impact of using raw detector responses (D) for the ADM considering several tracer activities and considering a detector dead time (τ) of 6 µs.

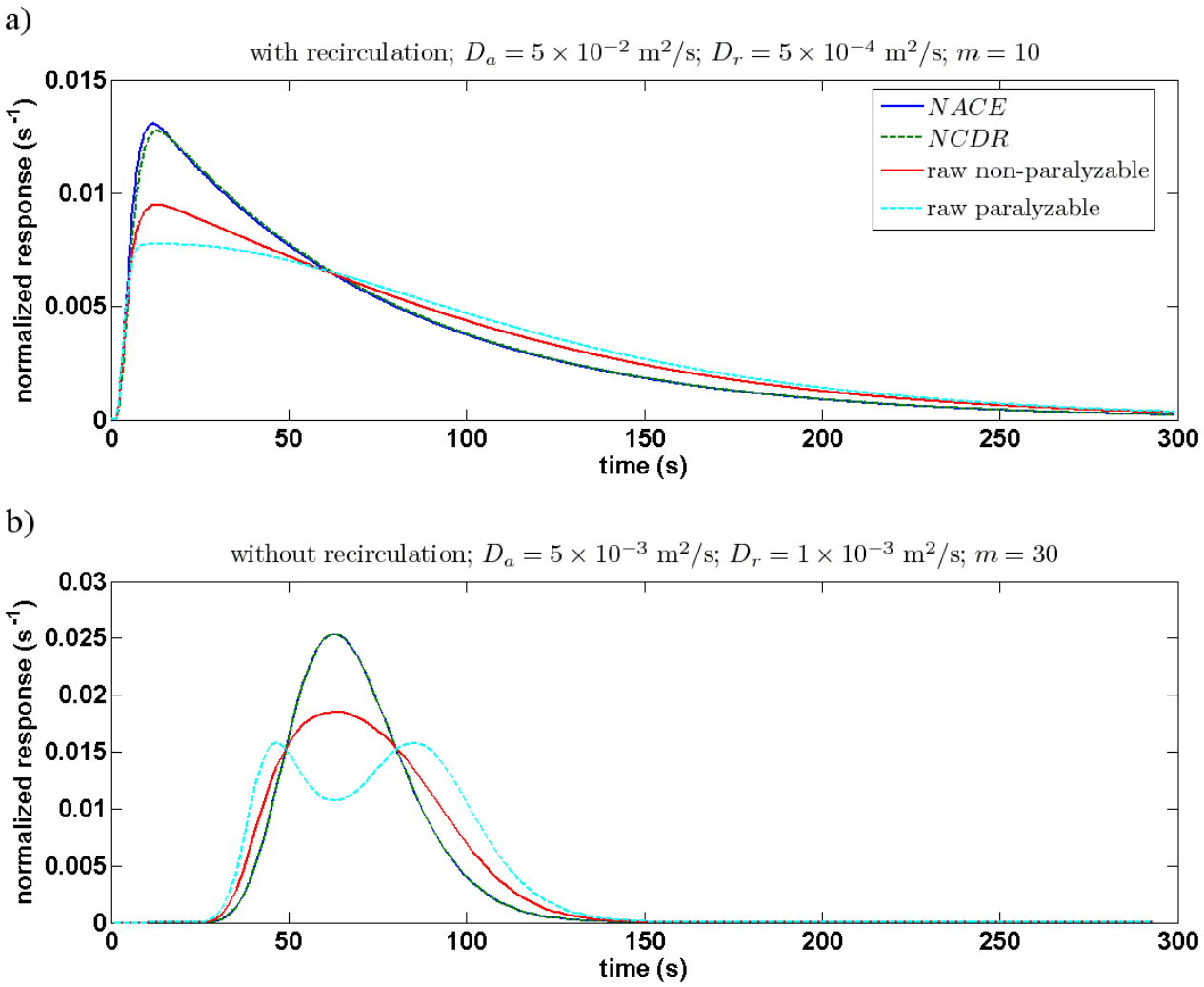

Figure 3-6: *NACE* , *NCDR* , normalized raw paralyzable and normalized raw non-paralyzable detector responses for hydrodynamic models with and without recirculation; a) with recurculation; b) withouth recirculation.

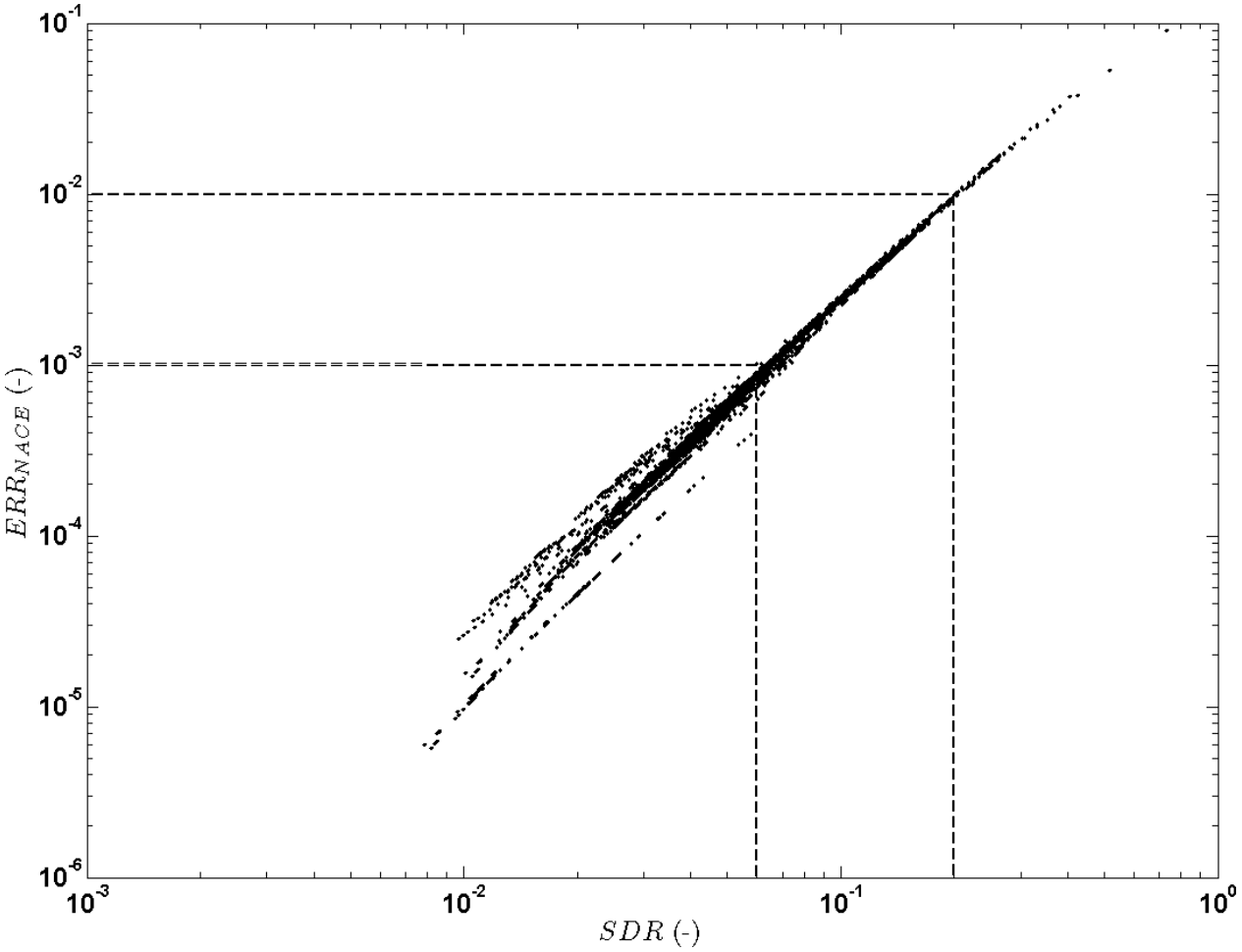

Figure 3-7: *NACE* error due to the axial spread (*AS*) of the detector efficiency, considered space–time tracer concentration have uniform radial velocity and concentration distributions.

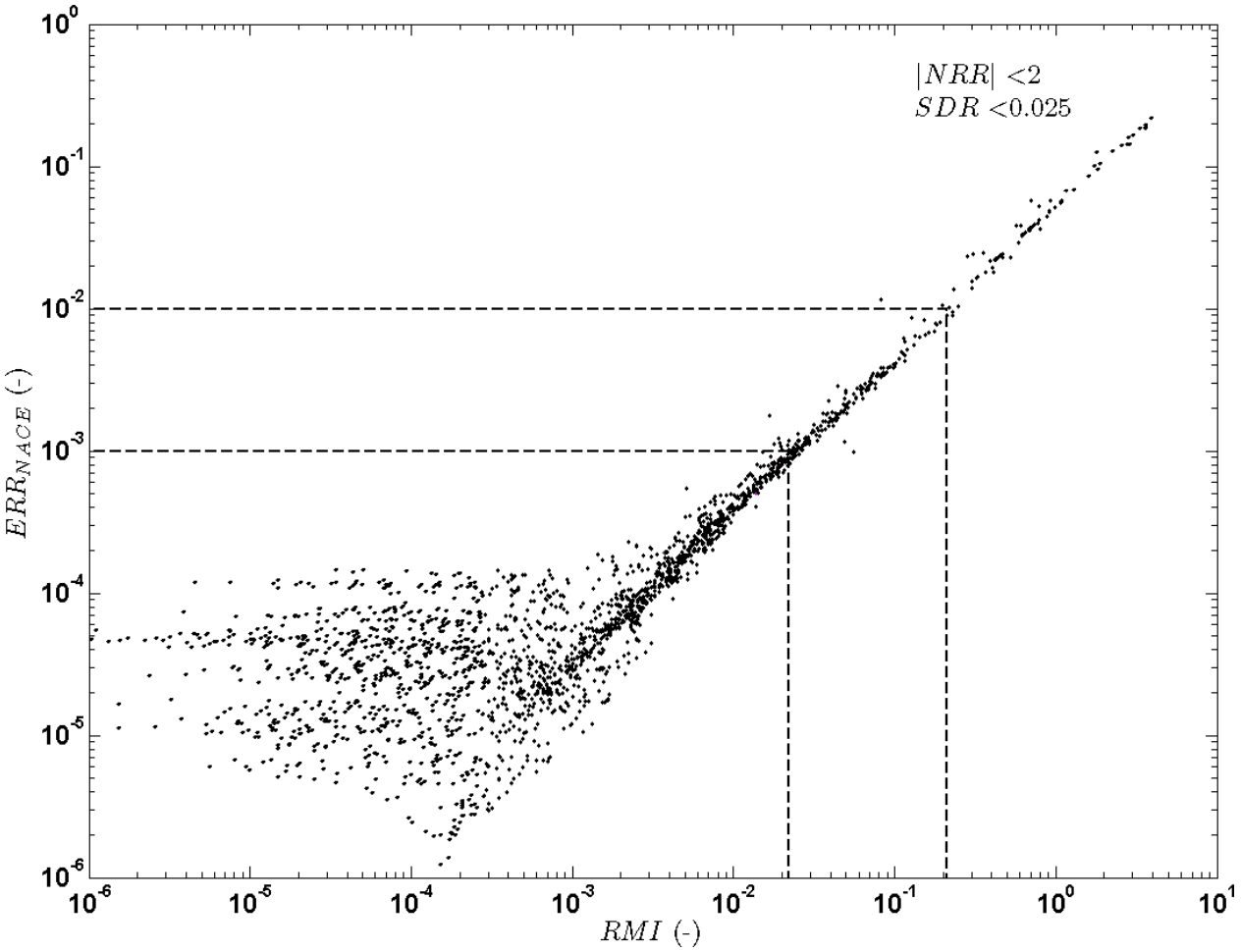

Figure 3-8: *NACE* error due to the radial non-uniformity of the detector efficiency distribution and the space–time tracer concentration, detector efficiencies have $|NRR|$ smaller than 2 and *SDR* lower than 0.025.

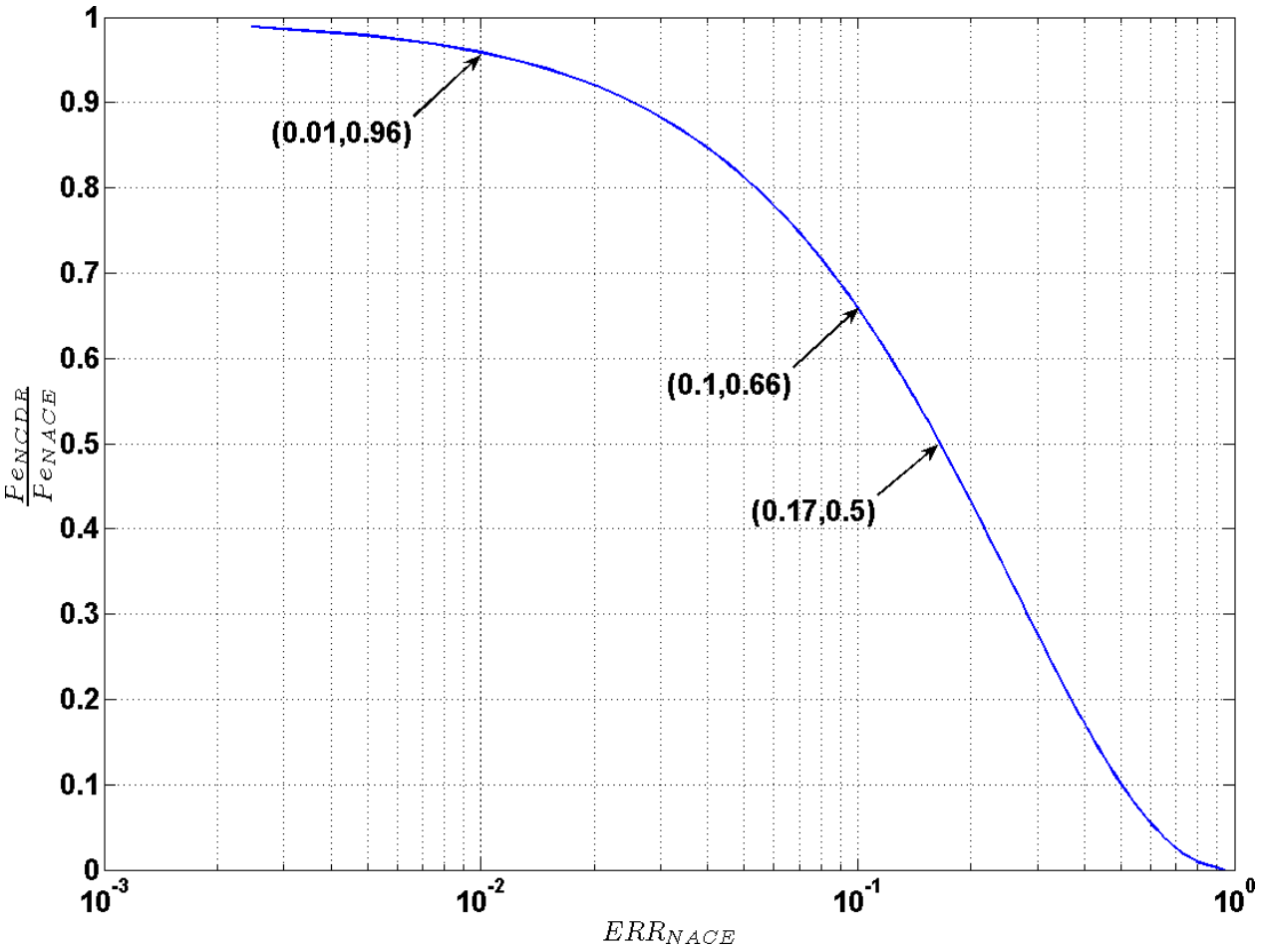

3-9: Influence of the *NACE* error on the determined *Pe* values for the ADM.

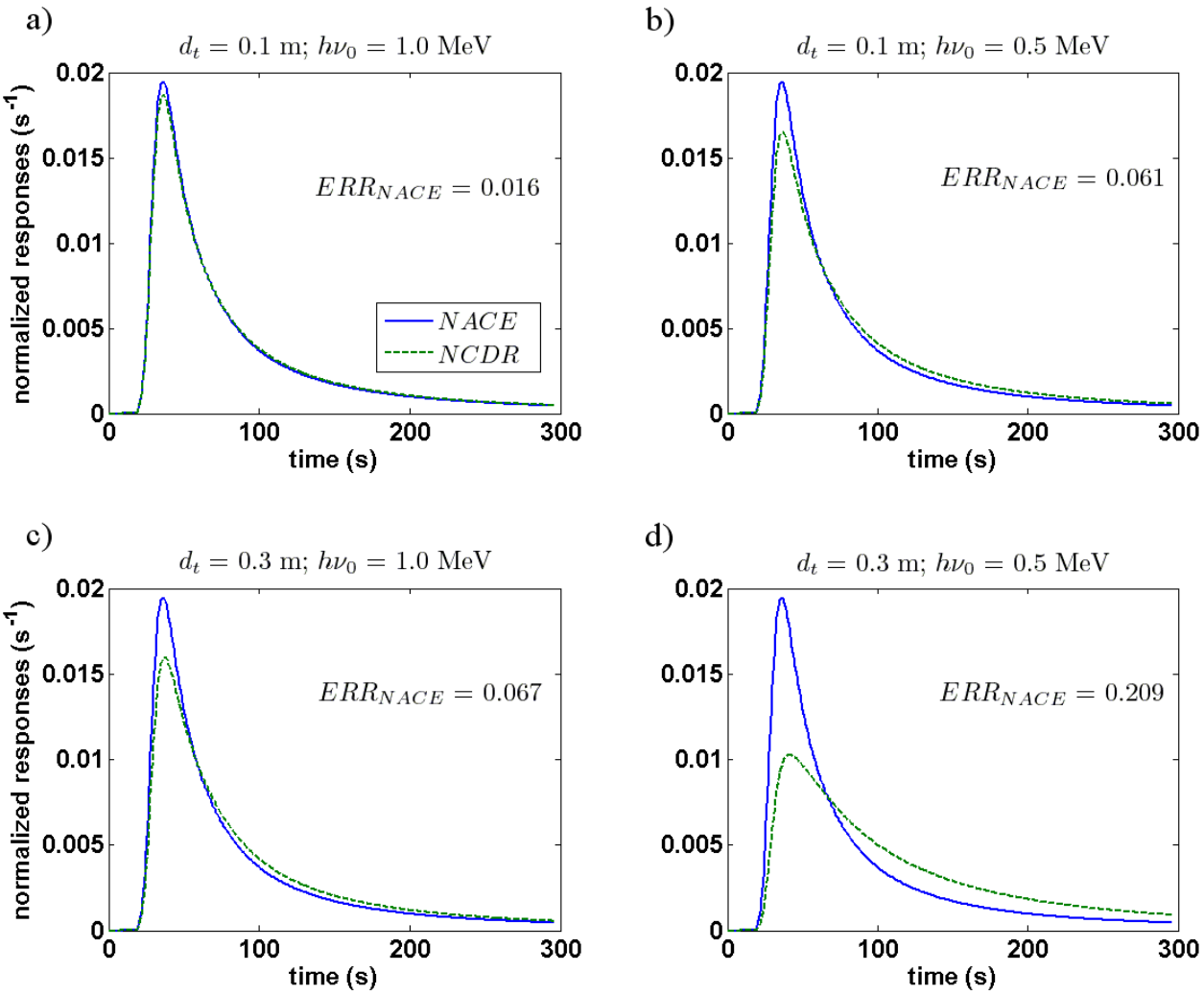

Figure 3-10: Influence of the detector setup and gamma-ray energy on the corrected detector response.

CHAPITRE 4 ARTICLE 3: GAS–SOLID STRUCTURE IN THE VICINITY OF A SPARGER NOZZLE IN A FLUIDIZED BED

Pierre Sauriol, Heping Cui and Jamal Chaouki

Department of Chemical Engineering, École Polytechnique de Montréal,

C.P. 6079, succ. Centre-Ville, Montréal, Quebec, Canada, H3C 3A7

4.1 Abstract

A new experimental approach is proposed to investigate the gas–solid structure in the vicinity of a sparger nozzle in a fluidized bed. The approach consists in performing an injection velocity sweep with a fiber-optic probe located at a fixed position downstream the sparger nozzle. Following this approach, the local gas–solid structure was investigated for different nozzle orientations (downward, horizontal and upward). For a given fluidized media (FCC catalyst, Geldart A) and superficial gas velocity (0.9 m/s), the local gas–solid structure was dependent upon the measurement position, sparger nozzle orientation and injection velocity. Four distinct impact zones were identified from the average local solid holdup data, with the boundaries corresponding to the characteristic jet lengths (L_{min}, L_{max} and L_b). Locally, the major hydrodynamic parameters of the gas–solid structure (e.g. average holdup, phase holdup, phase fraction, phase changeover frequency) showed nearly linear dependence with the injection velocity, allowing for an easy estimation of the gas–solid structure. Dynamic aspects of the gas–solid structure were investigated. A simple analysis suggests that the frequency of the pulsating jet (between L_{min} and L_{max}) was in the order of 1 and 1.5 Hz. Comparison of the collected data with existing correlations indicated that none of the correlations are capable of adequately predicting the penetration lengths, under the present test conditions. This is especially true for the upward and horizontal sparger nozzles, for which correlations have mostly been developed using Geldart B and D particles and operated at superficial velocities at or near the minimum fluidization velocity.

Keywords: Fluidization; Hydrodynamics; Sparger; Nozzle; Jet; Jet penetration length.

4.2 Introduction

Gas injection by means of spargers in a fluidized bed reactor is common practice in industrial processes, especially where fast exothermic reactions such as partial oxidation and combustion reactions are taking place (Dry and Judd, 1986; Patience and Bockrath, 2010; Sotudeh-Gharebaagh and Chaouki, 2000; Yates et al., 1991). For those reactions, spargers play a key role in introducing reactant gases separately at different locations of the fluidized bed media in order to avoid potentially explosive homogeneous mixtures. Due to their intricate structure, and more importantly their nozzle design, spargers may significantly affect the local hydrodynamics, hence influence the global reactor performance (Hutchenson et al., 2010). Moreover, the jetting structure often associated with high injection velocities has been reported to considerably intensify the momentum, heat and mass transfers through enhanced gas and solid entrainment (Behie et al., 1971; Bi and Kojima, 1996; Briens et al., 2008; Donadona and Massimilla, 1978; Gbordzoe and Bergougnou, 1990; Molodtsof and Labidi, 1995). These improved transfer rates in regions where solid holdup is sparse may impact the performance of reactors differently depending on the desired reaction. For gas–solid catalytic processes where homogeneous side-reactions are probable, the presence of jetting zones may cause severe selectivity and yield reduction. On the other hand, for non-catalytic reactions (i.e. natural gas combustion), the jetting zones have been reported to account for most of the reaction (Sotudeh-Gharebaagh, 1998).

Many factors such as the fluidized bed operating conditions, the particle properties, the injection velocity and orientation influence the flow pattern of the injected gas in a fluidized bed. Typically, the injected gas can be described by two important parameters: its boundary and its gas–solid structure. The boundary limits the zone of influence, whereas the gas–solid structure determines how the injected gas influences the momentum, heat and mass transfer, ultimately the reaction.

Most studies have focused on establishing the boundary, mainly the jet penetration length and to a lesser extent its shape (jet half-angle). The majority of studies covered upward grid nozzles (Cleaver et al., 1995; Hirsan et al., 1980; Merry, 1975; Wen et al., 1982; Yang and Keairns, 1979; Yates et al, 1986) where solid movement differs from the rest of the fluidized bed due to the presence of the grid. As for sparger nozzles, they are usually divided into four categories according to the nozzle orientation. Upward sparger nozzles have been studied mostly in jetting

fluidized beds (Guo et al, 2001b; Hong et al., 1996; Luo et al, 1999; Wang (CH) et al., 2010; Zhong and Zhang, 2005), while horizontal (Berruti et al., 2009; Chen and Weinstein, 1993; Guo et al., 2010; Hong et al., 1997; Merry, 1971; Xuereb et al, 1991a) inclined (Hong et al., 1997; Xuereb et al, 1991a) and downward (Shen et al., 1991; Sotudeh-Gharebaagh and Chaouki, 2000; Yates et al., 1991) sparger nozzles were usually studied in fluidized beds.

One of the major drawbacks from the many investigations conducted on gas jets in fluidized beds comes from the various definitions, measurement techniques (visual observation, pressure probes, Pitot tube probes, high speed video cameras, X-rays, optical probes, capacitance probes, photodiodes), system dimensions (2D, semi-circular (2.5D), 3D) and configurations (grid, spargers, fluidized beds, jetting fluidized beds) which have often resulted in discrepancies amongst the existing correlations. Vaccaro et al. (1997b) presented an extensive comparison between the various experimental techniques used. From their analysis, they divided the measurement techniques into two groups according to their ability to measure the characteristic jet length: $L_{j,b}$ and $L_{j,max}$, respectively the deepest penetration of high momentum bubbles issuing from the jet structure and the maximum length of the continuous jet void (Hirsan et al., 1980). However, recent studies by Zhong and Zhang (2005), which combine Pitot tube measurements and image analysis, contradict Vaccaro's classification. As for the influence of the experimental setup, several efforts have shown that the proximity of walls and surfaces have a significant impact on the shape of the jet (Müller et al., 2009; Rowe et al., 1979) and its length (Pore et al., 2010; Wen et al., 1982). Most studies and correlations is that they are limited to superficial velocities near the minimum fluidization velocity (e.g. U_g/U_{mf} <3), which especially for Geldart A particles does not represent operating conditions of industrial significance.

The choice of appropriate sparger nozzles for gas injection is not a simple task. While most published studies have primarily focused on the boundary in the form of the jet penetration length for practical design purposes (McNeil et al., 1984), it is necessary to improve our knowledge of the gas–solid structure in the vicinity of sparger nozzles in order to fully understand and predict the influence of the injected gas on the local hydrodynamics and the global performance of a fluidized bed. The purpose of the present study is to investigate the boundary and the gas–solid structure in the vicinity of a sparger in a fluidized bed using a fiber-optic probe. Although fiber-optic probes are classified as an intrusive measurement technique, a recently conducted

comparative study has shown that the time-averaged solid holdups obtained with fiber-optic probes are in agreement with those from non-intrusive measurement techniques including electrical capacitance tomography, X-ray computed tomography, and radioactive particle tracking (Dubrawski et al., 2011).

4.3 Experimental Procedure

Experiments were carried out under ambient conditions in a column with an inner diameter of 0.15 m and a height of 1.50 m. The experimental apparatus is depicted in Fig. 4.1. Air was introduced into the column through a porous plate distributor. FCC particles (Geldart A, $\rho_p = 1673\ \mathrm{kg/m^3}$, $d_p = 70\ \mu\mathrm{m}$, $\varepsilon_{s,mf} = 0.55$, $U_{mf} = 0.003\ \mathrm{m/s}$ (calculated using Wen and Yu's correlation), $U_c = 0.77\ \mathrm{m/s}$ (determined experimentally from pressure fluctuations) were used as bed material. For every run described herein, the static bed height was 0.17 m and the superficial gas velocity (U_g) was 0.9 m/s, thus the bed was operated in the turbulent regime. This velocity/regime was chosen because it is more representative of industrial applications. A single-nozzle sparger with a 2 mm opening was used for all runs. The sparger nozzle was positioned at the column centerline and 0.15 m above the porous plate distributor. In between runs, the sparger/nozzle arrangement could easily be accessed in order to change the sparger nozzle orientation (downward, upward and horizontal). The fiber-optic probe tip was positioned along the sparger nozzle axis to measure instantaneous local solid holdup. The distance between the probe tip and the sparger nozzle opening could be varied. Unless specified otherwise, the distance was kept at 15 mm. Inserts in Fig. 4.1 detail the fiber-optic probe/sparger nozzle arrangements for all three orientations studied. For each arrangement, the injection velocity (u_j) was varied between 0 and 100 m/s.

The reflective fiber-optic probe consisted of two distinct fiber bundles (emitter and receiver). The probe had a tip of less than 3 mm in diameter and its effective measurement volume was determined to be less than 1 $\mathrm{mm^3}$. The probe response was calibrated according to previously published work by Cui et al. (2001). The sampling frequency (976 Hz) and the number of data points ($2^{16} = 65536$) were such that the signals were statistically repeatable and representative of the operating conditions.

4.4 Results and Discussion

The flow near the sparger nozzle may differ from the bulk of the fluidized bed depending of the injection velocity. Fig. 4.2 shows the local solid holdup 15 mm downstream of the sparger opening for three different injection velocities (10 m/s, 50 m/s and 92 m/s). These velocities were selected because for at the measurement location, they clearly exhibited different behaviors; coincidently, these velocities are also of interest because they correspond to typical injection velocities recommended respectively for low, normal and high attrition resistant particles. Results for an injection velocity of 10 m/s were similar, in terms of the gas–solid structure, to those obtained when no gas is injected through the sparger nozzle. The injection velocity has a great influence over the local flow structure, especially at high velocities where the injected gas carries enough momentum to hinder the bulk fluidized bed behavior.

4.4.1 Time-averaged Properties

The mean solid holdup was studied with respect to the injection velocity. The local gas–solid structure changes considerably with increasing injection velocity for all sparger nozzle orientations studied. From Fig. 4.3, the changes in the average local solid holdup for each sparger nozzle orientation can be described by linear relationships between the average local solid holdup and the injection velocity. At low injection velocity, for the downward and horizontal sparger nozzles, no gas penetration is observed at the measurement position. The local solid holdup remains constant, at the same value as when no gas is fed through the sparger nozzle. At low injection velocities, the upward sparger nozzle shows a slightly different behavior as the local solid holdup slowly drops with increasing velocity. This phenomenon is attributed to high momentum bubbles originating from the sparger nozzle. The bubble frequency and size increase as the injection velocity is increased, resulting in a lower solid holdup. From the experimental data, it is difficult to clearly identify the transition velocity, $u_{j,bubbling}$, which for the upward sparger nozzle is between 0.5 and 2 m/s. For the downward and horizontal sparger nozzles, the intense bubbling is not observed.

As the injection velocity is increased, a transition velocity marking the beginning of a more sustained gas penetration is reached. This transition velocity is identified as the jetting onset velocity, $u_{j,onset}$, and is equivalent to 29, 15 and 34 m/s for the downward, upward and horizontal

sparger nozzles, respectively. These transition velocities are consistent with the trends whereby for a given injection velocity, downward and horizontal nozzles yields jets of similar lengths, while upward nozzles yields jets that are nearly three times longer (Zenz, 1968). As the injection velocity is increased further, the momentum results in more injected gas breaking free through the emulsion phase of the fluidized bed. A jetting structure is periodically forming and this phenomenon continues until a fully sustained penetration and local domination of the injected gas over the fluidized bed is reached. This transition velocity is identified as the permanent jetting velocity, $u_{j,perm}$, and is equivalent to 84, 67 and 85 m/s for the downward, upward and horizontal sparger nozzles, respectively. The permanent jetting velocity delimits the beginning of a nearly constant segment in the average solid holdup vs. injection velocity curve. This zone is known as the permanent jet zone. The solid holdup inside the permanent jet structure was directly determined for all three orientations studied (downward sparger nozzle: 0.041; upward sparger nozzle: 0.042; horizontal sparger nozzle: 0.061). The amount of entrained particles inside the jet structure was reported as being the major factor influencing the momentum and heat transfers in the jetting region (Donadono and Massimilla, 1978). Further experimental work is required to determine how the bed operating conditions, particle properties and injected gas influence the particle entrainment within the jet structure. Note that the transition injection velocities found for both downward and horizontal sparger nozzles are close, which is consistent with the recommend use of horizontal data to estimate downward conditions for which data and correlations are sparse (Pell, 1990; Zenz, 1968).

The influence of the distance between the sparger nozzle and the probe tip was studied for a downward sparger nozzle and the results for three different sampling positions are presented in Fig. 4.4. The general shape of the three curves exhibit the same distinctive patterns introduced earlier in Fig. 4.3. The only difference is that the transition velocities, $u_{j,onset}$ and $u_{j,perm}$, increase with increasing distance between the sparger nozzle opening and the sampling position.

The work by Hirsan et al. (1980) was instrumental in defining the characteristic jet lengths observed for an upward nozzle, namely: L_{min} (the minimum jet length), L_{max} (the maximum jet length), and introducing L_b the length corresponding to the deepest penetration depth of high momentum jet bubbles. Although they have presented L_b as the most important jet length for

design purposes, most studies on jet length have focused on L_{max}. Based on the various jet lengths, four impact zones are defined according to the influence the injected gas has on the fluidized bed. The impact zones are defined locally relative to each sparger nozzle. The size and geometry of the impact zones will be affected amongst other things by the fluidized bed properties (U_g, ρ_g, d_p, ρ_p), the injected gas properties (u_j, ρ_j) and the sparger nozzle design (d_j, H_j). These impact zones are presented in Figs. 4.3 and 4.4 where the average local solid holdup is plotted against the injection velocity for various sparger nozzle orientations and sampling locations. The impact zones are defined as follows:

The *no impact* zone — The injected gas does not affect the local bed hydrodynamics, as if no sparger is present. The injected gas may be absent or present in the form of bubbles that mimic those of the fluidized bed. They do not carry an excess momentum compared to the rest of the bubbles from the fluidized bed. The average local solid holdup in this zone is that of the fluidized bed, identified on the figures as $\overline{\varepsilon}_{s,FB}$. This zone will be observed for any position located at a distance L downstream of the sparger nozzle along its axis, for which $L > L_b$. Typically, this is the case when L is great or u_j is small.

The *permanent jet* zone — The injected gas locally dominates the fluidized bed hydrodynamics resulting in a permanent void often referred to as a permanent jet. The average solid holdup in this zone is relatively low as compared to the surrounding fluidized media. From the experimental results, the average local solid holdup remains constant and is identified on the figure as $\overline{\varepsilon}_{s,j,perm}$. This zone will be observed for $L < L_{min}$. Typically, this is the case when L is small or u_j is great.

The *pulsating jet* zone — The local hydrodynamics are never permanently established, constantly varying between two extremes: L_{min} and L_{max}. It is a transition zone between *no impact/intense bubbling* and *permanent jet* where the void keeps on growing until the bubble possesses enough

momentum and/or its buoyancy force causes it to break away from the void. This results in a periodic necking of the jetting structure. This zone will be observed for $L_{max} > L > L_{min}$.

The *intense bubbling* zone — High velocity bubbles originating from the sparger nozzle affect the local hydrodynamics. Those bubbles carry enough momentum to distinguish themselves from the rest of the fluidized bed. Usually overlooked by most authors, the high momentum bubbles are considered to be the most important parameter for design purposes. This zone will be observed for $L_b > L > L_{max}$.

Each zone reflects a distinct local interaction between the injected gas and the fluidized bed. There exists a relationship between the injection velocity and the different characteristic jet lengths (L_b, L_{max} and L_{min}). By varying the injection velocity, while keeping the same sampling position relative to the sparger nozzle, it is possible to determine the transition velocities for which the distance between the sampling point and sparger nozzle tip (L) corresponds to a characteristic jet length. In other words, when u_j is equal to $u_{j,onset}$, the characteristic jet length L_{max} will be equal to L and so on. The corresponding transition velocities are illustrated in Figs. 4.3 and 4.4.

Since the fluidized bed structure may be described in terms of a dilute phase and a dense phase, the results are analyzed with respect to each phase in order to extract more information and improve the understanding of the phenomenon involved. This analysis requires that a criterion be set in order to differentiate between each phase based on the solid holdup. Cui et al. (2001) introduced the minimum probability density method in order to determine a minimum probability voidage, which corresponds to the transition between the dense phase and the dilute phase. Any data point that has a voidage lower than the minimum probability voidage is considered to be part of the dense phase, and vice versa. In the present study, the minimum probability voidage without gas injection was 0.58.

The distribution of particles in each phase was studied to clarify the gas–solid structure and its dependence on the injection velocity and orientation. As shown in Fig. 4.5, the average solid holdup in the dilute phase, $\overline{\varepsilon}_{s,dilute}$, changes with increasing injection velocity, following similar

trends observed with the overall solid holdup presented in Fig. 4.3. The linear trends depicted in Fig. 4.5 (and the following) are constructed based on the transition velocities found for an easy comparison. The average solid holdup in the dense phase remains almost constant throughout the range of injection velocities investigated for all sparger nozzle orientations, ranging from 0.50 at low injection velocity to 0.45 at high injection velocity. In order to complement this analysis, the dilute phase fraction was computed and the results are presented in Fig. 4.6. The observed trends are similar to those in the figures presented for the overall solid holdup and the dilute phase solid holdup.

In summary, the upward sparger nozzle influences the local flow structure to the greatest extent. Its transition velocities, $u_{j,onset}$ and $u_{j,perm}$, are lower than for the other two sparger nozzle orientations studied. The upward sparger nozzle also leads to the formation of high momentum bubbles, which were not observed with the downward and horizontal sparger nozzles. In general, for all three sparger nozzle orientations, the local solid holdup and the solid holdup in the dilute phase decrease with increasing injection velocity while in the pulsating jet zone. In the permanent jet zone, all hydrodynamic properties remain constant. Based on the findings herein and inspired by reports of a flame-like jet structure, an attempt was made to illustrate the gas–solid structure in the vicinity of a sparger nozzle and is presented in Fig. 4.7 for downward and upward sparger nozzles.

4.4.2 Dynamic Properties

While the time-averaged properties reveal general trends and allow for a good understanding of the phenomenon at stake, dynamic properties can shed light on the stochastic nature of the phenomenon. Dynamic fluctuations of the flow structure influence the interaction of gas and solids, and furthermore, the momentum, heat and mass transfer. This type of information is important for modeling purposes and simulation of reaction systems. Altogether five dynamic aspects were investigated in order to complement the steady-state analysis.

The standard deviation of the local solid holdup was calculated. For all three orientations studied the standard deviations remained constant at 0.16 at low injection velocities and decreased linearly towards a constant value of 0.025 at higher velocities. The observed transition velocities are slightly higher than $u_{j,onset}$ and $u_{j,perm}$ obtained based on the average holdups.

To understand the dynamic distribution of gas and solids in the local flow structure, the probability distribution functions of local solid holdup from 0 to $\varepsilon_{s,mf}$ were analyzed at various injection velocities (Fig. 4.8). At the same injection velocities, the frequency analysis of the instantaneous solid holdup was also performed. At a low injection velocity of 10 m/s, the two-phase flow structure exhibits continuous double-peak probability densities of local solid holdup (Fig. 4.8a). For the downward sparger nozzle, the sampling position is in the no impact zone, while for the upward sparger nozzle, the sampling position is in the intense bubbling zone. In this case, the probability of having dilute phase elements is slightly increased and the probability of having dense phase elements is correspondingly lower. For both the upward and downward sparger nozzles, the maximum probability is observed for solid holdups around 0.10. On the amplitude-frequency scale, fluctuations ranging between 0 and 5 Hz due to the motion of bubbles and emulsion/clusters are observed. At an intermediate injection velocity of 50 m/s (Fig. 4.8b), the double peak structure disappears. The dilute phase probability is important with a maximum probability observed for a solid holdup of 0.04; this corresponds to the pulsating jet. The frequency analysis of this condition shows that the injected gas breaks up emulsion packets, resulting in major frequencies between 0 and 10 Hz. At the high injection velocity of 92 m/s (Fig. 4.8c), the dense phase peak has totally disappeared leaving only the dilute phase present with a maximum probability for a solid holdup very close to 0.02. This corresponds to the permanent jet. The frequency analysis yields no dominant frequency. The permanent jet behavior fully dominates the local flow structure.

In order to give a quantitative description of the fluctuations that were described by frequency analysis, the phase changeover frequency from dilute to dense to dilute phase (Fig. 4.9) and duration of the dense phase occurrence were investigated. The observed trends are common to most figures presented thus far. For the downward and horizontal sparger nozzles, at velocities below $u_{j,onset}$, the phase changeover frequency as well as the duration of the dense phase elements remain constant at 4.8 Hz and 0.042 s, respectively. As for the upward sparger nozzle, the phase changeover frequency and the duration of the dense phase elements generally decrease as the injection velocity is increased. For injection velocities between $u_{j,onset}$ and $u_{j,perm}$, the phase changeover frequency and the dense phase occurrence duration linearly decrease with increasing injection velocity for all sparger nozzle orientations studied. At high injection velocity, the phase

changeover frequency and the duration of the dense phase elements are close to zero due to the almost complete absence of the dense phase elements in the permanent jet zone.

Finally, the investigation should also focus on the pulsating jet zone in order to determine its typical frequency (i.e. the frequency at which the jet fluctuates between L_{min} and L_{max}). Since frequency analysis failed to clearly identify such behavior, an alternative approach is proposed. The analysis is based on the assumption that the pulsating jet may be represented by a sequence of interlaced windows corresponding either to the fluidized bed or to the permanent jet. A 0.25-second moving average filter is run on the solid holdup data in order to eliminate the impact of bubbles from the fluidized bed. Using the filtered signal, a threshold value ($\varepsilon_{s,tr}$) is established to distinguish between fluidized bed elements and permanent jet elements. The transition holdup is selected such that the fraction of elements corresponding to the permanent jet obtained from the moving average data equals that obtained from the time averaged data such as defined by Eq. (4.1). Figure 4.10, presents typical filtered solid holdup curves and the threshold holdups computed for the each sparger nozzle velocity are identified by a dotted line. The jetting frequency is estimated by counting the number of occurrences of pulsating jet elements within a given time period under injection velocity between $u_{j,onset}$ and $u_{j,perm}$. With this approach, the jetting frequency was determined to range between 1 and 1.5 Hz for both upward and downward sparger nozzles, compared to the 7-8 Hz frequency reported for grid nozzles (Yates et al., 1986).

$$f_{j,perm} = \frac{\overline{\varepsilon}_{s,FB} - \varepsilon_{s,tr}}{\overline{\varepsilon}_{s,FB} - \overline{\varepsilon}_{s,j,perm}} \tag{4.1}$$

4.5 Comparison with Correlations from the Literature

The computed transition velocities and corresponding jet lengths will be compared with existing correlations from the literature. As mentioned in the introduction, several correlations for the jet penetration lengths have been published, but were based for the most part on grid nozzles. Studies focusing on the jet length from sparger nozzles and resulting in a correlation are sparse and selected ones are summarized in the following. Note that most correlations are for L_{max} and a few have been found for the prediction of L_b. No correlations found in preparation for this study targeted L_{min}. The correlations and the corresponding jet lengths are presented in Table 4.1. The

injection velocity entered corresponds to the transition velocity determined from average solid holdup during the injection velocity sweeps. The experimental jet length is the distance between the fiber-optic probe and the nozzle tip which was held constant during the injection velocity sweep.

4.5.1 Downward Sparger Nozzles

Downward sparger nozzles have been the subject of very few published experimental efforts. The most widely known is that of Zenz (1968) who first proposed a chart to predict the jet penetration length in a fluidized bed. Zenz's chart is applicable to downward sparger nozzles, as well as horizontal and upward sparger nozzles and grids. It is not limited to gas–solid fluidization as it also includes data collected on gas-gas, gas-liquid, liquid-solid systems for particles ranging from types A to D according to Geldart's classification. Zenz's chart is intended for applications where the injected fluid is solely the fluidizing medium, which differs from the context of the present study. Zenz's chart was converted to a numerical format using Fig. 3-1 given by Pell (1990). Yates et al. (1991) studied the influence of overlapping opposing jets on particle attrition, and proposed a simple correlation for the prediction of the maximum jet penetration length from downward sparger nozzles. Their experimental work was performed in an incipiently fluidized bed of calcined alumina (Geldart A particles).

4.5.2 Upward Sparger Nozzles

In comparison to upward grid nozzles, upward sparger nozzles have not been widely investigated. Luo et al. (1999) studied the jet penetration length from a pair of upward sparger nozzles in a 2.5D jetting fluidized bed operated at minimum fluidization. The authors used additional data from the literature to cover a wide range of particles (from Geldart A to D) and bed properties. Amongst the data considered are results from single and multiple grid nozzles in incipiently fluidized beds. Guo et al. (2001b) also proposed a correlation based on experiments on Geldart B and D particles in a jetting fluidized bed operated at velocities between 1 and 3 times the minimum fluidization velocities.

Since Hirsan et al. (1980) were the first to define and correlate for the prediction of L_b (and also L_{max}), their correlations will be evaluated. They have focused on fluidized beds of Geldart B

particles operated at elevated pressure. Musmarra (2000) also proposed a correlation for the prediction of L_b, which will be considered. Musmarra's experimental work focused on beds of Geldart B and D particles, but they also included data from other authors who experimented in fluidized beds of Geldart A particles.

4.5.3 Horizontal Sparger Nozzles

Merry (1971) investigated and correlated the jet length from horizontal sparger nozzles in a fluidized bed operated under ambient conditions with Geldart B and D particles. Guo et al. (2010) proposed a correlation based on experimental work conducted on Geldart A and B particles operated near the minimum fluidization. The correlation accounts for the effect of fluidization velocity in a narrow range of fluidization velocities, 1-2 times the minimum fluidization velocity, which prevents its use in the current context. Hong et al. (1997) proposed a correlation for the prediction of the jet penetration length from inclined sparger nozzles (i.e. -10°–10° relative to horizontal) in beds of Geldart D particles. Their proposed correlation includes the effect of inclination angle, and may be extended used for horizontal sparger nozzles.

4.5.4 Comments on the Correlations

The calculated characteristic jet lengths from the correlations are reported in Table 4.1. For most correlations, the calculated jet lengths are in poor agreement with the experimental values typically greater than 100% difference. This is believed to the result of inappropriate range of application, most importantly the particle size and superficial velocity.

For the downward nozzles, the correlation of Yates et al. (1991) yielded jet lengths that were close (25%) to the experimental values. Their correlation predicted slightly longer jet penetration lengths than those measured. This is believed to be explained by the superficial velocity which is not accounted for in their correlation. The particles used in the present work were very similar to those in their experiments. Zenz's correlation (1968) for downward nozzle was found to agree with the jet penetration length at the lower injection velocity (corresponding to an experimental jet length of 5 mm). For longer jet lengths (high injection velocities, the correlation of Zenz is found not to account enough for the change in injection velocity.

For the upward sparger nozzle, both correlations used for the prediction of L_b differ significantly from the experimental measurement, even though a wide range of injection velocities was considered. The correlations of Hirsan et al. (1980) correlations predict very short penetration lengths which are believed to be caused by the superficial velocity ratio term. In the present study, the superficial velocity ratio is 100 times greater than the maximum ratio considered for their correlation. On the other hand, Musmarra's correlation (2000) predicts large L_b values. The correlations of L_{max} by Luo et al. (1999) and Guo et al. (2001b) give estimates that are between 100-130% greater than the experimentally determined lengths. Luo et al.'s correlation is based on various experimental work conducted in fluidized beds with sparger nozzles and grid nozzles. Particles used for their experimental work were varied from A to D according to Geldart's classification in an incipiently fluidized bed. Guo et al.'s work is based on Geldart B and D particles and considers that the superficial velocity does not have an impact beyond 2.5 times the minimum fluidization velocity which in the present case limits the correction as this ratio can be very high for Geldart A particles. It is postulated that these differences could be in part explained by the limited or unaccounted effect of the superficial velocity. As was the case with the correlation of Hirsan et al. (1980) for L_b, their correlation of L_{max} yields very short penetration lengths. Interestingly, the correlation of Yang (1981) which is based on a subset of data from Hirsan et al. shows the opposite trend. Yang's correlation does not account for the effect of the superficial velocity. Finally, the L_{max} obtained using the correlation of Zenz's is found to be in fair agreement with the experimental data, 50% shorter than the experimental value.

The predicted L_{max} obtained for horizontal sparger as determined by the correlations of Merry (1971), Hong et al. (1997) and Benjelloun et al. (1991) are found to agree with each other. These are twice as large as the experimentally determined length, however, this discrepancy could be explained by the fact that none of the correlations account for the effects of superficial velocity. In fact the correlations of Merry and Hong et al. account for the solid holdup in the bed which depends on the superficial velocity but this factor only results in an increase in the jet length as the velocity is increased. As was the case with the upward sparger nozzle, the correlation by Zenz (1968) was found to yield jet length in fair agreement with the experimental data.

4.6 Conclusion

In an effort to investigate the gas–solid structure in the vicinity of a sparger nozzle, a fiber-optic probe was used to measure the instantaneous local solid holdup near the tip of a single sparger nozzle. The results of the experimental work exhibited discernable characteristics that helped analyze the local gas–solid structure. The local flow structure in the vicinity of a sparger nozzle in a fluidized bed depends strongly on the injection velocity and orientation. By increasing the injection velocity, for all the three sparger nozzle orientations tested, four characteristic gas–solid structures were identified: at low gas velocities, the *no impact* zone; with slightly higher injection velocity, the *intense bubbling* zone (for the upward sparger nozzle only); at intermediate injection velocities, the *pulsating jet* zone; at high injection velocities, the *permanent jet* zone. On a time-averaged scale, the gas–solid structure showed linear relationship between the hydrodynamic properties (local solid holdup, solid holdup in the dilute phase and dilute phase fraction) and the injection velocity. Transition velocities, $u_{j,bubbling}$, $u_{j,onset}$ and $u_{j,perm}$, were easily determined from the average local solid holdup. To these transition velocities correspond the characteristic jet penetration lengths: L_b, L_{max} and L_{min}. Generally, the transition velocities were similar for the downward and horizontal sparger nozzles, while they were significantly lower for the upward sparger nozzle.

On a dynamic scale, the flow structure showed changes from the dominant low frequency (0–5 Hz) fluctuations at low injection velocities (*no impact* zone) to very low random fluctuations at high injection velocities (*permanent jet* zone). The dynamic aspects of the jetting structure were also investigated. The jetting frequency was found to range between 1 and 1.5 Hz. The probability distribution function of local solid holdup clearly showed the effect of the injection velocity in the establishment of the flow behaviors. A progressive transition from a double-peak distribution at low injection velocity to a single-peak narrow distribution at high injection velocity is observed from the experimental data. The single-peak narrow distribution corresponds to the predominant dilute phase fraction at high injection velocity.

The experimental jet lengths were compared with existing correlations. The particle size appears to have a great influence on the predicted jet lengths. In general, correlations developed for fluidized beds of coarse particles (Geldart B and D) are not well suited for fine particles (Geldart

A). Another drawback from the correlations is that the influence of the fluidizing velocity is not always taken into account since most of them were developed for incipiently fluidized beds.

Further investigations are required to offer better jet length estimations which will account for the effect of the superficial velocity and the use of Geldart A particles under conditions that are closer to industrial applications. Specifically, efforts need to focus on the downward sparger nozzles and the investigation the investigation of L_b and L_{min} for which too few data is available given their importance on erosion and mass transfer.

4.7 Notation

d	diameter, m
f	time-based fraction, -
L	distance between the sampling point and sparger nozzle tip, m
L_b	jet bubble penetration length (maximum penetration of high momentum jet bubbles), m
L_{max}	maximum jet penetration length (maximum length of pulsating void), m
L_{min}	minimum jet penetration length (length of permanent void), m
U_g	superficial gas velocity, m/s
u_j	injection velocity, m/s
$u_{j,bubbling}$	injection velocity corresponding to the transition between the "no impact" and the "intense bubbling" zones for upward nozzles, m/s
$u_{j,onset}$	injection velocity corresponding to the transition between the "no impact" (horizontal and downward nozzles) or the "intense bubbling" (upward nozzles) and the "pulsating jet" zones, m/s
$u_{j,perm}$	injection velocity corresponding to the transition between the "pulsating jet" and the "permanent jet" zones, m/s

z	variable equivalent to $\ln\left(\rho_j u_j^2\right)$ used in correlations by Zenz (1968) (refer to Table 4.1), $\rho_j u_j^2$ is in Pa

Greek Letters

ε	local instantaneous phase holdup, -
$\bar{\varepsilon}$	local average phase holdup, -
μ	viscosity, Pa·s
θ	sparger nozzle inclination angle relative to horizontal, º
ρ	density, kg/m^3

Subscripts

c	refers to conditions at transition to turbulent fluidization
cf	refers to conditions at complete fluidization
dilute	refers to the dilute phase fraction
div	refers of the minimum voidage condition
FB	refers to the conditions of the bed when is fluidized but no gas is injected
g	refers to the gas in the fluidized bed
j	corresponds to the injected gas (based on conditions at the tip of the nozzle)
j, *perm*	corresponds to conditions of the permanent jet
mf	refers to conditions at minimum fluidization
p	refers to the particle
s	refers to the solid phase

4.8 Acknowledgements

The authors gratefully acknowledge the Postdoctoral Fellowships awarded to Heping Cui by the Natural Sciences and Engineering Research Council of Canada (NSERC), and also the excellent work and technical assistance of Mr. Jean Huard.

4.9 References

Behie, L.A., Bergougnou, M.A., Baker, C.G.J., Base, T.E., 1971. Further Studies on Momentum Dissipation of Grid Jets in a Gas Fluidizied Bed. The Canadian Journal of Chemical Engineering 49, 557–561.

Benjelloun, F., Liégeois, R., Vanderschuren, J., 1991. Détermination des longueurs de jets de gaz horizontaux dans les lits fluidisés, in: Laguérie, C., Guigon, P. (Eds.), Récents progrès en génie des procédés: La Fluidisation, pp. 108–115.

Berruti, F., Dawe, M., Briens, C., 2009. Study of Gas–Liquid Jet Boundaries in a Gas–Solid Fluidized Bed. Powder Technology 192, 250–259.

Bi, J., Kojima, T., 1996b. Prediction of Temperature and Composition in a Jetting Fluidized Bed Coal Gasifier. Chemical Engineering Science 51, 2745–2750.

Briens, C., Berruti, F., Felli, V., Chan, E., 2008. Solids Entrainment into Gas, Liquid, and Gas–Liquid Spray Jets in Fluidized Beds. Powder Technology 184, 52–57.

Chen, L., Weinstein, H., 1993. Shape and Extent of Voids Formed by a Horizontal Jet in a Fluidized Bed. AIChE Journal 39, 1901–1909.

Cleaver, J.A.S., Ghardiri, M., Tuponogov, V.G., Yates, J.G., Cheesman, D.J., 1995. Measurement of Jet Angles in Fluidized Beds. Powder Technology 85, 221–226.

Cui, H., Mostoufi, N., Chaouki, J., 2001a. Gas and Solids Between Dynamic Bubble and Emulsion in Gas-fluidized Beds. Powder Technology 120, 12–20.

Donadono, S., Massimilla, L., 1978. Mechanisms of Momentum and Heat Transfer between Gas Jets and Fluidized Beds, in: Davidson, J.F., Keairns, D.L. (Eds.), Proceedings of the Second Engineering Foundation Conference on Fluidization, (Cambridge, England), Engineering Foundation, New York, pp. 375–380.

Dry, R.J., Judd, M.R., 1986. Split Feed Fluidised Bed Reactors: Mass Transfer in the Sparger Region, in: Østergaard, K., Sørensen, A. (Eds.), Proceedings of the Fifth Engineering Foundation Conference on Fluidization, (Elsinore, Denmark), Engineering Foundation, New York, pp. 47–54.

Dubrawski, K., Bi, H.T., Chaouki, J., Ellis, N., Grace, J.R., Kantzas, A., Lim, C., Patience, G.S., Pugsley, T., Zhu, J.X., 2011. Comparison of Invasive and Non-invasive Fluidization Hydrodynamic Measurement Techniques. (manuscript in preparation 2011).

Gbordzoe, E.A.M., Bergougnou, M.A., 1990. Mass Transfer from a Central Jet Introduced into a Large Two-dimensional Fluidized Bed. Powder Technology 62, 67–75.

Guo, Q., Yue, G., Zhang, J., Liu, Z., 2001b. Hydrodynamic Characteristics of a Two-dimensional Jetting Fluidised Bed with Binary Mixtures. Chemical Engineering Science 56, 4685–4694.

Guo, Q., Si, C., Zhang, J., 2010. Flow Characteristics in a Jetting Fluidized Bed with Acoustic Assistance. Industrial & Engineering Chemistry Research 49, 7638–7645.

Hirsan, I., Sishtla, C., Knowlton, T.M., 1980. The Effect of Bed and Jet Parameters on Vertical Jet Penetration Length in Gas Fluidized Beds. Paper presented at 73rd Annual AIChE Meeting (Chicago, Illinois, USA), AIChE.

Hong, R., Li, H., Cheng, M., Zhang, J., 1996. Numerical Simulation and Verification of a Gas–Solid Jet Fluidized Bed. Powder Technology 87, 73–81.

Hong, R., Li, H., Li, H., Wang, Y., 1997. Studies on the Inclined Jet Penetration Length in a Gas–Solid Fluidized Bed. Powder Technology 92, 205–212.

Hutchenson, K.W., La Marca, C., Patience, G.S., Laviolette, J.-P., Bockrath, R.E.,2010. Parametric Study of n-butane Oxidation in a Circulating Fluidized Bed Reactor, Applied Catalysis A: General 376, 91–103.

Luo, G., Zhang, J.-Y., Guo, Q., Zhang, B., 1999. Study on Jet Flow from Two Vertical Nozzles in a 500 mm I.D. Semi-circular Fluidized Bed. Chemical Engineering & Technology 22, 247–251.

McNeil, K.M., Hancock II, A.W., Zenz, F.A., 1984. Flow Phenomena in a Two-dimensional Fluidized Bed, Powder Technology 38, 101–105.

Merry, J.M.D., 1971. Penetration of a Horizontal Gas Jet into a Fluidized Bed. Transactions of the Institution of Chemical Engineers 49, 189–195.

Merry, J.M.D., 1975. Penetration of Vertical Jets into Fluidized Beds. AIChE Journal 21, 507–510.

Molodtsof, Y., Labidi, F., 1995. Jets in Fluidized Beds: Flow Structure and Gas Mixing, in: Large, J.F., Laguérie, C. (Eds.), Proceedings of the Eighth Engineering Foundation Conference on Fluidization, (Tours, France), Engineering Foundation, New York, pp. 279–285.

Müller, C.R., Holland, D.J., Davidson, J.F., Dennis, J.S., Gladden, L.F., Hayhurst, A.N., Mantle, M.D., Sederman, A.J., 2009. Geometrical and Hydrodynamical Study of Gas Jets in Packed and Fluidized Beds Using Magnetic Resonance. The Canadian Journal of Chemical Engineering 87, 517–525.

Musmarra, D., 2000. Influence of Particle Size and Density on the Jet Penetration Length in Gas Fluidized Beds. Industrial & Engineering Chemistry Research 39, 2612–2617.

Patience, G.S., Bockrath, R.E., 2010. Butane Oxidation Process Development in a Circulating Fluidized Bed. Applied Catalysis A: General 376, 4–12.

Pell, M., 1990. Gas Fluidization, Elsevier, Amsterdam.

Pore, M., Holland, D.J., Chandrasekera, T.C., Müller, C.R., Sederman, A.J., Dennis, J.S., Gladden, L.F., Davidson, J.F., 2010. Magnetic Resonance Studies of a Gas–Solids Fluidised Bed: Jet–Jet and Jet–Wall Interactions. Particuology 8, 617–622.

Rowe, P.N., MacGillivray, H.J., Cheesman, D.J., 1979. Gas Discharge from an Orifice into a Gas Fluidised Bed. Transactions of the Institution of Chemical Engineers 57, 194–199.

Shen, Z., Briens, C.L., Bergougnou, M.A., Kwauk, M., 1991. Jet Presence Probability in a Two-dimensional Fluidized Bed. Powder Technology 67, 93–101.

Sotudeh-Gharebaagh, R., 1998. Combustion of Natural Gas in a Turbulent Fluidized Bed Reactor, PhD Thesis, École Polytechnique de Montréal, Montréal, QC, Canada.

Sotudeh-Gharebaagh, R., Chaouki, J., 2000. Gas Mixing in a Turbulent Fluidized Bed Reactor. The Canadian Journal of Chemical Engineering 78, 65–74.

Vaccaro, S., Musmarra, D., Petrecca, M., 1997b. A Technique for Measurement of the Jet Penetration Height in Fluidized Beds by Pressure Signal Analysis. Powder Technology 92, 223–231.

Wang, C.H., Zhong, Z.P., Li, R., E, J.Q., 2010. Prediction of Jet Penetration Depth Based on Least Square Support Vector Machine. Powder Technology 203, 404–411.

Wen, C.Y., Deole, N.R., Chen, L.H., 1982. A Study of Jets in a Three-dimensional Gas Fluidized Bed. Powder Technology 31, 175–184.

Xuereb, C., Laguérie, C., Baron, T., 1991a. Étude du comportement des jets continus horizontaux ou inclinés introduits dans un lit fluidisé par un gaz, I: Morphologie des jets. Powder Technology 67, 43–56.

Yang, W.-C., 1981. Jet Penetration in a Pressurized Fluidized Bed. Industrial & Engineering Chemistry Fundamentals 20, 297–300.

Yang, W.-C., Keairns, D.L., 1979. Estimating the Jet Penetration Depth of Multiple Vertical Grid Jets. Industrial & Engineering Chemistry Fundamentals 18, 317–320.

Yates, J.G., Bejcek, V., Cheesman, D.J., 1986. Jet Penetration into Fluidized Beds at Elevated Pressures, in: Østergaard, K., Sørensen, A. (Eds.), Proceedings of the Fifth Engineering Foundation Conference on Fluidization, (Elsinore, Denmark), Engineering Foundation, New York, pp. 79–86.

Yates, J.G., Cobbinah, S.S., Cheesman, D.J., Jordan, S.P., 1991. Particle Attrition in Fluidized Beds Containing Opposing Jets. AIChE Symposium Series 87, 13–19.

Zenz, F.A., 1968. Bubble Formation and Grid Design. Institution of Chemical Engineers Symposium Series 30, 136–139.

Zhong, W., Zhang, M., 2005. Jet Penetration Depth in a Two-dimensional Spout–fluid Bed. Chemical Engineering Science 60, 315–327.

Table 4.1: Comparison between jet lengths obtained experimentally and calculated from selected correlations.

Author	Correlation	u_j (m/s)	Jet length (mm)	
			Cal.	Exp.
Downward nozzle				
Zenz (1968) Adapted from Fig. 3-1 in Pell (1990).	$\frac{L_{max}}{d_j} = \begin{cases} 0.1810z + 2.427 & \text{for } \rho_j u_j^2 \le 150 \text{ Pa} \\ 4.266\times10^{-2} z^3 - 0.4055z^2 + 1.032z + 2.979 & \text{for } 150 \text{ Pa} < \rho_j u_j^2 \le 1.5\times10^4 \text{ Pa} \\ 5.067z - 35.39 & \text{for } \rho_j u_j^2 > 1.5\times10^4 \text{ Pa} \end{cases}$ where $z = \ln\left(\rho_j u_j^2\right)$.	7 29 46	6 10 13	5 15 25
Yates et al. (1991)	$\frac{L_{max}}{d_j} = 2.8\left[\frac{\rho_j}{\left(\rho_p - \rho_j\right)} \cdot \frac{u_j^2}{g d_j}\right]^{0.4}$	7 29 46	7 22 32	5 15 25
Upward nozzle				
Hirsan et al. (1980)	$\frac{L_b}{d_j} = 26.6\left[\left(\frac{\rho_j}{\rho_p}\right)^2 \cdot \frac{u_j^2}{g d_p}\right]^{0.335} \left(\frac{U_g}{U_{cf}}\right)^{-0.24}$	0.5-2	0.7-1.9	15
Musmarra (2000)	$\frac{L_b}{d_j} = 3.0\left(\frac{u_j^2}{g d_j}\right)^{0.32} \left(\frac{\rho_j u_j d_p}{\mu_j}\right)^{-0.37} \left(\frac{\rho_j}{\rho_p}\right)^{-0.33} \left(\frac{d_p}{d_j}\right)^{0.24}$	0.5-2	48-70	15
Zenz (1968) Adapted from Fig. 3-1 in Pell (1990).	$\frac{L_{max}}{d_j} = \begin{cases} 0.1810z + 2.427 & \text{for } \rho_j u_j^2 \le 25 \text{ Pa} \\ 0.2882z^3 - 3.183z^2 + 11.71z - 11.34 & \text{for } 25 \text{ Pa} < \rho_j u_j^2 \le 1825\times10^4 \text{ Pa} \\ 12.66z - 75.90 & \text{for } \rho_j u_j^2 > 1825 \text{ Pa} \end{cases}$ where $z = \ln\left(\rho_j u_j^2\right)$.	15	10	15
Luo et al. (1999)	$\frac{L_{max}}{d_j} = 119\left(\frac{u_j^2}{g d_j}\right)^{0.18} \left(\frac{\rho_p u_j d_p^2}{\mu_j d_j}\right)^{-0.024} \left(\frac{\rho_j}{\rho_p}\right)^{0.49}$	15	31	15

Table 4.1: Comparison between jet lengths obtained experimentally and calculated from selected correlations (continued).

Author	Correlation	u_j (m/s)	Jet length (mm)	
			Cal.	Exp.
Upward nozzle (continued)				
Hirsan et al. (1980)	$\frac{L_{max}}{d_j} = 19.3\left[\left(\frac{\rho_j}{\rho_p}\right)^2 \cdot \frac{u_j^2}{g d_p}\right]^{0.415} \left(\frac{U_g}{U_{cf}}\right)^{-0.54}$	15	0.8	15
Yang (1981)	$\frac{L_{max}}{d_j} = 7.65\left(\frac{U_{cf,P=atm}}{U_{cf,P=P_g}} \cdot \frac{\rho_j}{\left(\rho_p - \rho_j\right)} \cdot \frac{u_j^2}{g d_j}\right)^{0.472}$	15	41	15
Guo et al. (2001b)	$\frac{L_{max}}{d_j} = \begin{cases} 19.18\left[\frac{\rho_j}{\left(\rho_p - \rho_j\right)} \cdot \frac{u_j^2}{g d_j}\right]^{0.2383} \left(\frac{U_g}{U_{mf}}\right)^{-0.3616} & \text{for } \frac{U_g}{U_{mf}} \le 2.5 \\ 11.52\left[\frac{\rho_j}{\left(\rho_p - \rho_j\right)} \cdot \frac{u_j^2}{g d_j}\right]^{0.1966} & \text{for } \frac{U_g}{U_{mf}} > 2.5 \end{cases}$	15	35	15
Horizontal nozzle				
Zenz (1968) Adapted from Fig. 3-1 in Pell (1990).	$\frac{L_{max}}{d_j} = \begin{cases} 0.1810z + 2.427 & \text{for } \rho_j u_j^2 \le 150 \text{ Pa} \\ 4.266\times10^{-2} z^3 - 0.4055z^2 + 1.032z + 2.979 & \text{for } 150 \text{ Pa} < \rho_j u_j^2 \le 1.5\times10^4 \text{ Pa} \\ 5.067z - 35.39 & \text{for } \rho_j u_j^2 > 1.5\times10^4 \text{ Pa} \end{cases}$ where $z = \ln\left(\rho_j u_j^2\right)$.	34	11	15
Merry (1971)	$\frac{L_{max}}{d_j} = 5.25\left(\frac{\rho_j}{\rho_p \bar{\varepsilon}_s} \cdot \frac{u_j^2}{g d_p}\right)^{0.4} \left(\frac{\rho_g}{\rho_p}\right)^{0.2} \left(\frac{d_p}{d_j}\right)^{0.2} - 4.5$	34	28	15

Table 4.1: Comparison between jet lengths obtained experimentally and calculated from selected correlations (continued).

Author	Correlation	u_j (m/s)	Jet length (mm)	
			Cal.	Exp.
Horizontal nozzle (continued)				
Benjelloun et al. (1991)	$\frac{L_{max}}{d_j} = 5.52\left[\frac{\rho_j}{\left(\rho_p - \rho_j\right)} \cdot \frac{u_j^2}{g d_j}\right]^{0.27}$	34	30	15
Hong et al. (1997)	$\frac{L_{max}}{d_j} = 1.64\times10^6\left(\frac{\rho_j}{\rho_p \bar{\varepsilon}_s} \cdot \frac{u_j^2}{g d_p}\right)^{0.327}\left(\frac{\rho_g}{\rho_p}\right)^{1.974}\left(\frac{d_p}{d_j}\right)^{-0.040}\left(\frac{\theta}{180°}+\frac{\pi}{2}\right)^{0.148}\left(\frac{H_j}{H_0}\right)^{0.028} - 3.8$ where horizontal $\Rightarrow \theta = 0°$.	34	31	15

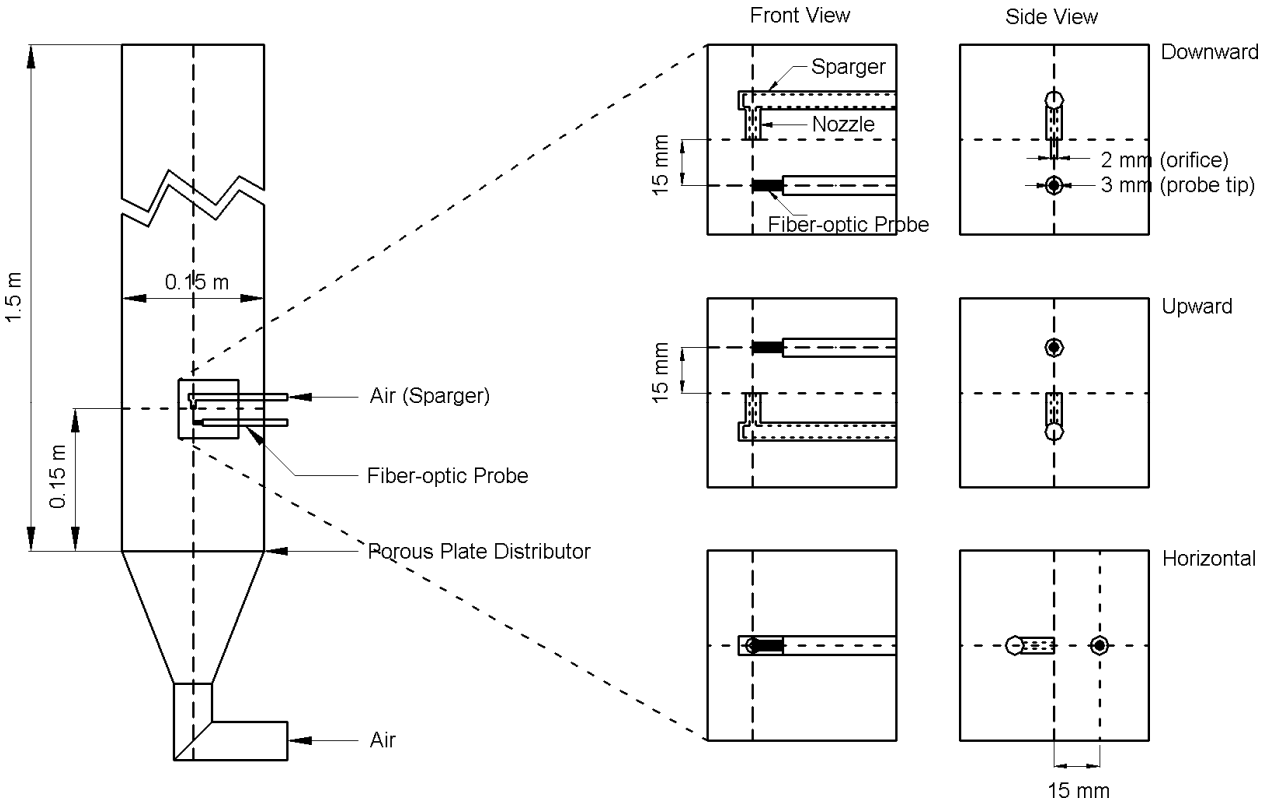

Figure 4-1: Schematic diagram of the experimental setup.

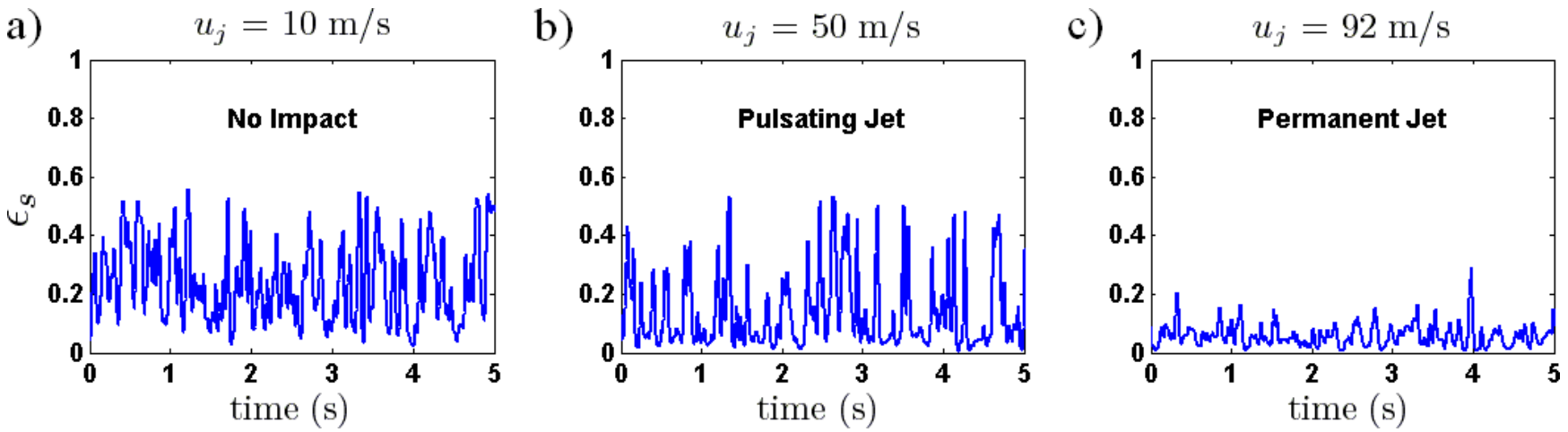

Figure 4-2: Typical signals of local particle holdup measured 15 mm downstream a downward oriented nozzle for different injection velocities.

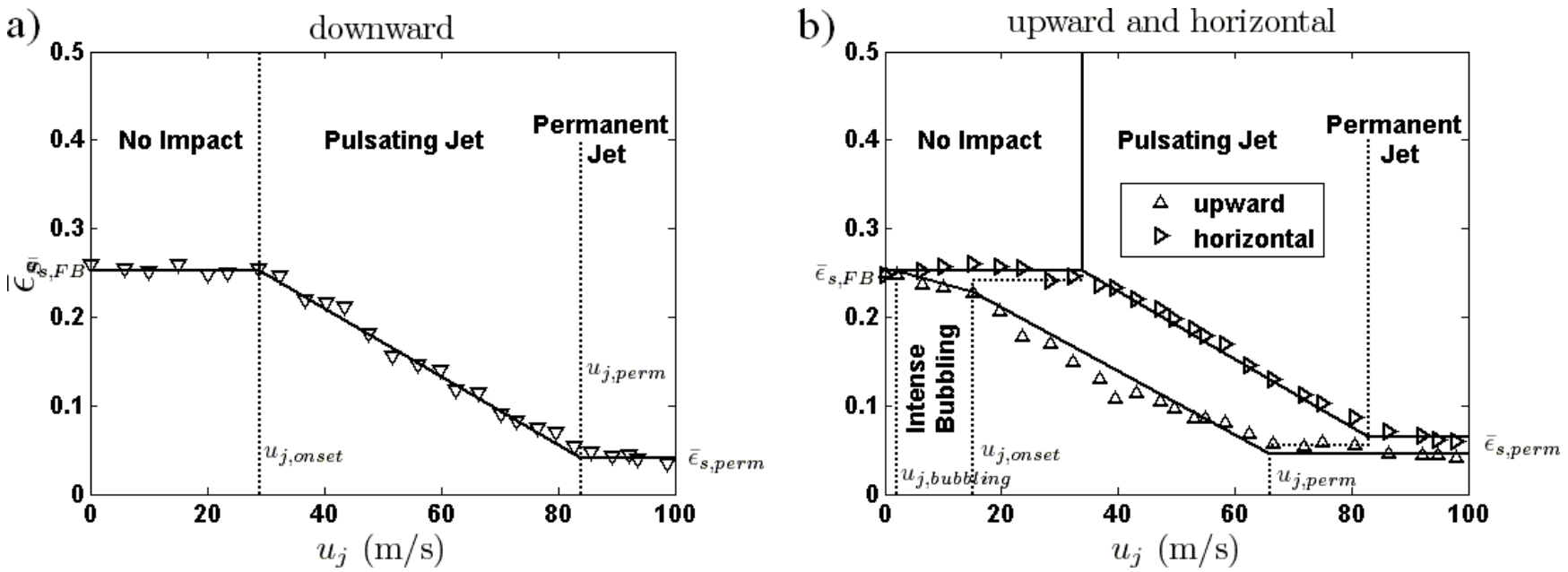

Figure 4-3: Average solid holdup versus injection velocity measured 15 mm downstream nozzle.

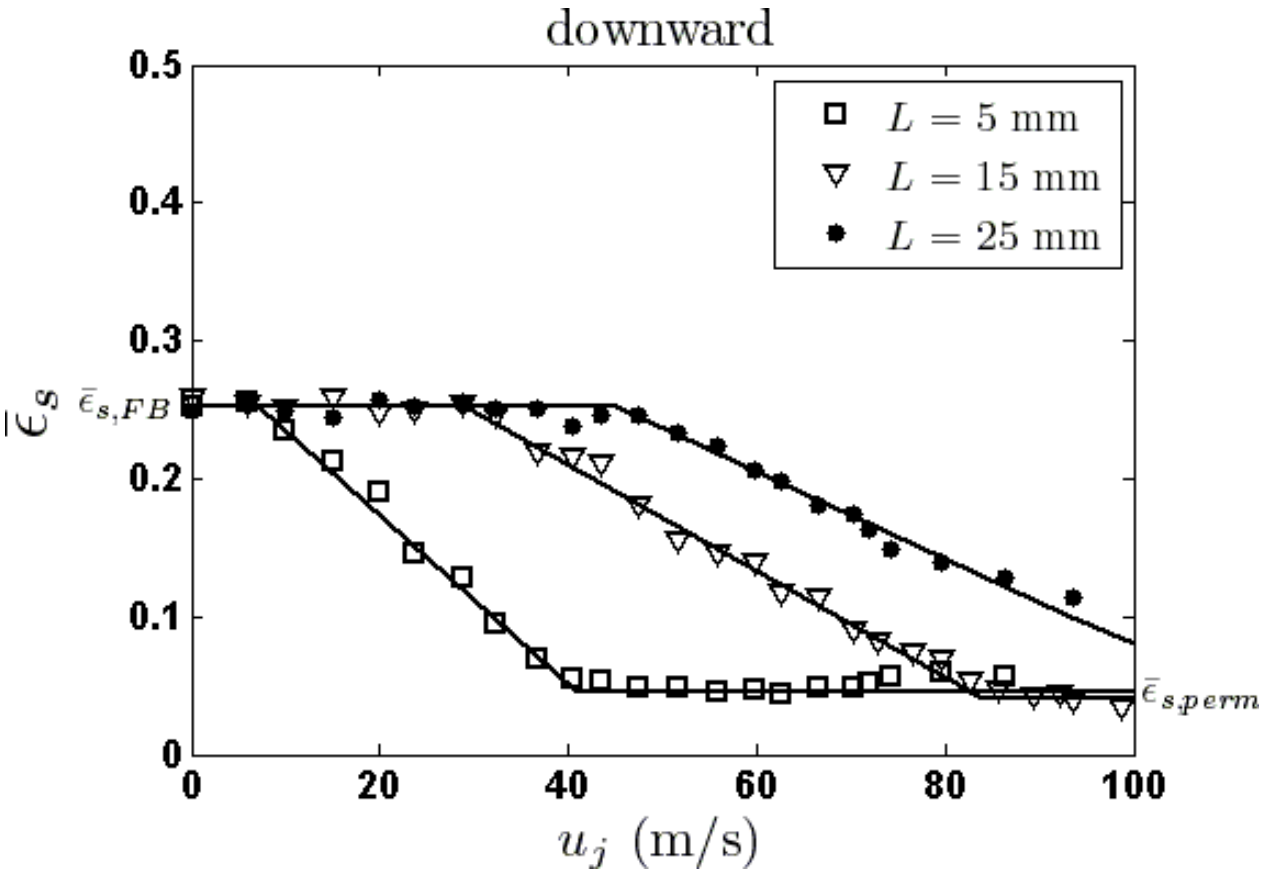

Figure 4-4: Influence of measurement distance from a downward oriented nozzle.

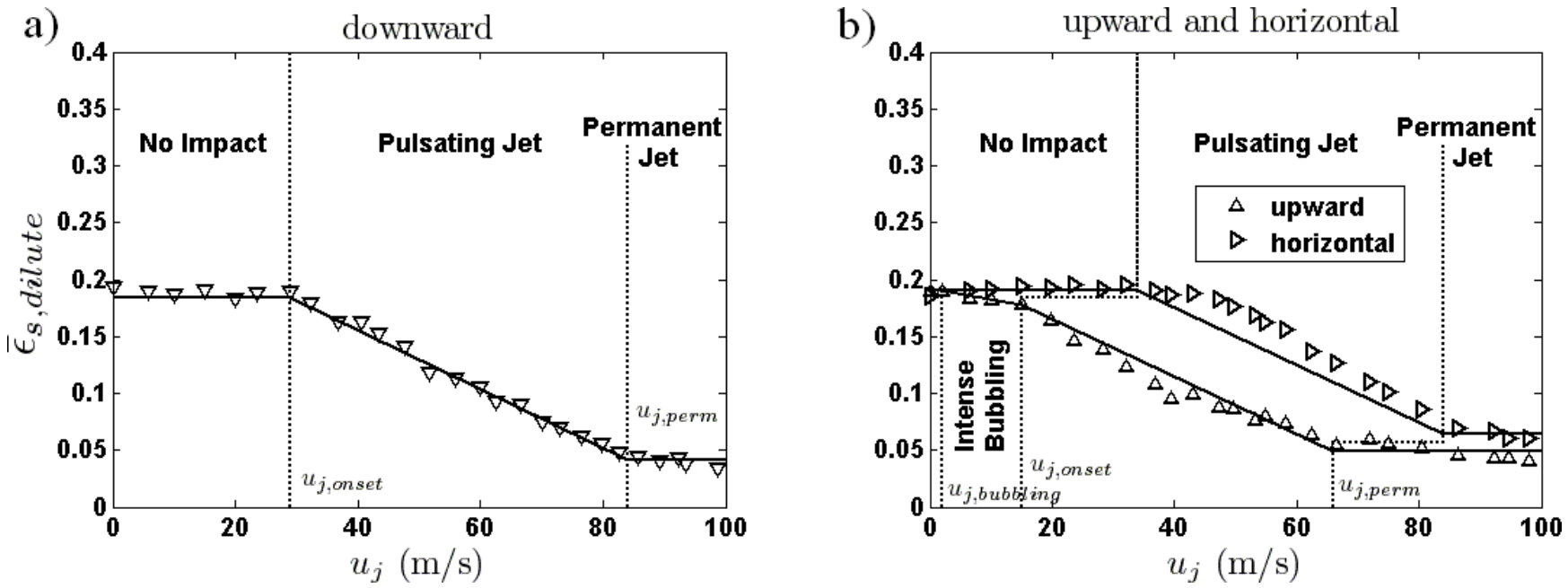

Figure 4-5: Effect of injection velocity on the average particle holdup in the dilute phase elements. Broken lines are plotted using the transition velocities determined in Fig. 4-3.

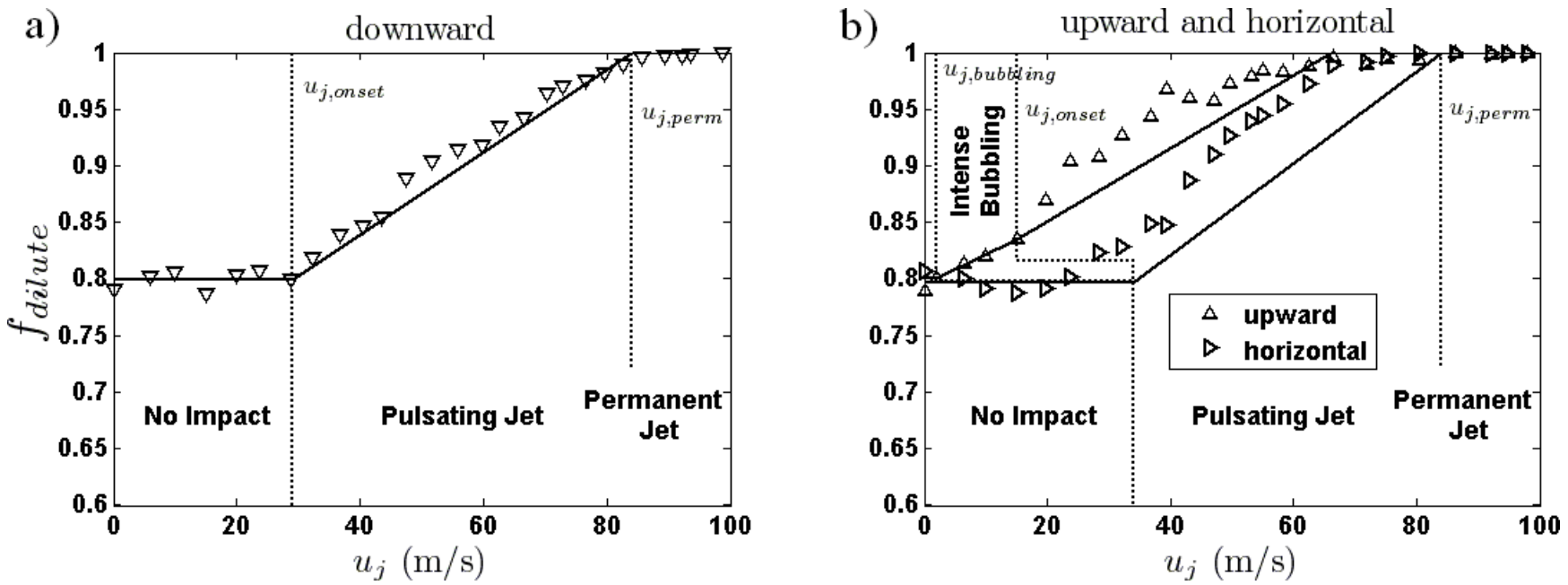

Figure 4-6: Evolution of the local dilute phase fraction as a function of injection velocity. Broken lines are plotted using the transition velocities determined in Fig. 4-3.

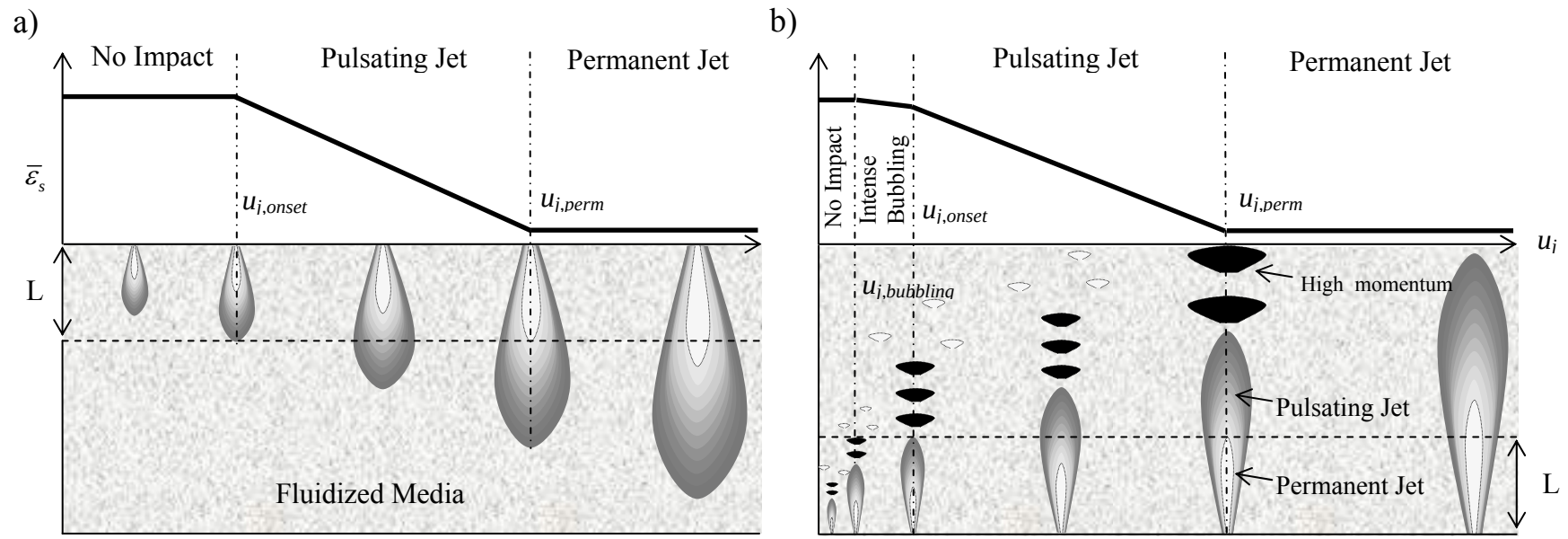

Figure 4-7: Analogy between reported flame-like gas-solid structure and observed particle holdup.

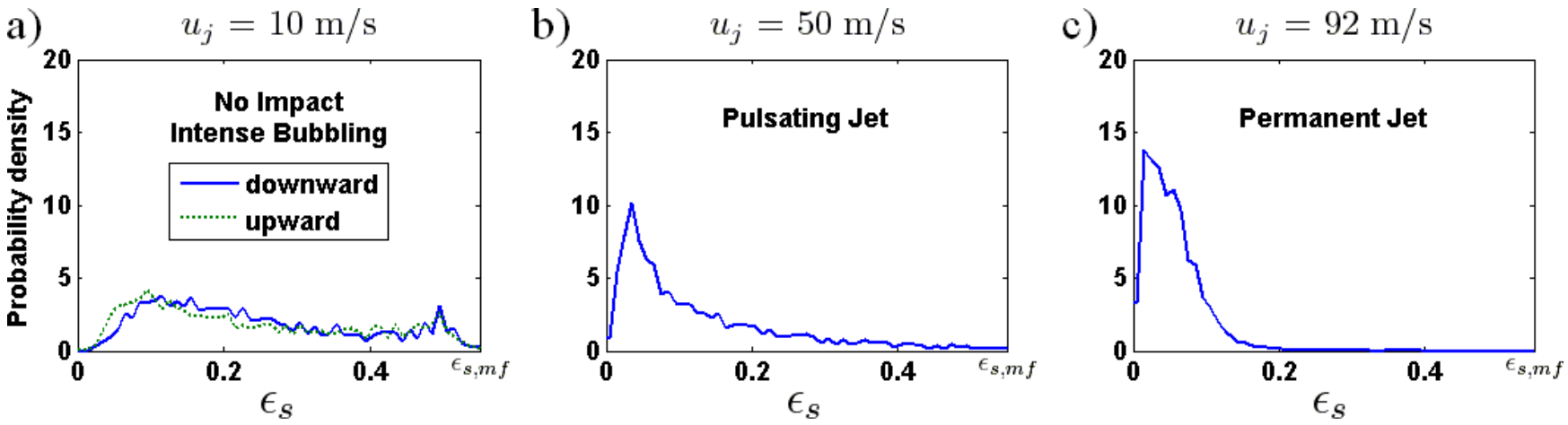

Figure 4-8: Probability distribution function of local particle holdup measured 15 mm downstream a downward oriented nozzle for different injection velocities.

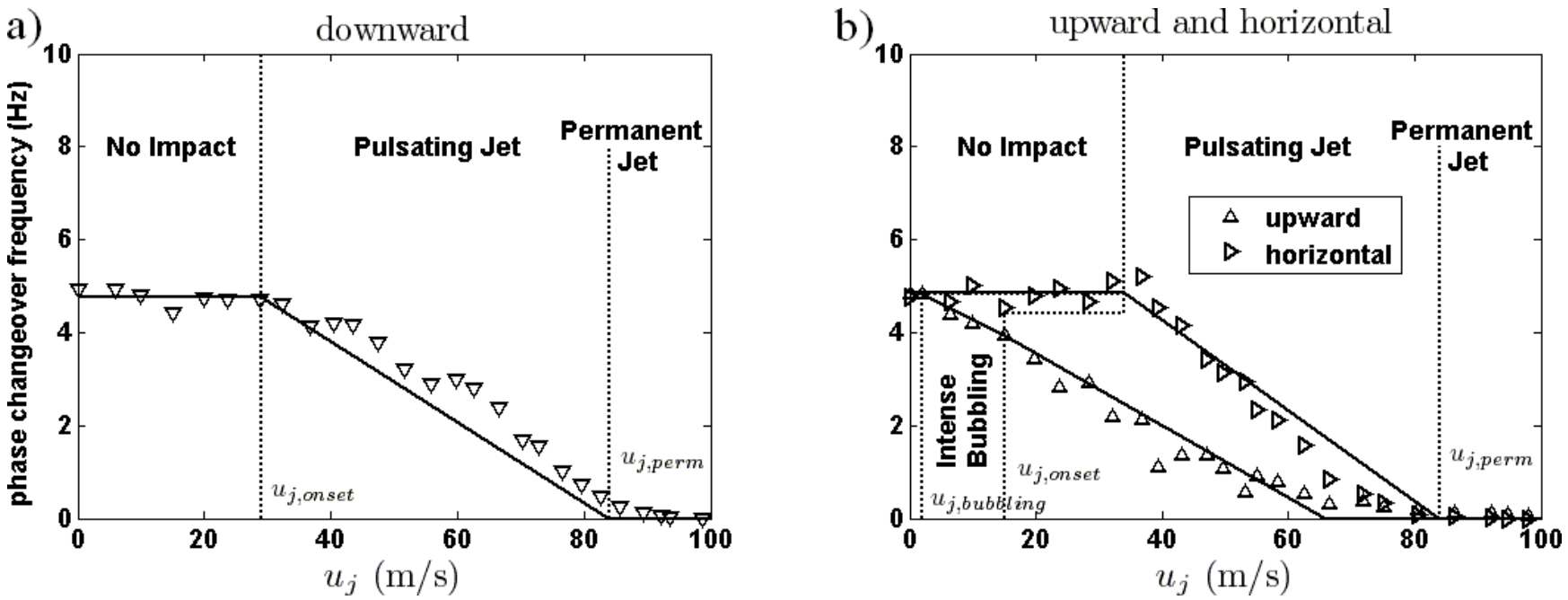

Figure 4-9: Phase changeover frequency as a function of injection velocity.

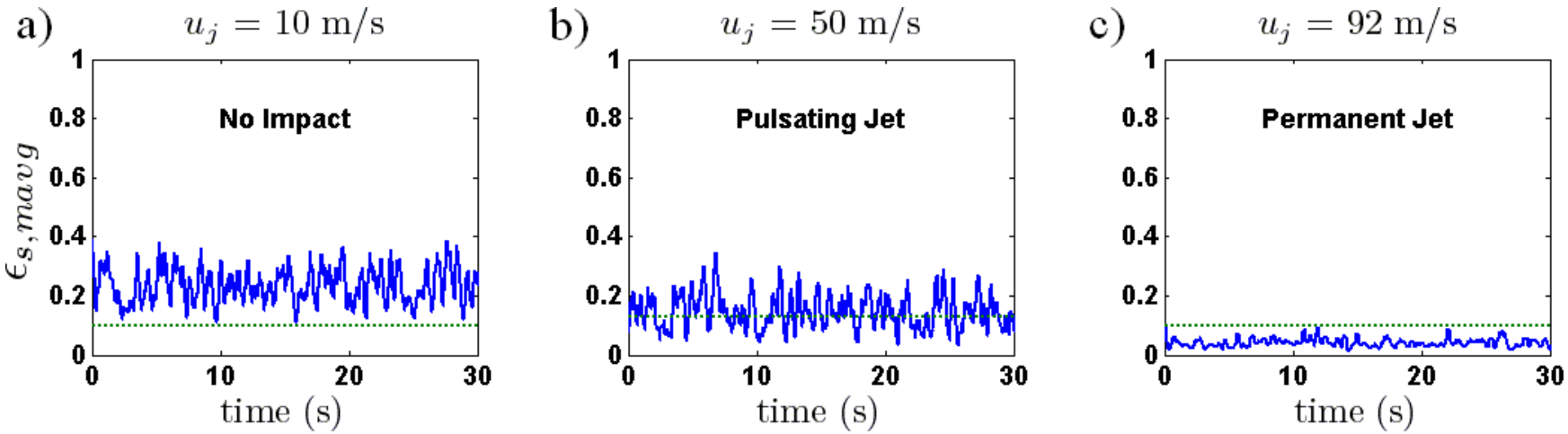

Figure 4-10: Distinction between fluidized bed and permanent jet behaviors.

CHAPITRE 5 ARTICLE 4: GAS JET PENETRATION LENGTHS FROM UPWARD AND DOWNWARD NOZZLES IN DENSE GAS–SOLID FLUIDIZED BEDS

Pierre Sauriol, Heping Cui and Jamal Chaouki

Department of Chemical Engineering, École Polytechnique de Montréal,

P.O. Box 6079, Station Centre-ville, Montréal, Québec, Canada, H3C 3A7

5.1 Abstract

The penetration lengths of gas jets issuing from upward and downward injection nozzles were measured in a dense fluidized bed of Geldart A to Geldart B particles, operated at superficial velocity well beyond the minimum bubbling velocity. Nozzle orientation, injection velocity and injected gas density were found to be the parameters having the most influence on the jet penetration lengths. Three distinct jet penetration lengths were determined with the upward nozzle: L_{min}, L_{max} and L_b, in accordance with Knowlton and Hirsan's definition, while with the downward nozzle, only L_{min} and L_{max} were observed.

The jet penetration lengths were correlated with respect to dimensionless groups in a systematic approach in an effort to identify the most important terms. For each nozzle orientation, the analysis yielded unique correlation format which could be applied to each characteristic jet length by changing the correlation parameters. Fundamental distinctions between the upward and downward nozzles were uncovered. The mechanism responsible for the jet momentum dissipation was found to be gravitational forces acting on the jet volume for the upward nozzle and drag forces exerted on the particles for the downward nozzle. Five new correlations were derived for the prediction of the characteristic jet lengths for upward and downward nozzles. The correlations retained for the upward nozzle were also found to be in good agreement with data from a high pressure fluidized bed.

Keywords: Fluidization; Hydrodynamics; Momentum transfer; Instrumentation; Jet penetration length; Correlation.

5.2 Introduction

In industrial fluidized bed reactors, the injection of gas-phase reactants through nozzles located downstream from the main distributor is common practice to avoid potentially explosive conditions and promote selectivity (Dry and Judd, 1986, Patience and Bockrath, 2010). The injection of gas high velocity gas through these nozzles can lead to the formation of so-called jets which are characterized by enhanced momentum, heat and mass transfer rates (Vaccaro et al., 1997). Entrainment of gas and solids from the fluidized bed into the high velocity jet can lead to the premature failure of the reactor due to particle attrition or erosion of bed internals (Knowlton and Hirsan, 1980). Jets can play a key role in the performance of the reactors, thus nozzle design requires serious consideration.

The jet penetration length is one of the key nozzle design parameters and several correlations have been proposed for its prediction (Benjelloun et al., 1990; Blake et al., 1990; Guo et al. 2001, 2010; Hirsan et al., 1980; Hong et al. 1997; Merry, 1975; Yang, 1981; Yates et al., 1991; Zenz, 1968). However, due to limitations in the experimental approaches, these correlations are often limited to a narrow validity window (e.g. near minimum fluidization velocity) and most have been developed for upward and horizontal nozzles. Furthermore, the jet length predicted by most correlations corresponds to L_{max}, a distance which is not sufficient to prevent jet erosion of bed internals. Knowlton and Hirsan (1980) have shown that high momentum bubbles issuing from the jet structure can penetrate the bed beyond L_{max} up to L_b, for which very few data and correlations have been reported. None of the correlations gathered from the literature and very few data targeted L_{min}, a distance of importance to the momentum, heat and mass transfer in the jet region, since it corresponds to the region with the greatest velocity difference between the jet and the fluidized bed.

Despite limitations in predicting the jet length from correlations, several studies have explored the impact of nozzle design and operating conditions. Every study encountered reported that the jet penetration lengths increase with the injection velocity and the injector diameter. The impact

of nozzle orientation has seldom been investigated systematically within a single study, but Zenz (1968) showed that downward and horizontal nozzles yield jets of similar length, typically three times shorter than for upward nozzles. Benjelloun et al. (1991) and Wang et al. (2010) have shown that the injection of denser gases yields longer jets, which is consistent with trends observed on pressurized fluidized beds (Knowlton and Hirsan, 1980; Yates et al., 1986). Systematic investigation of particle properties on the penetration length is rare due of the difficulty in obtaining particles differing only in the studied aspect. Hirsan et al. (1980) have shown that increases in particle density and diameter result in shorter jet lengths. It is generally reported that in excess of minimum fluidization velocity, an increase in superficial velocity results in shorter jet lengths (Chyang et al., 1997; Hirsan et al., 1980; Knowlton and Hirsan, 1980; Vaccaro et al. 1989; Wang et al. 2010; Xuereb et al., 1991; Yates et al. 1986) using Geldart B and D particles. Guo et al. (2010) recently showed that for FCC particles (Geldart A), an increase in superficial velocity, with U_g/U_{mf} between 1 and 2, presumably below U_{mb}, resulted in an increase in jet penetration length. Hong et al. (1997) and Zhong and Zhang (2005) and have shown that lowering the position of the injector relative to the bed surface and the initial bed height, even in laboratory-scaled fluidized beds, resulted in noticeably shorter jet lengths.

In a prior work, an experimental approach using a reflective fiber-optic probe to determine the local structure of a gas jet was proposed (Sauriol et al., 2011). The approach was suitable for dense fluidized beds operated at superficial velocities in excess of the minimum bubbling velocity (U_{mb}) and allowed for the determination of L_{min}, L_{max} and L_b. The present effort builds on this prior knowledge and attempts to highlight the impact of operating conditions on the jet penetration length for upward and downward nozzles.

5.3 Experimental Setup and Procedure

The experimental procedure used in the present study was developed in earlier work (Sauriol et al., 2011). For a given fiber-optic probe measurement position, located at a distance L downstream from the injector along the injection axis, plots of the average local solid holdup against injection velocity exhibit transition velocities indicative of one of four jet impact zones: 1) no impact; 2) intense bubbling; 3) pulsating jet; 4) permanent jet. To these transition velocities correspond a characteristic jet length: L_b, L_{max} and L_{min}.

The experimental apparatus consisted of a 152 mm ID by 1.5 m tall Plexiglas column mounted on a perforated plate distributor with 160 0.8 mm holes. The column was topped by a vertical acceleration section feeding into a cyclone which returned the entrained solids near the top of the column. The column was divided into three sections, 0.6, 0.6 and 0.3 m tall from bottom to top respectively. The middle section could be removed to allow direct access to the injector and fiber-optic probe located in the bottom section. The bottom section was equipped with an array of ports located along the axis with a 50 mm pitch.

The injector depicted in Fig. 5.1, consisted of an 80 mm long threaded shaft with a 0.8 mm ID. The shaft was welded near its top onto a 150 mm long 6.35 mm OD feeding tube. An 80 mm long sleeve with a 10 mm OD was screwed onto the shaft. Three interchangeable injection tips with 10 mm OD and 2.4, 4.9 and 7.2 mm orifices could be mounted onto the tip side of the sleeve. The sleeve could be adjusted so that the distance between the feeding tube and the injection tip covered a 75-140 mm span. This span was sufficient to cover the distance between two consecutive column ports, thus allowing a wide range of effective injection locations and measurement distances. The sleeve position was held in place with a lock nut. Adjustment of the injector location relative to the probe tip was made by first positioning the injector tip in contact with the probe tip either directly or indirectly by way of two calibrated gauges of 30 and 80 mm. From the point of contact, sleeve rotations were added or removed to achieve the desired distance. A distinct marking on the sleeve body allowed for an easy assessment of the number of rotations, with each rotation corresponding to a tip displacement of 1.06 mm. The injector could be mounted with the nozzle in the upward or downward orientation and was positioned along the centerline of the column. The tip of the injector was typically located between 0.15 and 0.30 m from the distributor.

Single bundle reflective-type fiber-optic probes were used for the local solid holdup measurements (also shown on Fig. 5.1). The probe body was a 6.35 mm OD tube and the probe tip consists of a 50 mm long 0.9 mm OD needle which was press-fit into the end of the probe body. A 2 mm OD protective sheath was affixed to the tip of the needle to provide support for a 1 mm-thick window which minimized the impact of the blind region on the solid holdup measurements (Cui et al., 2001). Despite the presence of a sheath, the more abrasive particles, coupled with the vicinity of a strong jet, could cause significant erosion of the sheath after as little as a week of continuous operation. A replacement probe was always available to limit the

down time. The effective measurement location was considered to correspond to the axis of the fiber-optic probe and thus the distances were corrected to account for the sheath radius. The tip of the fiber-optic probe was positioned 1 mm short of the injection axis so that its effective measurement volume coincided with the injection axis.

The solids used for the investigation were intended to cover heat carriers used in homogeneous combustion systems as well as common catalysts and are summarized in Table 5.1. The bed height at rest was varied between 0.2 and 0.75 m. The main fluidization gas, which consisted of dry air, was monitored by one of two rotameters covering a range of superficial velocities from 0.015 to 0.7 m/s. The injected gas consisted of air, helium, CO_2 or argon. CO_2 was used during the first series of runs, but difficulties in maintaining constant flow at the higher injection rates, due to the evaporative cooling of the CO_2, resulted in argon being preferred. The injection flow rate was monitored by one of four rotameters covering mass flow rates between 1.2×10^{-6} and 7.0×10^{-3} kg/s based on rotameter operating pressure between 0 and 2 atm (gauge) with dry air. The range of operating conditions covered in the present study is summarized in Table 5.2.

Static charges buildup was a concern during the runs. This was particularly true at the high injection velocities and with the coarser particles, and increased with the experimental time. To minimize the effect of static charges, the bottom section of the column was equipped with grounded copper wires along the inside wall and the probes and injector were also grounded. Furthermore, trace quantities of an ammonium compound were occasionally added to the bed material. Despite these measures, the impact of static charges, although significantly reduced, could still be noticed during some of the runs.

5.4 Results

The experimental data were divided into 5 sub-sets according to the injection orientation and the characteristic jet length. The injection of gas in the upward orientation leads to three distinct transition velocities: $u_{j,bubbling}$, $u_{j,onset}$ and $u_{j,perm}$, corresponding respectively to $L = L_b$; $L = L_{max}$ and $L = L_{min}$, whereas the downward orientation leads to two transition velocities $u_{j,onset}$ and $u_{j,perm}$, corresponding respectively to $L = L_{max}$ and $L = L_{min}$. The data sub-sets were analyzed to highlight the general trends that existed between the operating parameters and observed jet penetration lengths. Within the range of operating parameters, nozzle orientation,

injection velocity and injected gas density were found to be the top contributing parameters to the jet penetration lengths. The influence of injector diameter appears to be important with the upward nozzle where an increase of injector diameter results in longer jet lengths, while no clear trend can be established for the downward nozzle. Particle diameter and density appear to exert more important effects with the downward nozzle, smaller particles and denser particles lead to shorter jet lengths, especially on L_{min}. Finally, increases in superficial velocity and bed height appear to reduce the jet penetration lengths. These trends will be further inspected in the following section in an effort to derive jet penetration length correlations from the experimental data.

During the experiments, a technical advantage of the downward nozzle became obvious when running with the coarser particles (Geldart B). Never once during the runs did the downward nozzle become blocked. On the other hand, while running at low injection velocities with the upward nozzle, nozzle blockage occurred in nearly 2 percent of the runs conducted with Geldart B particles.

5.5 Correlation

5.5.1 System Variables and Dimensionless Groups

An effort was made to correlate the experimental data to allow for the prediction of jet penetration lengths. The correlations are based on the nondimensionalization of injection and fluidized bed properties. It was assumed that the jet length ratio could be expressed as the product of dimensionless numbers. Given that the system is described by a set of 19 variables (L, d_j, d_p, ρ_p, ρ_g, ρ_j, u_j, U_g, U_{mb}, μ_g, μ_j, $P_{g,\infty}$, P_j, ε_{ref}, $\overline{\varepsilon}_g$, $\overline{\varepsilon}_s$, g, H_{ref}, H_j) involving 3 dimensions (mass, time, length), the Buckingham π theorem stipulates that as many as 16 independent dimensionless groups can be formed. Instead of defining that many dimensionless groups, the set was reduced by combining some of the variables to more sensible forms. This was the case of the bed height (H_0 or H_{mf}) and injection location (H_j) which were not included in the analysis as height H_j/H_{mf} or aspect ratios H_0/d_t, as proposed by Hong et al. (1997), and Zhong and Zhang (2005) respectively. The reason for not including such ratios is because of their limited range in the context of the present study and concerns when extrapolating to larger

geometries. Instead, it was preferred to define the bed pressure (P_g) as that of the bed at the position of the injector which indirectly accounts for the bed height and the injection location in accordance with Eq. (5.1). Thus the bed pressure effectively replaces four variables.

$$P_g = P_{g,\infty} + \rho_p \int_{H_j}^{H_{bed}} \left(1-\varepsilon_g\right) dH \approx P_{g,\infty} + \rho_p \left[H_{ref}\left(1-\varepsilon_{ref}\right) - H_j\left(1-\bar{\varepsilon}_g\right)\right] \tag{5.1}$$

From the remaining variables, and based on existing correlations found in the literature, dimensionless groups were defined for the analysis. It was noted from existing correlations that there is not a general consensus as to the length scaling factor to be used in the formulation of dimensionless groups; some authors have used particle diameter as well as injector diameter for both injection Reynolds and Froude numbers. One of the objectives of the present effort will be to look at the influence of this choice, not only on the Froude and Reynolds numbers but also on the jet length ratio, which so far has exclusively been looked at in terms of a L/d_j ratio, a default choice for single-phase systems but not necessarily for particulate systems. The key dimensionless groups considered are summarized in Table 5.3.

Analysis of the injection velocity data indicates that under some injection conditions choked flow was reached within the injector. When chocked flow is reached, the injection velocity is equal to that of the speed of sound and incremental mass flow out of the injector is the result of a proportional density (and pressure) increase. Consequently, when chocked flow occurs, the pressure difference between the injected gas and the gas in the fluidized bed at the same axial position is not zero and contributes to the momentum. Thus the momentum term included in the Froude numbers must be corrected to account for the pressure difference contribution. When sub-sonic flow exists, the pressure difference term is omitted.

5.5.2 Bed Voidage Estimate

Instead of relying on bed voidage measurements, which are not always available during the design phases, and for which good estimates are difficult to achieve due to correlation limitations, it was decided to standardize its estimate within the present effort. Comparison between bed voidage estimates and selected experimental data is presented in Fig. 5.2. It was first attempted to estimate the bed voidage and fluidized bed height from the simple two-phase model using the generalized bubble size model proposed by Choi et al. (1998). The results yielded by the model

were found to disagree with the experimental observations yielding average bed voidages that were lower than the measured values. An alternative approach proposed by Hilal and Gunn (2002), which yields an average solid holdup, was also considered. The approach developed for Geldart B particles yielded very high bed voidages, especially for the Geldart A particles in the range of velocities covered within the present study. For sake of comparison the simple correlation by King (1989) is included for FCC. Finally, a method loosely based on Zenz's dimensionless velocity-diameter plot was formulated. It is assumed that the average bed voidage increases exponentially with superficial velocity from minimum bubbling velocity (U_{mb}) to the transition to fast fluidization velocity (U_{se}), described by Eq. (5.2). Equation 5.2 shares similarities with the Richardson-Zaki equation. U_{se} is estimated from Eq. (5.3) (Abba, 2001). The average bed voidage at U_{se} is taken as 0.8 for Geldart A, 0.85 for Geldart AB and 0.9 for Geldart B particles. Experimental data collected during the experiments and those from the work of Dubransky et al. (2011) were in reasonable agreement with this simple estimator.

$$\bar{\varepsilon}_g = \varepsilon_{g,mb} + \left(\bar{\varepsilon}_{g,se} - \varepsilon_{g,mb}\right)\frac{\ln\left(U_g/U_{mb}\right)}{\ln\left(U_{se}/U_{mb}\right)} \tag{5.2}$$

$$Re_{se} = \frac{\rho_g U_{se} d_p}{\mu_g} = 1.68 Ar^{0.469} \tag{5.3}$$

5.5.3 Formulating a Correlation

A systematic way of determining the most relevant dimensionless groups was followed. The procedure consisted in ranking the various dimensionless groups with respect to their ability to describe the experimental data on their own (e.g. $L/x = C\left(\pi\right)^{\alpha}$) and then, considering the most relevant groups as starting points, the correlations were refined by adding other groups and assessing their impact on the prediction quality. An effort was made to limit the total number of dimensionless groups involved in the correlations. For instance, it was found that the injection two-phase Froude number yielded nearly the same results as the triplet of the injection single-phase Froude number, injected gas-to-solid density ratio and average solid holdup, thus the injection two-phase Froude number was preferred. The effort was repeated for all five data sub-sets.

For the upward nozzle, two correlation formats were found to be acceptable for all three characteristic jet lengths. Eq. (5.4) yields a marginally better agreement with the experimental data than Eq. (5.5), but counts one more dimensionless group, both formats will be considered for analysis. The resulting correlation parameters are summarized in Table 5.4.

$$\text{Upward: } \frac{L}{d_j} = C\left(Fr_{2,j}\right)^{\alpha_1}\left(Re_g\right)^{\alpha_2}\left(Ar_g\right)^{\alpha_3} \tag{5.4}$$

$$\text{Upward: } \frac{L}{d_j} = C\left(Fr_{2,j}\right)^{\alpha_1}\left(\frac{U_g}{U_{mb}}\right)^{\alpha_2} \tag{5.5}$$

The correlations for the upward nozzle based on the Eq. (5.4) are similar for all characteristic jet lengths, the major difference being the constant and the exponent affected with the Froude number. The exponents expressing the dependency with respect to the fluidized bed Reynolds number is found to be nearly constant at -0.35 for every characteristic jet lengths. The negative value is consistent with the reported trends that the jet penetration lengths decrease with respect to superficial velocity. As for the Archimedes number, its coefficient nearly constant at 0.25 is consistent with the reported trends that larger particles which are less mobile yield higher penetration lengths. The observed trends for the correlations based on Eq. (5.5) are similar with respect to the Froude number. The negative exponent of the fluidized bed velocity ratio is consistent with the trends that jet penetration length decrease with increasing superficial velocity. At the same time, the denominator shares similarities with the Archimedes number used in Eq. (5.4). It is an indication of the ease with which particles are fluidized and may get entrained in the jet.

For the downward nozzle, Eq. (5.6) was found to be the most adequate correlation format for both characteristic jet lengths. The resulting correlation parameters are summarized in Table 5.4.

$$\text{Downward: } \frac{L}{d_p} = C\left(\frac{\rho_j}{\rho_p}\cdot Fr_{1,p}\right)^{\alpha_1}\left(Ar_g\right)^{\alpha_2}\left(\frac{U_g}{U_{mb}}\right)^{\alpha_3} \tag{5.6}$$

It should be noted that the present formulation uses the particle diameter as the length scaling factor in the jet length ratio and the Froude number, however, the Froude term alone is not sufficient to describe adequately the jet length ratio when using the particle diameter as the length scaling factor. When used alone, the coefficient of determination (R^2) is found to be close to 0.6,

while using the injector diameter as the length scaling factor yields coefficient of determination near 0.8. However, when the Archimedes number is combined to the Froude number with the particle diameter as length scaling factor, the coefficient of determination reaches 0.9, a value that cannot be surpassed when working with the injector diameter as the scaling factor despite the introduction of more terms, such as in Eq. (5.4). The highest coefficient of determination obtained with the injector diameter as length scaling factor is 0.85, while that obtained from Eq. (5.6) is 0.93 in L_{min} and 0.91 in L_{max}.

The correlations for the downward nozzle based on Eq. (5.6) are consistent with observation that the injection velocity results in longer jet lengths. The fluidization velocity ratio is found to have an influence on L_{min} in similar proportions to what was found with the upward nozzles based on Eq. (5.5). Its influence on L_{max} however is very small but in the opposite direction. Note that based on the present experimental data, the injector diameter and the solid holdup do not appear to have significant effects on the downward jet penetration.

5.5.4 Physical Meaning Behind the Correlations

The correlations formulated in the previous have been developed purely with the statistical objective of maximizing the coefficient of determination while keeping the overall number of dimensionless numbers as low as possible. Three formulations described were retained. There exists a significant difference in the choice of length scaling factor used between the proposed upward and downward nozzle correlations. These observations suggest that the mechanism responsible for the jet momentum dissipation is fundamentally different according to the jet orientation. The injector diameter as length scaling factor in the upward correlations suggests that buoyancy forces account for the jet momentum dissipation which can be derived from Turner's theory of buoyant fluids (Guo et al., 2001; Zhong and Zhang, 2005). The particle diameter as length scaling factor in the downward correlations suggests that the drag forces exerted on the entrained particles are responsible for the jet momentum dissipation (Merry, 1971). In his analysis Merry, considered that at the jet boundary the momentum was attributable to the solid traveling at the terminal velocity, which resulted in an additional dependency with respect to the density ratio, such as found in the correlations of Hirsan et al. (1980) (density ratio to the power 2) and Merry 1975 (density ratio to the power 1.5). No such dependency was found

herein (density ratio to the power 1), this is more consistent with the boundary conditions being the equilibrium between an immobile particle and the entrained fluidized bed gas moving at the terminal velocity. This assumption can be used to write

$$\frac{L}{x} \propto \left(\frac{\rho_j u_j^2}{\rho_g u_{t,g}^2} \right)^{\alpha} \tag{5.7}$$

Considering Stokes law, the terminal velocity term is found to be

$$u_{t,g}^2 \propto \frac{\left(\rho_p - \rho_g\right)}{\rho_g} \cdot g d_p Ar_g \tag{5.8}$$

thus yielding the jet length ratio

$$\frac{L}{x} \propto \left[\frac{\rho_j}{\left(\rho_p - \rho_g\right)} \cdot \frac{u_j^2}{g d_p Ar_g} \right]^{\alpha} \approx \left(\frac{\rho_j}{\rho_p} \cdot \frac{u_j^2}{g d_p Ar_g} \right)^{\alpha} = \left(\frac{\rho_j}{\rho_p} \cdot Fr_{1,p} \right)^{\alpha} \left(Ar_g \right)^{-\alpha}. \tag{5.9}$$

This is consistent with the two first terms of Eq. (5.6), to which more flexibility given with respect to the Archimedes number. The negative exponent associated with the Archimedes number in Eq. (5.9) is also found in Table 5.4.

5.5.5 Comparison with Existing Correlations

The new correlations proposed are compared with selected correlations from the literature (refer to Table 5.5) and the experimental data. Due to the lack of correlations developed for downward nozzles, correlations intended for horizontal nozzles are used for comparison, as they have been found in the past to be of similar magnitude (Pell, 1990; Zenz, 1968). Note that Zenz's correlations were converted to kg-m-s and extended, using Fig. 3-1 from Pell (1990), to cover a wider range of $\rho_j u_j^2$, otherwise in their usual form the correlations are typically limited to $\rho_j u_j^2$ greater than 1825 Pa for upward nozzles and greater than 1.5×10^4 Pa for downward and horizontal nozzles. Aside from Zenz's correlations, all other selected correlations use dimensionless groups. The dominant group which accounts for the injection velocity is a Froude number. Most correlations use the injector diameter as the length scaling factor while the correlations of Hirsan et al., Hong et al., and Merry use the particle diameter. The correlation by Hirsan et al. also differs in that the Froude number contains the density ratio to the power 2.

5.5.5.1 Upward Nozzle

The results for the upward nozzle are presented in Fig. 5.3-5.5. The abscissa corresponds to the jet length predicted according to Eq. (5.4) and the ordinates present experimental data (not presented in Fig. 5.4 so not to overload) and predictions made with correlations reported in the literature. As can be seen in Fig. 5.3 and 5.5, the experimental data is typically spread along constant L/d_j, this is a result of the experimental approach where the distance between the probe and injector is set and the transition velocity determined. For a given set of distance, particle and injector diameter to which correspond constant L/d_j and L/d_p, several runs are performed varying the other operating parameters (e.g. injected gas, superficial velocity, bed height). The correlation of the experimental data was typically better than ±30% for L_{min}, better than ±40% for L_{max} and better than ±50% for L_b. This was also the case for predictions made by Eq. (5.5) which is found to lie within ±5% of the predictions made with Eq. (5.4).

Due to lack of existing correlation based on L_{min}, the data of Knowlton and Hirsan (1980) was used to adapt the correlations proposed by Hirsan et al. and Yang (refer to Table 5.5) so to describe Knowlton and Hirsan's L_{min} data. The Yang-type and the Hirsan-type fit of L_{min} yield jet penetration lengths that deviate in two different directions when compared with the present data set, even though derived from the same experimental data. The Hirsan-type fit appears slightly more spread out but with a nearly constant offset corresponding to a factor 5. This would be consistent with excessive weight being given to the gas density term in the Hirsan-type fit. As for the Yang-type fit, the slope observed is slightly more important than what is described by experimental data. It is believed that the inclusion of the pressure correction terms within the group formed by the Froude number as resulted in slightly higher dependencies with respect to the injection velocity. Since the Froude number is the dominant dimensionless group affecting the jet penetration length, the higher coefficient in the Yang-type fit yields a noticeably steeper slope.

As was the case with L_{min}, Hirsan et al.'s correlation of L_{max} (Fig. 5.4) yields jet penetration lengths that are systematically low by a factor 5 and Yang's correlation shows a steeper slope than the experimental data, but with some degree of agreement with the experimental data for L_{max}/d_j below 10. The correlations by Zenz, Blake et al., and Guo et al. show increasingly good

agreement with the experimental data when L_{max}/d_j exceeds 10. At L_{max}/d_j below 10, the extended part of Zenz's correlation ($\rho_j u_j^2$ < 1825 Pa) yields what appears to be a plateau which does not agree with the experimental trends or what is predicted by any other correlations. The trends observed for L_b (Fig. 5.5) are consistent with what was previously described for L_{min} and L_{max} with respect to Hirsan's correlation. The Yang-type fit is however showing relatively good agreement with the experimental data although, on average, the predictions are 25% larger than the current experimental data and slightly more spread out.

Under the test conditions covered herein, the two types of correlations proposed (Eq. 5.4 and Eq. 5.5) appear equivalent and fairly good within the tested conditions. However, it was made obvious from comparing the correlations of Hirsan et al. and Yang, that good agreement is not guaranteed when extrapolating to different conditions. To assess how well the proposed correlations handle out of range conditions, they were compared with the experimental data of Knowlton and Hirsan (1980) which cover operating pressures ranging from 3 to 50 atmospheres. The results are presented in Fig. 5.6-5.8. It is evident from the results that the correlations described by Eq. (5.4) do not extrapolate well to high pressure conditions. They are typically lower by a factor 4 in L_{min}, 3 in L_{max} and 2 in L_b. The reason for the underprediction of the correlations based on Eq. (5.4) is because of the weight given to the gas density in the fluidized bed (ρ_g) via the Reynolds and the Archimedes numbers. Under the current test conditions, the gas density in the fluidized bed was kept nearly constant (1.2–1.3 kg/m^3) and did not play a significant role; while it was varied between 5 and 60 kg/m^3 in Knowlton and Hirsan's work. The correlations based on Eq. (5.5), the predicted values of L_{min} and L_{max} are typically in good agreement with the experimental data at the lower end of the L/d_j, while at the higher end, the jet penetration length become undervalued for gas-to-particle density ratio (ρ_g/ρ_p) above 100. In L_b, the predictions based on Eq. (5.5) follow the same trend (tailing off at density ratios above 100). However, the values are higher at the bottom end and fall in agreement with the experimental data at the upper end.

5.5.5.2 Downward Nozzle

The results for the downward nozzle are presented in Fig. 5.9 and 5.10. As no other source of data or correlations for L_{min} (Fig. 5.9) was identified, only the experimental data is presented against the correlation based on Eq. (5.6).

As for L_{max} (Fig. 5.10), most correlations yield jet length predictions that are spread out due to their representation on an L_{max}/d_p basis from their original L_{max}/d_j formulation. In general, the correlations lead to several parallel lines corresponding to the different particle sizes. Only Yates et al. (1991) specifically studied downward nozzles, but they limited their investigation to one type of particle which prevents any comparison with respect to the influence of the particle size. The correlation of Hong et al. includes a term to account for the injection angle, in the present case, a value of -90° corresponding to a downward nozzle was used even thought the correlation was developed with smaller angles. The correlations of Hong et al. and Merry, both of which use the particle diameter as the Froude length scaling factor, include a subtracted constant that can yield small and even negative jet lengths. The influence of the subtracted constant can be observed up to L_{max}/d_p in excess of 200 and does not agree with the experimental trends. The correlations of Benjelloun et al., Yates et al. and Zenz exhibit slopes that are parallel to and in modest agreement with the experimental data. Of the compared correlations, that of Yates et al. is the one that agrees the most with the experimental data, despite yielding jet penetration lengths that are typically 50% longer.

Lack of complementary data for dissimilar conditions such as elevated pressure and temperature, prevents from further validating the proposed correlations as was achieved with the upward nozzles.

5.5.6 Comments about the proposed correlation of L_{min}, L_{max} and L_b

Based on the present effort, it was found that the correlation of data was better for L_{min} (typically better than ±30%) followed by L_{max} (±40%) and L_b (±50%). The measurement accuracy of each type of jet penetration lengths can account for some of the variability, however, during the experimental work, it was found that the relative uncertainty in the determination of $u_{j,perm}$

(associated with L_{min}) was greater than that of $u_{j,bubbling}$ (L_b) and $u_{j,onset}$ (L_{max}), which on its own should have resulted in a greater spread in L_{min}. A potential explanation is based on the jet definitions given by Rowe et al. (1979) and Knowlton and Hirsan (1980). The length corresponding to L_{min} is generally described as a flamelike void, while between L_{min} and L_{max} the jet is described as a series of rapidly rising bubbles (Rowe et al.) with periodic necking (Knowlton and Hirsan). As for L_b, Knowlton and Hirsan introduced it as the deepest point where bubbles issuing from the jet penetrated the bed seemingly undisturbed by the bed material after they have detached from the jet. Given these descriptions, it would be expected that more complex mechanisms are involved in the description of L_{max} and L_b than for L_{min}. In addition to the initial rapid momentum dissipation described by L_{min}, L_{max} should involve considerations about jet bubbles interactions and L_b should involve bubble-bed interactions. Since these mechanisms are distinct and act upon the injected gas in a consecutive manner, by relying on a correlation which involves a single product, all mechanisms get lumped together which could explain the observed evolution of the spread in the different types of jet penetration lengths.

5.6 Conclusions

A recently proposed approach relying on the use of a fiber-optic probe was used with satisfactory results at superficial velocities in excess of the minimum bubbling velocity. The evolution of the average particle holdup measured in a fixed location downstream of the injector nozzle during an injection velocity sweep, allowed for the determination of transition velocities corresponding to L_{min}, L_{max} and L_b from a single run. The data confirmed that with the upward nozzle, the three characteristic jet penetration lengths exist, while with the downward nozzle, only L_{min} and L_{max} were observed.

The most influent parameters affecting the jet penetration length were found to be the nozzle orientation, the injection velocity and the injected gas density. Other operating parameters such as particle density, superficial gas velocity and injector diameter. A simple approach to estimate the average bed voidage was proposed. This average voidage was used to account for effects of superficial velocity. The average voidage was used to determine the pressure at the injection

location which depends on the solid properties but also the initial bed height and injection location.

The jet penetration data was correlated against the experimental data from the present study. The better correlations all involved the use of two-phase Froude numbers to which complementary terms describing the state of the fluidized bed were added. Based on the length scaling factor required in the Froude number, it was postulated that the mechanism responsible for momentum dissipation differs according to the nozzle orientation. With the upward nozzle, the jet momentum dissipation is dominated by gravitational forces acting on the jet volume; with the downward nozzle, jet momentum dissipation is caused by drag forces acting upon the particles.

Two forms of correlations were found to yield seemingly equivalent results based on the present experimental for the upward nozzle. The correlations' predictions were compared with data from Knowlton and Hirsan (1980) which were obtained under dissimilar conditions (e.g. pressurized fluidized bed with large injector diameter). Only the following form was found to be in good agreement with both sets of data:

$$\frac{L_{min}}{d_j} = 2.99\left(Fr_{2,j}\right)^{0.35}\left(\frac{U_g}{U_{mb}}\right)^{-0.35}$$

$$\frac{L_{max}}{d_j} = 8.37\left(Fr_{2,j}\right)^{0.30}\left(\frac{U_g}{U_{mb}}\right)^{-0.30}$$

$$\frac{L_b}{d_j} = 23.1\left(Fr_{2,j}\right)^{0.25}\left(\frac{U_g}{U_{mb}}\right)^{-0.30} .$$

For the downward nozzle, two forms of correlations are proposed. Although the first form which relies on the particle diameter as the length scaling factor is in better agreement with the experimental data, concerns about the suitability of the correlation when extrapolating to higher pressure conditions has illustrated for the upward nozzle lead to the inclusion of the second form. For near atmospheric conditions the jet penetration lengths can be estimated from

$$\frac{L_{min}}{d_p} = 40.6\left(\frac{\rho_j}{\rho_p}\cdot Fr_{1,p}\right)^{0.40}\left(Ar_g\right)^{-0.25}\left(\frac{U_g}{U_{mb}}\right)^{-0.25}$$

$$\frac{L_{max}}{d_p} = 93.8\left(\frac{\rho_j}{\rho_p}\cdot Fr_{1,p}\right)^{0.30}\left(Ar_g\right)^{-0.25}\left(\frac{U_g}{U_{mb}}\right)^{0.05}.$$

Complementary data at elevated temperature and high pressure conditions, especially for the downward nozzle, are needed to further validate the proposed correlations. The lack of dependence of the jet penetration length with respect to injector diameter needs to be further investigated over a wider range of diameters.

5.7 Acknowledgement

The authors are grateful for the financial support of the Natural Sciences and Engineering Research Council of Canada (NSERC). The authors also wish to thank Mr. Jean Huard for modifying and manufacturing of the experimental equipment, and Mr. Guillermo Solano Rosas and Dr. Rachid Mabrouk for their assistance carrying out the experimental work.

5.8 Notation

Ar	Archimedes number (refer to Table 5.3), -
C	constants used in jet length correlations (refer to Eqs. 5.4-5.6 and Table 5.4), -
d	diameter, m
Fr	Froude number (refer to Table 5.3), -
g	gravitational constant, $g = 9.81$ m/s^2
H	height or axial position in the bed, m
L	distance between the nozzle tip and the fiber-optic probe effective measurement location, m
L_b	jet bubble penetration length (maximum penetration of high momentum jet bubbles), m
L_{max}	maximum jet penetration length (maximum length of pulsating void), m
L_{min}	minimum jet penetration length (length of permanent void), m
P	pressure, Pa

Re	Reynolds number (refer to Table 5.3), -
U	superficial velocity, m/s
u_j	injection velocity, m/s
$u_{j,bubbling}$	injection velocity corresponding to the transition between no penetration and high momentum bubbles at the measurement location, m/s
$u_{j,onset}$	injection velocity corresponding to the transition between high momentum bubbles and pulsating jet at the measurement location, m/s
$u_{j,perm}$	injection velocity corresponding to the transition between pulsating jet and permanent jet at the measurement location, m/s
x	variable used to designate the length scaling factor in dimensionless numbers, m
z	variable equivalent to $\ln\left(\rho_j u_j^2\right)$ used in correlations by Zenz (1968) (refer to Table 5.5), $\rho_j u_j^2$ is in Pa

Greek letters

α	exponents used in jet length correlations (refer to Eqs. 5.4-5.6 and Table 5.4), -
ε	local volumetric fraction, -
$\overline{\varepsilon}$	average volumetric fraction (estimated from Eq. 5.2 and Eq. 5.3), -
μ	viscosity, Pa·s
θ	nozzle inclination angle relative to horizontal used in correlation by Hong et al. (1997) (refer to Table 5.5), °
ρ	density, kg/m^3

Subscripts

0	refers to the fluidized bed at rest (U_g = 0 m/s)
1	refers to the single phase Froude number (refer to Table 5.3)
2	refers to the two-phase Froude number (refer to Table 5.3)

bed	refers to the fluidized bed operated at U_g
cf	refers to the fluidized bed at complete fluidization
g	refers to the gas in the fluidized bed at the same axial position as the nozzle tip
g,∞	refers to the gas conditions above the bed surface
j	corresponds to the injected gas (based on conditions within the injector at the tip)
mb	refers to the fluidized bed at minimum bubbling
mf	refers to the fluidized bed at minimum fluidization
p	refers to the particles
ref	refers to known a reference fluidized bed conditions (0 , mb or mf)
s	refers to solid fraction
se	refers to the fluidized bed at the onset of transport fluidization (significant entrainment)
t	refers to the column

5.9 References

Abba, I.A., 2001. A Generalized Fluidized Bed Reactor Model across the Flow Regimes, PhD Thesis, University of British Columbia, Vancouver, BC, Canada.

Abrahamsen, A.R., Geldart, D., 1980. Behavior of Gas-fluidized Beds of Fine Powders – Part 1. Homogeneous Fluidization. Powder Technology 26, 35–46.

Benjelloun, F., Liégeois, R., Vanderschuren, J., 1991. Détermination des longueurs de jets de gaz horizontaux dans les lits fluidisés, in: Laguérie, C., Guigon, P. (Eds.), Récents progrès en génie des procédés: La Fluidisation, pp. 108–115.

Blake, T.R., Webb, H., Sunderland, P.B., 1990. The Nondimensionalization of Equations Describing Fluidization with Application to the Correlation of Jet Penetration Height. Chemical Engineering Science 45, 365–371.

Choi, J.H., Son, J.E., Kim, S.D., 1998. Generalized Model for Bubble Size and Frequency in Gas-Fluidized Beds. Industrial & Engineering Chemistry Research 37, 2559–2564.

Chyang, C.S., Chang, C.H., Chang, J.H., 1997. Gas Discharge Modes at a Single Horizontal Nozzle in a Two-Dimensional Fluidized Bed. Powder Technology 90, 71–77.

Cui, H.P., Mostoufi, N., Chaouki, J., 2001. Comparison of measurement techniques of local particle concentration for gas–solid fluidization, in: Kwauk, M., Li, J., Yang, W.C. (Eds.), Proceedings of the Tenth Engineering Foundation Conference on Fluidization, (Beijing, China), Engineering Foundation, New York, pp. 779–786.

Dry, R.J., Judd, M. R., 1986. Split Feed Fluidised Bed Reactors: Mass Transfer in the Sparger Region, in: Østergaard, K., Sørensen, A. (Eds.), Proceedings of the Fifth Engineering Foundation Conference on Fluidization, (Elsinore, Denmark), Engineering Foundation, New York, pp. 47–54.

Dubrawski, K., Bi, H.T., Chaouki, J., Ellis, N., Grace, J.R., Kantzas, A., Lim, C., Patience, G.S., Pugsley, T., Zhu, J.X., 2011. Comparison of Invasive and Non-invasive Fluidization Hydrodynamic Measurement Techniques. (manuscript in preparation 2011).

Guo, Q., Yue, G., Zhang, J., Liu, Z., 2001. Hydrodynamic Characteristics of a Two-dimensional Jetting Fluidised Bed with Binary Mixtures. Chemical Engineering Science 56, 4685–4694.

Guo, Q., Si, C., Zhang, J., 2010. Flow Characteristics in a Jetting Fluidized Bed with Acoustic Assistance. Industrial & Engineering Chemistry Research 49, 7638–7645.

Hilal, N., Gunn, D.J., 2002. Solid hold up in gas fluidised beds. Chemical Engineering and Processing 41, 373–379.

Hirsan, I., Sishtla, C., Knowlton, T.M., 1980. The Effect of Bed and Jet Parameters on Vertical Jet Penetration Length in Gas Fluidized Beds. Paper presented at 73rd Annual AIChE Meeting (Chicago, Illinois, USA), AIChE.

Hong, R., Li, H., Li, H., Wang, Y., 1997. Studies on the Inclined Jet Penetration Length in a Gas–Solid Fluidized Bed. Powder Technology 92, 205–212.

King, D., 1989. Estimation of Dense Bed Voidage in Fast and Slow Fluidized Beds of FCC Catalyst, in: Grace, J.R., Shemilt, L.W., Bergounou, M.A. (Eds.), Proceedings of the Sixth

Engineering Foundation Conference on Fluidization, (Banff, Alberta, Canada), Engineering Foundation, New York, pp. 1–8.

Knowlton, T.M., Hirsan, I., 1980. The Effect of Pressure on Jet Penetration in Semi-cylindrical Gas-fluidized Beds, in: Grace, J.R., Matsen, J.M. (Eds.), Proceedings of the Third Engineering Foundation Conference on Fluidization, (Henniker, New Hampshire), Engineering Foundation, New York, pp. 315–324.

Merry, J.M.D., 1971. Penetration of a Horizontal Gas Jet into a Fluidized Bed. Transactions of the Institution of Chemical Engineers 49, 189–195.

Patience, G.S., Bockrath, R.E., 2010. Butane Oxidation Process Development in a Circulating Fluidized Bed. Applied Catalysis A: General 376, 4–12.

Pell, M., 1990. Gas Fluidization, Elsevier, Amsterdam.

Rowe, P.N., MacGillivray, H.J., Cheesman, D.J., 1979. Gas Discharge from an Orifice into a Gas Fluidised Bed. Transactions of the Institution of Chemical Engineers 57, 194–199.

Sauriol, P., Cui, H., Chaouki, J., (submitted 2011). Gas–Solid Structure in the Vicinity of a Sparger Nozzle in a Fluidized Bed. Powder Technology.

Vaccaro, S., Musmarra, D., Costanza, F., Filla, M., Massimilla, L., 1989. Diagnostics of Gas Injection in Fluidized Beds by Pressure Signal Analysis, in: Grace, J.R., Shemilt, L.W., Bergounou, M.A. (Eds.), Proceedings of the Sixth Engineering Foundation Conference on Fluidization, (Banff, Alberta, Canada), Engineering Foundation, New York, pp. 245–252.

Vaccaro, S., Musmarra, D., Petrecca, M., 1997. Evaluation of the Jet Penetration Depth in Gas-Fluidized Beds by Pressure Signal Analysis. International Journal of Multiphase Flow 23, 683–698.

Wang, C.H., Zhong, Z.P., Li, R., E, J.Q., 2010. Prediction of Jet Penetration Depth Based on Least Square Support Vector Machine. Powder Technology 203, 404–411.

Xuereb, C., Laguérie, C., Baron, T., 1991. Étude du comportement des jets continus horizontaux ou inclinés introduits dans un lit fluidisé par un gaz, I: Morphologie des jets. Powder Technology 67, 43–56.

Yang, W.-C., 1981. Jet Penetration in a Pressurized Fluidized Bed. Industrial & Engineering Chemistry Fundamentals 20, 297–300.

Yates, J.G., Bejcek, V., Cheesman, D.J., 1986. Jet Penetration into Fluidized Beds at Elevated Pressures, in: Østergaard, K., Sørensen, A. (Eds.), Proceedings of the Fifth Engineering Foundation Conference on Fluidization, (Elsinore, Denmark), Engineering Foundation, New York, pp. 79–86.

Yates, J.G., Cobbinah, S.S., Cheesman, D.J., Jordan, S.P., 1991. Particle Attrition in Fluidized Beds Containing Opposing Jets. AIChE Symposium Series 87, 13–19.

Zenz, F.A., 1968. Bubble Formation and Grid Design. Institution of Chemical Engineers Symposium Series 30, 136–139.

Zhong, W., Zhang, M., 2005. Jet Penetration Depth in a Two-dimensional Spout–fluid Bed. Chemical Engineering Science 60, 315–327.

Table 5.1: Particles used in the investigation.

Particles	Label	[1] d_p (m)	ρ_p (kg/m^3)	[2] U_{mf} (m/s)	U_{mb} (m/s)	ε_{mb}	Geldart
Alumina	A	200×10^{-6}	3930	0.041		0.50	B
FCC catalyst	F	70×10^{-6}	1675	0.003	0.006	0.51	A
Poly-propylene	P	250×10^{-6}	880	0.025		0.44	AB
Sand 1	S1	90×10^{-6}	2650	0.008		0.50	AB
Sand 2	S2	170×10^{-6}	2650	0.021		0.45	B
Sand 3	S3	405×10^{-6}	2650	0.164		0.45	B
VPO catalyst	V	75×10^{-6}	1200	0.002	0.007	0.54	A

1) d_p is the Sauter mean diameter.

2) U_{mf}, U_{mb} (calculated from Abrahamsen and Geldart, 1980), ε_{mb}, and Geldart classification are based on air at 23°C and 1 atm.

Table 5.2: Range of operating conditions covered in the experimental work.

Operating parameter	Range	
	Upward	Downward
Injector diameter d_j, mm	2.4, 4.9 and 7.2	2.4, 4.9 and 7.2
Measurement distance L, mm	5.2–113	5.2–76.2
Injected gas	Helium, Air, Argon, and CO_2	Helium, Air and Argon
[1]Injection velocity u_j, m/s	0.08–1013	0.08–1013
[2]Injection pressure ratio ρ_j / ρ_g	1–3.1	1–3.0
Solids used (refer to Table 5.1)	A, F, P, S1, S2, S3, and V	A, F, P, S1, S2, and S3
Superficial velocity U_g, m/s ($U_g / U_{mb} \geq 1.3$)	0.011–0.65	0.015–0.64
Bed height at rest H_0, m	0.23–0.77	0.19–0.74
Injector tip position H_j, m	0.124–0.274	0.161–0.307
Number of runs	1152	729

1) Injection velocity is limited to speed of sound at operating temperature (approx. 23°C): Helium 1013 m/s; Air 345 m/s; Argon 321 m/s; CO_2 268 m/s.
2) Injection pressure ratio only exceeds 1 when chocked flow occurs (velocity reaches speed of sound).

Table 5.3: List of dimensionless groups used for jet penetration correlation and their range.

Description	Dimensionless group	Range
Jet length ratio	L/x, where x is a length scaling factor (d_j and d_p were considered).	$x = d_j$: 1–50 $x = d_p$: 30–1500
Archimedes number	$Ar_i = \frac{g d_p^3 \rho_i \left(\rho_p - \rho_i\right)}{\mu_i^2}$	$i = g$: 20–6800 $i = j$: 2–1.6×10^4
Fluidized bed Reynolds number	$Re_g = \frac{\rho_g U_g d_p}{\mu_g}$	0.07–18
Injection Reynolds number	$Re_j = \frac{\rho_j u_j x}{\mu_j}$	$x = d_j$: 20–1.4×10^5 $x = d_p$: 0.3–2.4×10^4
Injection Froude number	$Fr_1 = \frac{u_j^2 + \left(P_j - P_g\right)/\rho_j}{gx}$, where $\left(P_j - P_g\right)$ accounts for pressure contribution to fluid momentum when chocked flow arises.	$x = d_j$: 3×10^{-2}–3.6×10^7 $x = d_p$: 0.8–1.2×10^9
Injection two-phase Froude number	$Fr_2 = \frac{\rho_j u_j^2 + \left(P_j - P_g\right)}{\rho_p \bar{\varepsilon}_s g x}$	$x = d_j$: 9×10^{-5}–8.5×10^4 $x = d_p$: 2.6×10^{-3}–1.6×10^5
Injector-to-particle size ratio	d_j/d_p	6–100
Density ratios	ρ_i/ρ_p	$i = g$: 3×10^{-4}–1.4×10^{-3} $i = j$: 4×10^{-5}–3×10^{-3}
Average fluidized bed voidage	$\bar{\varepsilon}_g$	0.47–0.75
Average fluidized bed solid holdup	$\bar{\varepsilon}_s = 1 - \bar{\varepsilon}_g$	0.25–0.53
Fluidized bed velocity ratio	U_g/U_{mb}	1.3–90

Table 5.4: Summary of coefficients used in jet penetration length correlations derived from experimental data with confidence intervals.

Orientation	Jet length ratio	Eq.	Correlation coefficients ([1]95% confidence range)			
			C	α_1	α_2	α_3
Upward	L_{min}/d_j	(5.4)	[2]0.346 (43) [3]0.418 (9)	0.357 (10) 0.35	-0.370 (32) -0.35	0.281 (21) 0.25
		(5.5)	2.99 (18) 2.99 (7)	0.348 (10) 0.35	-0.345 (28) -0.35	N/A
	L_{max}/d_j	(5.4)	1.50 (22) 1.31 (4)	0.295 (12) 0.30	-0.371 (44) -0.35	0.226 (28) 0.25
		(5.5)	8.24 (57) 8.37 (25)	0.286 (12) 0.30	-0.275 (36) -0.30	N/A
	L_b/d_j	(5.4)	3.82 (69) 3.54 (14)	0.256 (17) 0.25	-0.386 (62) -0.35	0.236 (39) 0.25
		(5.5)	22.9 (24) 23.1 (9)	0.246 (16) 0.25	-0.298 (50) -0.30	N/A
Downward	L_{min}/d_p	(5.6)	36.1 (51) 40.6 (8)	0.413 (15) 0.40	-0.249 (35) -0.25	-0.238 (35) -0.25
	L_{max}/d_p	(5.6)	89.5 (117) 93.8 (20)	0.285 (11) 0.30	-0.232 (14) -0.25	0.068 (34) 0.05

1) 95% confidence ranges are specified in a compact form: 0.346 (43) = 0.346 ± 0.043.
2) Top row contains original fitting results, where constants and exponents are adjusted simultaneously.
3) Bottom row contains the constant adjustment once exponents are fixed (rounded to increments of 0.05). These are used for experimental data and correlation comparisons.

Table 5.5: Selected correlations from the literature.

Reference	Correlation
Upward	
Blake et al. (1990)	$\frac{L_{max}}{d_j} = 26.9\left(\frac{u_j^2}{gd_j}\right)^{0.322}\left(\frac{\rho_j}{\rho_p}\right)^{0.325}\left(\frac{\rho_p u_j d_p^2}{\mu_j d_j}\right)^{-0.124}$
Guo et al. (2001)	$\frac{L_{max}}{d_j} = \begin{cases} 19.18\left[\frac{\rho_j}{(\rho_p-\rho_j)}\cdot\frac{u_j^2}{gd_j}\right]^{0.2383}\left(\frac{U_g}{U_{mf}}\right)^{-0.3616} & \text{for } \frac{U_g}{U_{mf}} \le 2.5 \\ 11.52\left[\frac{\rho_j}{(\rho_p-\rho_j)}\cdot\frac{u_j^2}{gd_j}\right]^{0.1966} & \text{for } \frac{U_g}{U_{mf}} > 2.5 \end{cases}$
Hirsan et al. (1980)	$\frac{L_b}{d_j} = 26.6\left[\left(\frac{\rho_j}{\rho_p}\right)^2\cdot\frac{u_j^2}{gd_p}\right]^{0.335}\left(\frac{U_g}{U_{cf}}\right)^{-0.24}$ $\frac{L_{max}}{d_j} = 19.3\left[\left(\frac{\rho_j}{\rho_p}\right)^2\cdot\frac{u_j^2}{gd_p}\right]^{0.415}\left(\frac{U_g}{U_{cf}}\right)^{-0.54}$
Hirsan-type fit	$\frac{L_{\min}}{d_j} = 7.22\left[\left(\frac{\rho_j}{\rho_p}\right)^2\cdot\frac{u_j^2}{gd_p}\right]^{0.37}\left(\frac{U_g}{U_{cf}}\right)^{-0.67}$ Derived from data by Knowlton and Hirsan (1980) according to format used by Hirsan et al. (1980).
Yang (1981)	$\frac{L_{max}}{d_j} = 7.65\left(\frac{U_{cf,P=atm}}{U_{cf,P=P_g}}\cdot\frac{\rho_j}{(\rho_p-\rho_j)}\cdot\frac{u_j^2}{gd_j}\right)^{0.472}$
Yang-type fit	$\frac{L_b}{d_j} = 19.7\left(\frac{U_{cf,P=atm}}{U_{cf,P=P_g}}\cdot\frac{\rho_j}{(\rho_p-\rho_j)}\cdot\frac{u_j^2}{gd_j}\right)^{0.257}$ $\frac{L_{min}}{d_j} = 5.13\left(\frac{U_{cf,P=atm}}{U_{cf,P=P_g}}\cdot\frac{\rho_j}{(\rho_p-\rho_j)}\cdot\frac{u_j^2}{gd_j}\right)^{0.395}$ Derived from data by Knowlton and Hirsan (1980) according to format used by Yang (1981).

Table 5.5: Selected correlations from the literature (continued).

Reference	Correlation
Upward (continued)	
Zenz (1968) Adapted from Fig. 3-1 in Pell (1990).	$\frac{L_{max}}{d_j} = \begin{cases} 0.1810z + 2.427 & \text{for } \rho_j u_j^2 \le 25 \text{ Pa} \\ 0.2882z^3 - 3.183z^2 + 11.71z - 11.34 & \text{for } 25 \text{ Pa} < \rho_j u_j^2 \le 1825\times10^4 \text{ Pa} \\ 12.66z - 75.90 & \text{for } \rho_j u_j^2 > 1825 \text{ Pa} \end{cases}$ where $z = \ln\left(\rho_j u_j^2\right)$.
Horizontal (and inclined)	
Benjelloun et al. (1991)	$\frac{L_{max}}{d_j} = 5.52\left[\frac{\rho_j}{\left(\rho_p - \rho_j\right)} \cdot \frac{u_j^2}{g d_j}\right]^{0.27}$
Hong et al. (1997)	$\frac{L_{max}}{d_j} = 1.64\times10^6 \left(\frac{\rho_j}{\rho_p \bar{\varepsilon}_s} \cdot \frac{u_j^2}{g d_p}\right)^{0.327} \left(\frac{\rho_g}{\rho_p}\right)^{1.974} \left(\frac{d_p}{d_j}\right)^{-0.040} \times \left(\frac{\theta}{180°} + \frac{\pi}{2}\right)^{0.148} \left(\frac{H_j}{H_0}\right)^{0.028} - 3.8$ Horizontal $\Rightarrow \theta = 0°$
Merry (1971)	$\frac{L_{max}}{d_j} = 5.25\left(\frac{\rho_j}{\rho_p \bar{\varepsilon}_s} \cdot \frac{u_j^2}{g d_p}\right)^{0.4} \left(\frac{\rho_g}{\rho_p}\right)^{0.2} \left(\frac{d_p}{d_j}\right)^{0.2} - 4.5$
Downward	
Yates et al. (1991)	$\frac{L_{max}}{d_j} = 2.8\left[\frac{\rho_j}{\left(\rho_p - \rho_j\right)} \cdot \frac{u_j^2}{g d_j}\right]^{0.4}$
Zenz (1968) Adapted from Fig. 3-1 in Pell (1990).	$\frac{L_{max}}{d_j} = \begin{cases} 0.1810z + 2.427 & \text{for } \rho_j u_j^2 \le 150 \text{ Pa} \\ 0.04266z^3 - 0.4055z^2 + 1.032z + 2.979 & \text{for } 150 \text{ Pa} < \rho_j u_j^2 \le 1.5\times10^4 \\ 5.067z - 35.39 & \text{for } \rho_j u_j^2 > 1.5\times10^4 \text{ Pa} \end{cases}$ where $z = \ln\left(\rho_j u_j^2\right)$.

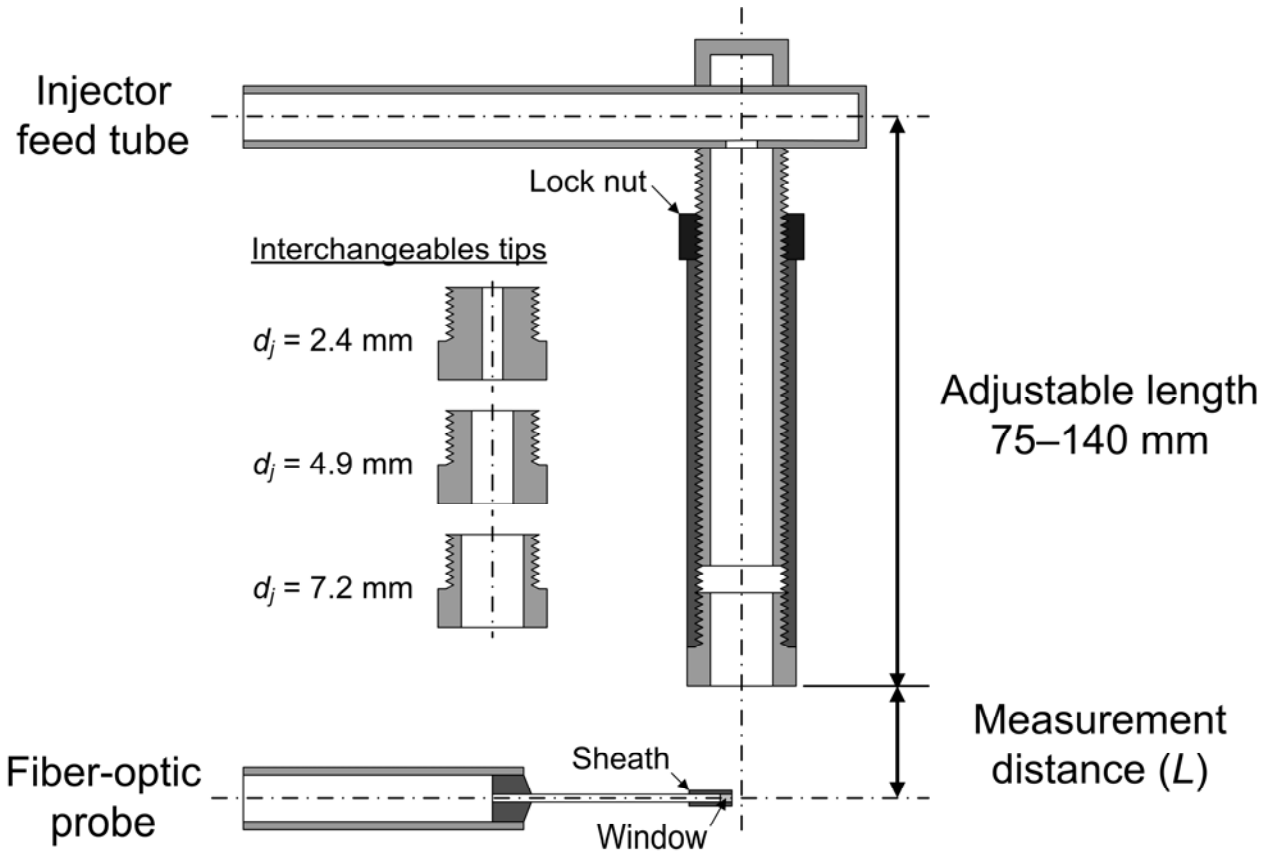

Figure 5-1: Schematic diagram of the adjustable injection nozzle with interchangeable tips and fiber optic probe in the downward nozzle configuration.

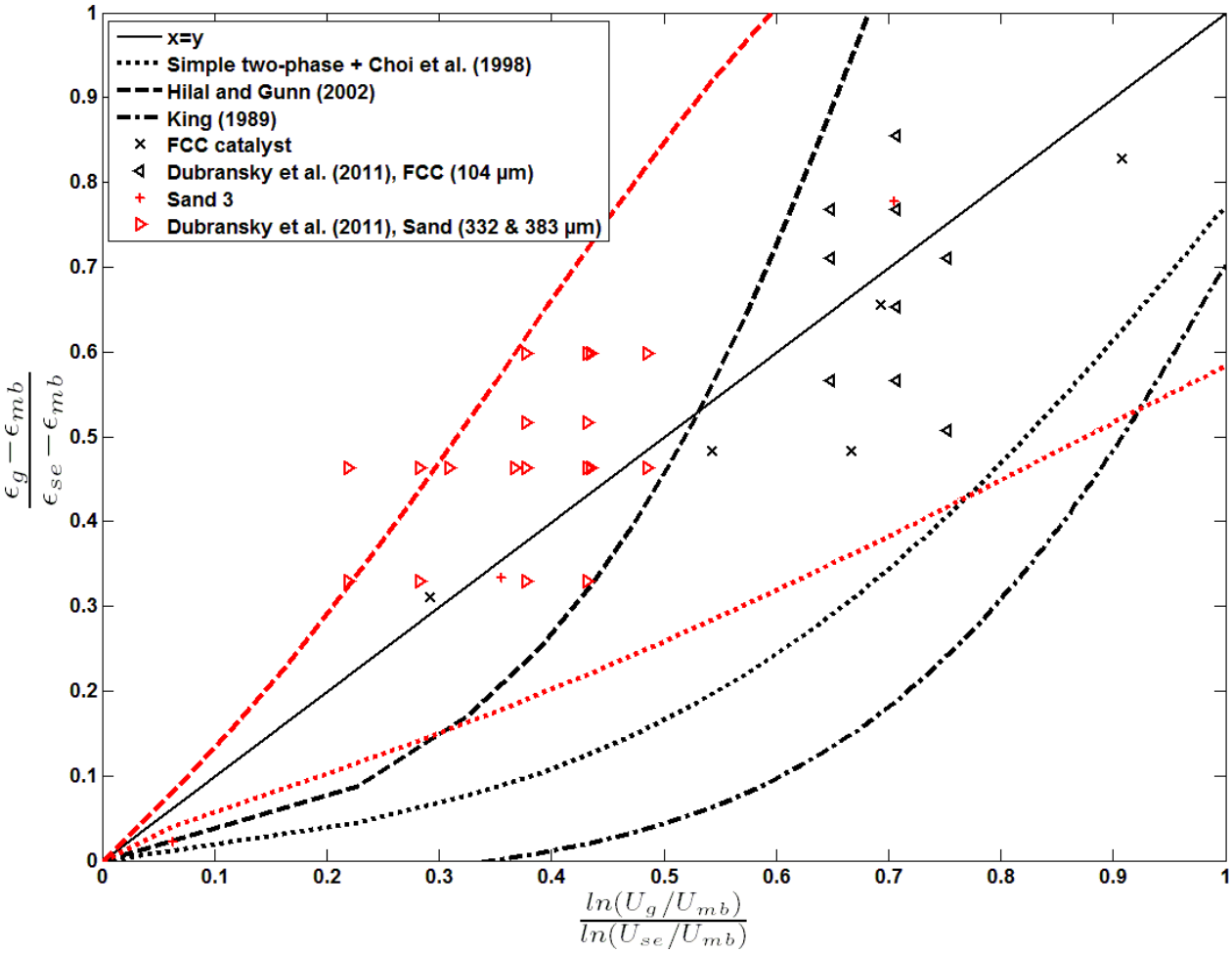

Figure 5-2: Comparison between measured and estimated bed voidage. Simple two-phase + Choi et al. (1998) is based on the average voidage for an initial bed height of 0.75m.

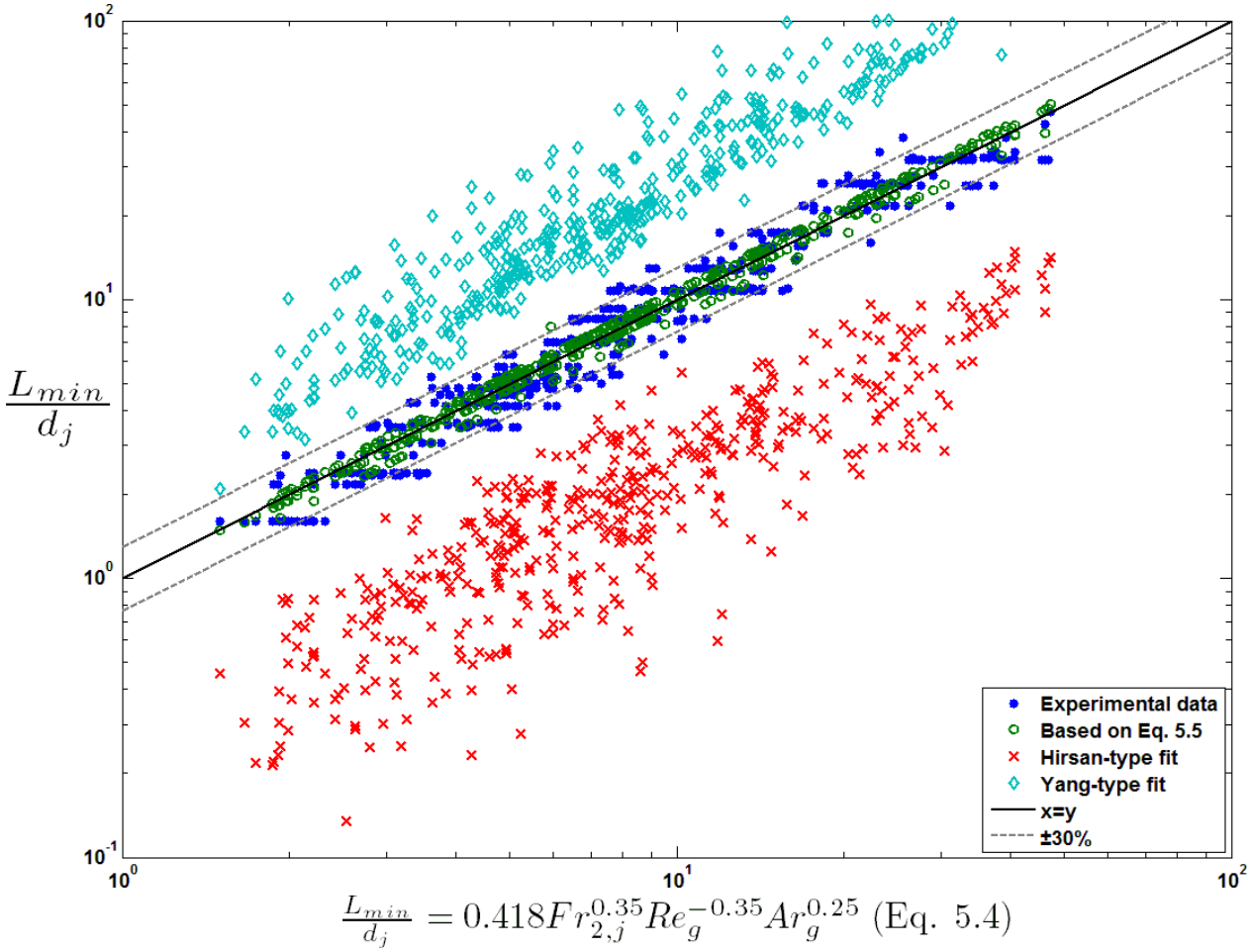

Figure 5-3: Comparison between measurement and correlations for L_{min} with an upward nozzle. Note uncertainty range is defined relative to minimum value (±30% corresponds to ×/÷1.3 with respect to x=y)

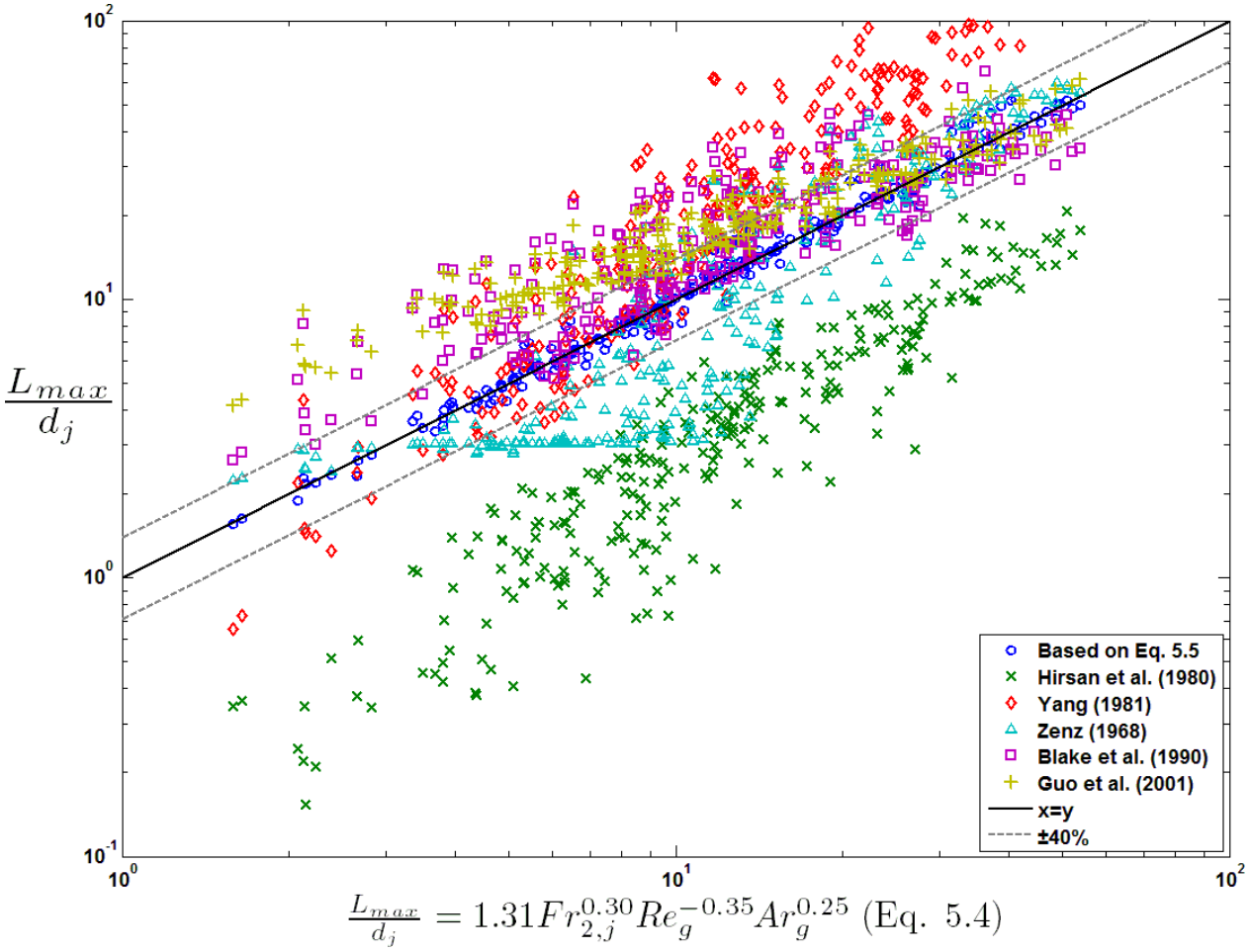

Figure 5-4: Comparison between measurement and correlations for L_{max} with an upward nozzle.

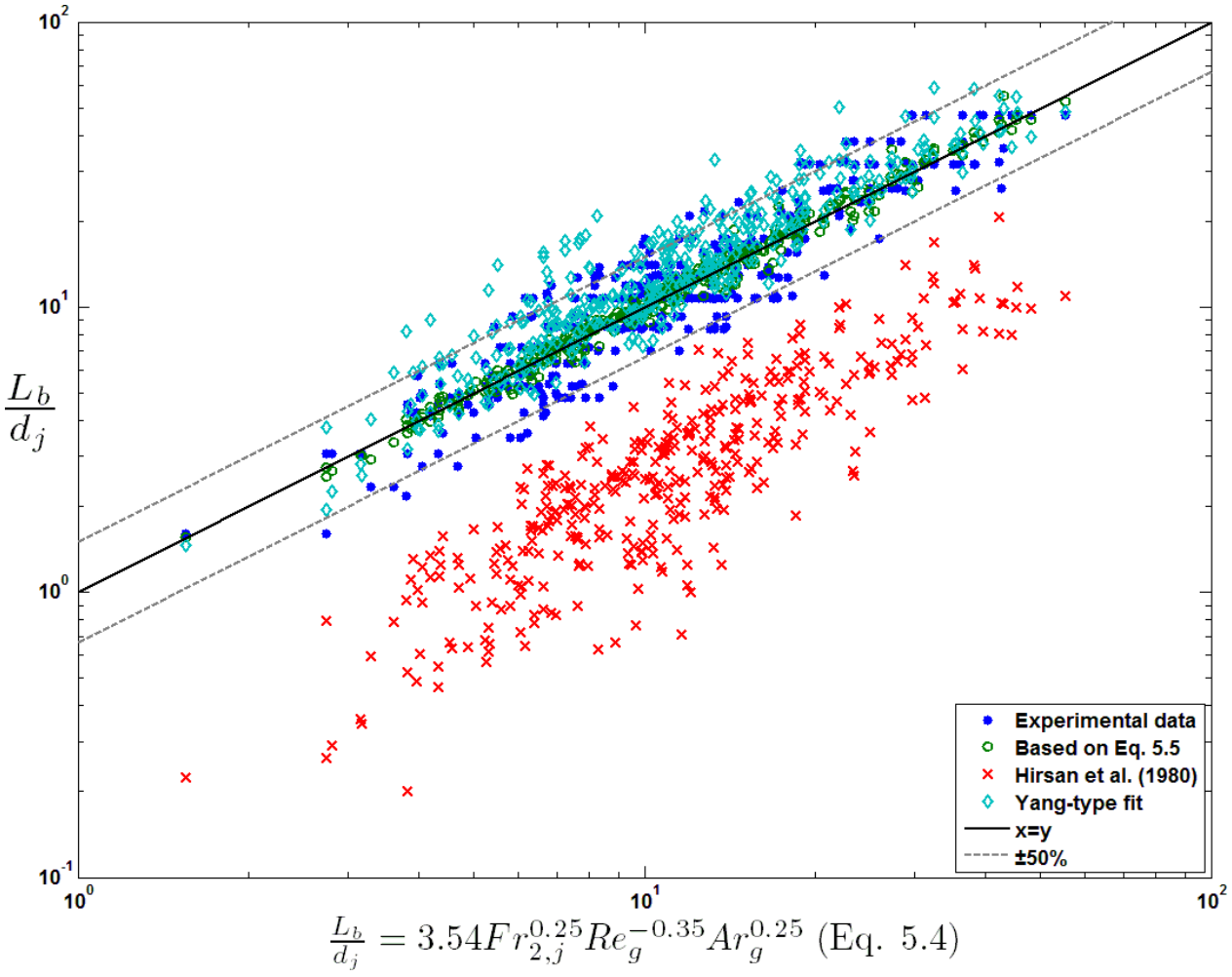

Figure 5-5: Comparison between measurement and correlations for L_b with an upward nozzle.

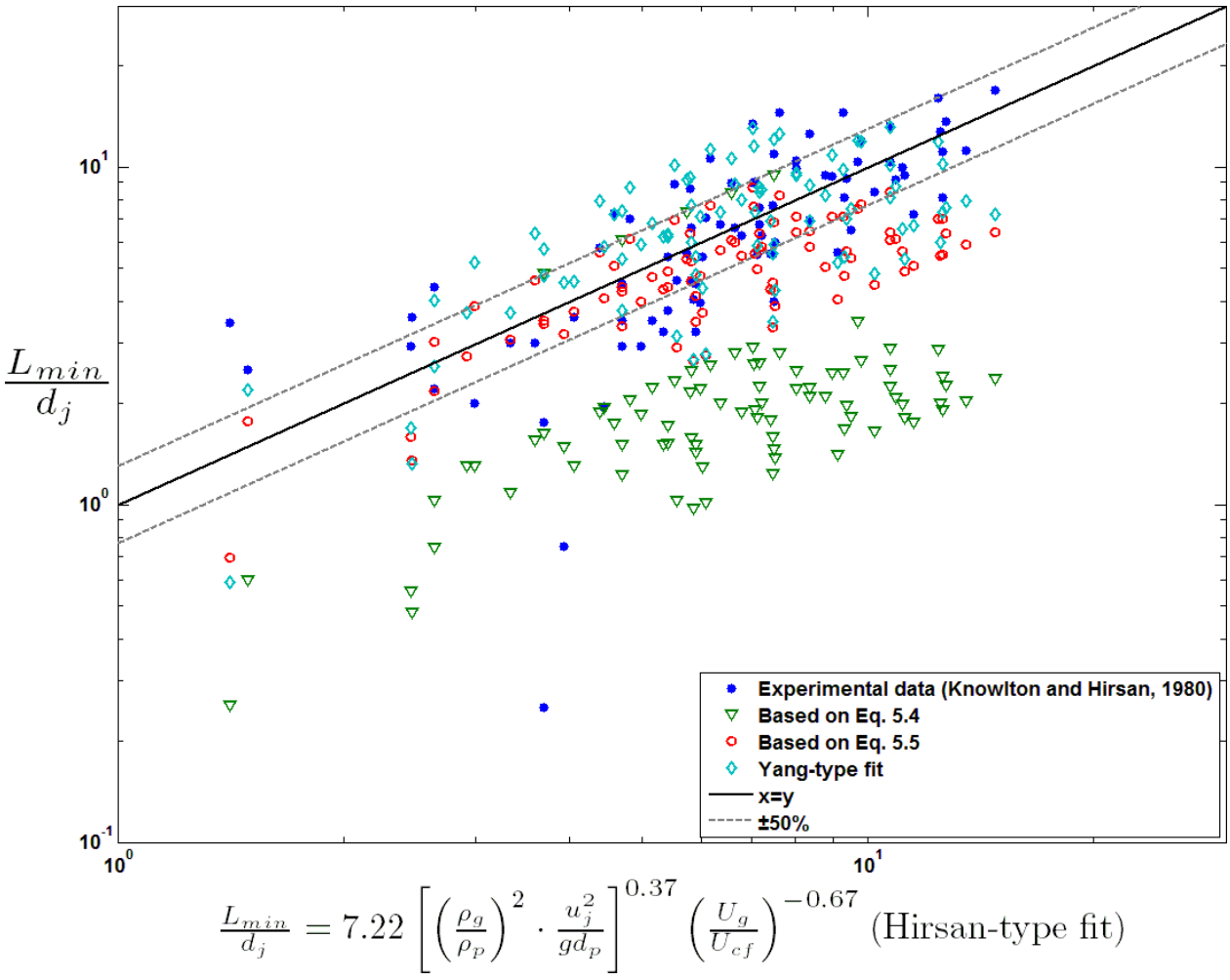

Figure 5-6: Comparison between data from Knowlton and Hirsan (1980) and proposed correlations for L_{min} with an upward nozzle.

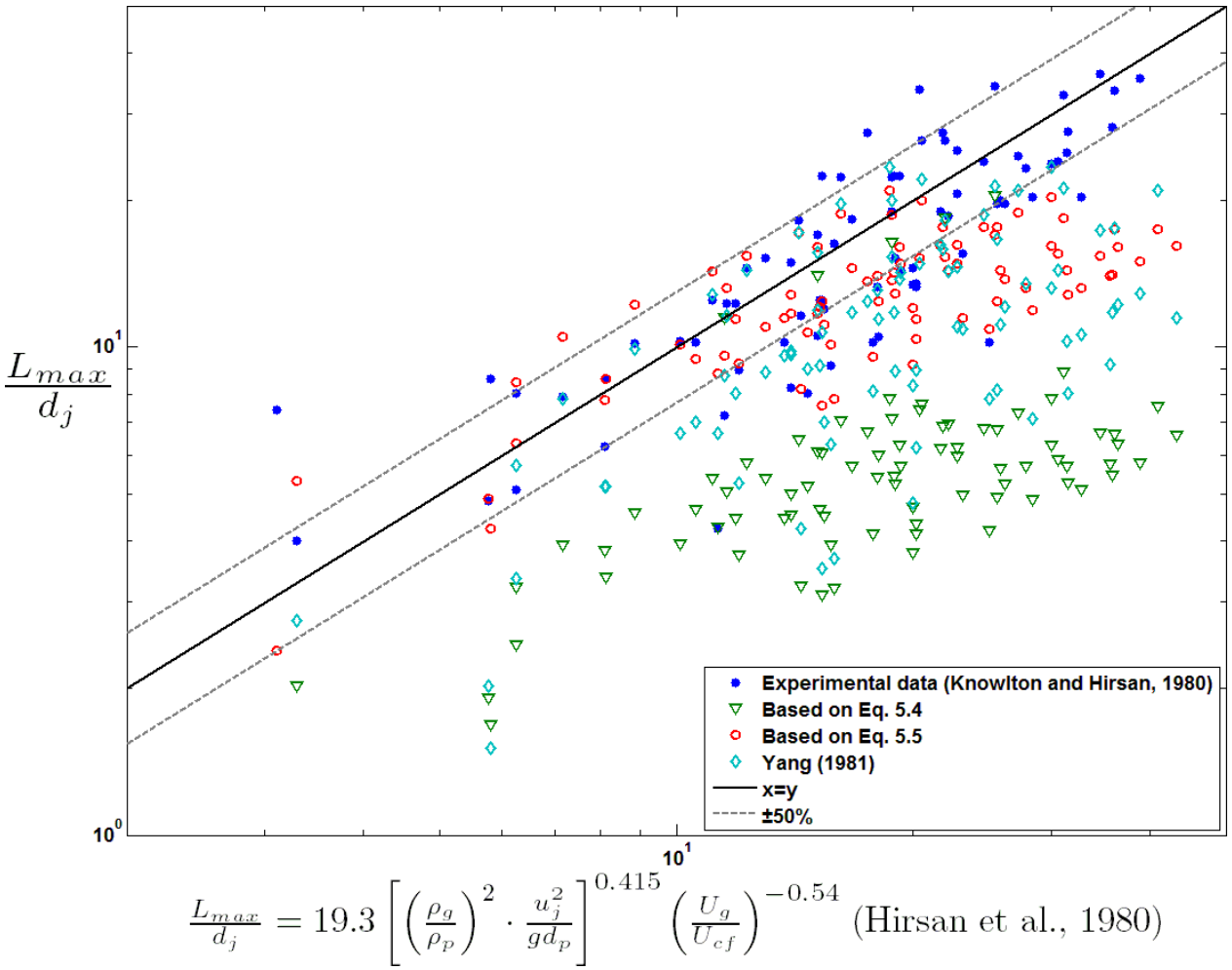

Figure 5-7: Comparison between data from Knowlton and Hirsan (1980) and proposed correlations for L_{max} with an upward nozzle.

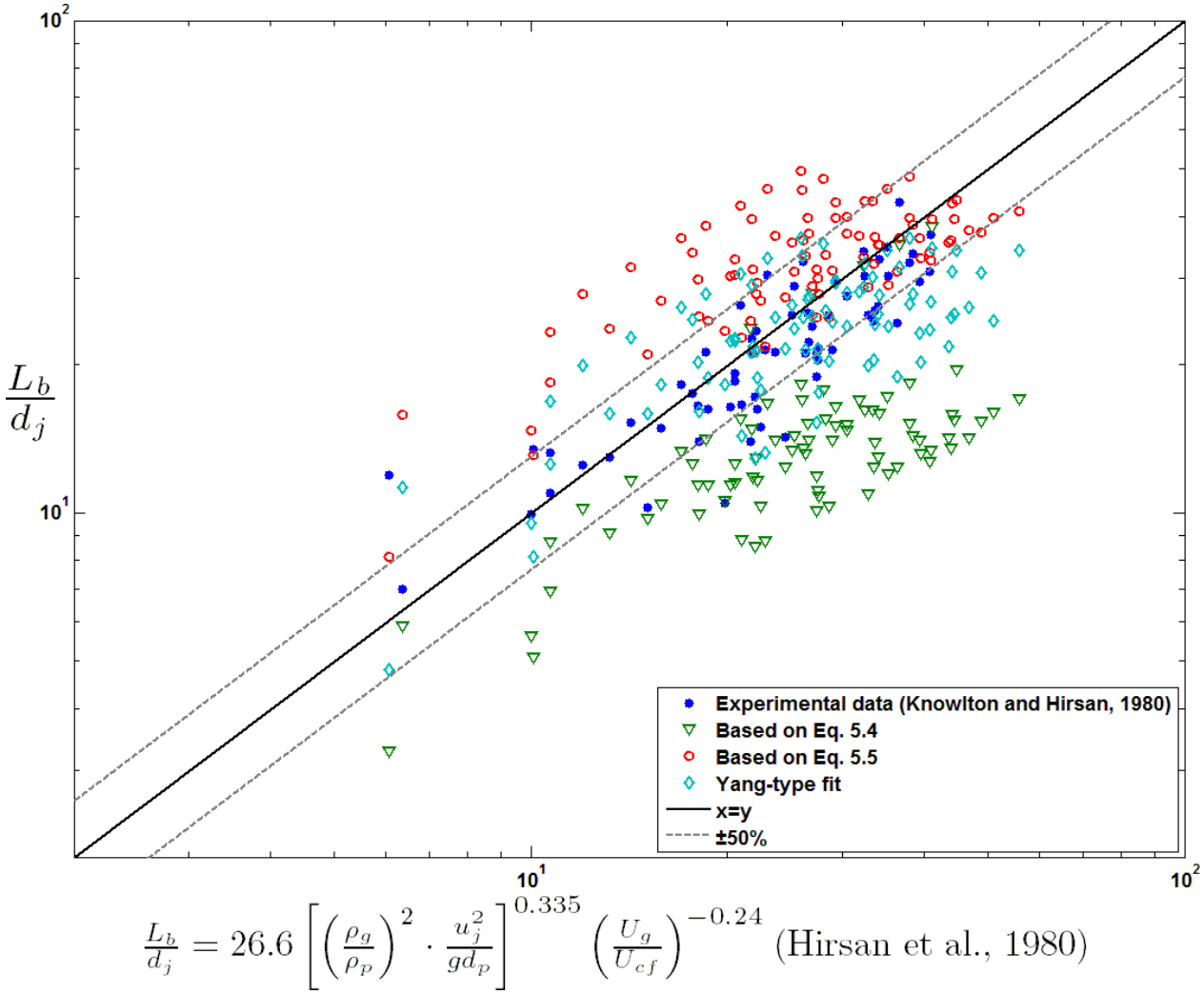

Figure 5-8: Comparison between data from Knowlton and Hirsan (1980) and proposed correlations for L_b with an upward nozzle.

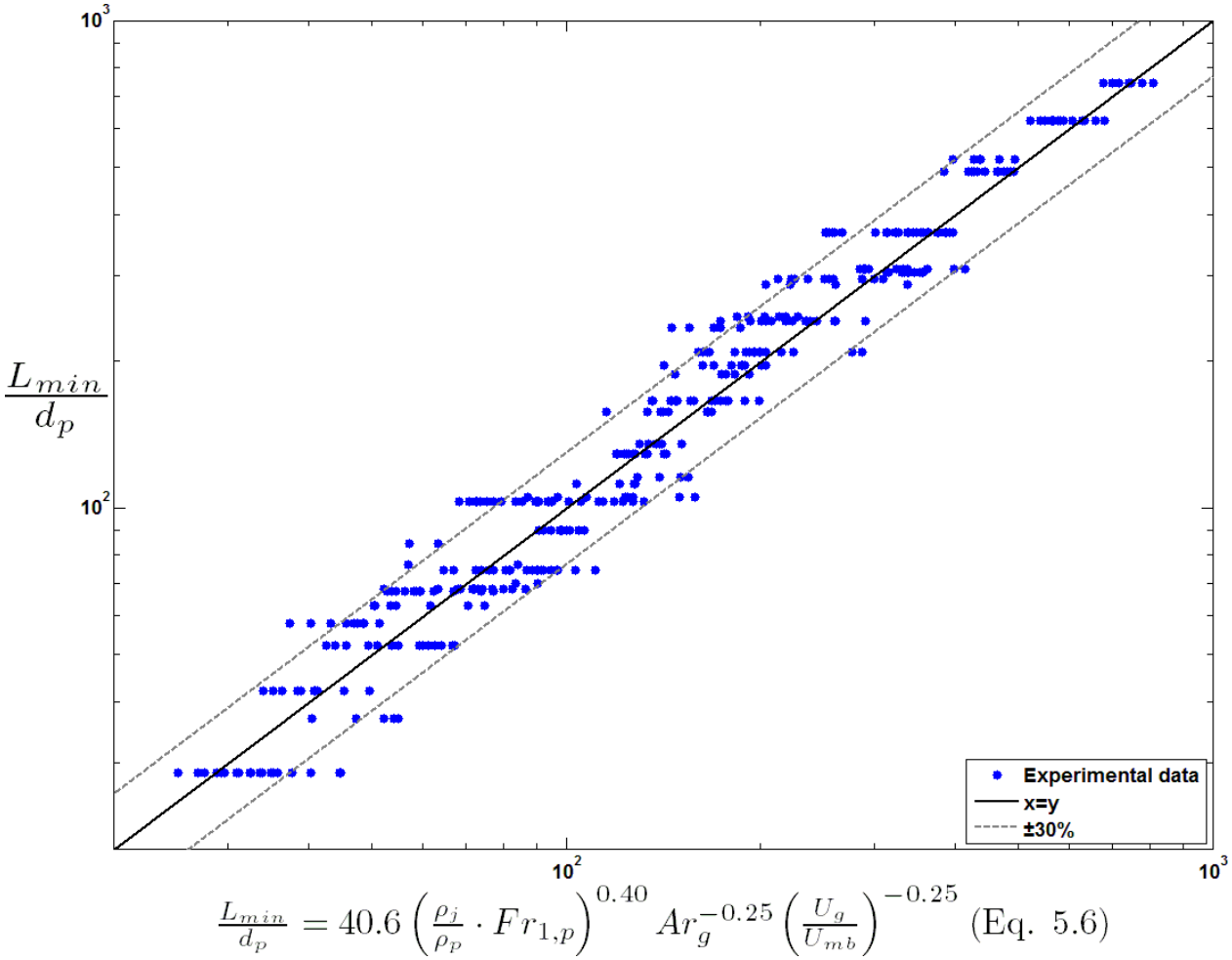

Figure 5-9: Comparison between measurement and correlations for L_{min} with a downward nozzle.

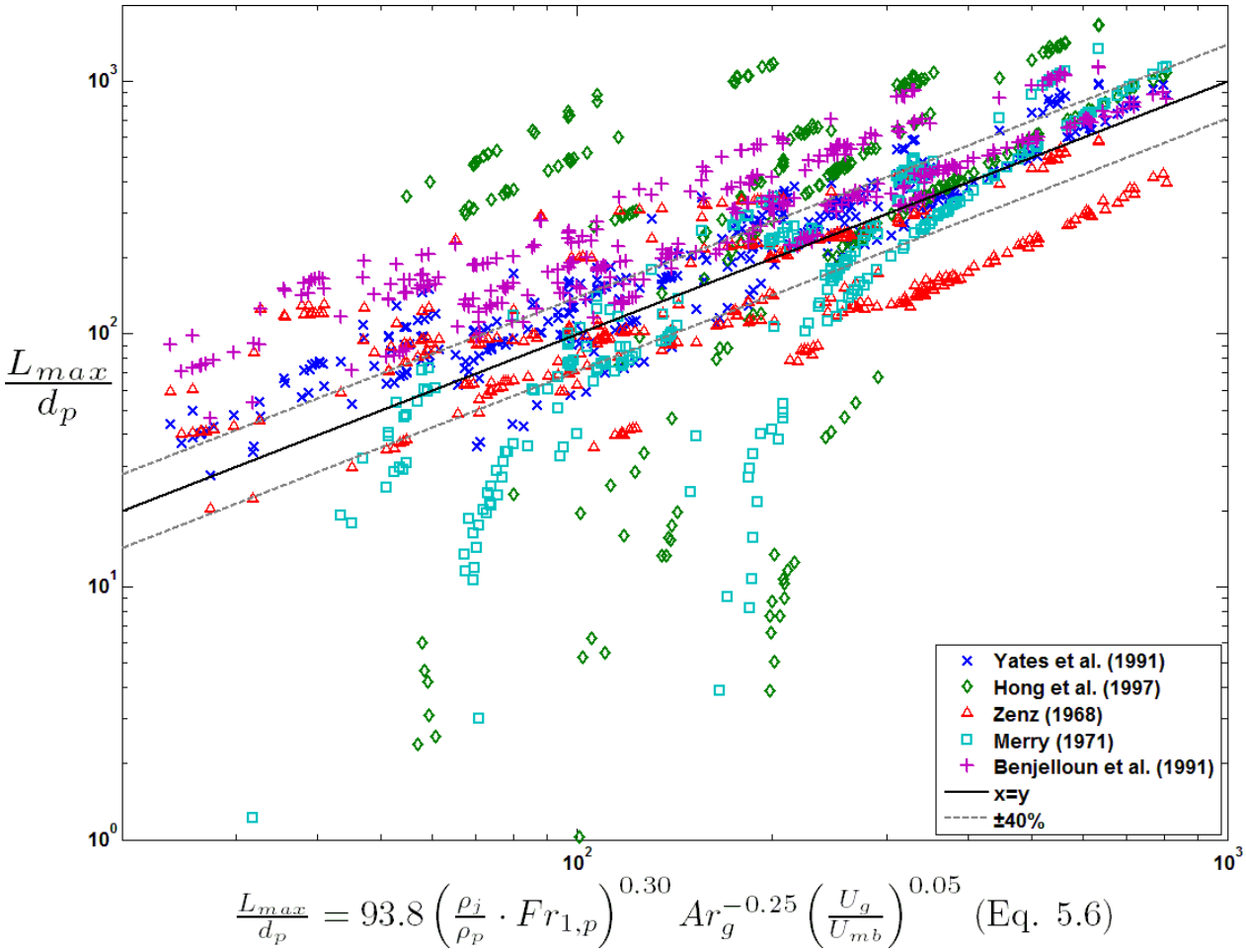

Figure 5-10: Comparison between measurement and correlations for L_{max} with a downward nozzle.

CHAPITRE 6 DISCUSSION GÉNÉRALE

Les objectifs du présent projet consistaient à développer et mettre en application des techniques de mesure afin de caractériser les jets de gaz dans les lits fluidisés.

Étant donné la disponibilité au laboratoire d'équipement de détection de rayons gamma, l'application des techniques de radiotraceurs afin de quantifier les concentrations de traceur dans le jet a été envisagée. L'évaluation des propriétés des détecteurs a montré que les facteurs de vue et l'atténuation du radiotraceur dans le milieu étaient plus importants que ce qui est généralement consentit. Lors de l'emploi de tels radiotraceurs dans l'analyse de distribution de temps de séjour, les détecteurs sont traités comme des intégrateurs parfaits. En considérant les effets additionels reliés à la distribution de vitesse et la géométrie du jet, l'emploi de radiotraceurs a été jugé être trop risqué pour être appliqué dans le contexte de l'étude des jets. Les outils de calculs qui avaient été développés dans l'étape préliminaire ont été réorientés vers l'analyse de la performance de radiotraceurs dans le contexte d'analyse de distribution de temps de séjour. Afin de minimiser ou de quantifier les erreurs inhérentes à la mesure des radiotraceurs, une série de critères ont été établis. Ces critères tiennent compte de la distribution axiale et radiale de l'efficacité du détecteur à mesurer les rayons gamma provenant du milieu, de la distribution radiale du radiotraceur, ainsi que des effets de saturation des détecteurs. Dans le contexte de l'étude des jets, la distribution radiale du traceur est très importante étant donné que le traceur est principalement présent dans le jet, au centre du lit, ce qui contribue beaucoup d'incertitude à la mesure. Un compromis possible serait d'effectuer ces mesures sur un jet isolé à la paroi d'un lit fluidisé 2D ou 2.5D.

Afin de permettre l'analyse de la structure de jets, une approche basée sur l'emploi d'une fibre optique a été développée. Cette approche basée sur un balayage de vitesse confère une robustesse au niveau de la connaissance du positionnement de la sonde par rapport à l'injecteur. Elle mène à l'observation de vitesses de transition lesquelles sont analogues aux longueurs de pénétration des jets rapportées par Knowlton et Hirsan (1980), par contre sur des unités tridimensionnelles. La technique est applicable à des vitesses de fluidisation importantes, au-delà de la vitesse minimale de bullage, s'apparentant aux conditions de fluidisation rencontrées dans

les réacteurs industriels (régime turbulent), à condition qu'on soit en présence d'un lit dense (porosité jusqu'à environ 0.8).

Finalement, l'approche de mesure de la structure des jets a été mise en application afin d'obtenir les vitesses de transition associées aux différentes longueurs caractéristiques de jet. Une campagne expérimentale incluant plusieurs paramètres d'opération, dont l'orientation de l'injecteur, la nature du gaz injecté, le type de particules, la vitesse superficielle, le diamètre de l'injecteur, ainsi que la hauteur du lit, a été entreprise. Les résultats expérimentaux ont permis de développer trois nouvelles corrélations pour les jets orientés vers le haut afin de prédire L_b, L_{max} et L_{min} (conformément aux définitions de Knowlton et Hirsan, 1980). Pour ce qui est des jets orientés vers le bas, deux corrélations pour la prédiction de L_{max} et L_{min} ont été développées. Les résultats obtenus ont montré l'importance du choix des nombres adimensionnels dans la formulation des corrélations. Les corrélations retenues pour les jets vers le haut s'avèrent en bon accord avec les résultats de Knowlton et Hirsan (1980), obtenus sur des lits fluidisés opérant à pression élevée. Pour ce qui est de jet vers le bas, le manque de données comparatives n'a pu permettre d'en établir la validité sur une plus large plage de conditions expérimentales. Les résultats et la formulation originale des corrélations pour les jets orientés vers le bas suggèrent que le mécanisme responsable de la dissipation de la quantité de mouvement du gaz injecté diffère de celle pour les jets vers le haut. Ces observations pourraient avoir un impact important sur les performances de buses d'injection en fonction de leur orientation.

De façon générale, les travaux accomplis dans le cadre de la thèse ont permis d'apporter des avancements importants sur la compréhension générale des jets. L'approche de mesure par fibre optique ouvre la porte à l'obtention d'un nombre plus important de résultats expérimentaux comprennant les diverses longueurs caractéristiques. Cette approche a l'avantage d'être basée sur les propriétés optiques qui ont mené aux définitions mêmes des longueurs de jet et devrait offrir plus de robustesse que les autres approches, telles les sondes de Pitot et sondes de pression dont la longueur résultante a fait l'objet de contestation au cours de dernières années. Additionnellement, les corrélations proposées viennent en partie combler un vide qui existe quant à la prédiction de longueurs L_b et L_{min} pour les jets vers le haut et L_{max} et L_{min} pour les jets vers le bas. Les résultats comparatifs acceptables et robustes en ce qui a trait aux corrélations pour les

jets orientés vers le haut donnent de la crédibilité à l'approche de mesure et notamment aux résultats obtenus pour les jets vers le bas, pour lesquels trop peu de données expérimentales ont fait l'objet de publication.

CONCLUSION ET RECOMMENDATIONS

L'approche par sonde à fibre optique s'avère intéressante dans sa facilité d'application. Suite aux travaux de la présente thèse, exécutés avec une fibre optique à réflexion, le rôle important de la fenêtre permettant de minimiser l'importance de la zone aveugle a été clairement observée. Par contre, la fragilité de la fenêtre a nécessité l'ajout d'une gaine protectrice, ce qui a contribué à doubler le diamètre du bout de la sonde et donc ainsi résulté en quatre fois plus de surface, tout en nécessitant le remplacement fréquent de la gaine et de la fenêtre (environ à chaque semaine selon les conditions et particules). Il semblerait que l'avantage d'une réduction de l'intrusivité ayant mené à l'adoption des sondes à réflexion au détriment des sondes à transmission n'est plus aussi intéressant lorsque l'ajout d'une gaine protectrice est requis pour l'application dans les jets. Il pourrait s'avérer intéressant de combiner le concept des mesures en infrarouge avec une sonde à transmission (deux tiges de fonctionnalité distinctes, une émettrice et l'autre réceptrice). Les sondes à transmission n'étant pas affectées par la région aveugle, l'ajout d'une fenêtre et d'une gaine protectrice ne serait pas requis. De plus, le volume de mesure étant bien délimité, les mesures de concentration de solide auraient l'avantage d'être moyenné sur un volume fixe.

Récemment, une technique de mesure de compositions gazeuse a été introduite par Laviolette et al. (2010), mettant en œuvre une telle sonde et un miroir afin de permettre la réflexion de la lumière infrarouge. L'emploi d'un tel dispositif intrusif aurait certainement des impacts sur les jets si on le plaçait au cœur même. Une configuration basée sur le principe de transmission plutôt que de réflexion, telle que proposée auparavant, serait envisageable. Le développement d'un tel système de mesure instantané et local de composition gazeuze, couplée à une mesure simultanée de solide, au moyen d'une sonde minimalement intrusive permettrait un avancement considérable de la connaissance sur les jets.

Les travaux accomplis ont mis en évidence le caractère singulier des jets orientés vers le bas. Malheureusement le manque de données comparatives est flagrant. Afin de permettre la validation, voire l'amélioration des corrélations proposées, surtout en ce qui a trait aux jets vers le bas, l'obtention de données complémentaires avec des plages de conditions d'opération plus vaste (e.g. taille d’injecteur plus gros) serait bénéfique.

En général, il y a un grand besoin de générer plus de données sous des conditions de pression et température élevées. L'approche proposée permet dans une certaine mesure l'opération à

n'importe quelle température et pression, cependant afin de modifier la position de l'injecteur et son diamètre, l'accès à l'injecteur et à la sonde même est requis, ce qui rend plus laborieuse l'opération à température élevée.

Finalement, il persiste une grande interrogation quant à l'importance de l'orientation des buses d'injection et la performance des réacteurs. Des études comparatives et simulations seraient souhaitables afin d'établir sous quelles conditions une orientation d'injecteur est préférable. Sur le plan expérimental, le choix de réaction type est crucial afin qu'elle permette suffisamment de sensibilité aux conditions d'injection pour en permettre une comparaison efficace. Certains aspects relatifs à la taille pourraient compliquer l'effort: un lit trop court pour des jets orientés vers le haut pourrait donner lieu à beaucoup de renardage, voire même des fontaines, et invalider les comparaisons.

LISTE DES RÉFÉRENCES

Abba, I.A., 2001. A Generalized Fluidized Bed Reactor Model across the Flow Regimes, PhD Thesis, University of British Columbia, Vancouver, BC, Canada.

Abrahamsen, A.R., Geldart, D., 1980. Behavior of Gas-fluidized Beds of Fine Powders – Part 1. Homogeneous Fluidization. Powder Technology 26, 35–46.

Abramovich, G.N., 1963. The Theory of Turbulent Jets, The M.I.T. Press, Cambridge.

Ariyapadi, S., Holdsworth, D.W., Norley, C.J.D., Berruti, F., Briens, C., 2003. Digital X-ray Imaging Technique to Study the Horizontal Injection of Gas–Liquid Jets into Fluidized Beds. International Journal of Chemical Reactor Engineering 1, A56.

Ariyapadi, S., Berruti, F., Briens, C., McMillan, J., Zhou, D., 2004. Horizontal Penetration of Gas–Liquid Spray Jets in Gas–Solid Fluidized Beds. International Journal of Chemical Reactor Engineering 2, A22.

Basov, V.A., Markhevka, V.I., Melik-Akhnazarov, T.K., Orochko, D.I., 1969. Investigation of the Structure of a Nonuniform Fluidized Bed. International Chemical Engineering 9, 263–266.

Beam, G.M., Wielopolski, L., Gardner, R.P., Verghese, K., 1978. Monte Carlo Calculations of Efficiencies of Right-circular Cylindrical NaI Detectors for Arbitrarily Located Point Sources. Nuclear Instruments and Methods 154, 501–508.

Beeckmans, J.M., Large, J.F., 1988. Estimated Effects of Process Variables on Jet Temperature in a U-Gas Reactor. Industrial & Engineering Chemistry Research 27, 963–969.

Behie, L.A., Bergougnou, M.A., Baker, C.G.J., Bulani, W., 1970. Jet Momentum Dissipation at a Grid of a Larger Gas Fluidized Bed. The Canadian Journal of Chemical Engineering 48, 158–161.

Behie, L.A., Bergougnou, M.A., Baker, C.G.J., Base, T.E., 1971. Further Studies on Momentum Dissipation of Grid Jets in a Gas Fluidizied Bed. The Canadian Journal of Chemical Engineering 49, 557–561.

Benjelloun, F., Liégeois, R., Vanderschuren, J., 1991. Détermination des longueurs de jets de gaz horizontaux dans les lits fluidisés, in: Laguérie, C., Guigon, P. (Eds.), Récents progrès en génie des procédés: La Fluidisation, pp. 108–115.

Berruti, F., Dawe, M., Briens, C., 2009. Study of Gas–Liquid Jet Boundaries in a Gas–Solid Fluidized Bed. Powder Technology 192, 250–259.

Bi, J., Kojima, T., 1996a. Experimental and Numerical Study on Gas Flow in the Grid Zone of Jetting-fluidized Beds. Chemical Engineering Communications 147, 55–73.

Bi, J., Kojima, T., 1996b. Prediction of Temperature and Composition in a Jetting Fluidized Bed Coal Gasifier. Chemical Engineering Science 51, 2745–2750.

Blake, T.R., Webb, H., Sunderland, P.B., 1990. The Nondimensionalization of Equations Describing Fluidization with Application to the Correlation of Jet Penetration Height. Chemical Engineering Science 45, 365–371.

Blake, T.R., Wen, C.Y., Ku, C.A., 1984. The Correlation of Jet Penetration Measurements in Fluidized Beds Using Nondimensional Hydrodynamic Parameters. AIChE Symposium Series 234, 42–51.

Briens, C.L., Bergougnou, M.A., 1984. Grid Leakage (Weeping and Dumping) in a Pilot Plant Size Gas Fluidized Bed. The Canadian Journal of Chemical Engineering 62, 455–463.

Briens, C., Berruti, F., Felli, V., Chan, E., 2008. Solids Entrainment into Gas, Liquid, and Gas–Liquid Spray Jets in Fluidized Beds. Powder Technology 184, 52–57.

Chen, J., Lu, X., Liu, H., Liu, J., 2008. The Effect of Solid Concentration on the Secondary Air-jetting Penetration in a Bubbling Fluidized Bed. Powder Technology 185, 164–169.

Chen, L., Weinstein, H., 1993. Shape and Extent of Voids Formed by a Horizontal Jet in a Fluidized Bed. AIChE Journal 39, 1901–1909.

Chen, L., Weinstein, H., 1997. Temperatire Distribution around Heated Horizontal Jet in Fluidized Bed. AIChE Journal 43, 2373–2375.

Chiba, T., Terashima, K., Kobayashi, H., 1972. Behaviour of Bubbles in Gas–Solid Fluidized Beds: Initial Formation of Bubbles. Chemical Engineering Science 27, 965–972.

Choi, J.H., Son, J.E., Kim, S.D., 1998. Generalized Model for Bubble Size and Frequency in Gas-Fluidized Beds. Industrial & Engineering Chemistry Research 37, 2559–2564.

Chyang, C.S., Chang, C.H., Chang, J.H., 1997. Gas Discharge Modes at a Single Horizontal Nozzle in a Two-dimensional Fluidized Bed. Powder Technology 90, 71–77.

Cleaver, J.A.S., Ghardiri, M., Tuponogov, V.G., Yates, J.G., Cheesman, D.J., 1995. Measurement of Jet Angles in Fluidized Beds. Powder Technology 85, 221–226.

Cui, H., Mostoufi, N., Chaouki, J., 2001a. Gas and Solids Between Dynamic Bubble and Emulsion in Gas-fluidized Beds. Powder Technology 120, 12–20.

Cui, H.P., Mostoufi, N., Chaouki, J., 2001b. Comparison of measurement techniques of local particle concentration for gas–solid fluidization, in: Kwauk, M., Li, J., Yang, W.C. (Eds.), Proceedings of the Tenth Engineering Foundation Conference on Fluidization, (Beijing, China), Engineering Foundation, New York, pp. 779–786.

Dan, S.; Jianzhi, W.; Huilin, L.; Yunhua, Z.; Juhui, C.; Gidaspow, D.; Ming, C., 2010. Numerical Simulation of Gas-particle Flow with a Second-order Moment Method in Bubbling Fluidized Beds. Powder Technology 199, 213-225.

Dawe, M., Briens, C., Berruti, F., 2007. Study of Horizontal Sonic Gas Jets in Gas–Solid Fluidized Beds, in: Berruti, F., Bi, X.(T.), Pugsley, T. (Eds.), Proceedings of the Twelfth Engineering Foundation Conference on Fluidization, (Vancouver, British Columbia, Canada), Engineering Foundation, New York, pp. 783–790.

Degaleesan, S., Dudukovic, M.P., Toseland, B.A., Bhatt, B.L., 1997. A Two-compartment Convective–Diffusion Model for Slurry Bubble Column Reactors. Industrial & Engineering Chemistry Research 36, 4670–4680.

Deole, N.R., 1980. Study of Jets in Three Dimensional Gas Fluidized Beds. M.S. Thesis, West Virginia University, Morgantown, WV, USA.

Din, G.U., Chughtai, I.R., Inayat, M.H., Khan, I.H., 2008. Axial Dispersion, Holdup and Slip Velocity of Dispersed Phase in a Pulsed Sieve Plate Extraction Column by Radiotracer Residence Time Distribution Analysis. Applied Radiation and Isotopes 66, 1818–1824.

Din, G.U., Chughtai, I.R., Inayat, M.H., Khan, I.H., Qazi, N.K., 2010. Modeling of a Two-phase Countercurrent Pulsed Sieve Plate Extraction Column – A Hybrid CFD and Radiotracer RTD Analysis Approach. Separation and Purification Technology 73, 302–309.

Donadono, S., Massimilla, L., 1978. Mechanisms of Momentum and Heat Transfer between Gas Jets and Fluidized Beds, in: Davidson, J.F., Keairns, D.L. (Eds.), Proceedings of the Second

Engineering Foundation Conference on Fluidization, (Cambridge, England), Engineering Foundation, New York, pp. 375–380.

Donsì, G., Massimilla, L., Colantuoni, L., 1980. The Dispersion of Axi-symmetric Gas Jets in Fluidized Beds, in: Grace, J.R., Matsen, J.M. (Eds.), Engineering Foundation Conference on Fluidization of the Third Engineering Foundation Conference on Fluidization, (Henniker, New Hampshire), Engineering Foundation, New York, pp. 297–304.

Dry, R.J., Judd, M.R., 1986. Split Feed Fluidised Bed Reactors: Mass Transfer in the Sparger Region, in: Østergaard, K., Sørensen, A. (Eds.), Proceedings of the Fifth Engineering Foundation Conference on Fluidization, (Elsinore, Denmark), Engineering Foundation, New York, pp. 47–54.

Du, B., Marashdeh, Q., Warsito, W. Park, A.-H.A., Fan, L.-S., 2007. Development of Electrical Capacitance Volume Tomography (ECVT) and Electrostatic Tomography (EST) for 3D Density Imaging of Fluidized Bed System, in: Berruti, F., Bi, X.(T.), Pugsley, T. (Eds.), Proceedings of the Twelfth Engineering Foundation Conference on Fluidization, (Vancouver, British Columbia, Canada), Engineering Foundation, New York, pp. 473–480.

Dubrawski, K., Bi, H.T., Chaouki, J., Ellis, N., Grace, J.R., Kantzas, A., Lim, C., Patience, G.S., Pugsley, T., Zhu, J.X., 2011. Comparison of Invasive and Non-invasive Fluidization Hydrodynamic Measurement Techniques. (manuscript in preparation 2011).

Dudukovic, M.P., Devanathan, N., Holub, R., 1991. Multiphase Reactors. Models and Experimental Verification. Revue de l'Institut Français du Pétrole. 46, 439–465.

Dunn, W.L., Gardner, R.P., 1972. Determination of Intrinsic Gamma-ray Detection Efficiencies for Cylindrical Geiger–Müller Tubes by Monte Carlo Methods. Nuclear Instruments and Methods 103, 373–384.

Filla, M., Massimilla, L., Vaccaro, S., 1983. Gas Jets in Fluidized Beds: The Influence of Particle Size, Shape and Density on Gas and Solids Entrainment. International Journal of Multiphase Flow 9, 259–267.

Filla, M., Massimilla, L., Musmarra, D., Vaccaro, S., 1986. Pressure Fluctuations Associated with Gas Injection in Fluidized Beds, in: Østergaard, K., Sørensen, A. (Eds.), Proceedings of the

Fifth Engineering Foundation Conference on Fluidization, (Elsinore, Denmark), Engineering Foundation, New York, pp. 71–78.

Franz, K., Boerner, T., Kantorek, H.J., Buchholz, R., 1984. Flow Structure in Bubble Columns. German Chemical Engineering 7, 365–374.

Freychet, N., Briens, C.L., Bergougnou, M.A., Large, J.F., 1989. A New Approach to Jet Phenomena Gas Entrainment and Recirculation in a Bidimensional Spouted Fluidized Bed. The Canadian Journal of Chemical Engineering 67, 191–199.

Gbordzoe, E.A.M., Freychet, N., Bergougnou, M.A., Large, J.F., 1988. Gas Transfer between a Central Jet and a Large Two-dimensional Gas-fluidized Bed. Powder Technology 55, 207–222.

Gbordzoe, E.A.M., Bergougnou, M.A., 1990. Mass Transfer from a Central Jet Introduced into a Large Two-dimensional Fluidized Bed. Powder Technology 62, 67–75.

Gharat, S.D., Joshi, J.B., 1992a. Transport Phenomena in Bubble Column Reactors. I. Flow Pattern. Chemical Engineering Journal and the Biochemical Engineering Journal 48, 141–151.

Gharat, S.D., Joshi, J.B., 1992b. Transport Phenomena in Bubble Column Reactors. II. Pressure Drop. Chemical Engineering Journal and the Biochemical Engineering Journal 48, 153–166.

Gidaspow, D., Lin, C., Seo, Y.C., 1983a. Fluidization in Two-dimensional Beds with a Jet. 1. Experimental Porosity Distributions. Industrial & Engineering Chemistry Fundamentals 22; 187–193.

Gidaspow, D., Ettehadieh, B., 1983b. Fluidization in Two-dimensional Beds with a Jet. 2. Hydrodynamic Modeling. Industrial & Engineering Chemistry Fundamentals 22, 193–201.

Godfroy, L., Larachi, F., Chaouki, J., 1999. Position and Velocity of a Large Particle in a Gas/Solid Riser Using the Radioactive Particle Tracking Technique. The Canadian Journal of Chemical Engineering 77, 253–261.

Grace, J.R., Lim, C.J., 1987. Permanent Jet Formation in Beds of Particulate Solids. The Canadian Journal of Chemical Engineering 65, 160–162.

Guo, Q., Liu, Z., Zhang, J., 2000. Flow Characteristics in a Large Jetting Fluidized Bed with Two Nozzles. Industrial & Engineering Chemistry Research 39, 746–751.

Guo, Q., Yue, G., 2001a. Gas Discharge Pattern in a Large Jetting Fluidized Bed with Vertical Nozzle. Industrial & Engineering Chemistry Research 40, 3689–3696.

Guo, Q., Yue, G., Zhang, J., Liu, Z., 2001b. Hydrodynamic Characteristics of a Two-dimensional Jetting Fluidised Bed with Binary Mixtures. Chemical Engineering Science 56, 4685–4694.

Guo, Q., Si, C., Zhang, J., 2010. Flow Characteristics in a Jetting Fluidized Bed with Acoustic Assistance. Industrial & Engineering Chemistry Research 49, 7638–7645.

He, Y.L., Qin, S.Z., Lim, C.J., Grace, J.R., 1994. Particle Velocity Profiles and Solid Flow Patterns in Spouted Beds. The Canadian Journal of Chemical Engineering 72, 561–568.

He, Y.L., Lim, C.J., Qin, S.Z., Grace, J.R., 1998. Spout Diameters in Full and Half Spouted Beds.

The Canadian Journal of Chemical Engineering 76, 702–706.

Hilal, N., Gunn, D.J., 2002. Solid hold up in gas fluidised beds. Chemical Engineering and Processing 41, 373–379.

Hirsan, I., Sishtla, C., Knowlton, T.M., 1980. The Effect of Bed and Jet Parameters on Vertical Jet Penetration Length in Gas Fluidized Beds. Paper presented at 73rd Annual AIChE Meeting (Chicago, Illinois, USA), AIChE.

Hong, R., Li, H., Cheng, M., Zhang, J., 1996. Numerical Simulation and Verification of a Gas–Solid Jet Fluidized Bed. Powder Technology 87, 73–81.

Hong, R., Li, H., Li, H., Wang, Y., 1997. Studies on the Inclined Jet Penetration Length in a Gas–Solid Fluidized Bed. Powder Technology 92, 205–212.

Huang, C.-C., Chyang, C.-S., 1991. Gas Discharge Modes at a Single Nozzle in Two-dimensional Fluidized Beds. Journal of Chemical Engineering of Japan 24, 633–639.

Hutchenson, K.W., La Marca, C., Patience, G.S., Laviolette, J.-P., Bockrath, R.E.,2010. Parametric Study of n-butane Oxidation in a Circulating Fluidized Bed Reactor, Applied Catalysis A: General 376, 91–103.

Hyndman, C.L., Guy, C., 1995. Gas Phase Flow in Bubble Columns: A Convective Phenomenon. The Canadian Journal of Chemical Engineering 73, 426–434.

Indenbirken, M., Schneider, T., Siepmann, V., Strauss, K., 2000. A New Model for the Propagation of Jets in Dilute Gas–Solid Crossflows. The Canadian Journal of Chemical Engineering 78, 468–477.

Kasban, H., Zahran, O., Arafa, H., El-Kordy, M., Elaraby, S.M.S., Abd El-Samie, F.E., 2010. Laboratory Experiments and Modeling for Industrial Radiotracer Applications. Applied Radiation and Isotopes 68, 1049–1056.

Kimura, T., Kojima, T., 1992. Numerical Model for Reactions in a Jetting Fluidized Bed Coal Gasifier. Chemical Engineering Science 47, 2529–2534.

Kimura, T., Matsuo, H., Uemiya, S., Kojima, T., 1994. Measurement of Jet Shape and Its Dynamic Change in Three-dimensional Jetting Fluidized Beds. Journal of Chemical Engineering of Japan 27, 602–609.

Kimura, T., Horiuchi, K., Watanabe, T., Matsukata, M., Kojima, T., 1995. Experimental Study of Gas and Particle Behavior in the Grid Zone of a Jetting Fluidized Bed Cold Model. Powder Technology 82, 135–143.

King, D., 1989. Estimation of Dense Bed Voidage in Fast and Slow Fluidized Beds of FCC Catalyst, in: Grace, J.R., Shemilt, L.W., Bergounou, M.A. (Eds.), Proceedings of the Sixth Engineering Foundation Conference on Fluidization, (Banff, Alberta, Canada), Engineering Foundation, New York, pp. 1–8.

Knowlton, T.M., Hirsan, I., 1980. The Effect of Pressure on Jet Penetration in Semi-cylindrical Gas-fluidized Beds, in: Grace, J.R., Matsen, J.M. (Eds.), Proceedings of the Third Engineering Foundation Conference on Fluidization, (Henniker, New Hampshire), Engineering Foundation, New York, pp. 315–324.

Ku, C.A., 1982. Jetting Phenomena in a High Temperature Fluidized Bed. M.S. Thesis, West Virginia University, Morgantown, WV, USA.

Kuipers, J.A.M., Prins, W., van Swaaij, W.P.M., 1991. Theoretical and Experimental Bubble Formation at a Single Orifice in a Two-dimensional Gas-fluidized Bed. Chemical Engineering Science 46, 2881–2894.

Kuipers, J.A.M., Tammes, H., Prins, W., van Swaaij, W.P.M., 1992. Experimental and Theoretical Porosity Profiles in a Two-dimensional Gas-fluidized Bed with a Central Jet. Powder Technology 71, 87–99.

Larachi, F., Cassanello, M., Chaouki, J., Guy, C., 1996. Flow Structure of the Solids in a 3-D Gas–Liquid–Solid Fluidized Bed. AIChE Journal 42, 2439–2452.

Laviolette, J.P., Patience, G.S., Chaouki, J., 2010. Simultaneous Quantitative Measurement of

Gaseous Species Composition and Solids Volume Fraction in a Gas/Solid Flow. AIChE Journal 56, 2850–2859.

Levenspiel, O., Fitzgerald, T.J., 1983. A Warning on the Misuse of the Dispersion Model. Chemical Engineering Science 38, 489–491.

Li, T., 2009. Numerical Investigation of the Gas/Spray Jet Interaction with Fluidized Beds. PhD Thesis, The University of British Columbia, Vancouver, BC, Canada.

Li, T., Pougatch, K., Salcudean, M., Grecov, D., 2008. Numerical Simulation of Horizontal Jet Penetration in a Three-dimensional Fluidized Bed. Powder Technology 184, 89–99.

Lin, W., Weinell, C.E., Hansen, P.F.B., Dam-Johansen, K., 1999. Hydrodynamics of a Commercial Scale CFB Boiler-study with Radioactive Tracer Particles. Chemical Engineering Science 54, 5495–5506.

Luo, C.-H., Uemiya, S., Kojima, T., 1997. Dynamic Behavior and Solid Volume Fraction Distribution in a Jetting Fluidized Bed. Journal of Chemical Engineering of Japan 30, 491–499.

Luo, G., Zhang, J.-Y., Guo, Q., Zhang, B., 1999. Study on Jet Flow from Two Vertical Nozzles in a 500 mm I.D. Semi-circular Fluidized Bed. Chemical Engineering & Technology 22, 247–251.

Luo, H., Svendsen, H.F., 1991. Turbulent Circulation in Bubble Columns from Eddy Viscosity Distributions of Single-phase Pipe Flow. The Canadian Journal of Chemical Engineering 69, 1389–1394.

Madonna, L.A., Lama, R.F., Brisson, W.L., 1961. Solids–Air Jets. British Chemical Engineering 6, 524–528.

Massimilla, L., Donsì, G., Migliaccio, N., 1981. The Dispersion of Gas Jets in Two-dimensional, Fluidized Beds of Coarse Solids. AIChE Symposium Series 77, 17–27.

Massimilla, L., 1985. Gas Jets in Fluidized Beds, in: Davidson, J.F., Clift, R., Harrison, D. (Eds.), Fluidization, second ed. Academic Press, London, pp. 133–172.

McMillan, J., 2007. Characterization of the Interactions between High Velocity Jets and Fluidized Particles. PhD Thesis, The University of Western Ontario, London, ON, Canada.

McNeil, K.M., Hancock II, A.W., Zenz, F.A., 1984. Flow Phenomena in a Two-dimensional Fluidized Bed, Powder Technology 38, 101–105.

Menzel, T., In der Weide, T., Staudacher, O., Wein, O., Onken, U., 1990. Reynolds Shear Stress for Modeling of Bubble Column Reactors. Industrial & Engineering Chemistry Research 29, 988–994.

Merry, J.M.D., 1971. Penetration of a Horizontal Gas Jet into a Fluidized Bed. Transactions of the Institution of Chemical Engineers 49, 189–195.

Merry, J.M.D., 1975. Penetration of Vertical Jets into Fluidized Beds. AIChE Journal 21, 507–510.

Miller, D.R., 1962. Injection Mixing of Gaseous Reactants. Chemical Engineering Progress 58, 77–84.

Molodtsof, Y., Labidi, F., 1995. Jets in Fluidized Beds: Flow Structure and Gas Mixing, in: Large, J.F., Laguérie, C. (Eds.), Proceedings of the Eighth Engineering Foundation Conference on Fluidization, (Tours, France), Engineering Foundation, New York, pp. 279–285.

Morooka, S., Ushida, K., Kato, Y., 1982. Recirculating Turbulent Flow of Liquid in Gas–Liquid–Solid Fluidized Bed. Journal of Chemical Engineering of Japan 15, 29–34.

Mudde, R.F.; Harteveld, W.K.; van den Akker, H.E.A.; van der Hagen, T.H.J.J.; van Dam, H., 1999. Gamma Radiation Densitometry for Studying the Dynamics of Fluidized Beds. Chemical Engineering Science 54, 2047–2054.

Müller, C.R., Holland, D.J., Sederman, A.J., Mantle, M.D., Gladden, L.F., Davidson, J.F., 2008. Magnetic Resonance Imaging of Fluidized Beds. Powder Technology 183, 53–62.

Müller, C.R., Holland, D.J., Davidson, J.F., Dennis, J.S., Gladden, L.F., Hayhurst, A.N., Mantle, M.D., Sederman, A.J., 2009. Geometrical and Hydrodynamical Study of Gas Jets in Packed and Fluidized Beds Using Magnetic Resonance. The Canadian Journal of Chemical Engineering 87, 517–525.

Mumuni, I.I., Dagadu, C.P.K., Danso, K.A., Adu, P.S., Affum, H.A., Lawson, I., Appiah, G.K., Coleman, A., Addo, M.A., 2011. Radiotracer Investigation of Clinker Grinding Mills for Cement Production at GHACEM. Research Journal of Applied Sciences, Engineering and Technology 3, 26–31.

Musmarra, D., Vaccaro, S., Filla, M., Massimilla, L., 1992. Propagation Characteristics of Pressure Disturbances Originated by Gas Jets in Fluidized Beds. International Journal of Multiphase Flow 18, 965–976.

Musmarra, D., 2000. Influence of Particle Size and Density on the Jet Penetration Length in Gas Fluidized Beds. Industrial & Engineering Chemistry Research 39, 2612–2617.

Nigam, K.D.P., Saroha, A.K., Kundu, A., Pant, H.J., 2001. Radioisotope Tracer Study in Trickle Bed Reactors. The Canadian Journal of Chemical Engineering 79, 860–865.

Oki, K., Ishida, M., Shirai, T., 1980. The Behaviour of Jets and Particles near the Gas Distributor in a Three-dimensional Fluidized Bed, in: Grace, J.R., Matsen, J.M. (Eds.), Proceedings of the Third Engineering Foundation Conference on Fluidization, (Henniker, New Hampshire), Engineering Foundation, New York, pp. 421–428.

Pablo Ramírez, F., Eugenia Cortés, M., 2004. The Determination of Residence Times in a Pilot Plant. Nuclear Instruments and Methods in Physics Research B 213, 144–148.

Pant, H.J., Sharma, V.K., Nair, A.G.C., Tomar, B.S., Nathaniel, T.N., Reddy, A.V.R., Singh, G.,2009a. Application of ^{140}La and ^{24}Na as Intrinsic Radiotracers for Investigating Catalyst Dynamics in FCCUs. Applied Radiation and Isotopes 67, 1591–1599.

Pant, H.J., Sharma, V.K., Vidya Kamudu, M., Prakash, S.G., Krishanamoorthy, S., Anandam, G., Seshubabu Rao, P., Ramani, N.V.S., Singh, G., Sonde, R.R., 2009b. Investigation of Flow Behaviour of Coal Particles in a Pilot-scale Fluidized Bed Gasifier (FBG) Using Radiotracer Technique. Applied Radiation and Isotopes 67, 1609–1615.

Pant, H.J., Yelgoankar, V.N., 2002. Radiotracer Investigations in Aniline Production Reactors. Applied Radiation and Isotopes 57, 319–325.

Patience, G.S., 1990. Circulating Fluidized Beds: Hydrodynamics and Reactor Modelling. PhD Thesis, École Polytechnique de Montréal, Montréal, QC, Canada.

Patience, G., Chaouki, J., 1993. Gas Phase Hydrodynamics in the Riser of a Circulating Fluidized Bed. Chemical Engineering Science 48, 3195–3205.

Patience, G.S., Bockrath, R.E., 2010. Butane Oxidation Process Development in a Circulating Fluidized Bed. Applied Catalysis A: General 376, 4–12.

Patil, D.J.; van Sint Annaland, M.; Kuipers, J.A.M., 2005. Critical Comparison of Hydrodynamic Models for Gas–Solid Fluidized Beds - Part I: Bubbling Gas–Solid Fluidized Beds Operated with a Jet. Chemical Engineering Science 60, 57-72.

Pei, P., Zhang, K., Yu, B., Gao, J., Wu, G., Wen, D., 2011. Dynamic Characteristics of Binary Mixtures in a Two-jet Fluidized Bed. Chemical Engineering Science 66, 1702–1714.

Pell, M., 1990. Gas Fluidization, Elsevier, Amsterdam.

Pore, M., Holland, D.J., Chandrasekera, T.C., Müller, C.R., Sederman, A.J., Dennis, J.S., Gladden, L.F., Davidson, J.F., 2010. Magnetic Resonance Studies of a Gas–Solids Fluidised Bed: Jet–Jet and Jet–Wall Interactions. Particuology 8, 617–622.

Pougatch, K., 2011. Mathematical Modelling of Gas and Gas–Liquid Jets Injected into a Fluidized Bed. PhD Thesis, The University of British Columbia, Vancouver, BC, Canada.

Pougatch, K., Salcudean, M., 2010. Numerical Simulation of Liquid Spray Dispersion in a Fluidized Bed. The Canadian Journal of Chemical Engineering 88, 648–654.

Radmanesh, R., Sauriol, P., 2001. Évaluation du mélange de la phase liquide d'un lit fluidisé triphasique par traçage radioactif. (unpublished results).

Raghunathan, K., Mori, H., Whiting, W.B., 1988. A Technique for Measurement of Jet Penetration in Hot Fluidized Beds. Industrial & Engineering Chemistry Research 27, 1011–1016.

Rees, A.C., Davidson, J.F., Dennis, J.S., Fennell, P.S., Gladden, L.F., Hayhurst, A.N., Mantle, M.D., Müller, C.R., Sederman, A.J., 2006. The Nature of the Flow just Above the Perforated

Plate Distributor of a Gas-fluidised Bed, as Imaged Using Magnetic Resonance. Chemical Engineering Science 61, 6002–6015.

Roach, P.E., 1993. Differentiation between Jetting and Bubbling in Fluidized Beds. International Journal of Multiphase Flow, 19, 1159–1161.

Rowe, P.N., MacGillivray, H.J., Cheesman, D.J., 1979. Gas Discharge from an Orifice into a Gas Fluidised Bed. Transactions of the Institution of Chemical Engineers 57, 194–199.

Ruud van Ommen, J., Pfeffer, R., 2010. Fluidization of Nanopowders: Experiments, Modeling, and Applications, in: Kim, S.D., Kang, Y., Lee. J.K., Seo, Y.C. (Eds.), Proceedings of the Thirteenth Engineering Foundation Conference on Fluidization, (Gyeong-ju, Korea), Engineering Foundation, New York, pp. 479–486.

Samuelsberg, A., Hjertager, B.H., 1996. Computational Modeling of Gas/Particle Flow in a Riser. AIChE Journal 42, 1536–1546.

Santos, V.A., Dantas, C.C., 2004. Transit Time and RTD Measurements by Radioactive Tracer to Assess the Riser Flow Pattern. Powder Technology 140, 116–121.

Sauriol, P., Cui, H., Chaouki, J., 2011a. Gas–Solid Structure in the Vicinity of a Sparger Nozzle in a Fluidized Bed. Powder Technology. (soumis en aout 2011)

Sauriol, P., Cui, H., Chaouki, J., 2011b. Gas Jet Penetration Lengths from Upward and Downward Nozzles in Dense Gas–Solid Fluidized Beds. Chemical Engineering Science. (soumis en aout 2011)

Seville, J.P.K., Morgan, J.E.P., Clift, R., 1986. Tomographic Determination of the Voidage Structure of Gas Fluidised Beds in the Jet Region, in: Østergaard, K., Sørensen, A. (Eds.), Proceedings of the Fifth Engineering Foundation Conference on Fluidization, (Elsinore, Denmark), Engineering Foundation, New York, pp. 87–94.

Shen, Z., Briens, C.L., Kwauk, M., Bergougnou, M.A., 1990a. Study of a Downward Grid Jet in a Large Two-dimensional Gas-fluidized Bed. Powder Technology 62, 227–234.

Shen, Z., Briens, C.L., Kwauk, M., Bergougnou, M.A., 1990b. Study of a Downward Gas Jet in a Two-dimensional Fluidized Bed. The Canadian Journal of Chemical Engineering 68, 534–540.

Shen, Z., Briens, C.L., Bergougnou, M.A., Kwauk, M., 1991. Jet Presence Probability in a Two-dimensional Fluidized Bed. Powder Technology 67, 93–101.

Sit, S.-P., Grace, J.R., 1981. Hydrodynamics and Mass Transfer in the Distributor Zone of Fluidized Beds, in: 2nd World Congress of Chemical Engineering, pp. 81–84.

Sit, S.-P., Grace, J.R., 1986. Interphase Mass Transfer during Bubble Formation in Fluidized Beds, in: Østergaard, K., Sørensen, A. (Eds.), Proceedings of the Fifth Engineering Foundation Conference on Fluidization, (Elsinore, Denmark), Engineering Foundation, New York, pp. 39–46.

Sotudeh-Gharebaagh, R., 1998. Combustion of Natural Gas in a Turbulent Fluidized Bed Reactor, PhD Thesis, École Polytechnique de Montréal, Montréal, QC, Canada.

Sotudeh-Gharebaagh, R., Chaouki, J., 2000. Gas Mixing in a Turbulent Fluidized Bed Reactor. The Canadian Journal of Chemical Engineering 78, 65–74.

Stegowski, Z., Furman, L., 2004. Radioisotope Tracer Investigation and Modeling of Copper Concentrate Dewatering Process. International Journal of Mineral Processing 73, 37–43.

Vaccaro, S., Musmarra, D., Costanza, F., Filla, M., Massimilla, L., 1989. Diagnostics of Gas Injection in Fluidized Beds by Pressure Signal Analysis, in: Grace, J.R., Shemilt, L.W., Bergounou, M.A. (Eds.), Proceedings of the Sixth Engineering Foundation Conference on Fluidization, (Banff, Alberta, Canada), Engineering Foundation, New York, pp. 245–252.

Vaccaro, S., 1997. Analysis of the Variables Controlling Gas Jet Expansion Angles in Fluidized Beds. Powder Technology 92, 213–222.

Vaccaro, S., Musmarra, D., Petrecca, M., 1997a. Evaluation of the Jet Penetration Depth in Gas-fluidized Beds by Pressure Signal Analysis. International Journal of Multiphase Flow 23, 683–698.

Vaccaro, S., Musmarra, D., Petrecca, M., 1997b. A Technique for Measurement of the Jet Penetration Height in Fluidized Beds by Pressure Signal Analysis. Powder Technology 92, 223–231.

Wang, C.H., Zhong, Z.P., Li, R., E, J.Q., 2010. Prediction of Jet Penetration Depth Based on Least Square Support Vector Machine. Powder Technology 203, 404–411.

Wang, F., Yu, Z., Marashdeh, Q., Fan, L.-S., 2010. Horizontal Gas and Gas/Solid Jet Penetration in a Gas–Solid Fluidized Bed. Chemical Engineering Science 65, 3394–3408.

Wen, C.Y., Horio, H., Krishnan, R., Khosravi, R., Rengarajan, P., 1977. Jetting Phenomena and Dead Zone Formation on Fluidized Bed Distributors, in: The Second Pacific Chemical Engineeering Congress (Denver, Colorado), AIChE, New York, pp. 1182–1189.

Wen, C.Y., Deole, N.R., Chen, L.H., 1982. A Study of Jets in a Three-dimensional Gas Fluidized Bed. Powder Technology 31, 175–184.

Wu, C.-S.; Whiting, W.B., 1988. Interacting Jets in a Fluidized Bed. Chemical Engineering Communications 73, 1-17.

Xuereb, C., Laguérie, C., Baron, T., 1991a. Étude du comportement des jets continus horizontaux ou inclinés introduits dans un lit fluidisé par un gaz, I: Morphologie des jets. Powder Technology 67, 43–56.

Xuereb, C., Laguérie, C., Baron, T., 1991b. Étude du comportement des jets continus horizontaux ou inclinés introduits dans un lit fluidisé par un gaz, Deuxième partie: Profils de vitesse du gaz dans les jets horizontaux. Powder Technology 64, 271–283.

Xuereb, C., Laguérie, C., Baron, T., 1992. Étude du comportement des jets continus horizontaux ou inclinés introduits dans un lit fluidisé par un gaz, III: Modélisation de la zone d'écoulement développé du jet. Powder Technology 72, 7–16.

Yanenko, N.N., 1971. The Method of Fractional Steps: The Solution of Problems of Mathematical Physics in Several Variables, Springer–Verlag, Berlin.

Yang, W.-C., 1981. Jet Penetration in a Pressurized Fluidized Bed. Industrial & Engineering Chemistry Fundamentals 20, 297–300.

Yang, W.-C., Keairns, D.L., 1978a. Design and Operating Parameters for a Fluidized Bed Agglomerating Combustor/Gasifier, in: Davidson, J.F., Keairns, D.L. (Eds.), Proceedings of the Second Engineering Foundation Conference on Fluidization, (Cambridge, England), Engineering Foundation, New York, pp. 208–214.

Yang, W.-C., Keairns, D.L., 1978b. Design of Recirculating Fludidized Beds for Commercial Applications. AIChE Symposium Series 74, 218–228.

Yang, W.-C., Keairns, D.L., 1979. Estimating the Jet Penetration Depth of Multiple Vertical Grid Jets. Industrial & Engineering Chemistry Fundamentals 18, 317–320.

Yang, W.-C., Keairns, D.L., 1980. Momentum Dissipation of and Gas Entrainment into a Gas-fluidized Two-phase Jet in a Fluidized Bed, in: Grace, J.R., Matsen, J.M. (Eds.), Proceedings of the Third Engineering Foundation Conference on Fluidization, (Henniker, New Hampshire), Engineering Foundation, New York, pp. 305–314.

Yang, W.C., Revay, D., Anderson, R.G., Chelen, E.J., Keairns, D.L., Cicero, D.C., 1983. Fluidization Phenomena in a Large Scale Cold Flow Model, in: Kunii, D., Toei, R. (Eds.), Proceedings of the Fourth Engineering Foundation Conference on Fluidization, (Kashikojima, Japan), Engineering Foundation, New York, pp. 77–84.

Yao, B.P., Zheng, C., Gasche, H.E., Hofmann, H., 1991. Bubble Behaviour and Flow Structure of Bubble Columns. Chemical Engineering and Processing 29, 65–75.

Yates, J.G., Bejcek, V., Cheesman, D.J., 1986. Jet Penetration into Fluidized Beds at Elevated Pressures, in: Østergaard, K., Sørensen, A. (Eds.), Proceedings of the Fifth Engineering Foundation Conference on Fluidization, (Elsinore, Denmark), Engineering Foundation, New York, pp. 79–86.

Yates, J.G., Cobbinah, S.S., Cheesman, D.J., Jordan, S.P., 1991. Particle Attrition in Fluidized Beds Containing Opposing Jets. AIChE Symposium Series 87, 13–19.

Yates, J.G., 1996. Effect of Temperature and Pressure on Gas–Solid Fluidization. Chemical Engineering Science 51, 167–205.

Yelgaonkar, V.N., Jayakumar, T.K., Singh, S., Sharma, M.K., 2009. Combination of Sealed Source and Radiotracer Technique to Understand Malfunctioning in a Chemical Plant. Applied Radiation and Isotopes 67, 1244–1247.

Yianatos, J., Contreras, F., Díaz, F., 2010. Gas Holdup and RTD Measurement in an Industrial Flotation Cell. Minerals Engineering 23, 125–130.

Yutani, N., Ho, T.C., Fan, L.T., Walawender, W.P., Song, J.C., 1983. Statistical Study of the Grid Zone Behavior in a Shallow Gas–Solid Fluidized Bed Using a Mini-capacitance Probe. Chemical Engineering Science 38, 575–582.

Zenz, F.A., 1968. Bubble Formation and Grid Design. Institution of Chemical Engineers Symposium Series 30, 136–139.

Zenz, F.A., 1989. Fluidization and Fluid–Particle Systems, PEMM-Corp, Nelsonville, NY.

Zhong, W., Zhang, M., 2005. Jet Penetration Depth in a Two-dimensional Spout–fluid Bed. Chemical Engineering Science 60, 315–327.